UNIVERSIDAD COMPLUTENSE DE MADRID
FACULTAD DE CIENCIAS FÍSICAS

TESIS DOCTORAL

Gamma and fast-timing spectroscopy of exotic tin isotopes around 132Sn

Espectroscopía gamma y de coincidencias ultrarápidas de isótopos de estaño alrededor del 132Sn

MEMORIA PARA OPTAR AL GRADO DE DOCTOR

PRESENTADA POR

Jaime Benito García

Director

Luis Mario Fraile Prieto

Madrid

UNIVERSIDAD COMPLUTENSE DE MADRID
FACULTAD DE CIENCIAS FÍSICAS

TESIS DOCTORAL

Gamma and fast-timing spectroscopy of exotic tin isotopes around 132Sn

Espectoscopía gamma y de coincidencias ultrarápidas de isótopos de estaño alrededor del 132Sn

MEMORIA PARA OPTAR AL GRADO DE DOCTOR

PRESENTADA POR

Jaime Benito García

DIRECTOR

Luis Mario Fraile Prieto

Universidad Complutense de Madrid
Facultad de Ciencias Físicas

Departamento de Estructura de la Materia, Física
Térmica y Electrónica

UNIVERSIDAD
COMPLUTENSE
MADRID

Gamma and fast-timing spectroscopy of exotic tin isotopes around ^{132}Sn

Espectroscopía gamma y de coincidencias ultrarrápidas de isótopos de estaño alrededor del ^{132}Sn

MEMORIA PARA OPTAR AL GRADO DE DOCTOR PRESENTADA POR

Jaime Benito García

Director: Luis Mario Fraile Prieto

September 2020

A mis familia

por todo el apoyo

y a mis amigos

por todos esos buenos momentos.

Lo importante es no dejar de hacerse preguntas

Albert Einstein

Agradecimientos

Por fin llegó ese día que creí que no llegaría nunca, por fin tengo tesis. Este ha sido un camino largo, y difícil a veces. Sin embargo, siento sinceramente que ha merecido la pena. No solo por todo lo que me he aprendido a lo largo de estos años, sino también por lo especial que ha sido toda esta etapa en mi vida a nivel personal. Por ello quiero daros las gracias a todos los que habéis contribuido a que yo pueda sacar esta tesis a lo largo de todos estos años

Al primero que tengo que dar las gracias es por supuesto a mi director Luis Mario. Muchas gracias por ofrecerme la oportunidad de hacer el doctorado en el grupo, por tu guía y toda la ayuda, todas las revisiones de esta tesis. Y sobre todo, gracias por tantas cosas que lo que me has enseñado a lo largo de estos años.

También te agradezco enormemente la oportunidad de ir a tantos experimentos y congresos. No solo he aprendido un montón de cosas, también he podido conocer muchas cosas y lugares fantásticos. Las fondu de queso en Ginebra, las montañas Rocosas, la impresionante Nueva York, las cervezas belgas, la preciosa Venecia, los increíbles paisajes de hielo de Finlandia... Por todos esos sitios y muchos más, MUCHAS GRACIAS Luis Mario.

También quiero agradecer a Monika y a Agnieszka por su ayuda y colaboración, y por las invitaciones a Varsovia para discutir sobre el análisis de los datos y la publicación de sus resultados.

Si por algo todos estos años han sido tan especiales, han sido por supuesto todos mis grandes compañeros con los que me he divertido tanto. Tengo que agradeceros enormemente a todos por conseguir que cada día en facultad mereciese la pena.

A mi compañero desde el inicio hasta el final Víctor, quien inició conmigo toda esta aventura. Irónicamente, a pesar de nuestras bizarras formas de hablar, creo que Víctor es con quien mejor me he llegado a entender. Casi todo lo que sé de detectores y de

informática se lo debo a él. Ha sido un excelente compañero de experimentos, de viajes, de cañas y de conversaciones de historia que solo nos parecen divertidas a nosotros. Muchas gracias Víctor, eres un fenómeno y mejor persona.

Y si hay alguien a quien tengo que agradecer por aguantarme tanto ese es por supuesto Pablo. Ha sido mi compañero de piso, de despacho, de metro, de junta, de tupper... muchas cosas desde luego. Con Pablo siempre había alguien dispuesto para irse de cañas, algún plan divertido, algún viaje pendiente que hacer, alguna que otra voltereta que dar, una colchoneta sobre la que saltar o algo con lo que disfrazarse. La palabra aburrimiento desaparecía del vocavulario con él. Muchas Gracias Pablo, me lo he pasado genial contigo todos estos años.

Y por supuesto he dar un enorme gracias al resto de compañeras del despacho. Las cuales han hecho que ir cada día a la facultad fuera tan divertido. A Vicky, mi "hermana mayor del fast-timing", a quien tengo que agradecer toda la ayuda durante la tesis. Hace ya tiempo que, se fue, pero todavía echamos menos su alegría y sus rocambolescas historias con las que nos entretenía cada día. Muchas gracias por toda tu ayuda a lo largo de la tesis Vicky. Algún día volveremos a ser socios en nuestra granja de "alvacas". A Paula, la gran promotora del combo ganador Cántaro-Suéltate el Pelo, de las cañas en el Calero, y de largos y entretenidos cafés después de comer. Y por supuesto Amaia, mi supercompi del descenso del Sella, "¡Eskuma!, ¡Esquerra!", y como no de nuestras noches estelares en la vía Láctea.

Y no me olvido por supuesto de los geniales Alex y Oli. Con quién siempre se podía contar para ver la última película de Star Wars o de Marvel, descubrirnos divertidos juegos como la Resistencia, y sobre todo para hablar de gatos (Tanto como querais y más).

También quiero agradecer a todos los miembros más seniors que han ido llegando al grupo y han contribuido a enriquecerlo tano: Joaquín, Dani, Raúl y Raúl de Diego.

Muchas gracias a José Manuel, de quién he aprendido una gran cantidad de cosas a raíz de tantas reuniones core. Y por supuesto a Paloma, a quien tanta lata he dado con tanto papeleo de tanto viaje.

Muchas gracias también a todos esos antiguos miembros del GFN, los cuales lo hicieron tan acogedor el en esos primeros años. A Vadym, Fran y Mariano, con sus entretenidas y acaloradas discusiones en la comida. Y por supuesto no puedo dejarme a Mailyn, nuestra simpática gallina cubana.

El tiempo pasa muy rápido, a medida muchos los que estabais al principio se iban yendo, iban llegaban nuevos y más jóvenes, y de repente te conviertes en uno de los veteranos del grupo. Muchas gracias a Miguel, Murias, Victor Jr, Fer, Clara, Andrea todos los nuevos integrantes del grupo que han conseguido que este siga siendo tan especial y divertido.

No me olvido tampoco de todos aquellos que pasaron temporalmente por el grupo, pero dejaron su marca: Jen, Estefanía, Julían, Aidana, Pauline, Araceli. Más allá del GFN también he de agradecer a todos buenos amigos que también han estado allí.

Por supuesto he de agradecer a Jorge, mi otro gran compañero de piso. Con él he compartido también gran cantidad de aventuras, las divertidas noches como estrellas del swing, nuestro camino a Santiago, nuestros días de submarinismo en Alicante, y como no nuestra visita a Pablo en Boston. Has sido un compañero de piso genial.

Muchas gracias a mis amigos del pueblo, en especial a Alejo y a Gio con quienes siempre podía contar para tomar algo cuando volvía a casa. Muchas gracias también a Rocío, Andrés, Gon y Jorge, con quien tan buenos momentos pasé en mis tiempos del grado en la facultad.

Y por supuesto no me olvido de los compañeros del CSIC Silvia y Javi, ni tampoco ese gran par de gallegos Jaco y Leti. Con quienes me hemos compartido tantos buenos días de cañas y de vermut, y que han ayudado a que el Madrid después del covid siga siendo divertido.

Por último, pero no por ello menos importante, no puedo olvidarme de mi familia. Muchisimas gracias por todo el apoyo que me han dado para que yo siguiese este camino. Especialmente quiero dar las gracias a mi madre por todo su cariño, constante preocupación y apoyo. Y a mi hermana Ana por ese arte y esa alegría que tanto he admirado siempre, y que tanto han animado la casa.

¡Muchísimas gracias a todos!

Summary

The evolution of the nuclear shell structure for nuclei with large neutron to proton ratios is an open problem in contemporary nuclear physics research. The study of the regions around exotic doubly-magic nuclei plays an important role in the understanding of how shell structure evolves, and provides key input for theoretical calculations, which can be then used over larger areas of the nuclear chart.

The present PhD work is focused on the study of the nuclear structure in the region around ^{132}Sn (Z=50 and N=82), the heaviest doubly-magic nucleus away from stability within reach at current experimental facilities.

The nucleus ^{132}Sn itself is of importance for the description of the exotic nuclear region around $N = 82$ and to provide insight into particle-hole couplings for both protons and neutrons. The nuclei with a valence particle or hole around ^{132}Sn are relevant for investigating the single-particle states in the region, and the matrix elements of the electromagnetic transitions interconnecting them. These observables are the main ingredients in large-scale shell-model calculations performed to understand the nuclear structure in the region. In addition, the study of nuclei with a few nucleons outside doubly-magic closed shells provides information about nucleon-nucleon correlations, and the onset of quadrupole collectivity close to magic numbers.

The region is also known to play an important role in the astrophysical rapid neutron capture process (r-process), which impacts elemental abundances in the solar system. The strength of shell closures away from stability influences the r-process path while the β-decay rates determine the relative abundances between the different elements. Moreover, beta-delayed neutron emission provides a delayed flux of neutrons once the initial neutron flux and temperature is turned off in the stellar environment. All these properties have an influence on the final abundance patterns.

In this PhD thesis we have investigated the nuclear structure of the tin isotopes ^{131}Sn, ^{132}Sn, ^{133}Sn and ^{134}Sn, populated in the β decay of $^{131-135}$In. Low-energy beams of radioactive indium ions were produced at the ISOLDE facility, at CERN, in the framework of a systematic β-decay investigation of exotic Sn isotopes around ^{132}Sn.

The measurements were performed at the ISOLDE Decay Station (IDS). The detector set-up consisted of 4 HPGe clover detectors, with outstanding energy resolution, aimed at γ-ray spectroscopy. Three scintillator detectors with excellent timing properties were also coupled to the set-up, including two $LaBr_3$(Ce) crystals, as γ-ray detectors, and a thin plastic scintillator for the detection of β-particles. The purpose of the latter was the measurement of lifetimes of excited levels by means of fast-timing methods. A complete set of programs has been written to perform the data analysis and derive the lifetime information of the levels under study. Additionally, a new methodology has been implemented to account and correct for the contributions of Compton background in the fast-timing measurements.

The excited structure of ^{132}Sn was studied in detail. It was populated both in the β decay of ^{132}In but also in the β-n decay of the ^{133g}In $(9/2^+)$ ground state and the ^{133m}In $(1/2^-)$ isomer, thanks to the isomer selection capabilities of the ISOLDE resonant ionization laser ion source (RILIS). A total of 17 new levels and 68 new γ-transitions have been added in the level-scheme of ^{132}Sn. A complete fast-timing investigation of the excited levels in ^{132}Sn has been performed, confirming and extending previous results. An interpretation of the level structure is provided in terms of particle-hole configurations arising from core breaking states both from the $N = 82$ and $Z = 50$ shells across the gap.

The ^{131}Sn isotope has one neutron less than the ^{132}Sn core. Low-lying single-hole configurations, and high-lying core-breaking states coexist in it. The excited levels in ^{131}Sn were populated in the β-decay of the three ^{131}In β-decaying states, ^{131g}In $(9/2^+)$, ^{131m1}In $(1/2^-)$ and ^{131m2}In $(21/2^+)$. The use of RILIS made it possible to disentangle the decay schemes, since it was able to independently ionize ^{131m1}In and ^{131g}In. The level-scheme of ^{131}Sn has been notably expanded in the work of this thesis, with the addition of 28 new γ-lines and 22 new excited levels. Thanks to the isomer selectivity, the direct β-feeding contributions from each ^{131}In β-decaying state was determined separately. The analysis led to an important revision of the logft values for the Gamow-Teller

and first forbidden transitions between single-hole states in the ^{131}In$\rightarrow^{131}$Sn β-decay, solving the discrepancy observed in previous studies. On the other hand, a large number of states located more than 2 MeV above the neutron separation energy that decay via γ-ray emission were observed. Our study indicates a strong correlation between the γ-ray competition and the existence of lower lying levels with similar spin in ^{130}Sn. The a short half-life of 18(4) ps was measured for the single-hole 332-keV $(1/2^+)$ state, confirming the enhanced *l-forbidden* M1 character for the 332 keV $\nu 3s_{1/2} \rightarrow \nu 3d_{3/2}$ transition. Additionally, half-lives below the ns range for the high-spin levels populated in ^{131m2}In decay have been measured for the first time.

Regarding the ^{133}Sn and ^{134}Sn tin isotopes, we have focused our study on the lifetimes of their excited levels. In ^{133}Sn a half-life of 25(12) ps was measured for the 854-keV $\nu p_{3/2}$ single particle state. This short half-life is in agreement with previous measurements, and also with the expected B(E2) transition rate for the single-particle $\nu p_{3/2} \rightarrow \nu f_{7/2}$ transition. On the other hand, the half-lives of all three states in ^{134}Sn arising from the $\nu f_{7/2}^2$ configuration have been measured. The result for the 2^+ state confirms the B(E2) rate previously measured by Coulomb excitation. For the 4^+ state we performed the first experimental measurement, yielding a half-life of 1.18(4) ns. A half-life of 81.7(12) ns was derived for the 6^+ level, with higher precision than previous measurements. In general the B(E2) reduced transition probabilities are systematically lower than those measured for similar two nucleons systems in the ^{132}Sn and ^{208}Pb regions. The available theoretical calculations do not fully reproduce the results, and in particular underestimate the B(E2; $4^+ \rightarrow 2^+$) transition rate.

As a result from our investigation the half-lives for the indium β-decaying states have also been measured. In this PhD thesis, we report new or more precise values for the half-lives of the ^{132}In g.s. and for the three β-decaying states of ^{131}In. The β-delayed neutron emission probabilities have also been deduced from the gamma intensities. Independent P_n values for the three ^{131}In β-decaying states have been derived, separately for the first time in this work, yielding $P_n[^{131g}\text{In}]$=2.4(6)%, $P_n[^{131g}\text{In}]$=1.2(6)% and $P_n[^{131m2}\text{In}]$=8.9(8)%. In the β-decay of ^{132}In a value of P_n=12(2)% has been obtained. For the decay of ^{133g}In, P_n=90(3)% is obtained, while for ^{133m}In, a P_n=93(3)% has been measured. These results need further confirmation by direct neutron measurements.

In conclusion, the results obtained in this PhD thesis provide a huge amount of new experimental information on the structure of Sn isotopes around the double Z=50, N=82 shell closure. The structure of ^{131}Sn, ^{132}Sn, ^{133}Sn and ^{134}Sn has been investigated. Results regarding the decay of ^{132}In and ^{133}In were summarized in two articles, published in *Physical Review C*.

Resumen

La evolución de la estructura de capas en núcleos exóticos con exceso de neutrones es un tema de investigación de actualidad en física nuclear. El estudio de núcleos situados en las regiones alrededor de los núcleos doblemente mágicos resulta de vital importancia para comprender la evolución de la estructura de capas a medida que nos alejamos del valle de estabilidad. Es además importante para poder realizar cálculos teóricos que puedan extenderse a regiones amplias e inexploradas de la tabla de núcleos.

Esta tesis doctoral se centra en el estudio de la región alrededor de ^{132}Sn (Z=50 y N=82), el núcleo exótico doblemente mágico más pesado al alcance de las instalaciones experimentales actuales. El propio núcleo ^{132}Sn es de gran importancia para entender la estructura nuclear alrededor de N= 82. Sus estados excitados proporcionan información acerca de las posibles excitaciones, tanto de neutrones como por protones, del *core*, que surgen del acoplamiento entre una partícula y un hueco. Los núcleos con una partícula de valencia (o hueco) alrededor de ^{132}Sn son relevantes para investigar los estados de partícula independiente así como las probabilidades reducidas de transición entre ellos. Estos núcleos proporcionan observables que son los ingredientes fundamentales en cálculos de modelo de capas a gran escala, que son de gran utilidad para comprender la estructura nuclear de los núcleos en la región, y otros todavía más exóticos. Los núcleos con unos pocos nucleones (o huecos) acoplados a un doblemente mágico proveen información directa sobre correlaciones nucleón-nucleón y sobre la aparición de efectos cuadrupolares colectivos en el entorno de los números mágicos.

Esta región posee también importancia en el ámbito de la astrofísica nuclear. Esto se debe a su papel en el proceso astrofísico de captura rápida de neutrones (proceso r), el cual influye notablemente en las abundancias de los distintos elementos en el sistema solar. La robustez de los cierres de capas lejos de la estabilidad repercute en el recor-

rido del proceso r, mientras que las vidas medias de desintegración β determinan las abundancias relativas entre los diferentes elementos. Además la desintegración β con emisión retardada de neutrones es responsable del flujo de neutrones una vez que el flujo de neutrones inicial y la temperatura se desactivan en el entorno estelar, por lo que influyen en los patrones de abundancia finales.

En este trabajo de tesis se ha estudiado experimentalmente la estructura nuclear de los isótopos de estaño ^{131}Sn, ^{132}Sn, ^{133}Sn y ^{134}Sn poblados en la desintegración β de isótopos de indio. El experimento se realizó en las instalaciónes de ISOLDE en el CERN, que proporcionó los haces de iones radiactivos de indio a baja energía. Este experimento se llevó a cabo en el contexto de una investigación global de isótopos exóticos de Sn alrededor del ^{132}Sn.

Las medidas experimentales se llevaron a cabo en la IDS, la estación de desintegración de ISOLDE. Entre los detectores de radiación empleados en el experimento se incluían 4 detectores cuádruples de HPGe para espectroscopia γ de alta resolución. El sistema experimental incorporaba también dos detectores γ basados en cristales centelladores de $LaBr_3$(Ce) y un plástico centellador delgado como detector β. Los tres detectores de centelleo se caracterizaban por su excelente respuesta temporal, con el objetivo de realizar medidas de vidas medias de estados excitados nucleares por medio de la técnica de coincidencias ultrarrápidas. En el transcurso de esta tesis se han desarrollado una serie de herramientas y programas con el objeto de llevar a cabo el análisis de datos. Además, se ha implementado una nueva metodología para estimar y corregir la contribución de fondo Compton a las medidas de tiempos.

La estructura del ^{132}Sn se ha estudiado en detalle. Sus estados excitados se poblaron tanto en la desintegración β de ^{132}In como en la desintegración β-n del ^{133}In. El uso de RILIS permitió separar la desintegración beta del estado fundamental $(9/2^+)$ de la del isómero $(1/2^-)$ del ^{133}In. En el esquema de niveles del ^{132}Sn se han añadido un total de 17 niveles y 68 nuevas transiciones γ. También se ha realizado una investigación completa de las vidas medias de los niveles excitados del ^{132}Sn, confirmando y ampliando los resultados anteriores. Se ha interpretado la estructura del núcleo en función de configuraciones partícula hueco que surgen de la ruptura de las capas cerradas tanto de la $N = 82$ de los neutrones como de la $Z = 50$ de los protones.

El isótopo ^{131}Sn tiene un neutrón menos que el núcleo ^{132}Sn, lo que da lugar a configuraciones de partícula independiente con un solo hueco en $N = 82$, junto a estados a más alta energía que provienen de la ruptura del *core*. En este trabajo los niveles excitados en ^{131}Sn se poblaron en la desintegración β de tres estados diferentes del ^{131}Sn, el estado fundamental ^{131g}In $(9/2^+)$, y los isómeros ^{131m1}In $(1/2^-)$ y ^{131m2}In $(21/2^+)$. El uso de RILIS nos ha permitido desenmarañar los esquemas de desintegración, ya que fue posible la ionización independiente de ^{131m1}In y ^{131g}In gracias a RILIS. El esquema de niveles de ^{131}Sn se ha ampliado notablemente en esta tesis añadiendo 28 transiciones γ y 22 nuevos niveles excitados. Con la selección isomérica fue posible identificar la alimentación β desde cada uno de los estados. Nuestro análisis supone una importante revisión de los valores $\log ft$ de las transiciones Gamow-Teller y primeras prohibidas entre los estados de partícula independiente en la desintegración β ^{131}In $\rightarrow$ ^{131}Sn, resolviendo así las inconsistencias de estudios previos. Por otro lado se ha observado un gran número de estados ubicados más de 2 MeV por encima de la energía de separación de neutrones que se desintegran por emisión de radiación electromagnética. Nuestro estudio indica que existe una fuerte correlación entre la emisión de rayos γ desde estos estados no ligados para emisión de neutrones y la existencia de niveles de más baja energía en ^{130}Sn con valores similares de espín. Para el estado de partícula independiente $(1/2^+)$ a 332 keV (hueco de neutrones) se midió una vida media muy corta de 18(4), confirmando el carácter de transición M1 prohibida en l para la transición $\nu 3s_{1/2} \rightarrow \nu 3d_{3/2}$ de 332 keV. Además se han medido por primera vez vidas medias por debajo del rango de ns para los niveles de alto espín poblados en la desintegración del ^{131m2}.

En cuanto a los isótopos ^{133}Sn y ^{134}Sn, esta tesis se centra en el estudio de las vidas de sus estados excitados. En el ^{133}Sn se ha medido una vida media de 25(12) ps para el estado de partícula independiente $\nu p_{3/2}$ de 854 keV. Esta corta vida media está de acuerdo con las medidas publicadas así como con la probabilidad reducida de transición B(E2) esperada para la transición $\nu p_{3/2} \rightarrow \nu f_{7/2}$ entre estados con un sólo neutrón desapareado.

Por otro lado, se han medido las vidas medias de los tres estados de la configuración $\nu f_{7/2}^2$ en el ^{134}Sn. El resultado para el estado 2^+ confirma la probabilidad reducida de transición B(E2) medida previamente por excitación coulombiana. Para el estado 4^+ hemos realizado la primera medida experimental del período de semidesintegración, que

da como resultado 1.18(4) ns. También se ha obtenido un valor de 81.7(12) ns para el nivel 6^+, de mayor precisión que anteriores medidas. En general las probabilidades reducidas de transición B(E2) son sistemáticamente menores que las que se han medido para sistemas de dos nucleones similares en las regiones del ^{132}Sn y el ^{208}Pb. Los cálculos teóricos disponibles no reproducen plenamente los resultados y, en particular, subestiman la probabilidad transición de B(E2; $4^+ \rightarrow 2^+$).

Es también de señalar que en esta tesis se han medido las vidas medias de los estados de isótopos de indio que sufren desintegración β, con valores más precisos o nuevos de las vidas medias del estado fundamental del ^{132}In y de los tres estados ^{131}In. Por otra parte, también se ha estimado la probabilidad de emisión de neutrones a partir de las intensidades γ. Se han encontrado valores P_n para los tres estados que sufren desintegración β del ^{131}In, por primera vez de manera separada, resultando en $P_n[^{131g}\text{In}]$=2.4(6)%, $P_n[^{131g}\text{In}]$=1.2(6)% y $P_n[^{131m2}\text{In}]$=8.9(8)%. En la desintegración β del ^{132}In se ha obtenido un valor P_n=12(2)%. En el caso del ^{133g}In el resultado es P_n=90(3)% mientras que para el isómero ^{133m}In se ha medido P_n=93(3)%. Estos resultados tendrán que ser confirmados con medidas directas con espectroscopía de neutrones.

En conclusión, los resultados obtenidos en esta tesis proporcionan información nueva sobre la estructura de los isótopos de Sn en torno al doble cierre de capas Z=50 y N=82. Se ha investigado la estructura nuclear del ^{131}Sn, ^{132}Sn, ^{133}Sn y ^{134}Sn. Los resultados sobre la desintegración de ^{132}In e ^{133}In fueron recogidos en dos artículos que ya han sido publicados en *Physical Review C*.

Contents

1

Introduction

More than a century after its discovery by Rutherford [Rut11] the atomic nucleus remains one of most remarkable and challenging physical systems. It provides a unique playground for the competition of three of the interactions of Nature, the electromagnetic, the weak and the strong force. A wide range of quantum phenomena related to single particle and to many-body behaviour compete in the nucleus, leading to pairing effects, collective excitations, deformation, particle emission and other features.

The interaction between the nucleons, the fermions that constitute the nucleus, and its impact on nuclear properties still remains a challenge. In particular the evolution of nuclear structure far off the valley of stability, and its link to the fundamental nucleon-nucleon interaction, is one of the fundamental questions in nuclear physics.

Not long after the discovery of the atomic nucleus, a shell structure, mirroring the one established for atomic electrons, was proposed for the nucleus. Based on the isotonic nuclear abundances and on nuclear binding energies, K. Guggenheimer [Gug34a, Gug34b] and W. Elsasser [Els33, Els34a, Els34b], respectively, realised that protons and neutrons organize themselves in such a way that there is extra binding energy for nuclei with fixed numbers of protons or neutrons, the so-called magic numbers. Although Elsasser tried to formulate an single-particle model where each nucleon moves independently from the rest in a global potential, the correct explanation of the magic numbers did not succeed until the shell model was proposed in 1949 by Goeppert Mayer [May49] and Haxel, Jensen and Suess [HJS49]. The key ingredient to reproduce the known 2, 8, 20, 28, 50, 82, 126 magic numbers, arising from the shell gaps, was the addition of a spin-orbit term in the potential.

In spite of the success of the shell-model it is now recognized that the magic numbers are not universal, and that far from the valley of stability the known magic numbers disappear and new ones take over. One of the present challenges in modern nuclear-structure studies is the understanding of the evolution of the shell structure for large neutron over proton ratios. The regions around exotic doubly-magic nuclei, with closed neutron and proton shells, play here an important role.

Many efforts are being devoted worldwide to experimental and theoretical research in the regions around the doubly magic ^{78}Ni, ^{100}Sn, ^{132}Sn and ^{208}Pb. Experimental progress has been prominent in some of these areas of the nuclear chart, thanks to the advances of radioactive beam facilities and complementary techniques, which include high-energy and low-energy reactions, mass measurements, hyperfine interactions methods, and beta-decay spectroscopy, to name a few.

The present PhD thesis concentrates on the region around the doubly-magic nucleus ^{132}Sn (Z=50 and N=82), the heaviest doubly-magic nucleus away from stability within reach at current experimental facilities. The nuclides of interest were populated in the β decay of In isotopes, ranging from ^{131}In to ^{135}In.

The structure of ^{132}Sn is in itself important to describe the exotic nuclear region around $N = 82$ and to provide insight into particle-hole couplings for both protons and neutrons. Nuclei with a valence particle or hole around it, such as ^{131}Sn and ^{133}Sn, are relevant for the investigation single-particle states and electromagnetic transitions between them. These observables are the main ingredients in large-scale shell-model calculations performed to understand the nuclear structure in the region. The study of nuclei with a few nucleons outside doubly-magic closed shells, as for example ^{134}Sn, provides direct information about the nucleon-nucleon correlations and the onset of quadrupole collectivity in the vicinity of closed shells.

1.1 The nuclear shell model

The shell-model is one of the cornerstones of nuclear structure, since it provides a way to deal with the many-body problem. In terms of a many-body interaction W, that in first instance can be assumed to be only 2-body –and thus is written $W(i, j)$– a nuclear system with A fermions is described by the Schrödinger equation

$$H\psi_A = \left[\sum_{i=1}^{A} -\frac{\hbar^2}{2m}\Delta_i + \sum_{i<j}^{A} W(i,j)\right]\psi_A = E\psi_A \tag{1.1}$$

Higher order terms can be included in $W(i,j)$, in fact the three-body term is thought to play a major role in nuclear structure far from the valley of stability.

The central hypothesis of the nuclear shell model is the idea that the whole of the nucleons create a mean field in which each nucleon moves independently, and therefore the interaction can be described by a one-body potential that we can represent as $U(i)$. This leads to the expression

$$H\psi_A = \left[\sum_{i=1}^{A}\left(-\frac{\hbar^2}{2m}\Delta_i + U(i)\right) + \sum_{i<j}^{A}(W(i,j) - U(i))\right]\psi_A = [H_0 + V]\psi_A = E\psi_A \tag{1.2}$$

where the Hamiltonian now contains a one-body term H_0 and a residual interaction V. In the extreme single-particle shell model, the residual interaction is neglected, whereas as soon as we depart from stability the (two-body) residual interaction plays a prominent role. Based on the saturation and short-range properties of the nuclear force it is customary to use a Woods-Saxon or harmonic oscillator potential for $U(i)$. Figure 1.1 illustrates the orbitals built using the single-particle Hamiltonian H_0 with the harmonic oscillator potential (left), a Woods-Saxon potential (centre), and a Woods-Saxon potential plus a spin-orbit term (right). Only the latter is able to reproduce the known shell gaps leading to the nuclear magic numbers close to stability.

The independent particle approximation is limited to the vicinity of closed shells and the two-body interaction takes over once we move away from them. As discussed above, the magic numbers are known not to persist far from stability since the nuclear force introduces strong rearrangements of the nucleons.

When dealing with shell-model calculations of nuclei some knowledge of the nucleon-nucleon interaction is required. Since it is not feasible to deal with the full many-body problem, a truncated space containing an inert core and several valence orbitals for neutrons and protons is typically used. Starting from the free nucleon-nucleon interaction an effective interaction is derived using perturbation theory, and including the known (quasi-)symmetries and the exclusion principle. This procedure fails to reproduce saturation properties of nuclei and spin-orbit magic numbers [May48]. The

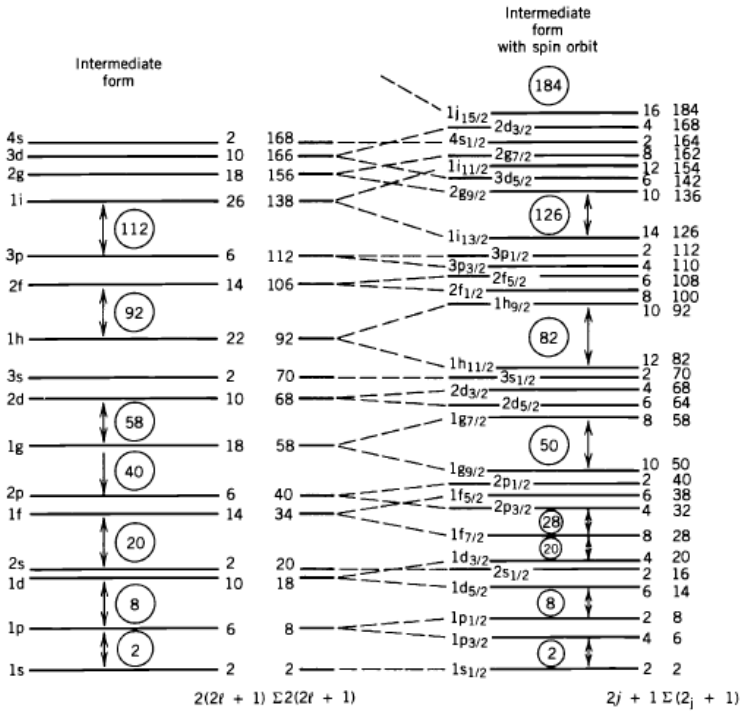

Figure 1.1: Single-particle shell model. (Left) Energy levels calculated using the Wood-Saxon Potential. (Right) Energy levels after including the spin-orbit term. This figure was taken from [Kra88]

restriction of the interaction to a two-body term is most likely at the origin of this problem and the addition of a three-body term has been proposed to better agree with experimental data [FM57].

A way to overcome the deficiency of the two-body effective interaction is to decompose the nuclear Hamiltonian in *multipole* terms. The monopole part represents the spherical mean field, and gives rise to the single particle energies and the global saturation properties. Moreover, it can be adjusted to experimental data to solve the shortcomings of the two-body force. In the case of a two-body interaction, the monopole component of the residual interaction V can be written as an average of the interaction over all possible magnetic substates of two nucleons in the orbits defined for angular momentum j and j', as follows:

$$V_{jj'} = \frac{\sum_J (2J+1) \langle jj' | V | jj' \rangle_J}{\sum_J (2J+1)} \tag{1.3}$$

with J the total angular momentum of the 2-body state (which can span all the allowed values). The above expression can be defined for two equal nucleons, neutrons (n) or protons (p), and for neutron-proton (np) pairs, leading to three potential components in the monopole Hamiltonian. Defining as ϵ_i^ν and ϵ_j^π the single-particle energies for neutrons and protons in a state i or j, respectively, and using the number operators $N_{i,j}^\chi$ to count the number of particles, the monopole Hamiltonian can be written in the following way:

$$\begin{aligned} H_{mon} = &\sum_i \epsilon_i^\nu N_i^\nu + \sum_j \epsilon_j^\pi N_j^\pi + \sum_{ij} V_{ij}^{\nu\pi} N_i^\nu N_j^\pi + \\ &+ \sum_{i \leq i'} V_{ii'}^{\nu\nu} \frac{N_i^\nu (N_{i'}^\nu - \delta_{ii'})}{1 + \delta_{ii'}} + \sum_{j \leq j'} V_{jj'}^{\pi\pi} \frac{N_j^\pi (N_{j'}^\pi - \delta_{jj'})}{1 + \delta_{jj'}} \end{aligned} \tag{1.4}$$

In case many-body interactions need to be considered, then higher order terms in N_i^ν, N_j^π have to be added.

The multipole decomposition provides the procedure within the shell-model framework to account for the effect on a given nucleon in an orbital by the rest of the nucleons. The effective single-particle energy (ESPE), defined as the opposite of the nucleon separation energy for the given orbital, depends linearly on the occupation number and takes account of the energy shift due to the interaction. This can be written as

$$\overline{\epsilon_j^\chi} = \epsilon_j^\chi(A) + \sum_{j'} \sum_{\chi'} V_{jj'}^{\chi\chi'} \langle N_{j'}^{\chi'} \rangle \tag{1.5}$$

where $\epsilon_j^\chi(A)$ refers to the single-particle energy of a given core with A nucleons and the sum indexes run over all valence orbitals above that core. The difference $\overline{\epsilon_j^\chi} - \epsilon_j^\chi(A)$ is usually defined as the *monopole drift*, and characterizes shell evolution in exotic regions of the nuclear chart. It can be sufficiently strong to drive the disappearance of the know magic numbers and the emergence of new ones. In the context of this thesis, the ESPEs of the single neutron-hole states and single neutron-particle states are particularly relevant for ^{131}Sn and ^{133}Sn, respectively.

The monopole part of the nuclear interaction can be decomposed in central, spin-orbit and tensor components. It is not straight-forward to identify the contribution of each of them to the shell evolution in exotic nuclear structure, but it seems that the central part of the interaction is driving the overall behaviour of the ESPEs, while the tensor part is affecting the splitting of ESPEs between spin-orbit partners [OSF+05],

because it acts with opposite sign for spin-orbit partners. This impacts especially the shell gaps that are defined by spin-orbit orbit partners, such as the Z=50 and N=82 ones, relevant for the ^{132}Sn region.

Finally, it should be mentioned that the multipole component of the Hamiltonian takes into account all the correlations between the valence nucleons. These include the important pairing interaction and quadrupole collective effects. Thus, the multipole is responsible for particle-hole excitations across shell gaps, which is important for the structure of ^{132}Sn. The depletion of a shell gap due to monopole drifts can make multipole effects dominant if the correlation energy is sufficiently low. In some regions of the nuclear chart intruder deformed configurations at low energy take over in the ground state. The competition between the monopole component, which pushes the nucleus to be spherical, and the multipole component, which drives it into a deformed shape is a common feature in nuclear structure far off stability and its disentanglement is not an easy task.

1.2 Shell structure in the ^{132}Sn region

As discussed above, the areas of the nuclear chart around doubly-magic nuclei with extreme neutron to proton ratios play a relevant role in the understanding of nuclear structure of exotic nuclei. In these areas the nucleon-nucleon interaction can be investigated, and then used to improve models in order to describe nuclear properties far from the valley of stability.

The heaviest doubly-magic nucleus away from stability that can be reached at present experimentally is ^{132}Sn, with Z=50 and N=82, see Figure 1.2. In the context of the shell model, the spin-orbit force drives the proton $\pi g_{9/2}$ orbital from the $4\hbar\omega$ harmonic oscillator shell down towards the $3\hbar\omega$ shell, and creates the $Z = 50$ shell gap. The situations is similar for the neutrons, with the spin-orbit splitting makes the $N = 82$ magic number by pushing the $\nu h_{11/2}$ orbital down to the $4\hbar\omega$ shell. No evidence has been found of the disappearance of the $Z = 50$ and $N = 82$ shell closures, although the quenching of the N=82 shell below ^{132}Sn has been discussed to explain the r-process $A\sim$130 peak (see below). Collective effects have also been discussed for neutron-rich Sn isotopes with just a few nucleons above ^{132}Sn.

Figure 1.2: Region of nuclei around the doubly magic ^{132}Sn.

Neutron single-particle states in the region can be understood by investigating the structure of ^{133}Sn, while single-hole states are relevant for ESPEs in ^{131}Sn. The reduced probabilities for the electromagnetic transitions between them also provide important information on the structure. Particle-hole couplings for both protons and neutrons across the $Z = 50$ and $N = 82$ shell gaps can be obtained from the spectroscopic investigation of ^{132}Sn itself.

The single-particle states in the region are represented in Figure 1.3 following the procedure described in [GLMP07] and [MNP$^+$95] and employing binding energies from [WAK$^+$17] and the excitation spectra from ^{131}Sn, ^{133}Sn, ^{133}Sb and ^{131}In.

The information on the single-proton states above $Z = 50$, the π $g_{7/2}$, $d_{5/2}$, $d_{3/2}$, $s_{1/2}$ and $h_{11/2}$ orbits, is obtained from the known experimental information on excited states in ^{133}Sb. Above the $g_{7/2}$ ground state, the $d_{5/2}$ and $h_{11/2}$ single-particle states have been known for long [BHR73, SLK$^+$78] from the energies of 962 keV and 2791 keV of excited sates populated in the β decay of ^{133}Sn. The $\pi d_{3/2}$ single-proton state has been later identified at 2440 keV in another β-decay study [SVFM$^+$98]. The single-particle $\pi s_{1/2}$ state remains experimentally unidentified. In [ACC$^+$97] it is fixed to 2800 keV to reproduce the experimental 2150-keV energy of the $1/2^+$ state in ^{137}Cs, which has a

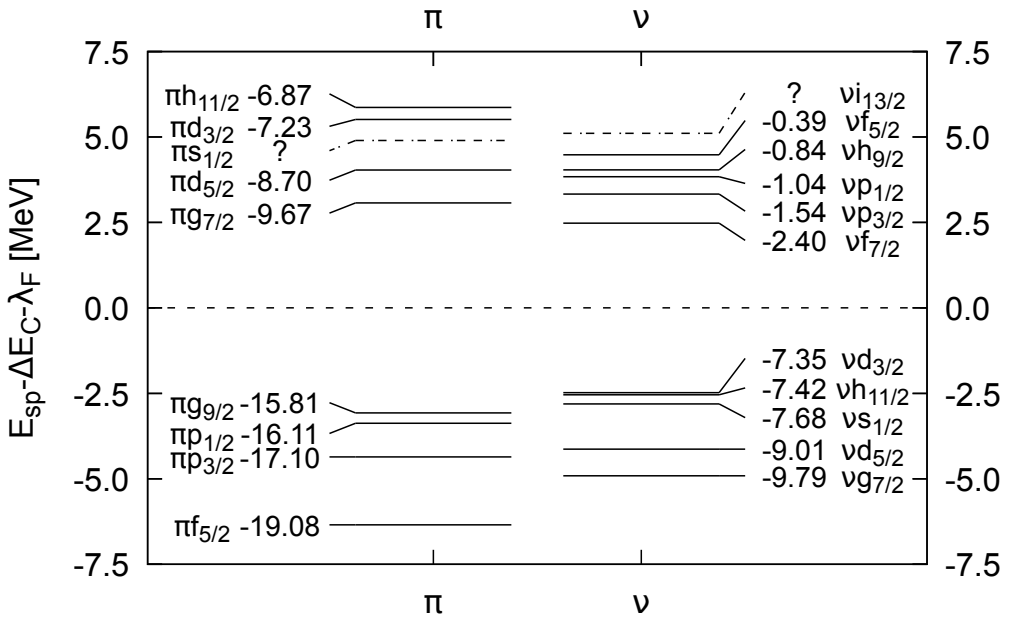

Figure 1.3: Experimental single-particle and single-hole energies for neutrons (ν) and protons (π) in the doubly-magic nucleus ^{132}Sn. Following [GLMP07] the energy origin is set in the center of the shell gap (λ_F) in order to remove Coulomb energy differences ΔE_C. Binding energies are taken from [WAK$^+$17]. The absolute single-particle energies are given in MeV.

dominant single-particle nature.

The single-hole proton states can be obtained from the structure of ^{131}In. All the relevant single-proton hole states have been experimentally established, relative to the $\pi g_{9/2}$, with the $\pi p_{1/2}$ state initially located at 363(37) keV [FZS88] (recently confirmed at 365(8) keV [TJG$^+$16]), and the $p_{3/2}$ at 1353 keV [TJG$^+$14]. More recently the $\pi f_{5/2}$ proton-hole orbital has been found at 2910(50) keV [VJA$^+$20].

The single-particle orbits above the $N = 82$ shell gap have been taken from low-lying states in ^{133}Sn: the $\nu f_{7/2}$ ground state and the $\nu p_{3/2}$, $\nu p_{1/2}$, $\nu h_{9/2}$ and $\nu f_{5/2}$ states at 854, 1367, 1561 and 2005 keV excitation energy [HBH$^+$96, HBH$^+$00, JAB$^+$10, JNA$^+$11, ASB$^+$14, VJD$^+$17]. The purity of the identified single-neutron states was demonstrated by the large spectroscopic factors measured in ^{132}Sn$(d,p)^{133}$Sn neutron transfer [JAB$^+$10]. Some of the single-particle levels have been investigated in the context of the experiment which is the basis of this PhD [PKF$^+$19]. The only single-

particle state that has not been experimentally identified to date is the $\nu i_{13/2}$ one. Although a tentative assignment at 2792 keV was made in [ASB+14], it is not sufficiently firm, and the proposed energy of 2669(70) keV [KBU+15] is based on systematics and excitation energies of neighbouring nuclei.

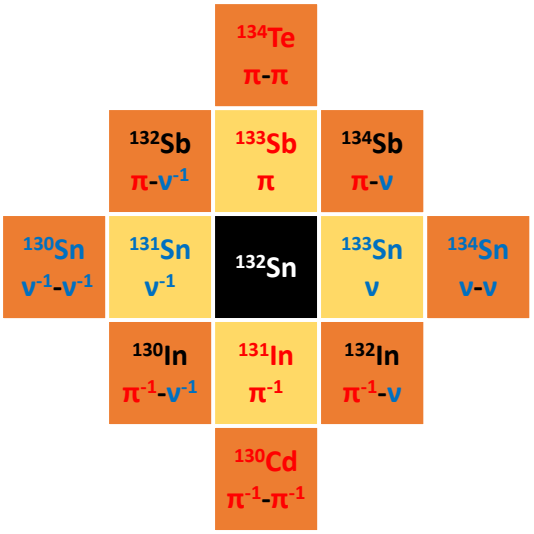

Figure 1.4: Proton and neutron configurations in nuclei around ^{132}Sn. We address ^{131}Sn, ^{132}Sn, ^{133}Sn and ^{134}Sn in this work.

Regarding the one-neutron hole nucleus ^{131}Sn, the ν $d_{3/2}$, $s_{1/2}$, $d_{5/2}$ and $g_{7/2}$ states have been populated in the β-decay of ^{131}In [DGH80, FB84, FGM+04a, DSA+19], ^{248}Cm fission [BDZ+01], ^{130}Sn$(d,p)^{131}$Sn direct neutron transfer reactions [KAA+12], and ^{132}Sn$(d,t)^{131}$Sn neutron pick-up reactions [OPA+18]. Their energies have been precisely determined by γ spectroscopy to be 333 keV ($s_{1/2}$), 1655 keV ($d_{5/2}$) and 2433 keV ($g_{7/2}$) with respect to the $d_{3/2}$ ground state. The position of the $\nu h_{11/2}$ state was suggested at 65 keV [FGM+04a], but has never been confirmed by γ coincidences.

These single particle states are the main ingredients for the description of neutron-rich nuclei around ^{132}Sn, and specifically those investigated in this PhD Thesis. The coupling of valence nucleons (or holes) to the doubly-magic core accounts for the low-lying states in nuclei surrounding ^{132}Sn, see Figure 1.4. In addition, excitations from the $N = 82$ and $Z = 50$ doubly-magic core are observed. In particular, the excited levels in ^{132}Sn can only be built at very high-energies as core-breaking states, leading to particle-hole (p-h) configurations where a proton or a neutron is promoted across the

shell gap. In the surrounding nuclei, such as the tin isotopes ^{131}Sn and ^{133}Sn, high-energy core-excitations built of valence nucleons coupled to the core-excited levels in the ^{132}Sn core are expected. In the case of ^{134}Sn, the coupling of two neutrons to the core leads to a rich variety of states.

1.2.1 Theoretical calculations in the ^{132}Sn region

Nuclei near the doubly-magic ^{132}Sn has triggered a considerable amount of theoretical efforts to understand nuclear structure in this exotic region. Shell model calculations have proven to be successful in the interpretation of the experimental information obtained about excited levels in these nuclei. The single-particle energies described above are one of the basic ingredients in shell model calculations. As already mentioned, the excited levels in the Sn nuclei around ^{132}Sn, can be grouped in two kinds: valence-nucleon excitations and core-breaking configurations. For each kind, different interactions have proven to be better suited for the theoretical description.

A microscopic approach dealing with valence-nucleon excitations is described in [CCG$^+$09], where a realistic effective interaction derived from the CD-Bonn nucleon-nucleon charge-dependent potential is used. The interaction was derived by fitting the proton-proton and proton-neutron data below 350 MeV that were available worldwide in 2000. This type of interactions have proven to be very successful to reproduce the low-energy states and the coupling of particles to the closed ^{132}Sn core. Several applications in the region [CCGI13a, CCGI13b] successfully describe the evolution of single-neutron and single-proton states outside the doubly-magic ^{132}Sn when nucleons, or pairs of nucleons, are added. Transition strengths pose a challenge to the description or nuclear states and are able to test details of the wave functions in this calculations. Reduced transition probabilities between single particle states will be discussed in this thesis for ^{131}Sn, ^{133}Sn and ^{134}Sn.

On the other hand, the description of core-excited configurations within the shell model presents some challenges mainly arising from the computational power required, which makes that the configuration space needs to be truncated to make calculations viable [UKK$^+$00, FBD$^+$01, ZBD$^+$96]. An example of this approach is given in [GCG$^+$09] where calculations for core-excited states in ^{132}Sn and also ^{132}In are presented. In this case the orbitals $\pi g_{9/2}$, $\pi p_{1/2}$, $\pi g_{7/2}$ and $\pi d_{5/2}$, both above and below the $Z = 50$ gap are included for protons (see Figure 1.3) while the $\nu s_{1/2}$, $\nu d_{3/2}$, $\nu h_{11/2}$, and $\nu f_{7/2}$,

$\nu g_{7/2}$ neutron orbitals are employed for neutrons, thus allowing for excitations across $N = 82$. For the neutrons, though, only one-particle one-hole excitations are allowed. An empirical nucleon-nucleon interaction is employed by scaling the two-body matrix elements from the ^{208}Pb in order to reproduce the positions of the known multiplets in ^{132}Sn (see Chapter 5). The model was extended in Ref. [TJG$^+$16] to include the missing $\pi d_{1/2}$ orbital, and the $d_{5/2}$, $g_{7/2}$ and $p_{3/2}$ neutron orbitals. These orbitals are of importance for the description of core-excited states both in ^{131}Sn and ^{132}Sn, as will be discussed later in this thesis. Further information is achieved by the measurement of reduced transition strengths.

Another approach, used with the aim of reproducing both valence-nucleon excitations and core-breaking states, consists in calculations employing an extended pairing-plus-quadrupole model with the addition of monopole corrections (EPQQM) [JHT$^+$11, WSJ$^+$13]. This technique uses a schematic spatial interaction in a multipole expansion, where the two-body matrix elements are calculated numerically, and it is rather successful in the region. A larger model space can be used, with the proton $f_{5/2}$, $p_{3/2}$, $p_{1/2}$, $g_{9/2}$, $g_{7/2}$ and $d_{5/2}$, and neutron $g_{7/2}$, $d_{5/2}$, $s_{1/2}$, $h_{11/2}$, $d_{3/2}$, $f_{7/2}$ and $p_{3/2}$ orbits included above the ^{78}Ni core. The model is able to reproduce the energy spectra of nuclei both above and below ^{132}Sn.

1.3 The astrophysical r-process

Nuclei in the ^{132}Sn region are also known to play an important role in the astrophysical rapid neutron capture process (r-process), which impacts elemental abundances in the solar system. The production of heavy elements ($A > 60$) is mostly driven by neutron capture processes, which take place in stellar scenarios where the isotopes are immersed within a dense neutron flux. The elements beyond ^{56}Fe are produced by a successive chain of neutron capture reactions and β decays. Depending on the strength of the neutron flux, we can distinguish between two different types of scenarios: the *slow* s-process and the *rapid* r-process.

The s-process occurs in scenarios with a weak neutron flux and is the responsible for the production of about half of the heavy elements. The seed neutrons are mainly produced by ^{13}C(α,n) and ^{22}Ne(α,n) reactions taking place during the stellar phases of carbon and helium burning. The time scale required for a nucleus to capture a

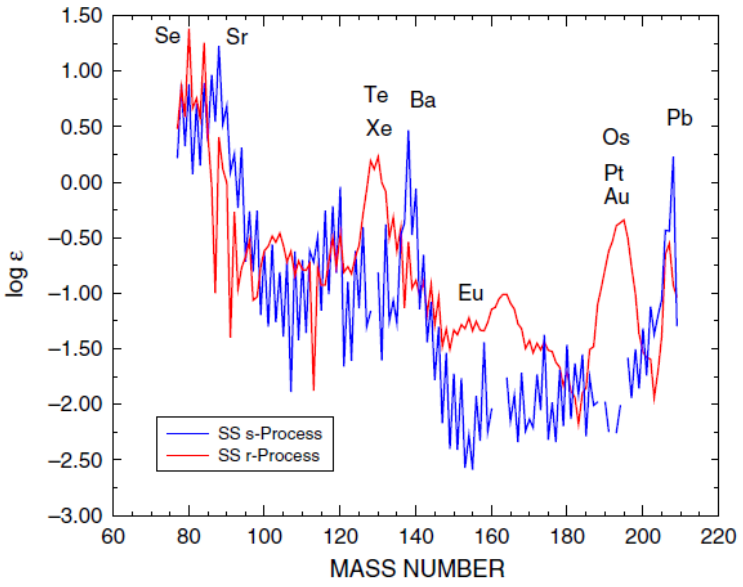

Figure 1.5: Abundances of elements due to teh s-process and r-process. Image taken from [GLMP07].

neutron is relatively long, longer than the β-decay mean lives, and hence the produced isotopes usually disintegrate by β-decay before capturing another neutron. This is way the s-process takes next to the valley of stability of the nuclear chart.

The second neutron capture process is the r-process, responsible for the abundances of the other half of the heavy elements. It takes place in scenarios with high neutron densities. Neutron capture reactions occur much faster than β decays. Isotopes are also submerged in a high density γ-ray flux, so that the isotopes continue capturing neutrons until they achieve equilibrium with photo-disintegration reactions (n,γ)$\rightleftharpoons$(γ,n). Neglecting the β-decay contributions, such equilibrium can be described with Equation 1.6 [CTT91], where $Y(Z,A)$ denotes the abundances of the respective ${}^{A}_{Z}X$ isotopes, $\langle\sigma_n\rangle_{ZA}$ and n_n the neutron-capture cross-section and neutron flux respectively, and $\lambda_\gamma(Z,A+1)$ is the photodesintegration rate.

$$\frac{dY(Z,A)}{dt} = \lambda_\gamma(Z,A+1)Y(Z,A+1) - n_n\langle\sigma_n\rangle_{ZA}Y(Z,A+1) \tag{1.6}$$

This equilibrium condition can be written as a function of the temperature T and

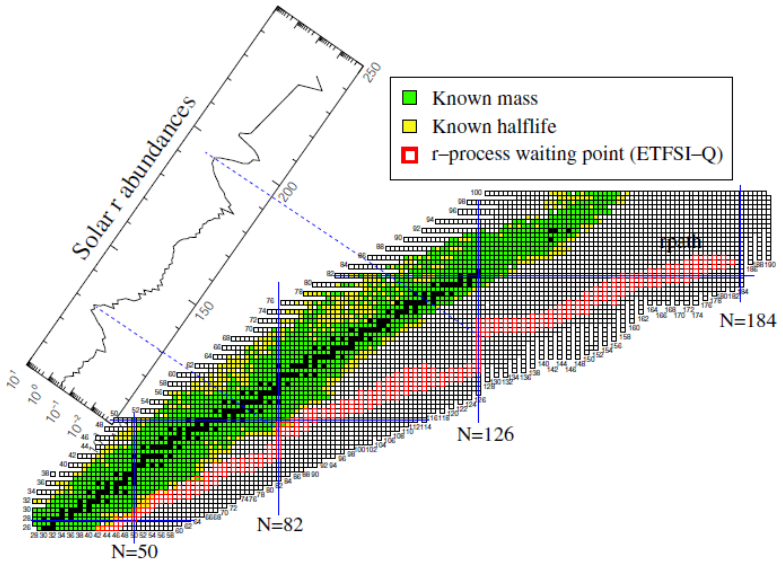

Figure 1.6: r-process path and solar r abundances. Most of the r-process path take place in region of the nuclear chart where the information about masses and lifetimes are very scarce. It can be noticed how the neutron magic numbers induce a halt in the neutron capture processes, changing the course of the r-process path. Figure taken from [GLMP07]

the neutron separation energies S_n of the involved isotopes:

$$\frac{Y(Z,A+1)}{Y(Z,A)} = n_n \left(\frac{2\pi\hbar^2}{m_u kT}\right)^{3/2} \left(\frac{A+1}{A}\right)^{3/2} \frac{G(Z,A+1)}{2G(Z,A)} exp\left[\frac{S_n(Z,A+1)}{kT}\right] \quad (1.7)$$

The nucleus with the maximum abundance for each isotope chain can be derived from equation 1.7. These nuclei are known as the waiting points, since the neutron captures are halted at them, hence they need to *wait* until they β decay to resume capturing neutrons. The r-process path is made up by the ensemble of waiting point nuclei. A key parameter that determines the r-process path for a given set of n_n and T conditions is the neutron separation energy S_n. On the other hand, the β-decay half-lives of the isotopes on the r-process path determine its dynamical time evolution.

In Figure 1.6 it is depicted the r-process path of waiting point isotopes in the Segré chart, along with the solar abundance of the elements produced by the r-process [GLMP07]. It can be noticed that the r-process path changes abruptly when neutron magic numbers are reached. This is due to the small neutron separation energies for nuclei with one extra neutron above neutron magic numbers, which induce a halt in the neutron capture processes. To continue the path to higher neutron numbers, the

isotopes previously need to undergo several β decays. Magic number nuclei are characterized by longer half-lives than the rest and they play a key role determining the time scale of the r-process. Moreover, these magic number nuclei regions become bottlenecks where the matter is accumulated, which results in the peaks observed in the r-process abundance distributions.

Experimental information on several nuclear properties is of paramount importance in abundance calculations [MW85]. Nuclear masses and neutron separation energies are the most crucial, since thy constrain the boundaries of the r-process path, determining the relative isotopic abundances. The β-decay rates, are the next most important data, since they determine the relative abundances between different elements. Another process that plays an relevant role is β-delayed neutron emission, which provides a delayed flux of neutrons once the neutron flux and temperature is turned off in the stellar environment [MW85], That is why they have an influence on the final abundance patterns.

The abundance peak for A=130 has its origin in the N=82 shell closure. How the shell gap evolves as we go deeper into the neutron-rich region has a big impact on mass abundance distributions [PKT97], and the quenching of the N=82 shell below ^{132}Sn has been advocated. In addition recent sensitivity studies [SMA] conclude that the P_n values and β-decay rates for In and Sn isotopes on the neutron-rich side region of ^{132}Sn have a sizeable impact on final abundances. Beta-decay half-lives and neutron emission probabilities have been measured in this thesis for the Sn isotopes under study.

Finally, it is also worth mentioning that the identification of the nucleosynthesis site for neutron-rich nuclei around $N = 82$ has been recently reported [BKWMP16, CBV$^+$17], associated to a *kilonova* [MMPD$^+$10]. The robustness of the $N = 82$ neutron shell is one of the important parameters that affects the modelling of r-process nucleosynthesis and plays a role in the description of the light curves arising from compact object mergers. The shell structure in this region is also necessary to understand the role of fission in the r-process [MPMZ$^+$07].

1.4 Motivation of this work

The present PhD thesis addresses the structure of the doubly-magic ^{132}Sn itself, the one-neutron-hole and one-neutron-particle nuclei ^{131}Sn and ^{133}Sn, and the ^{134}Sn tin

isotope, with a neutron pair coupled to the ^{132}Sn core. The main goals of our study are described below.

Investigation of ^{132}Sn

We propose to study the excited structure of ^{132}Sn to obtain direct information about the particle-hole couplings for both proton and neutron configurations. The coupling of single particle and single hole configurations (Figure 1.3) leads to multiplets of excited states with in principle low admixture of other configurations. Some of them have not yet been identified, and they will provide information on the nuclear two-body matrix elements to first order. The excited levels ^{132}Sn will be populated in the β decay of ^{132}In (7^-). This information will be complemented with the study of the β decay of ^{133}In, where we will profit from the isomer selectivity capabilities of the ISOLDE RILIS to study separately the decay of ^{133g}In ($9/2^+$) and ^{133m}In ($1/2^-$). The spectroscopic information will be completed with an extensive fast-timing study of the excited levels in ^{132}Sn.

We also aim to obtain a new a more precise measurements for the half-life and P_n values of the ^{132}In β-decay. Besides, the isomer selectivity will allow us to derive separately the P_n values for the ^{133g}In and ^{133m}In decays.

Investigation of ^{131}Sn

The ^{131}Sn isotope has one neutron less than the ^{132}Sn core. Low-lying single-hole configurations, and high-lying core-breaking states coexist in this nucleus. We aim at investigating the excited states in ^{131}Sn from the β-decay of ^{131}In. We will take advantage of the In isomer selectivity attained at ISOLDE to disentangle the decay schemes of the three β-decaying states in In. This feature will also make it possible to disentangle the contribution of each isomer to beta-feeding of states in ^{131}Sn. This information will help to understand the discrepancy observed in previous β-decay studies for the *log(ft)* values of first-forbidden transitions [FGM$^+$04a].

We will try to confirm the position of the $\nu h_{11/2}$ single-hole state, using the expected expansion of the level-scheme, and to identify core breaking states and their corresponding states in ^{132}Sn.

Another interesting feature in ^{131}Sn is the presence of levels at very high energies above the neutron separation energy which decay by γ emission. Taking advantage of the isomer selectivity we aim at a better understanding of their nature. To complete

this investigation, lifetimes of the excited levels will be studied using the fast-timing method, providing for the first time access to subnanosecond lifetimes in ^{131}Sn.

We aim to measure several properties about the three ^{131}In β-decaying states. Taking advantage of the improved yields and the isomer selectivity, we will try to derive new and more precise measurements for their half-lives P_n values separately for each ^{131}In β-decaying state.

Investigation of ^{133}Sn

The ^{133}Sn isotope, with one neutron coupled to the ^{132}Sn core, shows low-lying levels built on neutron single-particle configurations, while core-breaking states appear at higher excitation energies. In our experiment the ^{133}Sn excited levels were populated in the β decay of ^{133}In and in the β-n decay of ^{134}In. The new results derived from the γ-spectroscopy study of ^{133}In decay have been published in [PKF$^+$19]. For this isotope, in this PhD thesis we will focus only on the lifetime measurements. We aim at obtaining a new measurement for the lifetime of the 854-keV $\nu p_{3/2}$ single-particle state using the fast-timing method, from the analysis of the ^{134}In β-n decay. It will provide information about the single particle transitions in the region, and allow to compare to other indium isotopes and to other regions of the nuclear chart, specifically around the doubly-magic ^{208}Pb. Other lifetimes in this nucleus will be explored.

Investigation of ^{134}Sn

The two-neutron ^{134}Sn nucleus will be investigated from the β-decay of ^{134}In and the β-n decay of ^{135}In. In this PhD thesis we will focus only in lifetime measurements of the lowest-lying states in 134Sn, which are assumed to arise from a dominant $\nu f_{7/2}^2$ configuration. With this aim, a complete measurement of the lifetimes of the 2^+, 4^+ and 6^+ states will be performed. The measurement will allow the comparison to similar two-nucleon heavier tin isotopes to be made, and to interpret the results with the help of existing shell-model calculations.

The thesis is organized as follows. Chapter 2 gathers the basic information about β, β-n and γ decay. Chapter 3 describes the experimental methods used in the thesis, while chapter 4 deals specifically with fast-timing methods and the analysis tools developed. The results for ^{132}Sn, ^{131}Sn, ^{133}Sn and ^{134}Sn are presented in Chapters 5, 6, 7 and 8, respectively. Finally, conclusions are drawn in Chapter 8.5.

2

Radioactive decay processes

Exotic nuclei located outside from the stability are commonly unstable. These nuclei need to undergo a series of radioactive decays, where radioactive particles are emitted, until they reach an stable state. The study of the emitted radiation provides a lot of information about these nuclei. Nuclei with large N/Z ratio commonly decay by emission of β^- particles with short-lifetimes. Following to the β-decay the daughter nuclei may end up in an excited state. The de-excitation of these nuclei is usually done by emitting γ-rays. In some cases the nucleus can emit a neutron just after the β-decay. This process is called β-delayed neutron emission and its very common for nuclei with a large neutron excess. In this chapter it will be discussed the theoretical fundamentals of these radioactive decay processes.

2.1 Beta decay

The β decay is one of the most common decay process that may occur to exotic nuclei outside of the stability. These processes are caused by the nuclear weak interaction, which induce the conversion of a nucleon inside the nucleus to the other kind, emitting a β-particle and a neutrino in the process. When a neutron is transformed into a proton, it is called *negative* β-decay (β^-) and the emitted β-particle is an electron. Conversely, when a proton is transformed into a neutron it is called *positive* β-decay (β^+) being in this case a positron the emitted β particle. There exist a third possibility that compete with the β^+ decay known as the *electron capture* process (ϵ). In this case instead of

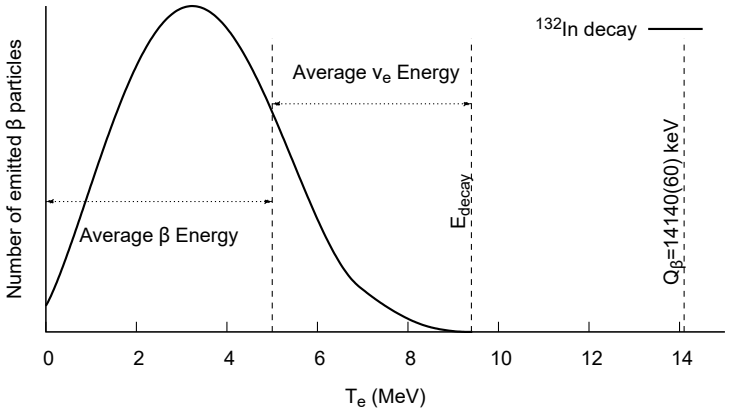

Figure 2.1: Energy distribution of the electrons emitted during the β-decay of ^{132}In.

emitting a positron, an electron from the inner atomic shell is captured by the nucleus.

The β-decay of the atomic nucleus, is one of the earlier discovered radioactive decays. Nevertheless, the understanding of this process took a long time. One of the bigger puzzles was the continuous energy spectrum of the β particles, see Figure 2.1. To solve this problem, Pauli proposed in 1931 the existence of a second particle emitted in the decay process that share the released energy with the β particle. This particle was called the *neutrino* (ν_e) for the β^+ and ϵ processes, or *antineutrino* ($\bar{\nu}_e$) in the β^-. Therefore, the different β-decay processes that may occur to a nucleus can be represented by the following equations

$$\beta^- \qquad {}^A_Z X_N \longrightarrow {}^A_{Z+1} X_{N-1} + \bar{\nu}_e + e^- \tag{2.1}$$

$$\beta^+ \qquad {}^A_Z X_N \longrightarrow {}^A_{Z-1} X_{N+1} + \nu_e + e^+ \tag{2.2}$$

$$\epsilon \qquad {}^A_Z X_N + e^- \longrightarrow {}^A_{Z-1} X_{N+1} + \nu_e \tag{2.3}$$

A key magnitude that determines whether a β-decay process is energetically allowed is the Q_β, which corresponds to the difference between the initial and final nuclear masses, including the emitted particles. The β decay is only possible when the Q_β value is positive. By neglecting the mass of the neutrinos, the energy balance for the

different types of β-decay process can be derived using the following equations:

$$Q_{\beta^-} = m(^A_Z X_N)c^2 - m(^A_{Z+1}X'_{N-1})c^2 \quad (2.4)$$

$$Q_{\beta^+} = m(^A_Z X_N)c^2 - m(^A_{Z-1}X'_{N+1})c^2 - 2m_e c^2 \quad (2.5)$$

$$Q_{CE} = m(^A_Z X_N) - m(^A_{Z-1}X'_{N+1}) - B_n \quad (2.6)$$

where $m(^A_Z X_N)$ corresponds to the tabulated atomic mass of the [WAK$^+$17] and m_e to the electron mass. In the electron capture decay the binding energy of the captured electron, B_n, needs to be taken into account. This Q_β also corresponds to the total energy with which the β-particle and neutrino are emitted $Q_\beta = T_e + E_\nu$. This relationship between the Q_β and the energies of the β particle and the neutrino is derived assuming that the daughter nuclei is much more heavier compared with them. The momentum conservation leads to a negligible contribution of the nucleus recoil.

The energy spectrum of the β particle goes from 0, when all the energy is received by the neutrino, to the maximum defined by Q_β, when all the energy is taken by the β.In Figure 2.1 the β-energy spectrum for the the ^{132}In decay is shown. In this example, the β-energy spectrum end at E_{decay} ~9.4 MeV, before reaching Q_β =14.14(6) MeV maximum. That is because the Q_β is defined by the energy difference between the ground states. However, the g.s. to g.s. transition is not allowed in ^{132}In decay due to the large spin difference. The maximun energy is thus defined by the energy difference with lowest lying excited state x that can be populated. The total released energy, E_{decay},corresponds to the Q_β minus the excitation energy of E_x populated level.

$$E_{decay} = Q_{beta} - E_x \quad (2.7)$$

The fact that the energy spectrum does not reach the Q_β value, indicates that the β transition between the ground states of ^{132}In and ^{132}Sn is not possible. This feature suggest that there is an strong influence of the final state that is populated during the β-decay process. A successful theory for the β-decay was developed by Fermi in 1934 [Kra88], based on the neutrino hypothesis proposed by Pauli. In its theory Fermi made the assumption that the interaction that causes the β transition is weak in comparison with the nuclear interaction the generates the quasi-stationary states in the nucleus. Therefore, this weak interaction is treated in the framework of the perturbation theory. Therefore, the transition rate of the β-decay can be expressed with Fermi's Golden Rule:

$$\lambda = \frac{2\pi}{\hbar}|V_{fi}|^2\rho(E_f) \quad (2.8)$$

where $|V_{fi}|$ denotes the matrix element of the weak interaction potential between the initial and final states, and the $\rho(E_f)$ value indicates the density of final states. In the calculation of $|V_{fi}|$ integral the nucleus wave functions, as well as the electron and neutrino wave functions have to be included. A methodology to address this problem is the so-called *allowed* approximation, which consist in keeping only the first term from the Taylor expansion of the electron and neutrino wave function.

$$d\lambda = \frac{2\pi}{\hbar} g^2 |M_{fi}|^2 (4\pi)^2 \frac{p^2 dp q^2}{h^6} \frac{dq}{dE_f} \tag{2.9}$$

where p and q are the momentum of the electron and the neutrino respectively, and $|M_{fi}|$ corresponds to the nuclear matrix element of the interaction. The final energy corresponds to the sum of energies of the electron and the neutrino. $E_f = E_e + E_\nu = E_e + qc$. The equation from 2.9, can be rewritten in terms of T_e to obtain the shape of the energy spectrum $N(T_e)$ [Kra88].

$$N(T_e) = \frac{g^2 |M_{fi}|^2}{2c^6 \pi^3 \hbar^7} ({T_e}^2 + 2T_e m_e c^2)^{1/2} (Q - T_e)^2 (T_e + m_e c^2) \tag{2.10}$$

Nevertheless, this formula did not managed to fully reproduce the the experimentally observed β energy spectrum. The discrepancy was caused by the Coulomb interaction between the nucleus and the emitted β-particle. To account for this effect, an extra factor was introduced known as the *Fermi function* $F(Z', p)$ or $F(Z', T_e)$, where Z' corresponds to the atomic number of the daughter nuclei. After including this factor into the Equation 2.9, and integrating over the whole range of the β momentum p, which goes from 0 to $p_{max} = \sqrt{E_{decay}^2 - m_e^2 c^4}$, the total decay rate λ is derived:

$$\lambda = \frac{g^2 |M_{fi}|^2}{2c^3 \pi^3 \hbar^7} \int_0^{p_{max}} F(Z', p) p^2 (E_{decay} - T_e)^2 dp \tag{2.11}$$

The result of this integral, will only depend on the atomic number of the daughter nuclei, and on the maximum energy of the β particle. Separating the integral part of Equation 2.11, it is obtained the *Fermi integral*, which is defined as:

$$f(Z', E_{decay}) = \frac{1}{(m_e c)^3 (m_e c^2)^2} \int_0^{p_{max}} F(Z', p) p^2 (E_{decay} - T_e)^2 dp \tag{2.12}$$

The values of the Fermi integral are estimated numerically, and their values for a given Z' and E_{decay} are tabulated. Considering the relationship between λ and the

half-life of the parent nuclei $\lambda = t_{1/2}/ln(2)$, it is very common to define the ft value.

$$ft_{1/2} = ln(2)\frac{2\pi^3\hbar^7}{g^2 m_e^5 c^4 |M_{fi}|^2} \tag{2.13}$$

In the *allowed* approximation, neither the β or the neutrino carries orbital angular momenta l. The particles are emitted carrying only their own spin, $s = 1/2$. The change in the angular momenta of the nucleus is equal to the total spin of the β and the neutrino. Taking this selection rule into account two types of decays can be distinguished. The *Fermi* decays where the β and the neutrino couples to a total $S = 0$, and the *Gamow-Teller* decay when they coupled to $S = 1$. Since neither the electron or the neutrino carries any *orbital* angular momentum, no parity change can occur between the initial and final nuclear state. Besides, the total change in angular momentum of the nucleus would be $\Delta I = 0$ for *Fermi* decays, and $\Delta I = 0, 1$ (except for $I_i = 0$ and $I_f = 0$ case) in the *Gamow-Teller* decay.

The transitions that do not fulfil the selection rules in the *allowed* approximation are known as *forbidden* transition. These transitions are possible, but they require to consider higher order terms of the emitted β or neutrino wave function expansion, in other words, to permit that the emitted particle carry an *orbital* angular momenta l. The *forbidden* decays are classified depending on the total l carried away by the emitted particles. Transitions with $l = 1$ are classified *first-forbidden* decays and those with $l = 2$ as *second-forbidden*. The *forbidden* transitions would be less likely that the *allowed* decays, and the transition rate for *first-forbidden* decays is much higher than for the *second-forbidden*.

Table 2.1: Classification of transitions in the β decay.

	ΔI	$\Delta\pi$	*log ft*
Allowed Fermi	0	*no*	2.9-3.7
Allowed Gamow-Teller	0,1 ($0\not\to 0$)	*no*	3.8-6.0
First-forbidden	0,1,2	*yes*	6-10
Second-forbidden	0,1,2,3	*no*	11-13

2.2 Gamma decay

Following the β-decay the nucleus may end in an excited state. These nuclei can reduce their energy by emitting one or more γ rays, until they reach the minimum energy state or ground state (g.s.). These γ rays are emitted with a mono-energetic spectrum, whose energies match the difference in energy between the initial and final state in the nucleus that they connect. The mechanism that drives this γ decay is in fact the electromagnetic interaction. Likewise to the β decay, the transition probability between two levels via γ-decay can be expressed in terms of the Fermi's Golden Rule:

$$\Gamma_{i\to f} = \frac{2\pi}{\hbar}|\langle\psi_i|H_{int}|\psi_f\rangle|^2\rho \tag{2.14}$$

This rule establishes that the transition rate is proportional to the squared matrix element of the electromagnetic operator between the initial ψ_i and final state ψ_f. In this case, the electromagnetic operator is very well known, this operator can be expanded in a series of infinite multipole terms $\mathcal{M}(X\lambda)$. Where X refers to the nature of the operator, electric E or magnetic M, and λ denotes the multipole order, which corresponds to the total angular momenta carried away by the γ-ray. Hence, the transition rate between two states $\Gamma_{i\to f}(X\lambda)$ can be expressed with the 2.16 Equation [Kra88], which depends strongly on the matrix element of the multipole operator 2.15 .

$$m_{fi}(X\lambda) = \int \psi_f^* \mathcal{M}(X\lambda)\psi_i dv \tag{2.15}$$

$$\Gamma_{i\to f}(X\lambda) = \frac{8\pi(\lambda+1)}{\lambda[(2\lambda+1)!!)]^2}\left(\frac{E_\gamma}{\hbar c}\right)^{2\lambda+1}[m_{fi}(X\lambda)]^2 \tag{2.16}$$

The long-wavelength limit requires that the wavelength of the γ is much larger than the size of the nucleus, most of the γ-transitions of a few MeV fulfills this limit. In this limit, the electromagnetic operators can be written in the form of Equations 2.17 and 2.18 [Ham75]. Where $\rho(\mathbf{r})$ describe the charge density, $\overrightarrow{j}(\mathbf{r})$ is the current density and $Y_{\lambda\mu}(\hat{\mathbf{r}})$ corresponds to the spherical harmonic of order λ,μ.

$$\mathcal{M}(E\lambda,\mu) = \int \rho(\mathbf{r}) r^\lambda Y_{\lambda\mu}(\hat{\mathbf{r}}) dr \tag{2.17}$$

$$\mathcal{M}(M\lambda,\mu) = \frac{-1}{c(\lambda+1)}\int \overrightarrow{j(\mathbf{r})}\cdot(\overrightarrow{\mathbf{r}}\times\overrightarrow{\boldsymbol{\nabla}})r^\lambda Y_{\lambda\mu}(\hat{\mathbf{r}})dr \tag{2.18}$$

The conservation of the parity and the angular momentum led up to a set of selection rules for the γ decay depending on the nature and multipole order of the emitted γ ray. The total angular momenta carried away by the γ-ray corresponds to the order of the multipole. The parity change induced in the nucleus depends on whether is an electric, $\pi(E\lambda)$ =(-1)$^{\lambda}$, or magnetic, $\pi(M\lambda)$ =(-1)$^{\lambda+1}$, transition. Taking this into account the following selection rules are derived:

$$\Delta\pi = \begin{cases} (-1)^{\lambda} & EL \\ (-1)^{\lambda+1} & ML \end{cases} \tag{2.19}$$

$$|J_i - J_f| \leqslant \lambda \leqslant J_i + J_f \qquad (no \quad \lambda = 0) \tag{2.20}$$

The λ=0 exception arise from the fact that monopole γ transitions do not exist. The monopole term corresponds to the electrical charge, which cannot be changed emitting one γ-ray. Thus, the lowest multipole order that can induce a γ decay is 1.

2.2.1 Electromagnetic transition multi polarities

The nuclear states $|\psi\rangle$ are characterized by their quantum numbers $|JM\rangle$, where J denotes the total angular momenta, and M its projection. As a consequence of the rotational symmetry, the $(2J+1)$ projections of a given state with different projections M are degenerate in energy. Hence, the total transition rate associated to a given γ transition, is obtained by averaging over all the projections of the initial state M_i and sum over all the projections in the final level M_j. Hence, the reduced transition probabilities $B(X\lambda; I_i \to I_f)$ is defined with the following expression:

$$B(X\lambda; J_i \to J_f) = \sum_{\mu, M_f} |\langle J_f M_f | \mathcal{M}(X\lambda, \mu) | J_i M_i \rangle|^2 \tag{2.21}$$

By means of the Winger-Eckart theorem, it is possible to remove the dependence with M_i and M$_j$, to define this reduced transition probability in terms of the reduced transition matrix elements $\langle J_f | |\mathcal{M}(X\lambda)| | J_i \rangle$:

$$B(X\lambda; J_i \to J_f) = \frac{1}{2J_i + 1} |\langle J_f | |\mathcal{M}(\mathcal{X}\lambda)| | J_i \rangle|^2 \tag{2.22}$$

Therefore, the total transition rate for a certain γ transition, can be written with the following expression:

$$\Gamma_\gamma(X\lambda) = \frac{8\pi(\lambda+1)}{\lambda[(2\lambda+1)!!)]^2}\left(\frac{E_\gamma}{\hbar c}\right)^{2\lambda+1} B(X\lambda; J_i \to J_f) \tag{2.23}$$

It should be noted that $\Gamma_\gamma(X\lambda)$ corresponds to the transition rate associated only with a certain $X\lambda$ multipolarity. Normally, the selection rules allow more than one multipolarity term to produce the γ transition. In those cases the total Γ_γ is obtained by summing up all the partial $\Gamma_\gamma(X\lambda)$ rates from the allowed multipoles. Nevertheless, the transition ratio decrease very quickly as the multiple order increase. The contribution from higher-order multipoles can be neglected in most of the cases. The multipole mixing mainly occurs between first allowed multipole, and the following that fulfills the selection rules. For example, it is very common the mixing between M1 and E2 multipole, since they have competitive transition rates. On the other hand, in cases where both E1 and M2 transitions are available, the E1 is much more dominant and thus the mixing of M2 multipule is very small. The mixing ratio δ, characterizing the mixing, is defined as the ratio between the transition rates from each multipole $\Gamma_\gamma(X\lambda)/\Gamma_\gamma(X'\lambda')$.

2.2.2 Internal conversion

Another electromagnetic process that can produce a transition between two excited levels is the internal conversion. This process is induced by the interaction of the electromagnetic fields of the nucleus with the electrons from the atomic orbits. When an internal conversion occurs, the energy difference between the initial and final state in the nucleus is transmitted to the electron, resulting in the emission of the electron. This process compete with the γ emission, it is usually characterized by the conversion coefficient α_c which is defined as the ratio between the intensity of the internal conversion and the γ emission. The α_c coefficient grows up as we increase the atomic number and multipolarity of the transition, but it decrease rapidly with the increasing transition energy. The total transition rate corresponds to the sum of both γ and internal conversion components, as is written in Equation 2.24. Usually, internal conversion is only competitive for low transitions energies, below 100 keV, where it can become the dominant process.

$$\Gamma = \Gamma_\gamma + \Gamma_c = \Gamma_\gamma(1+\alpha_c) \tag{2.24}$$

A special case when they play an key role is for $E0$ transitions. Since they are forbidden by the γ-decay the internal conversion becomes the only possibility for those transitions. Therefore, de-excitation via internal conversion can be measured experimentally by detecting the emitted electrons.

2.2.3 Lifetime of excited states

The transition rate for a given γ Γ_γ can be obtained directly by measuring the mean life of the level that de-excite $\Gamma_\gamma = \tau_\gamma^{-1}$. Very commonly the nucleus excited levels have more than one lower energy level at their disposal to decay via γ emission. The mean life of the level τ is related to the total decay rate of this level Γ_{Tot}, which corresponds to the sum over all the transition rates that can de-excite the level:

$$\frac{1}{\tau} = \Gamma_{tot} = \sum_i \Gamma_{\gamma_i}(1 + \alpha_{ci}) \tag{2.25}$$

Hence, the transition rate of a Γ_{γ_i} can be obtained if we know the lifetime of the level and the branching ratio of the emitted gammas br_{γ_i}. The branching ratio can be obtained experimentally by measuring the intensities of the γ-rays that de-excite the level:

$$br_{\gamma_i} = \frac{\Gamma_{\gamma_i}}{\Gamma_{tot}} = \frac{I_{\gamma_i}}{\sum_j I_{\gamma_j}(1 + \alpha_{ci})} \tag{2.26}$$

By introducing Equation 2.26 into 2.25, we can derive the value for the partial lifetime of an specific γ ray τ_γ:

$$\Gamma_{\gamma_i} = \Gamma_{tot} br_{\gamma_i} = \tau_{\gamma_i}^{-1} \qquad \tau_{\gamma_i} = \frac{\tau}{br_{\gamma_i}} \tag{2.27}$$

In conclusion, the measurement of the mean life of the excited nuclear state, along with the γ branching ratio, provides a direct measurement for the γ transition rate Γ_γ. Thus, by measuring these quantities, the $B(X\lambda)$ values can be derived taking unto account the relationship established in Equation 2.23. The only missing information would be the mixing ratio δ, which can be obtained from other kind of experiments.

2.2.4 Weisskopf estimates

A crude but useful theoretical prediction for the reduced transition probabilities, are given by the single-particle estimates, better known as *Weisskopf estimates* [Wei51]. These estimates are derived in the framework of the single-particle models, in these kind of models, the properties of the nuclear properties are attributed to a single or a few nucleons outside from closed shells. The derived formulas for the electric and magnetic reduced transition rates are written in Equations 2.28 and 2.29. The derivation of those formulas were done, assuming that the transition is carried out by one single nucleon moving between single particle orbits, and the radial wavefunction can be assumed to be constant inside the nuclear radius $R = 1.2A^{1/3}fm$. More details about their derivation are given in [Ham75].

$$B(E\lambda)_W = \frac{(1.2)^{2\lambda}}{4\pi}\left(\frac{3}{\lambda+3}\right)^2 A^{2\lambda/3}e^2 fm^{2\lambda} \tag{2.28}$$

$$B(M\lambda)_W = \frac{10}{\pi}(1.2)^{2\lambda-2}\left(\frac{3}{\lambda+2}\right)^2 A^{(2\lambda-2)/3}\mu_N^2 fm^{2\lambda-2} \tag{2.29}$$

These single-particle estimates constitute convenient units in which the experimentally measured transition rates can be expressed, providing a qualitative image of the nucleus. For example, transition rates with much larger values than the Weisskopf estimates indicates the existence of collective degrees of freedom. On the other hand, if the measurements reveals much smaller values, it will indicate the existence of some structure dependent effects in the nucleus.

2.3 Beta-delayed neutron emission decay

It is very common in neutron-rich nuclei to observe the emission of neutrons following the β decay. These kind of processes are energetically allowed when the Q_β of the decay is higher than the neutron separation energy S_n (Equation 2.30) of the daughter isotope. In those cases, the β strength is fragmented over the whole range of states within the Q_β energy window, being possible to populate levels above the neutron separation energy. Those levels are neutron unbound, an thus they can be de-excited by emitting one neutron in the process instead of emitting γ-rays.

$$S_n(^A_Z X_N) = m(^A_Z X_N)c^2 - m(^{A-1}_Z X_{N-1})c^2 \tag{2.30}$$

Far from the stability, in nuclei with large N/Z ratios, the Q_β is incremented at the same time than the S_n is reduced. Hence, the available energy may be higher than the separation energy for 2, S_{2n}, 3, S_{3n} or more neutrons, being possible to emit more than one neutron after the β decay in those cases. This process is schematically illustrated in Figure 2.2.

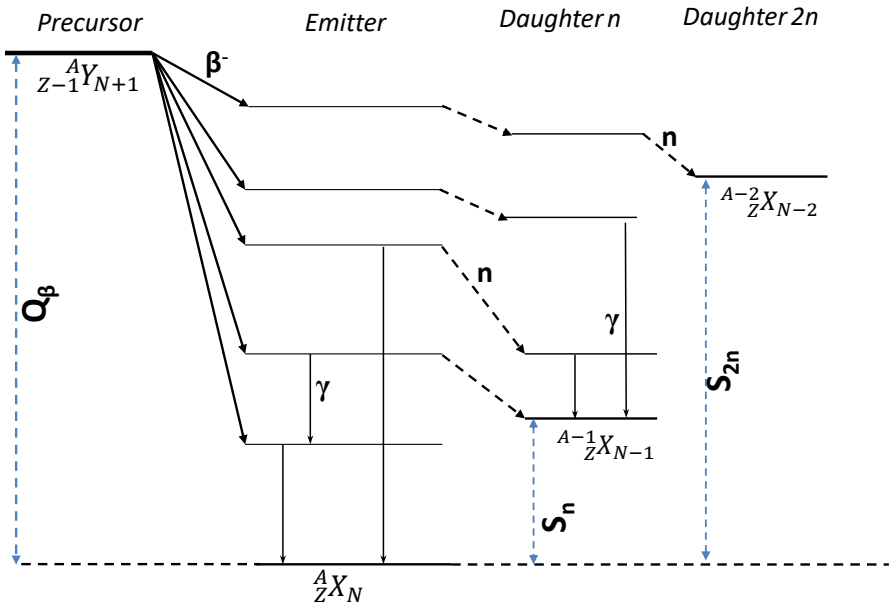

Figure 2.2: Schematic representation of the β-delayed neutron emission processes.

The β delayed neutron emission probability P_n, is in principle correlated to the size of the emission window $Q_{\beta n} = Q_\beta - S_n$. Theoretical methods that predict P_n usually assume that the levels located above the neutron separation energy decays almost exclusively by neutron emission [Mie14, MKM16].

2.3.1 Competition between γ-ray and neutron emission

It is often assumed that the competition between the emission of γ-ray and neutrons is only possible for levels within a small energy window of $\sim$100 keV above the S_n. Nevertheless, the existence of excited levels, that decay emitting γ-rays, located at very high energies above S_n have been observed in several nuclei. Examples of these phenomena are the decays of ^{87}Br [SNSEP72], ^{137}I [NSP$^+$75], ^{93}Rb [BT77], or more recently in the mass region of ^{132}Sn, such as ^{133}In [VJD$^+$17, PKF$^+$19] and ^{131}In [FGM$^+$04a, DSA$^+$19]. All these studies suggest that the neutron emission of these unbound states is strongly hindered by a nuclear structure effect. Recent studies using the total absorption γ-ray spectroscopy technique which has a much higher sensitivity for these levels [TVA$^+$15, SLN$^+$16, VTA$^+$17, RRF$^+$17, GTA$^+$19].

This large hindrance is caused by the large l orbital angular momenta of the emitted neutron required for those levels to decay via neutron emission. Levels whose requirement for neutron emission are $l\geq3$ would rather decay by γ-ray emission. Besides, the overlap of initial and final wave functions can also play an important role.

3

Experimental details.

The investigation of the nuclear structure of exotic nuclei entails their production in an excited state. The main motivation of this PhD thesis is the study of the excited structure of tin isotopes, located at both sides of the doubly-magic ^{132}Sn ($Z = 50$ and $N = 82$). There are a good number of methodologies and reactions that can be used to produce the nuclei in their excited states (β-decay, fission, Coulomb excitation, neutron capture, etc). During the IS610 experimental campaign, the excited states from tin isotopes were populated during the β-decay of exotic indium isotopes. The production of these exotic nuclear species is carried out in large-scale facilities, where state-of-the-art radiation detectors and electronics are used to obtain information about those isotopes.

The production of isotopes in the form of radioactive ion beams (RIB) is a standard methodology in the study of exotic nuclei. A well established method for the production of RIB is the isotope separation online (ISOL) technique. In one of the implementations of this technique, the exotic isotopes are produced by nuclear reactions (spallation, fragmentation or fission) on a massive target, triggered by the bombardment of high-energetic particles. Following the reaction, the products are extracted from the target, ionized, accelerated, mass separated and transported to experimental areas where they can be studied in detail.

3.1 The ISOLDE facility

For further particle acceleration, the proton beam is transferred from the PSB to the Proton Synchrotron (PS), which increase the beam energy up to 25 GeV. Hereafter, the protons are sent to the Super Proton Synchrotron (SPS) which pushes the beam up to 450 GeV. From this point the particles can be finally transferred to the LHC.

The experiments have been performed at the ISOLDE facility at the European Organization for Nuclear Research (CERN). The origin of the ISOLDE RIB facility goes back to the 1960 decade. The first experiment was approved by CERN in 1964. This experiment was finally realized three years latter in 1967, starting off more than 50 years of successful operation, and a large number of experiments carried out since then. Fifty years later, the facility has undergone a good number of changes and upgrades. In 1992, it was moved to its actual location, where it was attached to the CERN Proton-Synchroton Booster (PSB).

3.1.1 The CERN accelerator Complex

The accelerator complex at CERN is a series of particle accelerators, whose aim is to sequentially increase the particle energies before being injected in the Large Hadron Collider (LHC). The LHC is the final stage of this accelerator complex, there the particle beams can be accelerated up to a record energy of 6.5 TeV per beam. At the LHC, two beams circulate anticlockwise, until they reach their maximum energy, then they are brought into collision inside one of the four detectors, ALICE,ATLAS, CMS and LHCb. Nevertheless, those are not the only experiments that are carried out at CERN, most of the other accelerators from the chain have their own experimental halls where the beams of lower energies are used for a wide variety of experiments.

The accelerator sequence starts off with an hydrogen gas source. The H atoms are stripped down of their electrons in a duoplasmatron ion source by the application of a 92 kV extraction potential. The proton beam is injected into the linear accelerator Linac-2, the first accelerating stage at CERN. The Linac-2 is an Alvarez-design drift tube, where the energy of the proton is increased up to 50 MeV in three accelerating tanks with a 202.56 MHz radio-frequency. It started its operation in 1978 replacing the previous Linac-1, after 40 years of operation it was switch off permanently in 2018 at the start of the long Shutdown 2. The new Linac-4 accelerator, which can push the

proton energies up to 160 MeV, will replace Linac-2 during this shutdown. However, the Linac-2 was still operational when the experiment of this PhD thesis took place.

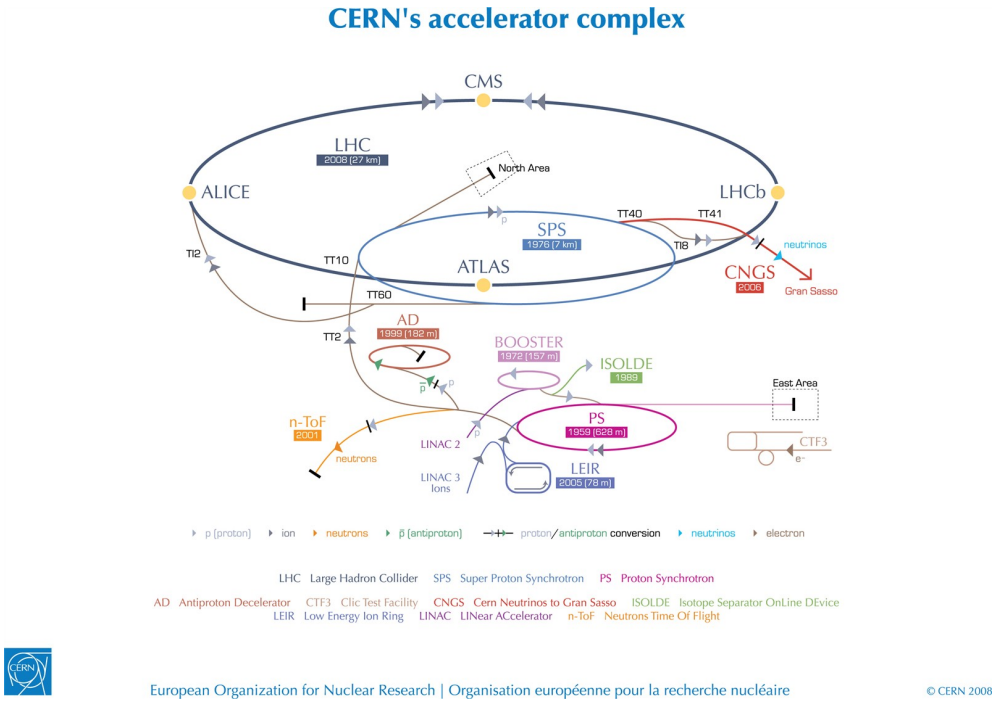

Figure 3.1: CERN accelerator complex.

The 50 MeV proton beam is transported through an 80 m line, and injected into the Proton Synchrotron Booster (PSB). The PSB is the smallest and first circular proton accelerator of the whole CERN complex. It consist of four superimposed rings of 25 meter radius, consisting of 32 dipoles and 48 quadruples each. In the PSB, the energy of the proton is increased up to 1.4 GeV. The protons are released in pulses of 2.4 μs length which are emitted every 1.2 second with a high intensity of 3.6×10^{13} protons/pulse. The proton pulses are grouped in supercycles, which contain a variable number of pulses between 30 and 50. Out of them, a certain amount of proton pulses emitted by the PSB can be delivered to ISOLDE. The pulses that are sent to ISOLDE are randomly distributed, but can be grouped in sequences.

3.1.2 Fission Target

The heart of the ISOLDE facility is the target and ion-source combination. The possibility of heating the target to temperatures up to 2000^{o}C, as well as to combine different

types of target materials and ion sources, gives access to about 1300 different isotopes from more than 75 elements.

Diferent targets can be used for the proton beam to interact. The target units used at ISOLDE are complex systems where a wide variety of species are created by means of fission, fragmentation or spallation reactions induced by the protons. The isotopes that can be produced are strongly influenced by several factors, such as the chemical properties, the energy of the beam and the target thickness. A common strategy to produce neutron-rich fission fragments is to place a proton to neutron converter on the beam path before the target [GML+14]. The neutron converter consist of a solid tungsten rod. When the proton beam impinges on the neutron converter spallation neutrons are produce. They are the ones in charge of inducing the fission in the target. This method reduces the contribution of spallation and fragmentation reactions that may occur and changes the location of the fission peak, reducing consequently the contribution of neutron deficient isobaric contaminants that are produced.

3.1.3 Ionization with RILIS

Once the isotopes are produced, they thermally diffuse out of the target into the ion source thanks to the heating. The isotopes need to be ionized so they can be extracted as an ion beam, by applying an electric field. Some of the methods employed to ionize the isotopes are the surface ionization, plasma ionization or resonant laser ionization. One of the key elements of ISOLDE is the Resonant Ionization Laser Ion Source (RILIS) [FCG+17]. It is based on the multi-step resonant excitation of atomic transitions using wavelength-tunable laser radiation. This is a powerful technique that takes advantage of the unique nature of the atomic energy level structure. In RILIS a set of multiple lasers are used, the wavelength of each laser is set to match the energy of the sequential transitions that the electrons need to undergo in order to leave the atom. The transition energies are characteristic of each element, this technique offers the possibility of ionize only the desired element, while keeping the remaining ones unaffected. The Z-selectivity granted by RILIS provides a effective tool by ionizing only the isotopes with the desired Z for a given A. Still isobars may be surface ionized, specially for alkali elements, and may be present as contaminants if the mass resolving power is not sufficient. The RILIS setup consist of three, tunable dye-type and three Titanium:Sapphire(Ti:Sa)-

type tunable lasers, all of them Nd:YAG pumped. This set of lasers allows RILIS to cover the wavelength range from 210 to 950 nm.

The isotopes produced in the target diffuse into a hot cavity. The RILIS laser illuminates the atoms inside the cavity with a repetition rate of 11 kHZ. The role of this cavity is to confine the atoms during the needed time to be ionized. The high temperatures of the cavity (T$\sim$2000^{o}C) provoke the emission of electrons from the hot metallic surface of the cavity. This effect generates a negative potential well that keeps the atoms for the time needed to be ionized, and prevents the ions of recombining when hitting the walls. The high temperatures can also produce the thermal ionization on the hot surface of atoms with a low ionization potential.

Besides the element selectivity provided by RILIS, there exists also the possibility of selecting an specific nuclear isomer in the produced ion beam [FCG^{+}17]. This possibility arises from the hyperfine separation of the atomic transitions used for resonance ionization, caused by the coupling with the angular momenta of the nucleus. To separate the isomers, the differences on the hyperfine structure need to bigger than the width of the excitation resonances in the hot-cavity. However, the RILIS laser cannot always resolve such differences in the ion source conditions. Therefore, the isomer selective ionization has been only achieved for a limited number of beams. The measurements performed in the two IS610 experimental campaigns that provided data for this PhD, took advantage of this feature to separate the production of the different indium isomers. The separation was better achieved for the odd mass indium isotopes, characterized by a pair ($9/2^{+}$ and $1/2^{-}$) of isomeric states, including a high-spin one. In Figure 3.2 the yield measured at the IDS for the different ^{129}In isomers, as a function of the RILIS laser frequency are plotted. This figure shows that the $9/2^{+}$ and $1/2^{+}$ states can be almost fully separated by tunning the ionization frequency to the right value, while the high-spin ($23/2^{+}$) isomer cannot be maximally ionized without interference from the other states.

3.1.4 Beam extraction, mass separation and transport to the experimental station.

The target/ion-source units at ISOLDE are coupled to target stations, more commonly known as the front-ends. The front-ends are the components in charge of extracting the ionized isotopes from the ion source into the beam line, which is done by a 60 kV

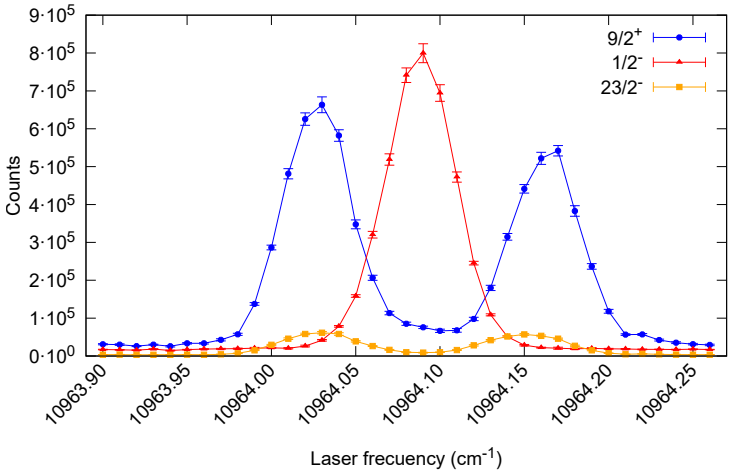

Figure 3.2: RILIS Frequency scan for the production of ^{129}In ion beam. The relative intensity for each β-decaying nuclear state has been deduced from the γ-rays intensities measured at the experimental station.

acceleration gap and an electrostatic quadrupole lens for the beam formation. The entire front-end is enclosed in a metallic airtight cage. To prevent sparks and the formation of nitric acid, dry air is continuously flowing into the acceleration gap. A technical challenge arises from the intense ionization of the air surrounding the target, that is produced by the 2 μA nominal current provided by the pulsed proton beam from the PSB. To avoid the risk of breaking down the high voltages, the high-voltage supply is turned off 35 μs before the arrival of the proton pulse, and restored about 5 ms after.

The transfer of ions from the target to the beam line, is controlled by an electrostatic deflector of 4.5 kV, which is known as the beam gate. This beam gate avoids that ions get inside the beam-line while it is closed, and let them through while it is open. The time interval that the beam gate its kept open, as well as the delay before being opening, are parameters that can be modified to improve the ratio between the desired isotope and the contaminants. It may be kept closed for a few ms after the proton to avoid the short-lived isotopes that are immediately ejected from the target of going into the beam line. After a certain time from opening the beam gate, it can be assumed that the remaining isotopes are potentially contaminants from continuously surface ionized isobars, and then the beam gate can be closed to reduce their transmission to the experimental area.

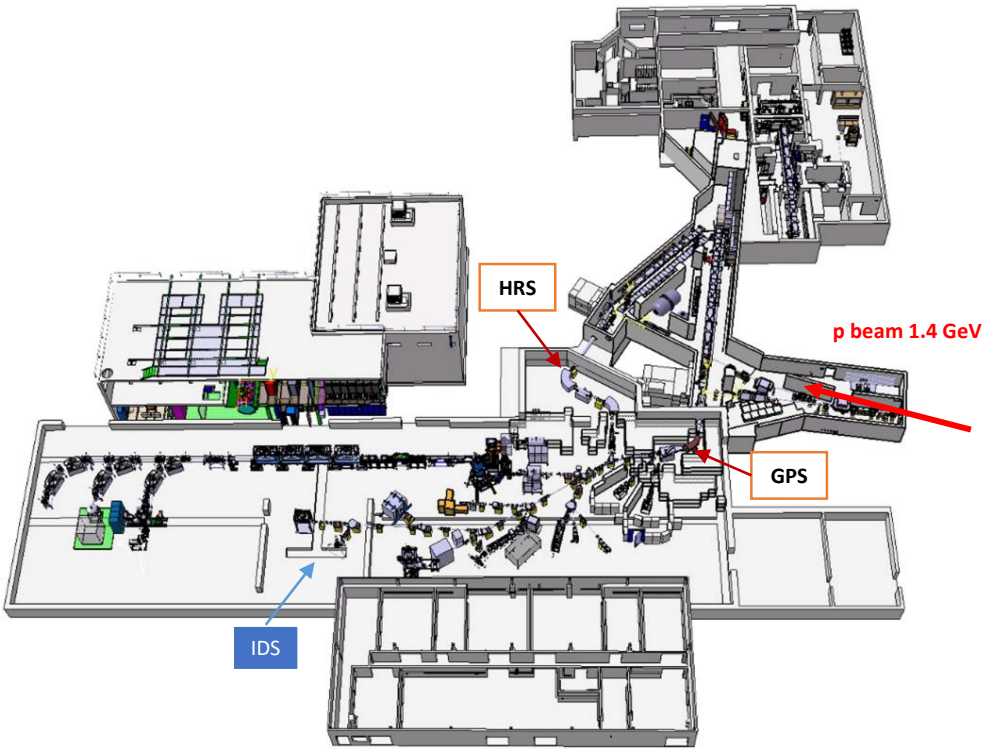

Figure 3.3: Schematic layout of the ISOLDE facility. The 1.4 GeV proton beam impinges from the right-hand side of the facility. Image taken from [CAB+17]

ISOLDE has at its disposal two different isotope separators, each of them has its own front-end which is situated in line with the proton beam from the PSB. The first and smaller separator is the General Purpose Separator (GPS). It consist of a double focus 70º Magnet with a mean bending radius of 1.5 m. The magnets allow to select three ion beams with mass range of 15% of the central mass, and transport them to three different experiments at the same time. Mobile electrostatic deflector plates with the shape of cylinders are used to select the mass. The second one is the High Resolution Separator (HRS), a two-stage mass separator with a much higher resolving power than GPS. It is composed of two C-type designed magnets with bending angle of 60º and 90º respectively. and 1 meter of radius in both cases. Nominally it can achieve resolving power of M/ΔM=15000, however, under normal working conditions the HRS has a resolving power of M/ΔM=5000.

The beam lines paths that emerge from the GPS and HRS continue separately until

they merge together in a merging switchyard, built with cylinder-shaped deflector plates and parallel condenser plates. These plates can be excited with two different polarities, allowing both HRS and GPS beams to be sent through a central beam line, although only one beam can go through at a time. Beyond this merging point, there is a beam distribution system, consisting of 3-way or 5-way switchyards and quadrupole lenses. It connects the beamline with all the experiments in the hall, granting the access to both mass separators. The beam distribution system is built is such a way that the transport of the beam is independent of the mass. Along the whole beam line, there is a complete set of diagnostic elements (Faraday cups, moving wire scanners or wire grids), that allow the monitoring of the beam transport all the way. The transport of the beam is responsibility of the users, who optimize the quadrupoles in order to minimize the beam losses until it reaches the experimental area, the IDS in our case.

Within the experimental hall at ISOLDE, a complete set of experimental setups and instrumentation is dedicated to a wide variety of physics research, including topics such as nuclear structure, nuclear astrophysics and fundamental physics. The low energy area, located just after the mass separators, allocates a number of permanent setups such as the ISOLDE decay station (IDS) dedicated to measure decay properties from radioactive species, the high-resolution laser spectroscopy set-ups as COLLAPS and CRIS, and high-precision mass spectrometers as ISOLTRAP.

The other important system at ISOLDE is the HIE-ISOLDE post-accelerator, an upgrade of the previous REX-ISOLDE accelerator. It makes it possible to increase the energy of the beam, for medium to heavy ion mass, up to 10 MeV/u. These accelerators largely enhance the research possibilities for nuclear structure and nuclear astrophysics studies. Some of the permanent experimental set-ups that are located after this post-acceleration stage are the high-resolution MINIBALL germanium detector array, and the new ISOLDE Solenoidal Spectrometer (ISS) dedicated to precision studies of inelastic scattering and transfer reactions.

3.2 The ISOLDE Decay Station

The ISOLDE Decay Station (IDS) [IDS] is a permanent setup dedicated to decay studies using the radioactive ion beams from ISOLDE. It was built with the aim of providing a versatile detection system located on a low background area. The core setup of the

IDS consists of four to six HPGe clover-type detectors for γ-ray spectroscopy. Different kind of setups can be coupled to the IDS to get sensitivity to different kinds of particles, and also to gain access to different physics properties from the isotopes decay. The IDS began its operation in 2014, since them it has hosted a good number of experiments employing a variety of setups. An extra HPGe detector can be added to the IDS along with a high-efficiency plastic scintillator for $\sim$90% of β detection efficiency. This configuration constitute the high efficiency $\beta\gamma$-spectroscopy setup, more information about this setup can be found in [LRB$^+$19]. Neutron Time of Flight (TOF) spectroscopy, using the VANDLE array [PIM$^+$16]. Charged particle spectroscopy, with the addition of the MAGISOL *Si-plugin* chamber, more information about this setup can be found in [FKT17]. And the fast-timing configuration for lifetime measurements, with the addition of $LaBr_3$(Ce) and fast-plastic scintillators detectors [Fra17, LMF$^+$16].

The experiment from which data were collected for this PhD thesis, got assigned number IS610 and took place in two separate campaigns, one in 2016 and the second one in 2018. It was performed at the IDS using the fast-timing configuration. The main goal of this experimental campaign was to study the excited structure of tin isotopes at both sides of the doubly magic ^{132}Sn, populated in the β decay of indium. The IDS setup for the fast-timing configuration consists of a set of detectors aimed at measuring the β and γ radiation emitted after the β-decay of the implanted isotopes, A picture of the setup can be seen in Figure 3.4. The detectors are arranged in close geometry surrounding the implantation point. The setup can be divided in two branches. The first branch is composed of four clover-type HPGe detectors for γ-ray spectroscopy mentioned above. The second branch is aimed to lifetime measurement of excited states using the Advanced Time-Delayed $\beta\gamma\gamma(t)$ (fast timing) technique [MGM89, MM89, Fra17].

The indium ions were implanted on a aluminized mylar tape inside a T-shaped vacuum chamber. The objective of the tape is to remove the implanted ions from the center of the setup after certain time interval, so that, the accumulated activity from the long-lived daughters is moved out. The tape station is placed below the implantation point, where the majority of the tape is stored rolled up in two reels. The tape station works in the same way than a reel-to-reel tape, the tape movement of the tape is produced by the spin of the reels driven by an electric motors. A tape controller system takes care of handling the tape, allowing to move it in different modes, be it continuous or in a step by step mode. The step-by-step movement can be controlled manually, but

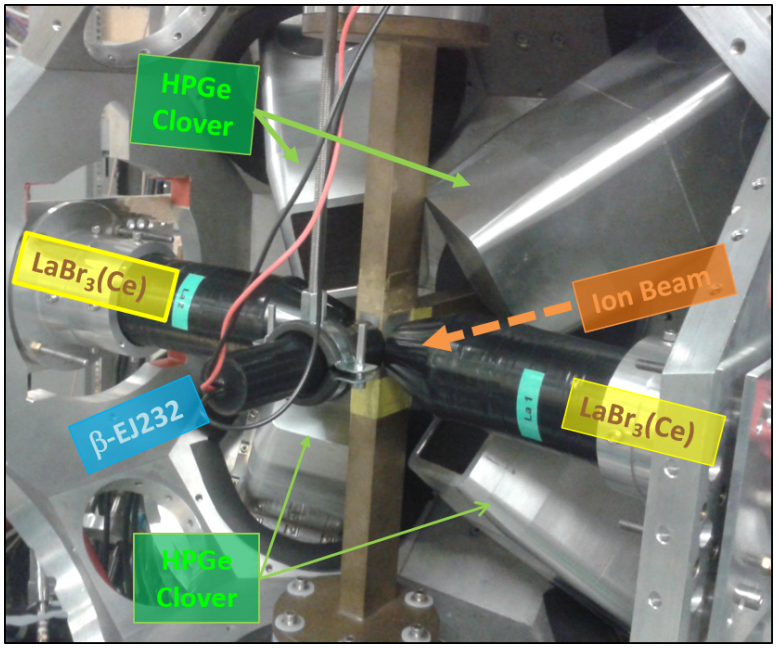

Figure 3.4: IDS setup of detectors used in IS610 experiment.+

it can also be configured to use external trigger signals. Usually, the tape is set to move using the super-cycle signal from the PSB, then the left-over activity is removed at the end of each supercycle, every ∼40 s. It can also be set to move with the proton pulse signal, in this case the tape is moved with every pulse sent to ISOLDE. By moving the tape every proton pulse, the activity of daughter isotopes is highly suppressed, but it puts the tape system under stress. Both methods have been used in our experiment.

3.2.1 HPGE Clover detectors

The core of the IDS setup is the set of four HPGe detectors, for high-energy resolution γ-spectroscopy. The IDS detectors are Camberra EUROGAM CLOVER type detectors [DBT+99], consisting of an assembly of four 4 HPGe crystals, which are allocated in a common cryostat, in order to reduce the quantity of material surrounding the crystals. These detectors are 70 mm long and have a 50 mm diameter. The full energy of a photon that has been scattered in one of the crystal and absorbed in a a second (or even a third) crystal can be reconstructed by applying add-back correction, where the full energy is obtained by summing the energy deposited in each crystal. Consequently, the clover-type detectors are characterized by a high absorption efficiency, which is

higher than four times the efficiency of a single crystal.The mean relative efficiency of each crystal is between 21 and 22 %, while the total relative efficiency achieved after the add-back correction is between 130 and 140%.

These detectors also show excellent energy resolution, having a 1.95(5) of FWHM for the 1332-keV peak, in total detection mode, and a very similar FWHM=2.11(5) in addback mode. Their time resolution is 5 to 6 ns FWHM for each crystal, measured in coincidence with a small BaF_2 scintillator at cobalt energies, which is rather good for a HPGe detector. All these characteristics have been taken from [DBT+99].

Due to these excellent qualities, these detectors are the main tool to extract the spectroscopic information. The time resolution is poor in comparison with scintillator detectors, and thus is not suitable for measuring lifetimes in the picosecond range, but still they are employed to measure half-lives in the range from tens of ns to μs. They play an important role in fast-timing measurements by providing a high-resolution extra coincidence gate.

3.2.2 $LaBr_3$(Ce) detectors

$LaBr_3$(Ce) scintillators have been the standard detectors for the fast-timing techniques during the last decade, the details about the fast-timing methods are explained in Chapter 4. They replaced BaF_2 scintillators, which were the traditional detectors employed for fast-timing measurements since the origin of the technique [MM89]. BaF_2 crystals coupled to XP2020 PMTs, are characterized by a very fast component of their output signal, which yields an excellent time resolution of 120 ps at cobalt energies. One of the main limitations of these detectors was the poor energy resolution of 9% to 10% for the 662-keV FEP in ^{137}Cs.

The commercial availability of the new $LaBr_3$(Ce) scintillators led to a drastic change for the application of the fast-timing technique. Lanthanum crystals are characterized by a high photon yield (63 photons/keV), a relatively high density ($\sim$5.3 gcm^{-3})) and a very sharp rise time [Gob]. All these qualities grant to the $LaBr_3$(Ce) an excellent energy resolution of $\sim$3% at 662 keV, notably superior than the $\sim$10% achieved for BaF_2 crytals of the same size while keeping a competitive time resolution of 140 ps at ^{60}Co energies [VMF+15]. This enhanced energy resolution is very advantageous for fast-timing measurements on exotic nuclei, which are usually characterized by complex decay schemes, with a large number of γ-rays of similar energies. This enhanced energy

resolution helps to disentangle overlapping peaks, as well as to improve the ratio between the FEP and Compton background underneath the peak. For these reasons the $LaBr_3$(Ce) has been the preferred choice for the application of the fast-timing technique during the last-decade [MBB$^+$10, ARM$^+$13, OFM$^+$13, RSB$^+$14].

For fast-timing measurements in the IS610 experiment two $LaBr_3$(Ce) detectors were used. These crystals have a shape of truncated cones with 1 inch height and bases of 1.5 inch and 1 inch. This choice was fruit of detailed studies, carried out by the Grupo de Física Nuclear at UCM (Madrid) by Vedia *et al* [VMF$^+$15, VCGF$^+$17, Fer19], where the performance of different crystals varying the Ce dopant concentration, as well the shape of the crystal was investigated. Both crystals were coupled to a 8-stage Hamamatsu R9779 2-inch photomultiplier (PMT)[Ham09a]. These PMT were chosen by their excellent timing capabilities, as well as good spectroscopic features. The use of two detectors assures a compact setup of high efficiency while reducing the level of complexity. The two $LaBr_3$(Ce) detectors were placed at the closest position possible from the implantation point $\sim$10 mm, at an angle of about 86^o to the direction to the ion beam.

3.2.3 Beta detector

In the IS610 experiment, the β detector played a double role. The first one was to define the starting time for the $\beta\gamma$(t) events in fast-timing measurements. The second role was to be used as a selection for β decay, to clean the γ-ray spectra. The β energy spectrum is a continuum, thus, the energy resolution of the detector is not a significant quantity for our study. The most desirable characteristic for the β-detector is the fast time response. With this aim, the plastic had the shape of a cylindrer with a width of 3-mm and a diameter of 25 mm. The use of a thin plastic, ensures that the β particles deposit almost the same energy, independently of the total energy of the β. This grants a quasi-uniform time-response for a wide range of β spectra. At the same time it provides a small sensitivity to γ-rays. For this reason an ultrafast EJ-232 plastic scintillator with a reported rise time of τ=350 ps [Elj], which is the commercial equivalent to the NE111A plastic, was employed. In order to obtain the best time resolution possible, the β plastic was coupled to the high speed 10-stage Hamamatsu H6610 (R5320) PMT, which has a very short rise time of 0.7 ns and a transit time spread (TTS) of 160 ps FWHM [Ham].

The β detector is placed in the direction of the beam, just behind implantation point (see Figure 3.4). It has the drawback of being behind two layers of tape at a nominal distance of ∼20 mm. The efficiency for the β particles that goes thought it should be ∼100%. Thus, given the position where it is located and the solid angle covered it is expected an efficiency of ∼15-30%. The efficiency should be similar, independently of energy of the β, however a big drop in tha efficiency can be observed between for decaying isotopes with low Q_β-E_x energies, caused by the threshold.

3.2.4 Electronics and acquisition

The detector signals are sent to a Nutaq digital acquisition system [nut], where they are read and digitized. Before that, the signals go through a pre-processing stage, consisting of a set of signal amplifiers and electronic NIM standard modules. The electronic processing paths can be divided in two separate branches, one dedicated to process the energy information, and a second one oriented to extract the timing information from the scintillators. The full electronics scheme is depicted in Figure 3.5.

3.2.4.1 Energy branch

The energy branch is very simple. The detectors output signals are treated separately before being introduced into the DAQ. The signal processing is different for each type of detector. For the 4 HPGe-clover detectors that produce a total of 16 signals, they are introduced into the GoBOX unit that adjust the gain and offset of the signals, before being fed to Nutaq.

In the case of $LaBr_3$(Ce) detectors the R9779 PMT has two separate output signals, the positive one from the dynode (DY) and the negative one from the anode (SIG). The dynode ones are used to retrieve the energy information. They are preprocessed by an ORTEC 113 Preamplifier, with an input capacity of 500 pF. Then, the signals are directed to the GoBOX, to adjust their gain before entering them into Nutaq.

In the case of the EJ232 β plastic, the energy signal is taken from the positive PMT dynode output. The processing of this energy signal differs slightly between the 2016 and the 2018 campaigns. In 2016 the signal was passed through an RC integrator before being fed to an ORTEC 474 Timing Filter Amplifier (TFA), which was configured with a coarse gain of ×10, fine gain of 7.25, and integration time of 200 ns. After the TFA the signal was sent to the GoBOX and then finally to Nutaq. In the 2018 campaig,

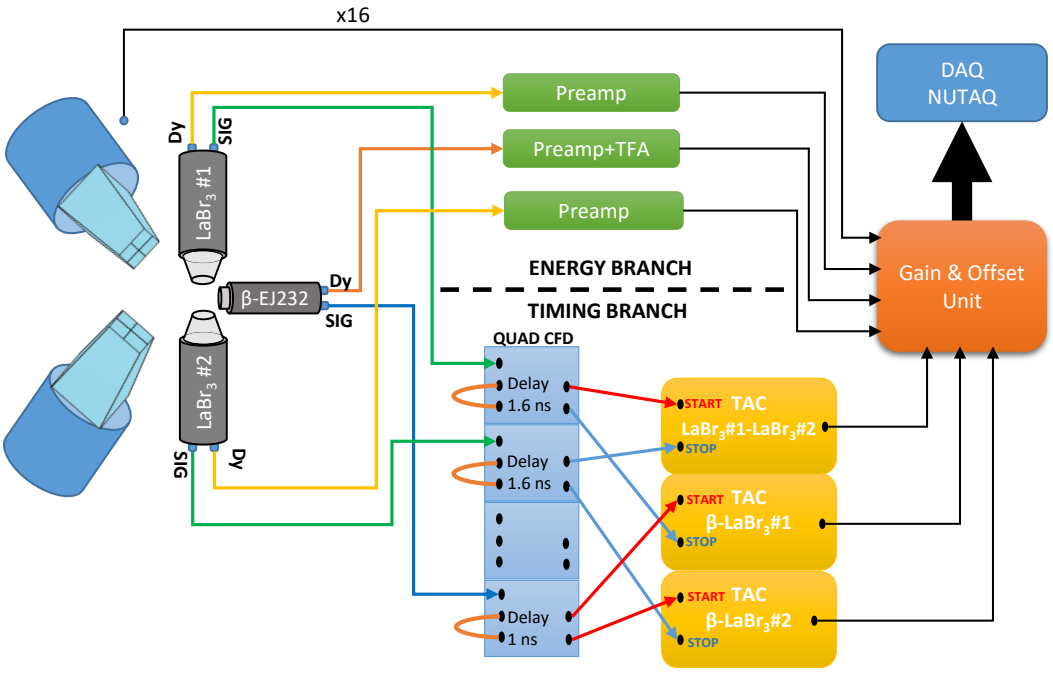

Figure 3.5: Electronic Setup scheme from IS610 experiment. The upper part shows the electronic scheme dedicated to pre-process the signals used to derive the energy information. The lower part corresponds to the timing branch of the electronic scheme. This part takes care of processing the timing information of the three scintillator detectors. A Quad CFD is used for the pre-processing of the timing signals, and three TAC modules are used to derive the time difference between the three detectors.

an ORTEC 142 Pre-amplifier was added between the between the RC circuit and the TFA. The settings of the TFA were also different, the coarse gain was set to x2, the fine gain was set at $\times 2$, the RC integration time was set to 500 ns and a differentiation time was set at 500 ns. Because of the different configurations, the energy resolution of the β-energy was smaller for the 2018 measurements.

3.2.4.2 Timing branch

The mission of the electronic timing section entails not only the pre-processing of signals before being digitized, but also to generate the time difference information for the coincidence events between scintillator detectors. The time resolution of the HPGe detectors is not suitable for ps lifetime measurement, and thus a separate timing section for them was not included . Nonetheless, their timing information was recovered in the

later event-building stage.

The timing information is measured from the negative signals extracted from the PMT anode outputs. The signals are directly sent to an ORTEC 935 Quadruple CFD (Constant Fraction Discriminator). The CFD module has 4 separate channels, thus the same module is used to process the signals from the three detectors. The three used CFD channels were operated using an external delay of 1.6 ns in for $LaBr_3$(Ce) channels, and 1 ns for the β-plastic signals. Regarding the other parameters from the CFD, the zero crossing value (Z) was set to +2 mV and the threshold (T) to -507mV for all three detectors. These parameters had been optimized earlier to maximize the time resolution of the system at the expense of a somewhat large, (but still reasonable) walk.

Following their passage through the CFD, two output signals were taken from each CFD channel. These output signals were distributed between three ORTEC 567 Time to Amplitude Converter (TAC) 200 MHz modules, which converts the time difference between the arrival of two signals in an output signal with an amplitude proportional to their time difference. After the arrival of the signal that is used as START, the TAC begins to rise the voltage until the stop signal is received, thus an output signal is generated when the two signals are sent to the TAC within the selected time range, whose height is proportional to the time difference between the signals. In the IS610 experiment three TAC modules were used, which were operated in the shortest 50 ns time range, in order to measure the time difference between the three combinations of fast-timing detectors. The first two are used for the time difference between the β-plastic and the two lanthanum detectors, while the third one is aimed at measuring the time differences between the two $LaBr_3$(Ce) detectors. The input and output cable lengths to the TAC modules were adjusted to place the prompt time peak in a suitable location in the TAC time range. Finally, the output signals from the TAC are sent to the GoBOX, and subsequently Nutaq, where they are treated like the other signals.

3.2.4.3 Digital Data acquisition system Nutaq

The task of sampling and recording the electrical signals, was done by the 14-bit 100 MHz Nutaq VHS-V4 data acquisition (DAQ) system [nut]. The IDS Nutaq DAQ consist of three acquisition cards of 16 channels each. The signals from all the different detectors, TACs and other logic signals such as the proton pulse, are accommodated

among all the channels, and digitized with a 10 ns sampling step. The digitized signals pass through a trapezoidal filter whose parameters are optimized independently for each type of signals. Finally the information relative to the amplitude of the pulse, its timestamp, and channel are sent to a computer and recorded in list-mode file [LAB$^+$01] with a maximum size of 2 GB.

The distribution of the signals among the Nutaq cards is summarized in Table 3.1. The distribution take into account the expected count rates (for buffer handling), the types of filters, and the event building procedure. The first two cards are used only for the energy signals from the 16 clover crystals, leaving half of the channels in both cards empty. The third card, takes care of digitizing the energy signals from both $LaBr_3$(Ce) detectors and the β-plastic, and the three TACs. Other kinds of information are also input into the third card. The T1 signal from the PSB, which is sent every time that a proton is sent to the target and provides a valuable timing information, is entered in the first channel. Other signals were the warning of the beam gate closure and the start and stop of the tape movement.

Table 3.1: Distribution of the the IDS signals in the Nutaq cards.

Channel N	Card 1	Card 2	Card 3
1	Clover 1-1	Clover 3-1	T1 Proton impact signal
2	Clover 1-2	Clover 3-2	TAC $LaBr_3$-1-$LaBr_3$-2
3	Clover 1-3	Clover 3-3	TAC β-$LaBr_3$-2
4	Clover 1-4	Clover 3-4	TAC β-$LaBr_3$-2
5	Clover 2-1	Clover 4-1	BG closed
6	Clover 2-2	Clover 4-2	Tape start
7	Clover 2-3	Clover 4-3	Tape stop
8	Clover 2-4	Clover 4-4	-
9	-	-	-
10	-	-	-
11	-	-	β Energy
12	-	-	$LaBr_3$-1 Energy
13	-	-	$LaBr_3$-2 Energy
14	-	-	-
15	-	-	-
16	-	-	-

3.3 Data sorting and analysis methodology

The stored data contains information about the amplitude of the signals, the input time to the DAQ, the channel and whether or not it was a pile-up event. However, the RAW data file does not have correlations between the incoming signals. Thus, the first step of the analysis is the event builder, where all the data are sorted by detector type and grouped in events measured within a specific coincidence time window.

The LST files that are generated by the event builder contain all the required parameters to extract the information about the decay under study. To analyse these data, a set of programs are required to sort out the multiparametric events, given a set of conditions, and to build the spectra that will be analyzed. The analysis can be distinguished in two main parts. The first part corresponds to the γ-ray spectroscopy, which consists in the identification of γ-rays belonging to the studied nuclei and their allocation in their corresponding level-scheme. The second part is oriented to the measurement of the half-lives of the excited states, which employs the information retrieved by the scintillator detectors and TAC modules in delayed coincidence events

3.3.1 Event builder

The event building processing is performed by the Nutaq4IDS tool, developed by R. Lică, *et al* [Lica]. This is a C++ software that reads RAW data files, group the data into events and produces output files in event list mode, which can be written in different format types. This tool requires only of a configuration file to work. The detectors can be calibrated also at this step by the input of an optional calibration file. In the configuration file the following parameters to build the events are defined:

- runName: Path and base name of the RAW data files.
- timegate: Coincidence time window. This value is set to 1μs by default.
- reftype: Defines the input signal that is used as time reference. For our experiment, it was the proton pulse arrival time signal.
- ref_unit: Defines the time units of the event relative to the reference. This value is set to 1 ms by default.
- run_unit: Time unit for the absolute time of the file. This value is set to 100 ms for this analysis.
- Format: Format of the output LST-events file.
  - gasp: GASPware format.

  - root: ROOT format.
  - list: Binary event lists.
  - stat: Print the count rate statistics of the whole file.
  - rate: Print the count rate statistics of the last buffer.

- Fold: Minimal number of detector hits required to define an event.
- Detector configuration: List of detector types, related to their respective DAQ channel ID and timestamp corrections to account for shifts due to the divergent electronic paths.

The nutaq4IDS event builder generates two output files, a log file including the count rate statistics for every channel, and an event list file written in the defined format. Regardless of the format, the events contains the following parameters:

- Timestamp of the event, written in the defined "run_unit" units.
- Low resolution time. It contains the time difference between the detection of the event and the the last signal in the channel used as reference (proton pulse in this case). This time is written in "ref_unit" units.
- Total multiplicity of the event: Number of detector hits that conforms the event.
- List of hit signals included in the event. For each signal in the event the following information is included:
  - Amplitude of the signal. Energy measured by the detector, or amplitude if no calibration file has been used.
  - High resolution time. It corresponds to the time of each hit within the event. The time is defined as the centroid time of all the signals that make up the event. This time is written in 10 ns units, which corresponds to the Nutq 100 MHz sampling rate.
  - Detector multiplicity (Only if root format is used). Number of event hits of each detector type.

3.3.2 γ-ray spectroscopy.

The study of the γ-ray spectra emitted in the decay under study, mainly relies in the information recorded in HPGe detectors. In our experiment there are three types of information that can be used for the identification of the γ-rays in the spectra. Firstly, their time distribution relative to the proton pulse arrival time is strongly correlated with the half-life of the isotope decay in which they are emitted. Secondly, to require an extra coincidence with the β-detector ensures that the γ-rays have been emitted in a β-decay, reducing the contribution of other kind of contaminants. Thirdly, the analysis of HPGe-HPGe γ-γ coincidence with presviusly known transitions led to unambiguous placement of the the γ-rays in the level-scheme.

This part of the analysis has been done using the event list-files written in the GASP format. The GASP-format event file was analyzed employing the tools from the GASPware data analysis package developed by D. Bazzacco *et al*[Baz]. The most important tool is the gsort program, it allows us to generate histograms and 2D or 3D matrices on any of the parameters that define the events. The working of the gsort program is controlled by a flexible configuration file, where we can define the histograms and matrices that we want to generate, set sorting conditions on any other parameter of the event, include calibration files and perform the addback correction on the HPGe-clover detectors. The other key tool is the xtrackn tool, which provides a graphical interface for the analysis of the γ-ray histogram and 2 dimensional matrices.

The γ-ray analysis relies in two kind of 2D matrices. The first two are the HPGe energy versus proton time matrices of singles and β-gated events, which are built using all the detected HPGe hits or only those registered in coincidence with the β detector respectively. They are used to extract the time information about the γ-rays, and also to measure the intensities of the γ-rays. The other type of matrices are the HPGe-HPGe coincidence symmetric matrices, β and non-β gated. They are used for the $\gamma - \gamma$ coincidence study.

3.3.3 Lifetime measurements

In this PhD thesis, the measurement of excited levels lifetimes are done by means of the fast-timing methods. These methods are based in the time correlation between two of the scintillator detectors. Other types of information, such as coincidence with other

detectors or the detection time of the evens, can also play indirectly an important role in the fast-timing analyis. A detailed description of the fast-timing methods is given in Chapter 4.

For the fast-timing analysis, within this PhD thesis it has been developed a series of tools in ROOT. The aim of these tools is to perform the sorting of the events, and at the same time take care of all the corrections needed to deal with systematics corrections in the analysis. The process of the analysis can be divided in two steps, a first presorting step, and the second where all the gating conditions are applied and the time distributions are generated.

The presorting step is done by the a program called FTGlobalTree. The mission of this program is to read the original event files generated by the nutaq4IDS program in .root format and select only those events relevant for the fast-timing analysis. Only those events where a signal from any of the TAC modules are registered, along with their corresponding $LaBr_3$(Ce) detectors, pass through this filter and are saved in the output .root file in the form of tree. Energy calibration, and detector energy drift corrections are also implemented in this step. The tree in the output file, contains the $LaBr_3$(Ce) and β detectors energy, the three TAC modules, the time relative to the proton pulse, and in the case there was a coincidence with any of the HPGe detectors, the energy measured by them.

After the presorting process, the next step entails the selection of a given combination of γ-ray events to analyze their time delayed distributions. Gating conditions on any other parameters can also be required in this step. The analysis follows in two separated paths, depending if we want to analyze the $\beta\gamma$(t) or the $\gamma\gamma$(t) time differences.

In $\beta\gamma$(t) events firstly a two 2d-histogram is built, which contain the $\beta\gamma$(t) TAC vs energy in each $LaBr_3$(Ce) detector. The BG_matrix program create these histograms taking into account all the gating conditions in any other parameter that are defined in an input file, including a coincidence gate in the HPGe detector or a time condition for the events. The correction of the *β-walk* is implemented in this step, (see section 4.4.2 from Chapter 4). In the last step the desired γ-ray peak in the $LaBr_3$(Ce) detector is selected and its corresponding time distribution is generated. The BG_Time_distribution program takes care of this step. It requires of three energy gates as input, which are used to estimate the time distributions of the selected peak and its Compton background contributions. This program takes care of correcting the

contribution of the Compton background, using the correction procedures described in Section 4.3 from Chapter 4. Three time distributions are generated, one for the peak, including FEP and Compton events, one for the estimated contribution of Compton background, and a third one for the estimated contribution of FEP events only.

The analysis of $\gamma\gamma$(t) events is very similar, but in this case the building of the time distribution is done in one step by only one program, the GG_Time_distribution. This program requires the definition of the energy gates in the START and STOP detector for the peak and background estimation. In addition, further conditions can also be specify on the other parameters to attain a better selectivity. The program reads the Tree and generate the corresponding time distributions, performing the corresponding corrections for the contribution of Compton background.

3.3.4 Lifetimes with HPGe detectors

The HPGe-clover detectors at the IDS station are not optimal to be used for lifetime measurements below the ps range, but their time resolution is more than sufficient to measure lifetimes longer than tens of nanoseconds. Hence, the measurement of long lived-isomers with half-lives in the range of 50 ns to μs, has been carried out using the timing information from the HPGe clovers. a measurement of time differences between detectors can be obtained using high-resolution relative time of the signals. Hence, the time difference between two detectors within the event is measured as the difference of the high-resolution time of two detectors hits.

For the HPGe detectors, the timing information was not directly measured with TAC modules, like for the scintillator detectors. This time correspond to the relative time, inside the event when each of the signals was received.

The processing of the event-list file was conducted by a code written in root, whose task consisted in reading the event tree file, compute the time differences between the selected detectors and save the needed information about the time and energies in an output file. In this analysis, only the time differences for the β-HPGe(t) and HPGe(t)-HPGe(t) coincidences have been derived. At the event building stage, all the incoming signals since the arrival of the first one are included in the event, within the defined coincidence window. When more than two signals are received, the coincidence time window for the later signal is smaller, which produces a non-linear behaviour of the

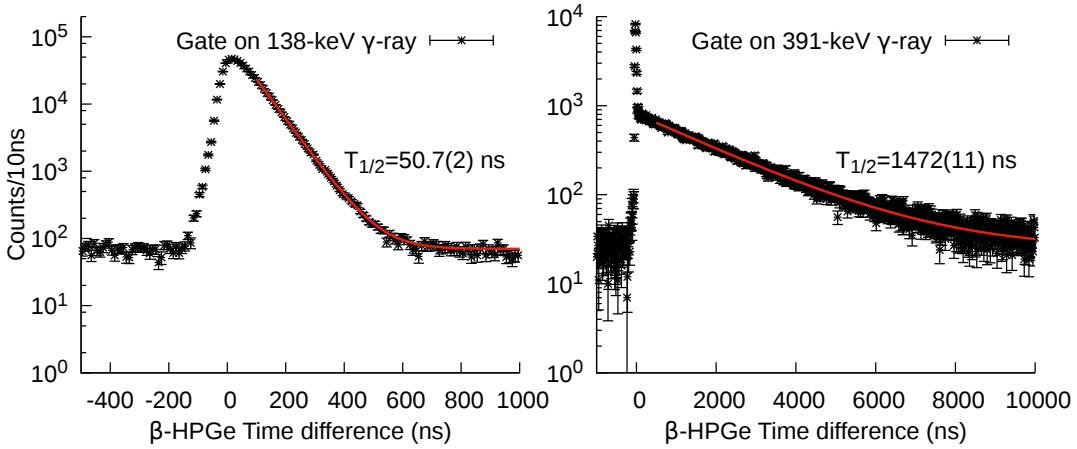

Figure 3.6: β-HPGe(t) Time spectra for the Test for the timing analysis with HPGe detectors. Long-lived isomers in ^{130}Sn. (Left) β-HPGe(t) time distribution of the 138-keV γ-ray that de-excite the 2084-keV (8^+) state. (Right) β-HPGe(t) time distribution of the 391-keV γ-ray that de-excite the 2434-keV (8^+) state.

time distributions. To avoid this issue only the events consisting of two detector entries are used in the lifetime analysis.

The validity of this methodology has been tested by analyzing the long-lived states in ^{130}Sn, they are excellent to test this method in the ns to μs range, which are $T_{1/2}$=52(3)ns from 2084.4-keV (8^+) level, and the $T_{1/2}$=1.61(15) μs from 2434.8-keV (10^+) level [FHS81]. In Figure 3.6, the β-HPGe(t) time-delayed distributions gated on the 138-keV and 391-keV transitions that de-excite the 2084- and 2434-keV level respectively, are shown. Both values are in agreement with the previous measurements [FHS81] within their errorbars.

3.4 Calibrations

We briefly discussed the calibration procedures of the detector setup, which can be divided in energy and efficiency calibrations performed for the HPGe, $LaBr_3$(Ce) and β-plastic detectors. The calibrations of the fast-timing setup will be covered in Chapter 4.

3.4.1 Energy Calibration

For the energy calibration of the γ-ray detectors, we study the spectrum of a source whose γ-ray energies are previously well known. The In isotopes are characterized by large Q_β values, hence it is expected to observed γ-rays of high energies, above 4 MeV, and the calibration sources that are used do not reach such higher energies. Therefore a first energy calibration was done using a standard source, but later an internal calibration using the γ-lines from the ^{132}In decay was used. The γ-rays in ^{132}Sn are an excellent internal calibration, since their energies are already known from previous studies [KRSS05]. Additionally the energy range of the strong γ-rays emitted in ^{132}In decay is very wide, with γ-lines in the energy range from 64 keV up to 4.4 MeV.

During this analysis, as well as in other recent indium decay studies in this same region [PKF$^+$19, DSA$^+$19], a good number of γ-rays up to 7 MeV are emitted and therefore, a precise energy calibration is required up to such energies. In order to extend the range of calibrated energies, high-energy neutron capture γ-rays were employed. These γ-lines are produced by the interaction of the thermal neutrons that are produced in the ISOLDE target area and reach the experimental setup. These neutrons are captured by the materials that surround the experimental setup, as well as by the detectors material. The most common neutron γ-lines can be related to transitions in Fe from the setup frame, H, O and Cl from the surrounding air, and Ge or Al from the HPGe-clover detectors. These γ-rays, along with their respective escape peaks, are used to fill in the missing range from 4 to 8 MeV.

3.4.1.1 HPGe-Clover

The 4 clover detectors are composed at their own of 4 HPGe crystals. For the sake of simplicity, the analysis of the HPGe γ-rays is done using the summed spectra from the 16 crystals. This requires that each crystal is calibrated separately before summing up all the information in one single spectra. The calibrations are very similar, but small deviations can be observed. The HPGe detectors are characterized by a linear energy response up to very high energies. In Table 3.2 there are summarized the calibration coefficients obtained for each clover crystal from the fit to a linear function $E = a_0 + a_1 \cdot Channel$, for this preliminary calibration of each crystal, only the γ-rays from ^{132}In decay were used. The neutron capture γ-lines were not included due to the low statistics

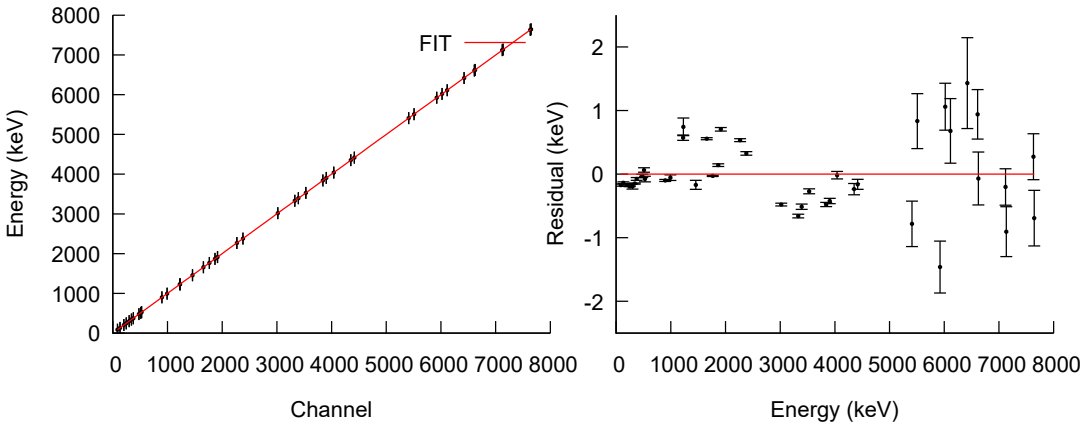

Figure 3.7: Energy calibration of the full HPGe-clover spectra. The high-energy neutron capture γ-rays have been included in the spectra including the γ-rays.

in the individual crystals. This preliminary calibration ensures the matching between the energies measured by all the crystals separately.

Table 3.2: Energy calibration coefficients for the 16 HPGe crystals. The parameters are from the linear fit $E = a_0 + a_1 \cdot Channel$ for the 16 clover-crystals.

Detector	a_0	a_1	Detector	a_0	a_1
Clover1-1	0.0350	0.5458	Clover3-1	0.5072	0.5984
Clover1-2	-0.5085	0.5532	Clover3-2	0.3191	0.5862
Clover1-3	-0.3560	0.5494	Clover3-3	0.3764	0.5832
Clover1-4	-0.8245	0.5408	Clover3-4	0.0223	0.5777
Clover2-1	-0.4170	0.5429	Clover4-1	-0.3443	0.5776
Clover2-2	0.0938	0.5690	Clover4-2	-0.4793	0.5607
Clover2-3	-0.2616	0.5515	Clover4-3	0.0735	0.5390
Clover2-4	-0.2096	0.5406	Clover4-4	-0.9878	0.5463

Once the individual crystals were calibrated, the statistics from all of them were combined in only one spectrum, applying the add-back correction in the process. This new full HPGe-clover spectra was analyzed again, including the high-energy γ-rays from neutron capture reactions. In Table 3.3 the γ-rays used for the full spectrum calibration are listed.

Figure 3.7 shows the result from the fit, for the combined HPGe spectrum. In the

Table 3.3: γ-lines used for the HPGe-clover energy calibration. γ-rays observed in the decay of ^{132}In and their daughters ^{132}Sn and ^{131}Sn were used. The high-energy range is covered with neutron capture γ-lines from ^{56}Fe mostly, and several from ^{27}Al and ^{40}Ca.

Process	E_γ(keV)	Process	E_γ (keV)
^{132}Sn decay	85.58	^{132}In decay 4042 DE	3019.1
^{132}In decay	132.5	^{132}In decay 4351 DE	3329.9
^{132}In decay	203.1	^{132}In decay 4416 DE	3394.2
^{132}Sn decay	246.87	^{132}In decay 4041 SE	3530.1
^{132}In decay	299.6	^{132}In decay 4351 SE	3840.9
^{132}Sn decay	340.53	^{132}In decay 4416 SE	3905.2
^{132}In decay	375.1	^{132}In decay	4041.1
^{132}In decay	479.1	^{132}In decay	4351.9
^{132}In decay	526.2	^{132}In decay	4416.2
e^++e^-	511	^{27}Al(n,γ)^{28}Al	5411.069
^{132}Sn decay	899.04	^{56}Fe(n,γ)^{57}Fe	5507.42
^{132}Sn decay	992.66	^{27}Al(n,γ)^{28}Al	5923.42
^{131}Sn decay	1229.28	^{56}Fe(n,γ)^{57}Fe	6018.42
^{131}Sn decay	1226.04	^{56}Fe(n,γ)^{57}Fe	6112.58
^{132}In decay	1457.5	^{40}Ca(n,γ)^{40}Ca	6420.7
^{132}In decay	1656	^{56}Fe(n,γ)^{57}Fe	6609.18
^{132}In decay	1766.5	^{56}Fe(n,γ)^{57}Fe	6623.58
^{132}In decay 2380 SE	1869.2	^{56}Fe(n,γ)^{57}Fe	7120.18
^{132}In decay	1914.4	^{56}Fe(n,γ)^{57}Fe	7134.58
^{132}In decay	2268.6	^{56}Fe(n,γ)^{57}Fe	7631.18
^{132}In decay	2380.2	^{56}Fe(n,γ)^{57}Fe	7645.58

left plot, we can observe that beyond 4 MeV the HPGe detectors still behave linearly. The image at the right-hand side depicts the residuals of the data points employed in the fit. We can notice the goodness of the fit, the deviations being well below 0.5 keV for energies below 5 MeV, while for the 6-8 MeV region, the average deviation is below 1 keV.

3.4.1.2 $LaBr_3$(Ce)

The main function of the $LaBr_3$(Ce) detectors is their use for fast-timing measurements, where selection of the γ lines is done with the help of coincidences with the HPGe and/or other conditions. Contrary to the HPGe detectors, a wide range and precise energy calibration for these detectors is not needed.

A common feature of high photon yield scintillators such as $LaBr_3$(Ce) detectors, is that they display a non-linear energy response. The main cause behind this lack of linearity seems to be the gain variance of the PMT [DdHvE95], because the intrinsic $LaBr_3$(Ce) yield is pretty linear. Studies of the performance of lanthanum crystals coupled to the Hamamatsu R9779 PMT [Ham09b], found that the linearity influenced by the voltage applied to PMT [VMF+15], maintaining a linear behaviour for voltage values below -1300 V.

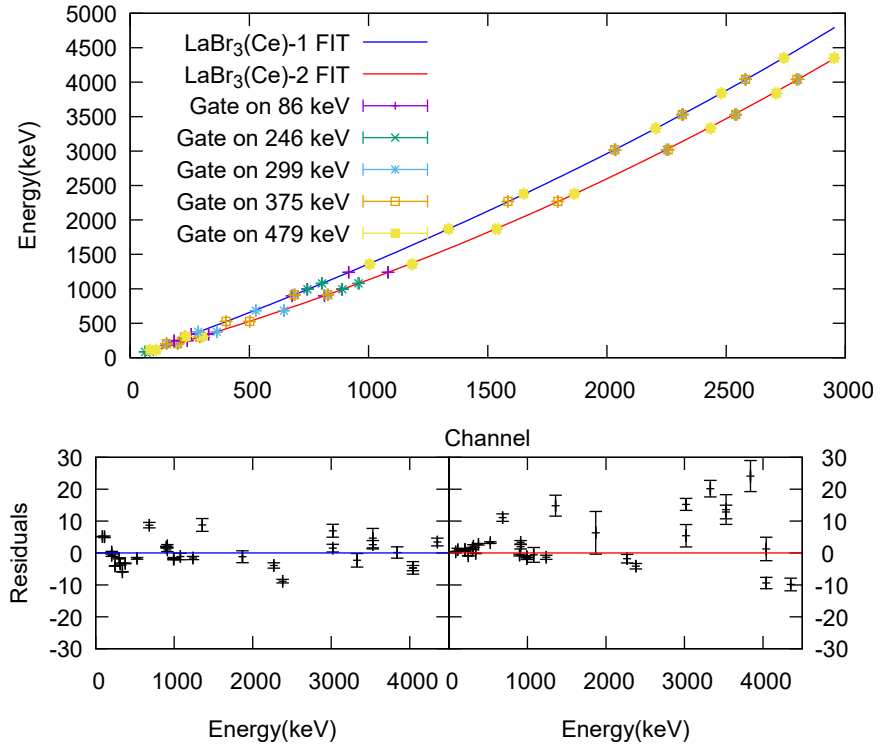

Figure 3.8: Energy calibration for the $LaBr_3$(Ce) detectors. The γ-rays emitted after ^{132}In decay were used for the fit. The Bottom plots show the residuals for each detector.

For the calibration of the $LaBr_3$(Ce) detectors, we have also used the γ-lines that are emitted after the decay of ^{132}In (Table 3.3). In this occasion the high-energy neutron capture γ-lines were not included. Only the more intense transitions were considered. For the determination of the energy centroid of the peaks, an extra coincidence gate with the "HPGe-clover" detectors was used. Figure 3.8 shows the energy calibration curves for the two $LaBr_3$(Ce) detectors. Both detectors show a linear behaviour for energies below 1 MeV, however, a deviation is observed when moving up to higher energies. To expand the calibration range up to the 4 MeV γ rays, a 4 degree polynomial function was used for both detectors, see equation 3.1. The overall agreement achieved with this calibration was very good, with an average deviation of the energies below 5 keV for lower energies, and $\sim$15 keV in the 4 MeV energy range.

$$Energy(keV) = a_0 + a_1 \cdot Chan + a_2 \cdot Chan^2 + a_3 \cdot Chan^3 + a_4 \cdot Chan^4 \qquad (3.1)$$

Table 3.4: Energy calibration coefficients both $LaBr_3$(Ce) detectors.

	a_0	a_1	a_2	a_3	a_4
$LaBr_3$(Ce)-1	14.0(34)	1.21(2)	$1.4(3)\times10^{-4}$	$-1.3(18)\times10^{-8}$	$4.0(32)\times10^{-12}$
$LaBr_3$(Ce)-2	5.0(9)	0.968(7)	$1.51(14)\times10^{-4}$	$7.3(110)\times10^{-9}$	$-3.6(239)\times10^{-13}$

3.4.2 Efficiency calibrations

The efficiency characterization for the γ-ray detectors, is done using a radioactive sources placed at the implantation point, whose γ-rays energies and intensities are well known. The total efficiency is mainly determined by two factors. Firstly, the solid angle covered by the detector indicates the fraction of particles that are emitted towards the detector. The second factor is the intrinsic efficiency, it indicates the fraction of impinging particles that are detected. This last factor may change depending of the energy of the particle. In this subsection the efficiency calibration for the HPGe-Clover, $LaBr_3$(Ce) detectors and β-plastic detector will be discussed.

3.4.2.1 HPGe-Clover

The measurement of the full-energy peak efficiency of the HPGe clover detectors is of vital importance to obtain the γ-ray intensities. For this reason, a complete set of γ-ray

calibration sources, including ^{152}Eu, ^{133}Ba, ^{88}Rb, ^{140}Ba and ^{138}Cs, were used during the IS610 experimental campaigns. This detailed calibration allow us to cover a wide range of energies up to the 4 MeV.

For simplicity, the γ-ray spectrum used to measure the efficiency, were built combining each segmented of the 16 HPGe clover segments. Hence, the obtained efficiency corresponds to the total efficiency of the whole HPGe setup of detectors. To measure the absolute FEP efficiency, in the first place the efficiency obtained for the ^{152}Eu source, whose activity was known, was calculated. Hereafter, the efficiency for the remaining sources was calculated separately, and then re-scaled, in order to match the ^{152}Eu efficiency within the overlapping energy ranges.

When the sixteen HPGe segments are combined, we can decide whether to apply the add-back correction or not. Without the add-back correction, the total FEP efficiency corresponds to the sum of efficiencies for each HPGe crystal. When the add-back correction is applied a fraction of FEP events are recovered, hence the total efficiency in add-back mode is higher than the sum of the individual efficiencies. In Figure 3.9 there are depicted the efficiency curves measured for the HPGe detectors with and without the add-back correction. The effectiveness of the add-back correction is better for high energies as expected. At 1 MeV the efficiency with the add-back correction is $\sim$1.4 times higher, but it increases up to 1.8 around 4 MeV. The benefit of using the add-back is clear, and most of the analysis has been done using the add-back corrected spectra.

The experimental values obtained for the efficiency have been fitted to the empirical curve described in equation 3.2. Using this single curve, the entire energy range of measured points could be satisfactory fitted. The inner plots in Figure 3.9 show the relative deviation of the experimental data from the fitted curves. The deviation is below 5% for both curves in the energy range below 3 MeV. Taking this into consideration, the uncertainty of the efficiency calibration has been estimated to be 5%. However, this value has been increased up to a conservative 20% in the energy region below 100 keV, where the curve bents down, as well as above 3.5 MeV where there is a lack of experimental measurements.

$$\epsilon(E) = \frac{c_0 + c_1 * log(E) + c_2 * log^2(E) + c_3 * log^3(E) + c_4 * log^4(E) + c_5 * log^5(E)}{E} \tag{3.2}$$

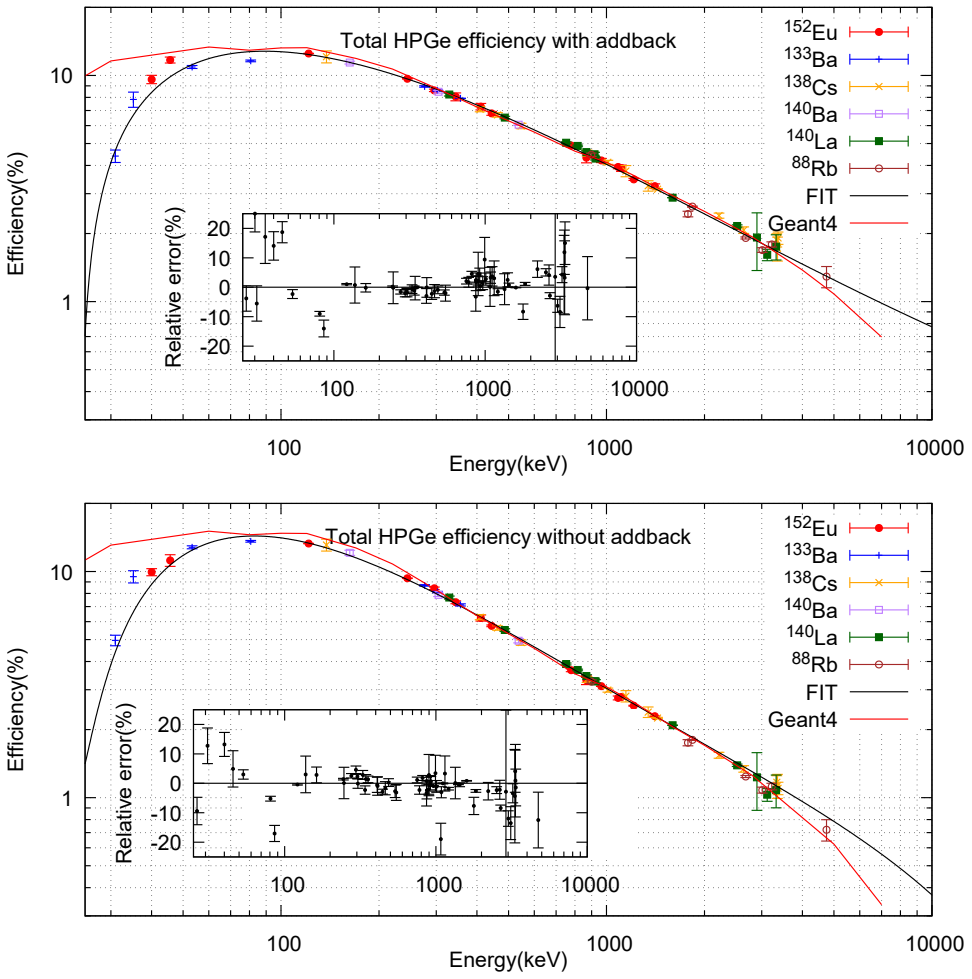

Figure 3.9: Absolute FEP efficiency of the HPGe array. (Top) FEP efficiency measured for the add-back corrected spectra. (Bottom) Absolute efficiency for without add-back correction. The insets show the relative deviation of the experimental points with regard to the fitted curve. The red lines show the predicted efficiency by a Geant4 simulation [Licb].

Table 3.5: Calibration coefficients for the HPGe total efficiency.

	c_0	c_1	c_2	c_3	c_4	c_5
Add-back	$5.20{\cdot}10^3$	$-4.57{\cdot}10^3$	$1.15{\cdot}10^3$	-55.4	-6.77	0.59
No Add-back	$4.42{\cdot}10^4$	$-4.34{\cdot}10^4$	$1.60{\cdot}10^4$	$-2.77{\cdot}10^3$	$2.31{\cdot}10^2$	-7.52

Using the γ-lines provided by the calibration sources, it was possible to cover the energy range up to 3.5 MeV with good accuracy. The lack of experimental data beyond

this point has been supplied by the efficiency predicted by Geant4 simulations, provided by R. Lica [Licb]. The simulated efficiency are drawn together with the experimental curves in Figure 3.9. It can be noticed that the simulated an experimental efficiencies are in excellent agreement for energies above 200 keV. However, the Geant4 simulated curves predict a drop in the efficiency above 3.5 MeV that cannot be empirically measured. For the energy range beyond 3.5 MeV, we have relied in the efficiency predicted by the Geant4 simulations.

3.4.2.2 $LaBr_3$(Ce)

The absolute full energy peak efficiency of the $LaBr_3$(Ce) detectors has been investigated using the same set of calibration sources that the HPGe detectors. In Figure 3.10, the efficiencies measured for both lanthanum detectors are shown. The lower energy resolution of the $LaBr_3$(Ce) detectors makes it more difficult to obtain a good measurement of the peak area in the spectrum. Hence, the measured efficiency points have sometimes strong deviations from the fitted curves $\sim 20\%$.

The efficiency curves have been fitted with the same empirical function used for the HPGe detectors (Equation 3.2), the parameters obtained by the fit are summarized in Table 3.6. For the close geometry configuration of the detectors used during the IS610 experiment, the efficiency of each $LaBr_3$(Ce) detector is similar to the efficiency of one HPGe-clover detector.

Table 3.6: Calibration coefficients for the $LaBr_3$(Ce)total efficiency. The c_3, c_4 and c_5 parameters were set to 0 in the calibration of the $LaBr_3$(Ce) detectors.

	c_0	c_1	c_2
$LaBr_3$(Ce)-1	-2.4(2)$\times 10^3$	9.8(7)$\times 10^2$	-78(7)
$LaBr_3$(Ce)-2	-2.7(3)$\times 10^3$	1.12(11)$\times 10^3$	-91(9)

3.4.2.3 Beta-plastic scintillator

The β-particles that impact on the plastic, deposit only a small fraction of their energy. Beta-particles are detected, whenever the β-detector is triggered, without regard of the deposited energy. The efficiency of the β detector can be measured from the ratio of intensities in the β-gated and singles spectra:

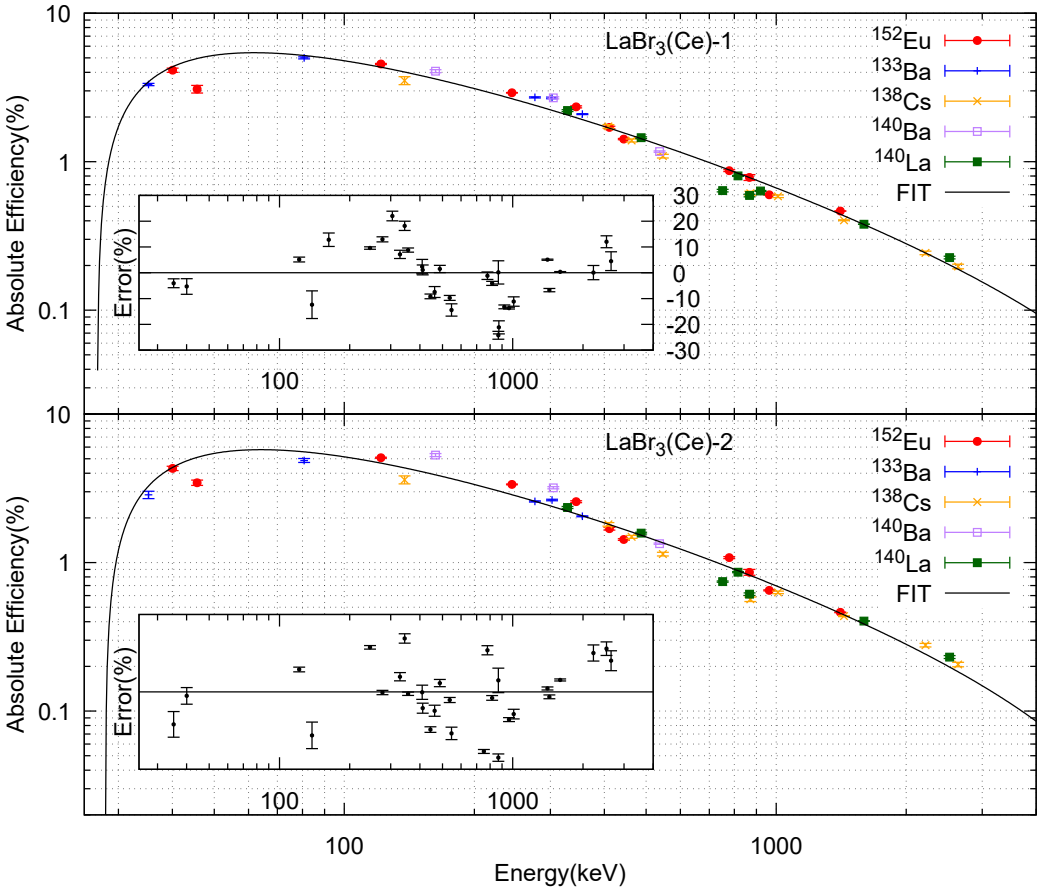

Figure 3.10: Absolute efficiency of the $LaBr_3$(Ce) detectors.

$$\epsilon_\beta = \frac{A_{\gamma-(\beta-gated)}}{A_{\gamma-(Singles)}} \tag{3.3}$$

The efficiency of the β-detector is usually assumed to be close to the 100% of the impinging β-particles. Considering the solid angle covered by the plastic, an efficiency $\sim$25 to 30% of the total emitted β-particles is expected. However, our analysis showed notorious deviations of the β-detector efficiency depending on the decay under study. In Table 3.7, the measured efficiency of the plastic scintillators for the decay of different indium and tin isotopes, as well as several calibration sources, is summarized. These efficiencies were estimated by analyzing the γ-ray spectra in the $LaBr_3$(Ce) detectors. We used the $LaBr_3$(Ce) to avoid the influence of the activity from isotopes implanted outside the expected implantation point. The HPGe detectors are sensitive to the

activity implanted in other places, such as the collimator, which appear in the singles spectra affecting to the apparent β efficiency.

Table 3.7: Efficiency of the β-detector. The Q_β values, have been taken from [WAK+17]. For the average E_β values we have considered those corresponding to the most intensely populated levels in the decay. The efficiency of the β-plastic have been calculated from the comparison of the β-gated and singles spectra measured at the $LaBr_3$(Ce) detectors.

Decay	ϵ_β (%)	Q_β (MeV)	Average E_β (MeV)
^{132}In$\rightarrow^{132}$Sn	∼25	14.14(6)	∼3
^{133}In$\rightarrow^{133}$Sn	∼30	12.9	∼5
^{132}In$\rightarrow^{132}$Sn	∼23	11.0(2)	∼3
^{131}In$\rightarrow^{131}$Sn	∼24	9.18(2)	∼3
^{132}Sn$\rightarrow^{132}$Sb	∼14	3.089(3)	∼0.7
^{131}Sn$\rightarrow^{131}$Sb	∼17	4.67(1)	∼1.7
^{138}Cs$\rightarrow^{138}$Ba	∼15	5.375(9)	∼1.0-1.7
^{88}Rb$\rightarrow^{88}$Sr	∼14	5.312(1)	∼1
^{140}Ba$\rightarrow^{140}$La	∼1	1.047(8)	∼0.2
^{140}La$\rightarrow^{140}$Ce	∼7	3.760(2)	∼0.4-0.6

The maximum efficiency of the detector is achieved for the decay of the In isotopes, which emit the most energetic β electrons. In those cases, the efficiency is close to the ∼ 25-30% situation where all the electrons that enter into the plastic are detected. In the decay of the daughters Sn isotopes, ^{138}Cs, and ^{88}Rb, the measured efficiency is notably lower ∼ 15%. This drop in the efficiency goes together with the drop of the average energy of the emitted electrons. This correlation between energy and efficiency becomes more evident by the extremely low efficiency of the plastic for the β-particles emitted in ^{140}Ba and ^{140}La decays.

In conclusion, the efficiency of the β-plastic has a strong dependence on the energy of the detected β particles. The origin of this correlation is most likely due to two factors. The fraction of β particles that are stopped before reaching the plastic, and the low energy threshold of the detector. In both cases, the low-energy regions are most affected, hence the decays with a lower β energy would loss a bigger fraction of all the emitted electrons.

3.5 Summary of the chapter

In this chapter, we provide a detailed description of different characteristic of the IS610 experiment, as well as the methodology of analysis employed for the measured data.

Section 3.1 provides an overview of the ISOLDE facility, as well as about its situation within the CERN accelerator complex. Within this section, it is described also how the Radioactive Ion Beams in ISOLDE are produced, including an overview about the target-ion source, RILIS, the ISOLDE mass separators and the experimental hall.

In section 3.2 the experimental configuration used in the IDS during our experiment is described. We report on the properties the HPGe-clover, $LaBr_3(Ce)$ and β-plastic detectors, as well as of the electronic setup, that takes care of the treatment of the signals produced in the detectors.

In section 3.3 an overview of the data analysis procedure is given. It is described the data processing, starting off with the uncorrelated detectors hits in the RAW files, their grouping in coincidence events by the event builder program, and finally their sorting into a collection of matrices and spectra that can be analyzed to extract the relevant information about the nuclei under study.

In section 3.4 we report on the energy and efficiency calibrations carried out for the IDS detectors used in our experiment. A large set of calibration sources were employed, including sealed γ-ray sources, online sources and internal calibration points.

4

Lifetime measurements with fast-timing methods

The lifetimes of the excited nuclear states provides relevant information about the underlying nuclear structure. As discussed in section 2.2.3, they give direct access to the reduced transition probabilities $B(X\lambda; J_i \rightarrow J_f)$ for the de-exciting transitions. Nowadays, the experimentally accessible range of lifetimes expands over more than 50 orders of magnitude. There is a variety of methods to determine the half-life of an excited level which can be divided into two main categories, direct and indirect methods. The direct methods are the Doppler shift and the Time Delayed Coincidences methods.

To measure lifetimes by Doppler-shift, the excited states are populated through nuclear reactions that promote the nucleus to an excited state, followed with a de-excitation by the emission ofγ-rays. The reaction product is slowed down or stopped and the lifetime is extracted from the comparison of the Doppler shifted emission of γ-rays (in flight) to the γ-rays emitted by the stopped isotopes. Doppler shift methods give access to lifetimes in the range from femtoseconds to tens of picoseconds.

In time delayed coincidence methods, the general principle consists of measuring the time difference between the population and the depopulation of an excited state. The time difference is obtained from electronic signals of radiation detectors tailored to measure the radiation that indicates the population and de-excitation of an specific level. On the other hand, nuclear resonances fluorescence experiments allow the measurement of shorter lifetimes beyond the limits of Doppler shift methods, by extracting the lifetime from the resonance width.

In this thesis the measurement of half-lives has been performed using time-delayed coincidences methods. Electronic time methods using HPGe detectors, due to their poor time resolution, are limited to the lifetimes longer than tens of nanoseconds. The lower bound of application of time-delayed methods was significantly pushed down to the picosecond range thanks to the implementation of the Ultra-Fast Timing technique. Time-delayed methods that make use of fast scintillators are generally known as fast-timing methods.

The Advanced Time-delayed $\beta\gamma\gamma$(t) method is a general procedure developed by H. Mach, M. Moszynski and R. Gill in the 1980s [MGM89, MM89], for the measurement of lifetimes in the low picosecond range. This technique relies on the use of triple coincidence $\beta\gamma\gamma$(t) where the timing information is obtained from the $\beta\gamma$(t) coincidence between two fast scintillators. For the detection of the β a thin plastic scintillator is employed, which provides a nearly uniform time response for the β particles. For the timing information of the γ-rays, a fast inorganic crystal scintillator is employed. Originally, the BaF_2 crystals coupled to fast photomultiplier tubes (PMTs) were used as γ detectors. Nowadays, $LaBr_3$(Ce) detectors have replaced them, due to their better energy resolution along with a competitive time response. However, given the limited energy resolution of scintillator detectors, a third γ coincidence is set in a high energy resolution HPGe detector, which does not contribute to the timing information, but provides the selectivity of the desired decay branch.

The availability of $LaBr_3$(Ce) crystals opened the possibility to extend ultra-fast timing techniques from $\beta\gamma$ to $\gamma\gamma$(t) delayed coincidences. In this case, the time difference information is derived from delayed coincidence between two $LaBr_3$(Ce) detectors. These techniques are especially suited for measuring lifetimes for in-beam experiments. The so-called *Generalized Centroid shift method* or *Mirror Symmetric Centroid shift method* [RPJR10, RMS$^+$13], constitutes a generalization of the fast-timing techniques oriented to measure lifetimes in the ps range via $\gamma\gamma$(t) coincidences.

4.1 The Advanced Time delayed $\beta\gamma\gamma$(t) method.

The principle of the method consists in the detection on a thin plastic of the β electron emitted in β-decay as a signal of the population of an excited level. The decay of the level is then signalled by the detection on the $LaBr_3$(Ce) detectors of the de-exciting

γ-ray. The time difference between both signals is measured by a Time to Amplitude Converter (TAC) module, which uses the β signal as the START and the γ signal as the STOP, to derive the time difference value. To minimize the time walk of the signals, Constant Fraction Discriminator (CFD) modules are employed before the TAC giving the time stamp of every pulse. The time spectrum provided by the TAC module has the form of a sum exponential decays functions $f(t) = \sum_i a_i e^{-t/\tau_i}$ for $t > 0$, which account for the contribution of the lifetimes of the excited levels τ_i that the nucleus can go through since the β-decay until the emission of the γ-ray selected in the $LaBr_3$(Ce). In the most simple scenario, the studied level is populated directly in the β-decay, and only its lifetime τ contributes to the decay function. The decay function is simplified to $f(t) = e^{-t/\tau}$. Nevertheless, it is important to take into account the response of the system, which is characterized by a finite time resolution along with an energy dependent time response. Consequently, the measured delayed time distribution $F(t_i)$ corresponds to the convolution of the expected time difference function $f(t)$ with the function $P(t_i)$, which gives the Prompt time distribution, and characterizes the intrinsic time response of the system.

$$F(t_i) = N \int_{t_0}^{+\infty} P(t_i - t) f(t - t_0) dt \tag{4.1}$$

The response function $P(t_i)$ provides the time resolution of the system, which includes the response due to the scintillators, PMT, CFD and TACs. The $P(t_i)$ time response function can be derived by measuring the time distribution of prompt γ-rays that are emitted from short-lived states ($\tau \leq$1 ps). This function is generally assumed to be of a quasi-Gaussian shape, whose centroid position C and sigma σ vary with the energy of the detected β or γ radiation. The function that describes the dependency of the centroid position with the energy is known as the detector time walk. Its precise calibration is of vital importance for the measurement of lifetimes with the centroid shift method. The calibration procedure for the walk functions is described in details in sections 4.4.2 and 4.4.3. The σ describes the time resolution of the system, having also a dependence with energy.

The lifetime of the excited level is measured by the analysis of the time distribution. The half-life can be extracted either by the de-convolution of the slope or by the centroid-shift method.

4.1.1 De-convolution method

For an excited level with a lifetime longer than the time resolution of the system, the lifetime of the level appears as an exponential decay on the right-hand side of the spectrum, namely the delayed part. Considering the most simple case, when only one level contributes to the time spectrum, and assuming a Gaussian-shape time-response, the time distribution $F(t_i)$ can be expressed with the following equation:

$$F(t_i) = N \int_{t_0}^{+\infty} \frac{e^{-\frac{(t_i-t)^2}{2\sigma^2}}}{\sqrt{2\pi\sigma^2}} \frac{e^{-(t-t_0)/\tau}}{\tau} dt \tag{4.2}$$

where N indicates the total number of events of the time spectrum, and t_0 is the centroid position of the prompt time distribution at the energy of the γ-ray. The denominator factors are the normalization factors. By integrating Equation 4.2 the resulting function take the form defined in Equation 4.3. This function contains two parts, an exponential function, related to the decay of the level, and the Gauss error function $erf(t)$, which accounts for the time response of the system.

$$F(t_i) = \frac{N}{2\tau} e^{-\frac{t_i-t_0}{\tau}+\frac{\sigma^2}{2\tau^2}} \left[1 + erf\left(\frac{t_i - t_0}{\sqrt{2}\sigma} - \frac{\sigma}{\sqrt{2}\tau}\right)\right] \tag{4.3}$$

In Figure 4.1 is shown an example of a time distribution from a long-lived state. The lifetime is determined by fitting the parameters of the function defined in 4.3 to the time spectrum (blue curve). The red curve represents the same function but assuming a prompt γ-ray $\tau \approx 0$. For the $\tau >> \sigma$ case, the delayed region where $(t_i - t_0) >> \sigma$ the error function becomes 1, and the time distribution can be fitted to a simple exponential decay $N/\tau e^{-\frac{t_i-t_0}{\tau}}$ function within this region. In these cases, the lifetime can be determined by fitting only this region of the spectrum to the exponential decay. For the case where the mean life is similar to σ, it is required to use the complete convoluted form of Gaussian plus exponential.

4.1.2 Centroid shift method

The centroid shift method is employed when the lifetime of the level of interest, is shorter or similar to the time resolution of the experimental setup, typically for lifetimes below 100 ps (depending on the energy range and detectors used). In those cases, the lifetime cannot be deduced from the fit of the exponential tail, since this exponential decay

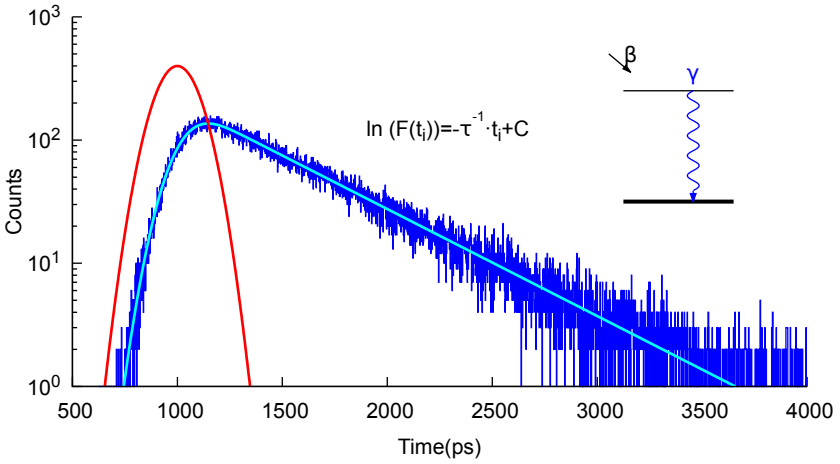

Figure 4.1: Time-delayed distribution of a long-lived state. The red-curves illustrates the expected time spectra for the prompt transition case. The lifetime of the levels appears at the right-hand side of the time spectrum as an exponential slope.

is hidden inside the time response function. Nevertheless, it is possible to track the effect of the lifetime in the time distribution from the shift that it induces to the overall time distribution. The centroid shift of time distribution can be seen in Figure 4.2. The black and blue distributions represent the time spectrum for γ-rays that de-excite a short-lived state. The red curve depicts the expected time distribution if the γ-ray would have de-excited a prompt level.

The shift of the overall time distribution $F(t_i)$ can be quantified with the first moment $\int tF(t)dt$, which corresponds to the center of gravity of the time distribution that is also called centroid position C. As demonstrated in [BHK55], for the simplest case where there is only one lifetime contribution to the time spectrum, the mean life of the level is equal to the shift in the centroid positions between the convoluted $F(t)$ and the prompt $P(t)$ time distributions.

$$\tau = \int_{-\infty}^{+\infty} tF(t)dt - \int_{-\infty}^{+\infty} tP(t)dt = C(F) - C(P) \tag{4.4}$$

The mean life is thus determined from the shift induced in the time-distribution by the lifetime, and therefore, a precise measure of the prompt centroid position for prompt γ-rays is required. This entails some difficulty since the centroid prompt position cannot be directly measured. To address this problem, the standard method consists in obtaining the centroid position for another reference γ-ray $C(P_{\gamma_{ref}})$ from the spectra,

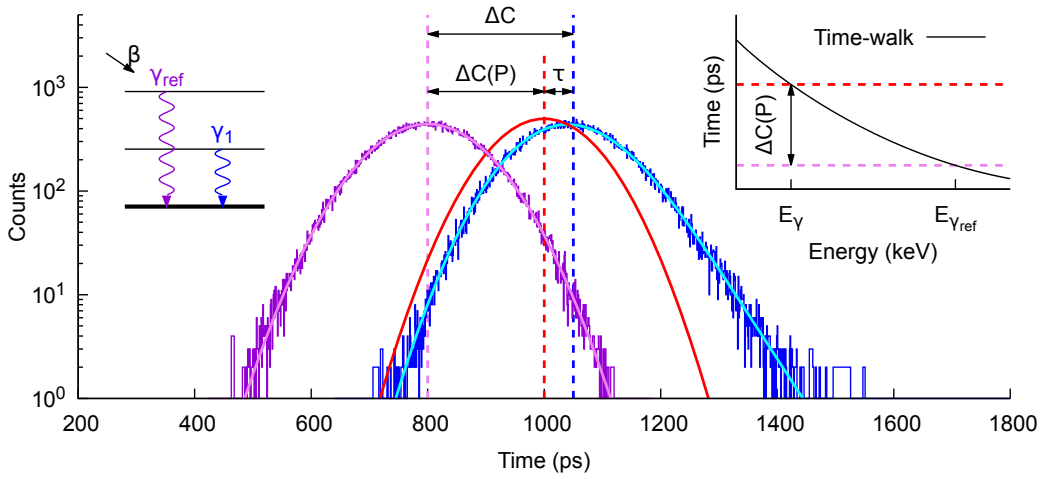

Figure 4.2: Example of the $\beta\gamma(t)$ Centroid shift analysis. The blue spectrum spectrum represents the time distribution corresponding to the delayed γ-ray, which de-excites the level of interest, while the violet distribution belongs to the prompt-reference γ-line. The red distribution corresponds to the expected prompt position of the delayed γ-ray, which is deduced from the centroid of the reference γ-ray and shift in the FEP walk curve.

which can be assumed to de-excite a level with a prompt lifetime. Due to the walk, the centroid position obtained for the reference transition does not correspond to the expected prompt position of the γ-ray under study, it is shifted. The shift introduced by the time walk, $\Delta C(P)$, can be obtained from the FEP walk curve, which is derived separately from the analysis of a set of calibration sources, see section 4.4.3.

An schematic example of the analysis is depicted in Figure 4.2. The analysis of half-lives via the centroid shift method has three uncertainty sources, the error in the centroid of the time distribution of the γ-ray that de-excites the levels, $\delta C(F)$, the error in the centroid of the reference prompt γ-ray, $\delta C(P_{\gamma_{ref}})$, and the uncertainty of the FEP walk calibration curve.

The described centroid shift method, is only valid for the most simple situation where only one lifetime contributes to the time distribution. In reality, the level-schemes populated in β-decay experiments are usually more complex. Each level can be fed either directly in the β-decay, or by γ-rays from higher-lying levels. The lifetimes of those upper levels contribute also to the shift in the time distribution of the γ-rays

under investigation:

$$C(F) - C(P) = \tau + \sum_k \alpha_k \tau_k \tag{4.5}$$

Where τ_k corresponds to the lifetime of the k level, and α_k is the fraction of decays that goes through the k level before reaching the level of interest. Therefore, the task of isolating the τ contribution to the shift might be very difficult. For these complex level-schemes, the use of triple $\beta\gamma\gamma$(t) becomes very important. Apart from reducing the background in the $LaBr_3$(Ce) energy spectra, the coincidence with a γ-ray on the HPGe detectors allow selecting the events from an specific de-excitation cascade, and constrain the lifetimes from higher-lying levels. In this way a clean selection of the decay branch can be obtained.

4.2 Fast-timing $\gamma\gamma$(t) methods.

The analysis methodologies described in the previous section for the $\beta\gamma$(t) timing techniques, can be extended to the $\gamma\gamma$(t) delayed coincidence system. The main difference between $\beta\gamma$ and $\gamma\gamma$ coincidences is that the lifetime is calculated from the time differences between the arrival of the γ-rays that populate and de-excite the level. The $\gamma\gamma$(t) method requires selecting two γ-rays, one in the START and the other in the STOP detector. The derived time distributions are thus influenced only by the lifetimes of the states that are in between the two selected γ-rays. This is a very convenient feature to study for instance the lifetimes of levels below long-lived isomers, and has been made possible by the advent of the fast scintillators with good energy resolution such as $LaBr_3$(Ce) crystals.

Due to the equivalence between the START and STOP detector, every pair of coincident γ-rays can be selected in two different ways, the delayed and anti-delayed. The delayed spectrum is obtained when the populating γ-ray is used as START, while in de-exciting γ-ray is used as STOP. In the delayed time-spectrum the lifetimes manifest with an exponential decay tail on the right-hand side of the spectrum, and the centroid position of the overall distribution is shifted to the right, by the mean life of the level. The anti-delayed time spectrum is obtained by inverting the selection of γ-rays in the detectors. The anti-delayed time distribution shows the same form but inverted in the time axis, the exponential tail appears on the left-hand side of the time distribution,

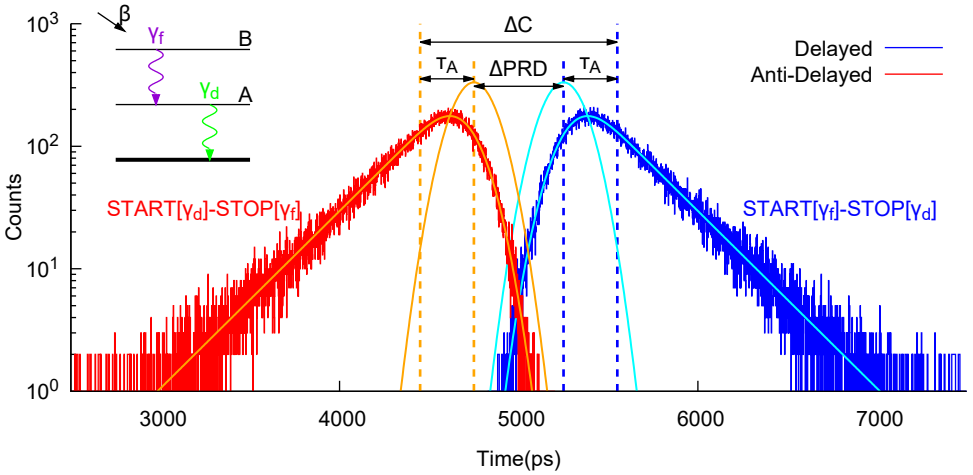

Figure 4.3: Lifetime analysis using the $\gamma\gamma$(t) method. Procedure to measure the mean-life of the A state in the example level-scheme showed at the left side. To derive the lifetime of a combination of two γ-rays needs to be selected in the two $LaBr_3$(Ce) detector, one that feds the level γ_f, and another one that de-excite it γ_d. Two time distributions can be derived for this combination of γ-rays, depending on which detector is used each γ-ray, the delayed (blue) and anti-delayed (red). Long lifetimes can be extracted by fitting decay-tails from both time distributions. For shorter lifetimes, the mean life can be derived from the centroid-shift measured between the delayed and anti-delayed time spectra. The centroid shift methods requires to account the time-walk contributions. ΔPRD value, which includes for the time walk in both $LaBr_3$(Ce) between the two selected energies, E_{γ_d} and E_{γ_f}.

and the centroid position is shifted one mean-life to the left of the expected prompt position.

For states with long lifetimes, the half-life life $T_{1/2}$ can be derived by fitting the exponential decay tails. The fit can be performed separately for the delayed and anti-delayed distributions, resulting in two independent measurements for the $T_{1/2}$ value. The short lifetimes have to be deduced from the shift in the centroid position The mean-life can be extracted using of the Mirror Symmetric Centroid Difference (MSCD) method [RPJR10], which take advantage of the symmetric properties of the $\gamma\gamma$(t) time-delayed coincidence. In the MSCD method, the mean life is calculated from the centroid difference between the delayed and anti-delayed distribution. The mean life is related to the centroid shift between both distribution by the following equation:

$$\Delta C = C(F_{Delayed}) - C(F_{Anti-Delayed}) = \Delta PRD + 2\tau \tag{4.6}$$

where PRD correspond to the Prompt Response Distribution, which describes the dependence of the prompt centroid position on the energies selected in both detectors. The ΔPRD value represents the shift in the PRD curves between the delayed and anti-delayed combination of gates. The PRD curve for every experiment is derived by $\gamma\gamma$(t) coincidences from known calibration sources. More information about this procedure can be found in section 4.4.3. The PRD contains the combined energy dependency of both $LaBr_3$(Ce) detector, and as is shown in the calibration sections 4.4.3, it can be derived from the FEP walk curves measured from $\beta\gamma$(t) coincidence for both START and STOP detectors:

$$PRD(E_{start}, E_{Stop}) = -FEP_{walk}^{START}(E_{start}) + FEP_{walk}^{STOP}(E_{stop}) \tag{4.7}$$

$$\begin{aligned} \Delta PRD &= PRD(E_{\gamma feeder}, E_{\gamma decay}) - PRD(E_{\gamma decay}, E_{\gamma feeder}) \\ &= -FEP_{walk}^{START}(E_{\gamma feeder}) + FEP_{walk}^{START}(E_{\gamma decay}) \\ &\quad + FEP_{walk}^{STOP}(E_{\gamma feeder}) - FEP_{walk}^{STOP}(E_{\gamma decay}) \end{aligned} \tag{4.8}$$

4.3 Compton background correction methodology

One of the biggest challenges that arise when analyzing a fast-timing experiment is the influence of Compton scattering background to the time spectra. This hampers the analysis due to the impossibility of separate the Full Energy Peaks (FEP) events from those of the Compton background when setting energy gates. These Compton events are the "side product" of higher-energy γ-rays, and hence they carry the time information of the γ-rays that produce them. The lifetime measurement of excited levels via the fast-timing method is based on the analysis of the time distribution of de-exciting γ-rays. Thereby, to obtain a reliable half-life value from our analysis we need to be sure that the influence of the Compton background events to the time distribution has been removed.

4.3.1 Correction methods for $\beta\gamma$(t) delayed coincidences.

The correction methodology that has been developed in this Thesis to characterize and correct for the contribution of Compton events in $\beta\gamma$(t) events is explained here. This

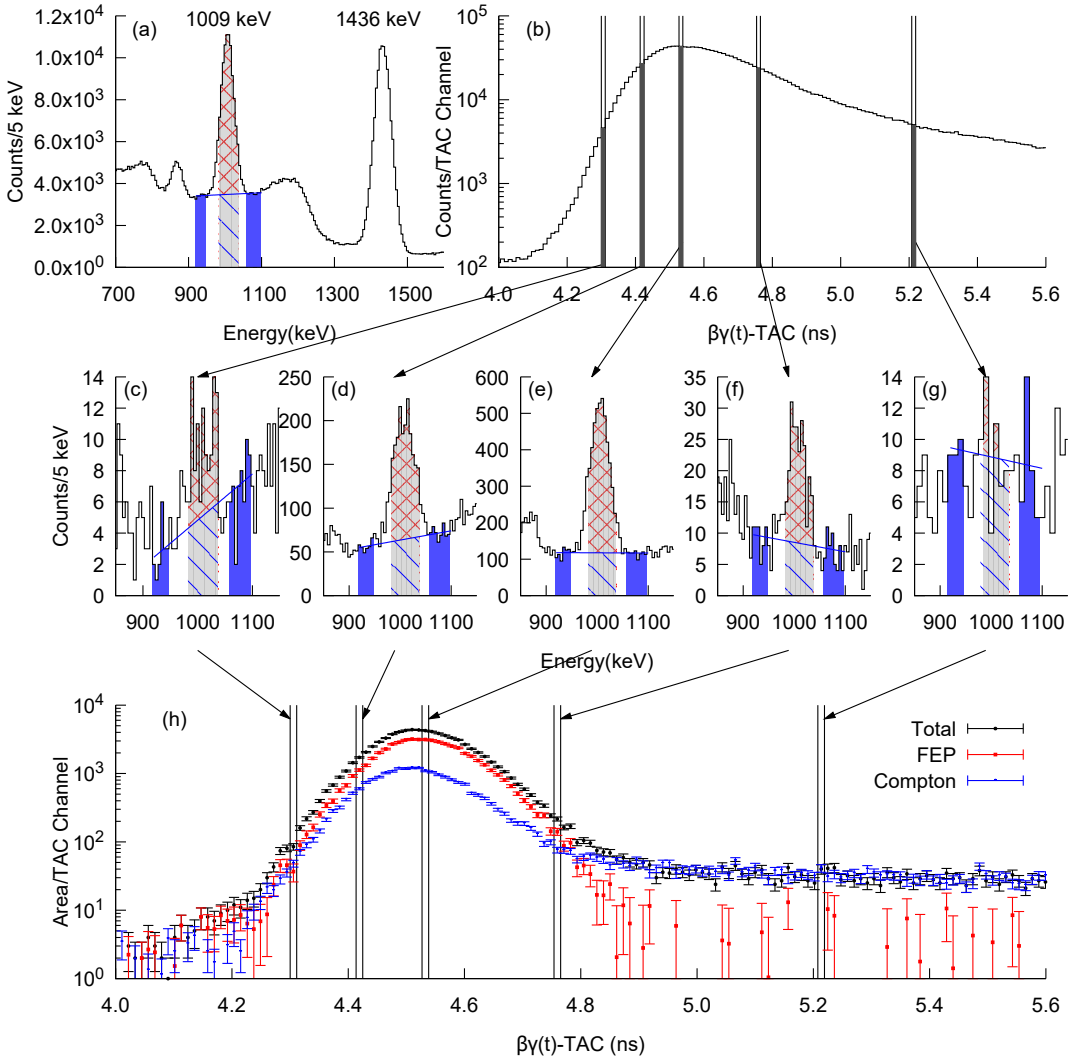

Figure 4.4: Compton correction procedure for $\beta\gamma$(t) events.(a) Total $LaBr_3$(Ce) energy projection from the β-$LaBr_3$(Ce)(t) events. In the same plot, there are also depicted the chosen energy gates to select the 1009-keV peak (grey) and for the estimation of the Compton background (blue) are also plotted. (b) Total TAC amplitude projection of β-$LaBr_3$(Ce)(t) events. (c-g) $LaBr_3$(Ce) energy projections for the colored bins from the TAC spectrum. In every spectrum, is depicted the estimation of the total amount of FEP vs Compton events. (h) Time distributions for the Peak(Black), Compton (blue) and FEP (red) events. See text for details.

was done with the aid of the 1009-keV line in ^{138}Cs which, has been used as an online calibration source.

Figure 4.4 shows the procedure to correct for the contribution of the Compton events to the time distribution. In the top-left plot, the β-gated $LaBr_3$(Ce) energy spectrum is represented. As shown, the 1009-keV γ-ray sits on a large Compton background, which is mostly generated by the 1436-keV γ-ray. If an energy gate is set on the 1009-keV peak, the obtained time distribution described by Equation 4.9, where $F(t_i)$ is the number of events registered within the selected energy gates at a given time t_i, will be the sum of both FEP and Compton components.

$$F(t_i) = F_{FEP}(t_i) + F_{Compton}(t_i) \tag{4.9}$$

It is not possible to perform an event-by-event separation of FEP and Compton events, but FEP events appear in the form of a Gaussian peak, whereas the Compton events are distributed in a linear background. Hence, it is possible to assess the relative contribution of the Compton and FEP events analyzing the γ-ray spectrum, and performing a statistical estimate of the amount of Compton events for every time bin.

This is exemplified in the spectrum from Figure 4.4 (a). The total amount of Compton events within the energy gates is obtained by a linear interpolation, where two selected regions from the background at both sides of the peak were used as a reference. This yields a relative FEP/Compton ratio of $\sim$1.7, for the full spectrum where all the $\beta\gamma$(t) events are included.

The procedure is the following: first, we set the energy gates that will be used to select the FEP and the two regions of reference to estimate the Compton, Figure 4.4 (a). Secondly, the time regions are selected on the time spectrum and projected to the $LaBr_3$(Ce) energy spectrum. From each projection, we estimate the total amount of Compton events within the FEP window, separately for every time bin. From this analysis, we derive the expected time distribution only for the Compton events beneath the peak, by removing the FEP contribution:

$$F_{Compton}(t_i) = \mathcal{L}(F_{Compton-Left}(t_i), F_{Compton-Right}(t_i)) \tag{4.10}$$

where $\mathcal{L}$ is a function that can be approximated by a linear function. An advantage of this method is that the time-shift or the varying time resolution of Compton events due to the Compton-walk are intrinsically considered.

A Compton time distribution is derived from this analysis. Every TAC bin contains the estimated Compton contribution. FEP time distribution is thus obtained by subtracting the derived Compton time-spectra from the events within the peak gate.

$$F_{FEP}(t_i) = F(t_i) - F_{Compton}(t_i) \tag{4.11}$$

The Compton, $F_{Compton}$, and Peak, F, time distributions are obtained from the adjacent set of events. Consequently, their statistical fluctuations are different, and then the FEP distributions errors are obtained from the error propagation and Compton uncertainties, according to Equation 4.12.

$$\delta F_{FEP}(t_i) = \sqrt{(\delta F(t_i))^2 + (\delta F_{Compton}(t_i))^2} \tag{4.12}$$

Figure 4.4 (h), displays the time distribution for all the events for the 1009-keV peak (black), along with their separate contributions, corresponding to FEP (red) and Compton (blue) events. In the total time spectra, at least two components are apparent at first sight: one of them prompt, corresponding to the Gaussian peak on the left, and a long-lived component which appears as an exponential slope on the right-hand side. When we look at the separated FEP and Compton time distributions, it can be noticed that the long-lived component is solely due to the Compton events. The corrected FEP time spectrum, shows only a pure prompt time distribution, which is consistent with the expected $T_{1/2}$ =5(4) ps [Son03] of the 2446-keV level, de-excited by the 1009-keV transition. The time resolution at this energy is FWHM=190 ps, that is σ=90 ps.

The methodology described in this Section holds a strong potential for removing the Compton contribution to the time spectra. It is valid for all types of Compton backgrounds arising from prompt and delayed γ-rays, even from long-lived states. But care should be taken when the FEP to Compton ratio is too low since the errors would become too large making it impossible to obtain a reliable result. On the other hand, under normal experimental conditions, it is common to have complex γ-rays spectra with overlapping peaks, whose time distributions cannot be separated by this methodology.

To reduce the Compton contribution an extra coincident condition on HPGe detectors can also be set [MGM89]. It does not contribute to the timing information but improves the selection of the γ-ray. This third coincidence has an extra importance for $\beta\gamma$(t) measurements, where the time difference carries the influence from the levels that the nucleus have gone through before emitting the $LaBr_3$(Ce)-gated γ-ray. The

HPGe-gated transition, is used then not only to clean the spectra, but also to select an specific cascade.

The third γ-ray in the HPGe detector is selected by means of an energy gate. Likewise in the $LaBr_3$(Ce) detectors, the Compton events underneath the FEP peak in the HPGe-energy spectrum are also included. These HPGe-Compton coincident events, may reduce the goodness of the selection by the HPGe gate, being in some cases the main cause of the Compton background in the $LaBr_3$(Ce) energy spectra, since they are produced by other γ-rays from the spectra,

In Figure 4.5 there are depicted the β-$LaBr_3$(Ce) gated on the 1436-keV (Top) and the 138-keV (Bottom) γ lines at the HPGe-Clover detectors. The inner plots represent the HPGe spectrum on the energy region of the selected γ-ray, along with the selected gates used for the FEP and the background. In the 1436-keV gate, the contribution from the background beneath the HPGe FEP can be neglected. By setting this gate, the Compton background below the 1009-keV γ-line in the $LaBr_3$(Ce) detector is almost completely removed. For other peaks located at lower energies, there is still a Compton background and hence corrections for the $LaBr_3$(Ce) background may be still required.

Regarding the β-$LaBr_3$(Ce) spectrum measured in coincidence with the 138-keV peak, Figure 4.5 (bottom), the contribution of events in coincidence with the HPGe Compton continuum is sizable. Most of the Compton background in the $LaBr_3$(Ce) spectrum is due to the germanium background. Hence, the removal of this contribution strongly reduces the Compton background in the $LaBr_3$(Ce) detector.

To remove the contribution of the Compton background in the HPGe detector, the analysis to derive the $F(t_i)$ and $F_{Comp}(t_i)$ time spectra described above (see Figure 4.4), is performed separately for the events in coincidence with the HPGe peak gate and those in the HPGe Compton gate.

$$F(t_i) = F^{HPGe-Peak}(t_i) - F^{HPGe-Comp}(t_i) \tag{4.13}$$

$$F_{Comp}(t_i) = F_{Comp}^{HPGe-Peak}(t_i) - F_{Comp}^{HPGe-Comp}(t_i) \tag{4.14}$$

The errors from the HPGe-Peak and HPGe-Compton time distributions are quadratically propagated to obtain the uncertainty of the time distributions Compton corrected.

$$\delta F(t_i) = \sqrt{(\delta F^{HPGe-peak}(t_i))^2 + (\delta F^{HPGe-Comp}(t_i))^2} \tag{4.15}$$

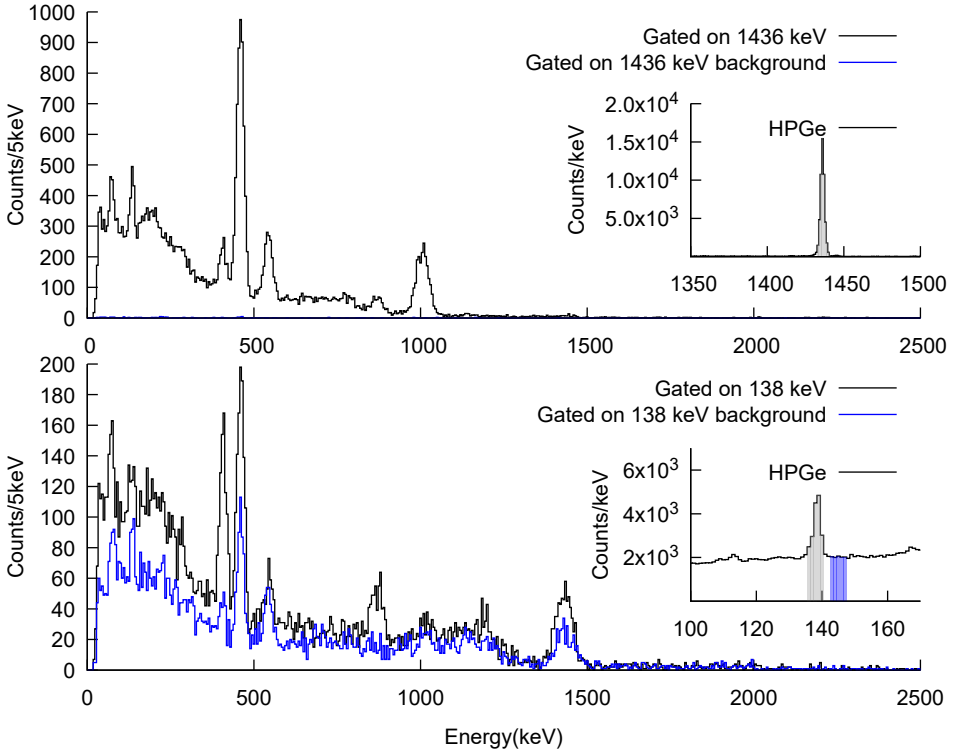

Figure 4.5: HPGe coincident β-gated $LaBr_3$(Ce) energy spectra to show the contribution of Compton events in the HPGe detectors. (Top) HPGe Coincident β-gated $LaBr_3$(Ce) spectra obtained by gating on the 1436-keV transition (black) and on the background on the right-hand side of the peak (blue). The inset plot illustrates the energy gates set in the HPGe spectra. In this case, the contribution of Compton events from the HPGe detector is negligible. (Bottom) spectra gated on the 138-keV transition at the HPGe detector. In this case, the Compton background in the HPGe accounts for around half of the events in the spectrum, including most of the Compton background in the $LaBr_3$(Ce) detector.

$$\delta F_{Comp}(t_i) = \sqrt{(\delta F_{Comp}^{HPGe-peak}(t_i))^2 + (\delta F^{HPGe-Comp}(t_i))^2} \tag{4.16}$$

In conclusion, a proper subtraction the Compton contribution to the time spectrum is essential. One of the best approaches to do so is to define an extra coincident condition on the HPGe clovers. However, the use of triple $\beta\gamma\gamma$(t) events has a great cost in statistics due to the low absolute efficiency of HPGe detectors, and does not warrant a complete removal of the Compton background in the $LaBr_3$(Ce) detector. To deal with the remaining background we can use the methodologies explained in this section to

deal with the Compton events in either $LaBr_3(Ce)$ and HPGe detectors. They can be employed simultaneously, in order to achieve a FEP time distribution completely free from the influence of Compton events. The procedures developed in this PhD thesis will be used later on in the analysis.

4.3.2 Analysis of $\gamma\gamma$(t) time delayed events.

As explained in Section 4.3.1, Compton scattering events underneath full energy peaks represent a major problem when measuring lifetimes via fast-timing methods. When using $\gamma\gamma$(t) coincidences the Compton contribution needs to be subtracted as well. The treatment of these Compton events entails a higher level of complexity in $\gamma\gamma$(t) measurements, because the Compton background is present underneath the FEP events on both the START and STOP peaks.

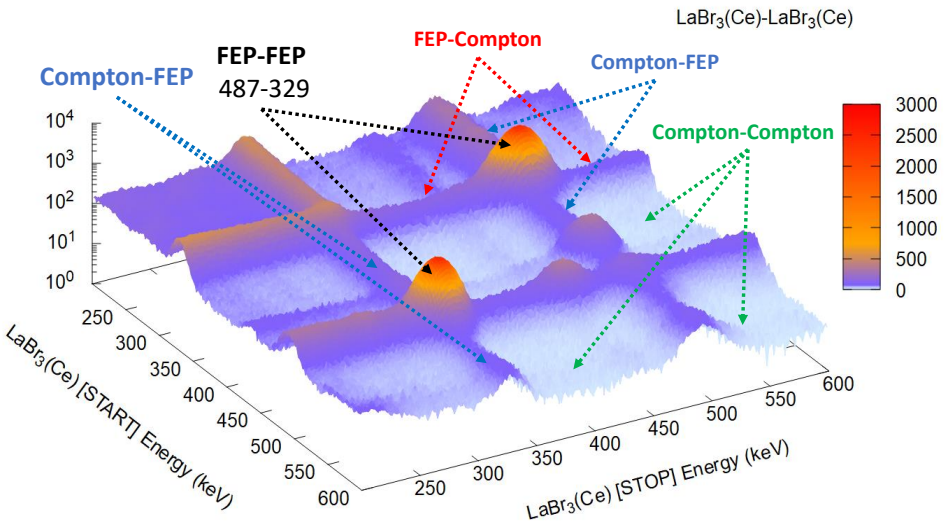

Figure 4.6: $\gamma\gamma$ coincidence matrix measured for the ^{140}Ba decay between two $LaBr_3(Ce)$ detectors.

Figure 4.6 depicts the $\gamma\gamma$(t) coincidence matrix measured using two $LaBr_3(Ce)$ detectors for the ^{140}Ba calibration source. Within the energy region shown in the spectrum, we can observe the peaks from the 329-487-keV cascade in ^{140}Ce for either the delayed START[329]-STOP[487] and anti-delayed START[487]-STOP[329] combinations.

The time distributions are obtained by setting a double energy gate. The Peak-Peak gate, contains the FEP-FEP events, where both γ-rays have left their entire energy in their respective detectors, but also includes events arising from the Compton background. These kinds of Compton background components can be identified, depending on which detector was the Compton event measured. In the FEP-Compton, the START detector measured a FEP and while the Compton is detected in the STOP $LaBr_3$(Ce). In the Compton-FEP events, the START signal is given by a Compton event and the STOP by a FEP. The Compton-Compton events correspond to the case when both start and stop signal are produced by Compton events. The Peak-Peak time distribution is thus composed by four contributions:

$$F_{Peak-Peak}(t_i) = F_{FEP-FEP}(t_i) + F_{FEP-Comp}(t_i) + F_{Comp-FEP}(t_i) + F_{Comp-Comp}(t_i) \tag{4.17}$$

For the lifetime measurements, the actual timing information is only provided by the $F_{FEP-FEP}(t_i)$ time distribution. Hence, the contribution from the other three components needs to be removed.

Each background component has a separate origin, and thus its time distribution has a specific behaviour which needs to be estimated individually. With this aim, we have developed a correction methodology based on the inspection of the nearby Compton background, equivalent to the one employed to correct the $LaBr_3$(Ce) Compton background for $\beta\gamma$(t) events, see Figure 4.4.

Figure 4.7 illustrates the analysis procedure to estimate each background component contributing to the total time spectrum as listed in Equation 4.17. The first step is to select one of the two peaks, either the delayed or anti-delayed coincidence, for the two γ-ray combination under study. This is done by means of double energy gate on their respective peaks at the START and STOP detector. By projecting the time distribution for these events, the Peak-Peak time distribution is obtained.

The next step in the analysis is the estimate of the others tree contributions from the nearby Compton background. However, the FEP-Compton and the Compton-FEP cannot be obtained directly from the spectrum, since is not possible to set a combination of gates that allows separating the FEP from the Compton underneath. Instead, the components that can be directly measured are the Peak-Compton, which correspond to the Compton events in the STOP detector measured in coincidence with the

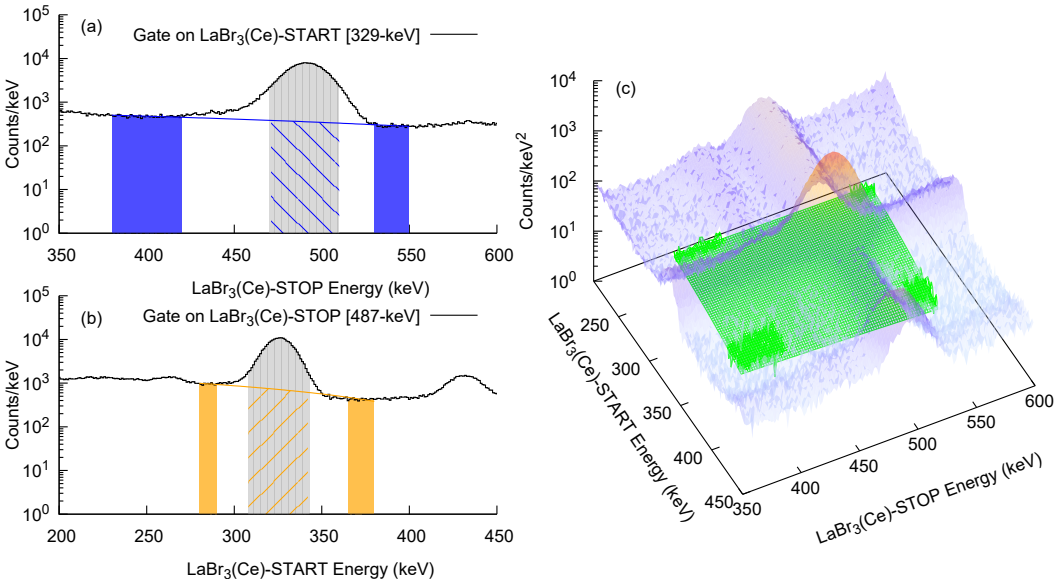

Figure 4.7: Analysis of the Compton background contributions in $\gamma\gamma$(t) coincident events.(a) Coincident $LaBr_3$(Ce)-STOP spectra gated on the 329-keV transition at the START detector. (b) Coincident $LaBr_3$(Ce)-STaRT spectra gated on the 487-keV transition at the STOP detector. (c) $LaBr_3$(Ce) $\gamma\gamma$ matrix and Compton-Compton background estimate. See text for details.

FEP+Compton in the start detector (Equation 4.18), and the Compton-Peak, corresponding to the Compton events in the START coincident with the FEP+Compton at the STOP detector (Equation 4.19).

$$F_{Peak-Comp}(t_i) = F_{FEP-Comp}(t_i) + F_{Comp-Comp}(t_i) \tag{4.18}$$

$$F_{Comp-Peak}(t_i) = F_{Comp-FEP}(t_i) + F_{Comp-Comp}(t_i) \tag{4.19}$$

By including the 4.19 and 4.18 equations into 4.17 Equation, it can be rewritten as:

$$F_{Peak-Peak}(t_i) = F_{FEP-FEP}(t_i) + F_{Peak-Comp}(t_i) + F_{Comp-Peak}(t_i) - F_{Comp-Comp}(t_i) \tag{4.20}$$

The Peak-Compton contribution is measured by fixing the gate on the peak at the START detector and projecting over the energy in the STOP detector. The Peak-

Compton contribution is calculated by a linear estimate from two nearby Compton regions, for each TAC channel separately. This procedure is equivalent to the one described in Figure 4.7 (a). The Compton-Peak component is derived similarly, but fixing the peak gate on the STOP detector instead, and analyzing the Compton background obtained in the projection in the STOP detector (see Figure 4.7 (b)).

Finally, the Compton-Compton contribution is measured by setting four reference areas in the energy matrix around the peak. These four regions are defined using the four combinations from the Compton pair of gates defined for each detector. By extending the assumption of the local linear behaviour of the Compton background in the energy spectra, the Compton-Compton background from the $\gamma-\gamma$ 2D energy matrix can be assumed to have the shape of a plane in the E_{START} vs E_{STOP} matrix. This is in principle valid locally. The contribution of Compton-Compton time distributions beneath the Peak-Peak gates is estimated from the plane defined by the four reference Compton-Compton regions, and separately for each TAC channel, see Figure 4.7 (c). Four time distributions are derived directly (Peak-Peak, Peak-Compton, Compton-Peak and Compton-Compton), which are are represented in Figure 4.8 (a). Using these four contributions the decoupled time distributions can be derived, using the following relationships:

$$F_{FEP-FEP}(t_i) = F_{Peak-Peak}(t_i) - F_{Peak-Comp}(t_i) - F_{Comp-Peak}(t_i) + F_{Comp-Comp}(t_i) \tag{4.21}$$

$$F_{FEP-Comp}(t_i) = F_{Peak-Comp}(t_i) - F_{Comp-Comp}(t_i) \tag{4.22}$$

$$F_{Comp-FEP}(t_i) = F_{Comp-Peak}(t_i) - F_{Comp-Comp}(t_i) \tag{4.23}$$

The errors of the derived time distribution are obtained by square propagation of the errors of each time distribution used to derive them:

$$\begin{aligned}(\delta F_{FEP-FEP}(t_i))^2 = {} & (\delta F_{Peak-Peak}(t_i))^2 + (\delta F_{Peak-Comp}(t_i))^2 \\ & + (\delta F_{Comp-Peak}(t_i))^2 + (\delta F_{Comp-Comp}(t_i))^2\end{aligned} \tag{4.24}$$

$$\delta F_{FEP-Comp}(t_i) = \sqrt{(\delta F_{Peak-Comp}(t_i))^2 + (\delta F_{Comp-Comp}(t_i))^2} \tag{4.25}$$

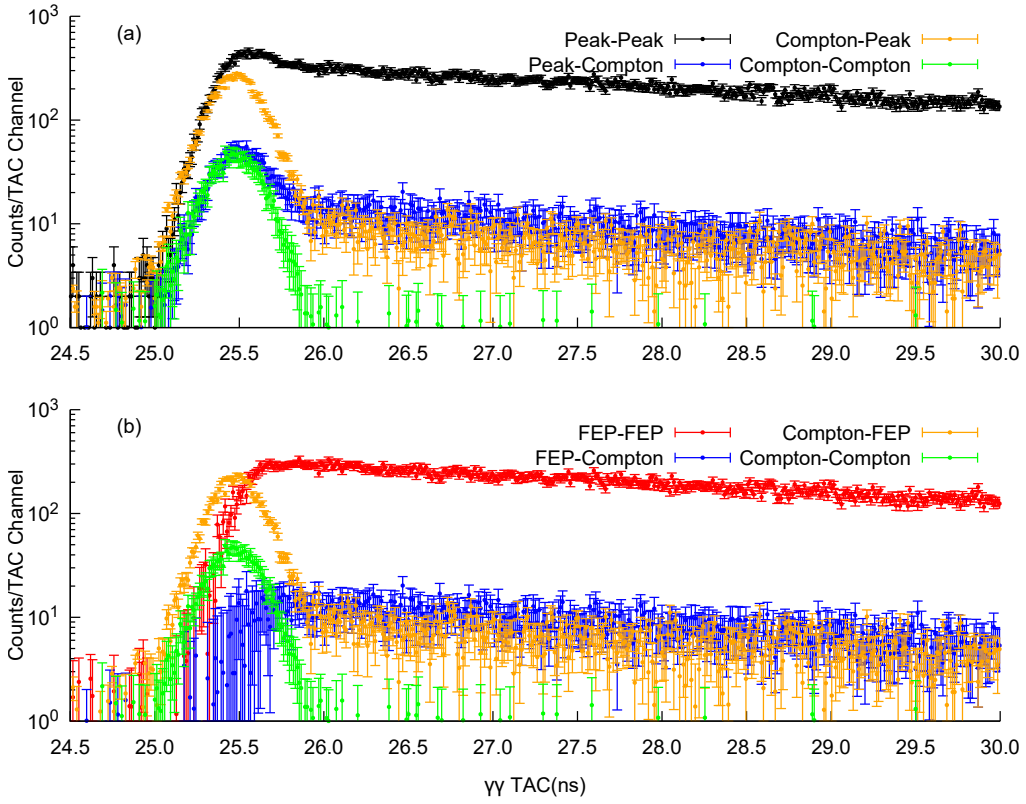

Figure 4.8: Analysis of the Compton background contributions in $\gamma\gamma$(t) coincident events. (a) Time distributions "directly" estimated from the energy gates. (b) *Decoupled* time distributions for the four components.

$$\delta F_{Comp-FEP}(t_i) = \sqrt{(\delta F_{Comp-Peak}(t_i))^2 + (\delta F_{Comp-Comp}(t_i))^2} \qquad (4.26)$$

Figure 4.8 (b) depicts the derived time distributions, for the FEP-FEP, FEP-Compton, Compton-FEP and Compton-Compton components. Each component has a different behaviour that can be correlated to the γ-rays that generate them. Given the selected energy gates, both FEP-FEP and FEP-Compton time spectra are started by the 329-keV transitions and stopped by the 487-keV FEP and Compton scattering from the 1596-keV γ respectively. Both show the behaviour of an exponential decay without any prompt component, which is in good agreement with the $T_{1/2}$=3.474(10) ns for the 2083 keV intermediate level. On the other hand, the Compton-FEP coincidences are mainly started by Compton scattering from 1596-keV γ and stopped by the 487-keV

FEP. The Compton-Compton background arises mostly from 871-1596 keV coincidences. For both Compton-FEP (orange) and Compton-Compton (green) events, the 1596-keV ($T_{1/2}$=0.0910^{48}_{-44} ps) level is the only intermediate level between them, and thus they produce a prompt time spectra.

To summarize, the procedure described in this section allows us to disentangle the actual contribution of the FEP events to the time spectra (FEP-FEP) from the contribution of the three types of background. To increase the selectivity and reduce the Compton background, further conditions can be applied, such as a requirement on the arrival of the protons on the target, a coincidence with the β detector or a third coincident condition on γ-rays in the HPGe detectors. These approaches reduce the background in the $LaBr_3$(Ce) energy spectra at the expense of a reduction in the total number of counts. For this reason, $\gamma\gamma\gamma$(t) analysis can not always be performed.

4.4 Time Calibrations

The measurement of half-lives by means of fast-timing methods [MGM89, MM89, RMS+13], requires a complete characterization of the time response of the timing system. In particular, the dependence of time response on the deposited energy needs to be calibrated. These time-response curves are also known as time-*walk* curves. The effect this *walk* produces in the time distribution is a time shift as a function of energy, which can be of the order of a few hundreds of ps within the studied energy range. Therefore, the correction of the shift in the time response is of vital importance for the analysis of lifetimes in the range below 100 ps, which are measured by the centroid shift method.

4.4.1 TAC calibration

As described earlier, in this experiment we are using TAC modules to convert time difference into pulse heights. Prior to time-*walk* calibrations, the channel to time equivalency has to be estimated. In both IS610 experimental campaigns, three TAC modules were employed at the same time to obtain the time differences for the three possible scintillators combinations. The TAC modules were calibrated using an ORTEC 462 Time Calibrator. This module generates two consecutive signals, a START and STOP, with an adjustable period and range and a very precise frequency. When the Time Calibrator is connected to the TAC modules, the time spectrum shows a set of Gaussian

Table 4.1: Time calibration of the TAC modules

	TAC-1 (ps/ch) β-$LaBr_3$(Ce)-1	TAC-2 (ps/ch) β-$LaBr_3$(Ce)-2	TAC-3 (ps/ch) $LaBr_3$(Ce)-1-$LaBr_3$(Ce)-2
2016	2.923(2)	2.933(2)	2.911(2)
2018	11.346(3)	11.440(3)	11.537(5)

peaks separated by a fixed time, which corresponds to the period. A linear calibration is performed to obtain the channel to ps equivalence. The results are shown in Table 4.1.

The validity of the time calibration was checked by measuring a well-known long half-life from the ^{140}Ba/^{140}La calibration source. The 2083-keV level in ^{140}Ce has a reported 3.474(10) ns half-life [MF95]. Using our set of detectors, this specific half-life can be measured either by the analysis of the time difference between the β plastic and each of the two $LaBr_3$(Ce) detectors or from the time difference between the two γ scintillator detectors. In Figures 4.9 and 4.10,the time spectra used to measure the half-life of the 2083-keV level for the 2016 and 2018 datasets respectively are shown. The β-$LaBr_3$(Ce)(t) time delay distributions were produced by setting a gate on the 329-keV peak in the HPGe detectors, and selecting the 487-keV transition to stop the TAC in the Lanthanum detectors. On the other hand, for the $LaBr_3$(Ce)-$LaBr_3$(Ce)(t) the 329-keV γ-ray that feeds the level, and the 487-keV transition that de-excites it were selected. This selection produced two time spectra, corresponding to the delayed and anti-delayed combination. In both cases, the method for correction of the Compton background described in the previous section was employed.

In all the cases, the half-life was obtained from the fit of the exponential slope of the time distributions. If we compare the obtained values from the 8 independent measurements, we find that all values are compatible with the previously measured half-life. There is a small difference for some of them, nevertheless, none of these deviations is larger than 1%, and they are included within the error bars. In conclusion, all indicates that the time calibrations derived from the Time Calibrator are trustworthy.

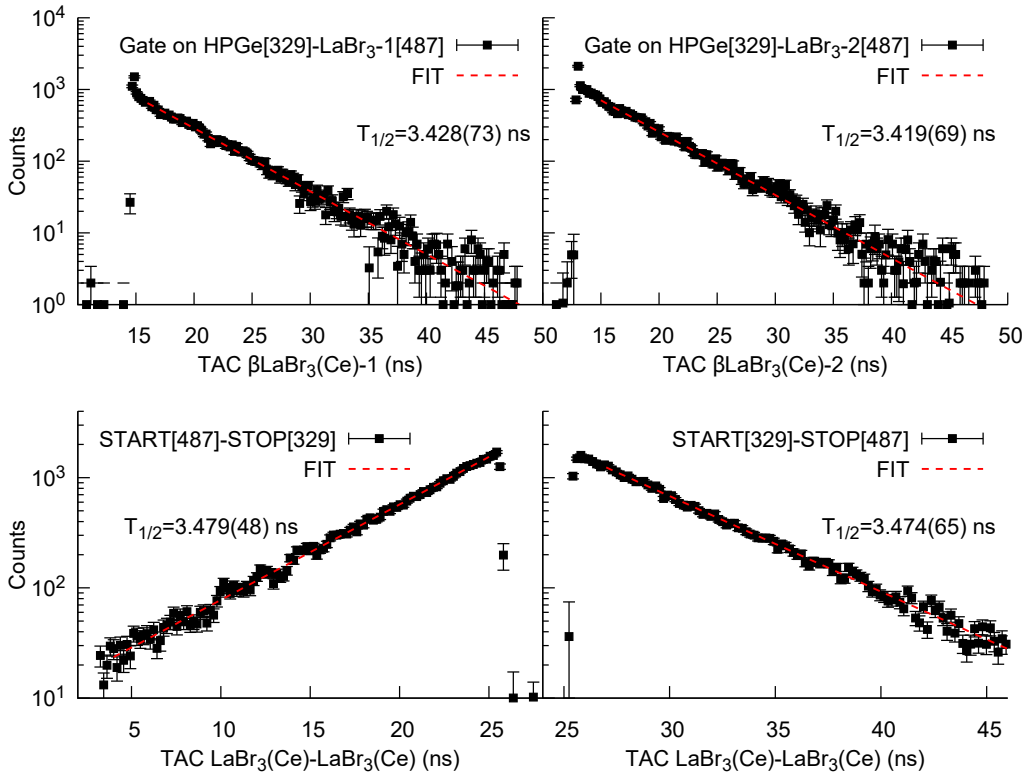

Figure 4.9: Half-life analysis of the 2083-keV level in ^{140}Ce. 2016 Dataset. (Top) $\beta\gamma$(t) time delayed distributions of the 487-keV transition for both $LaBr_3$(Ce) detectors. A gate on the 329-keV peak in the HPGe detector was included to improve the selection. Anti-delayed (bottom-left) and delayed (bottom-right)$\gamma\gamma$(t) time distributions for the 329-487-keV coincidence peak in the two $LaBr_3$(Ce) detectors. The lifetime in all the time distributions is measured by a fit to an exponential decay of the tails in the spectra.

4.4.2 β-Walk

In β decay, β-particles are emitted in a continuous energy distribution up to the maximum energy defined by the decay Q_β of the decay. To reduce the spread in the time response of the plastic detector due to the wide range of β energies, the thickness of the β-plastic is specifically chosen to be small, 3 mm. This makes that β-particles above certain energy leave a similar amount of their energy in the plastic, independently of the initial energy, which favours a homogeneous time response. Nonetheless, a small dependence of the time response with the energy remains. Beta particles travel in the detector in a rather chaotic way and may suffer many interactions in the detector. Moreover,

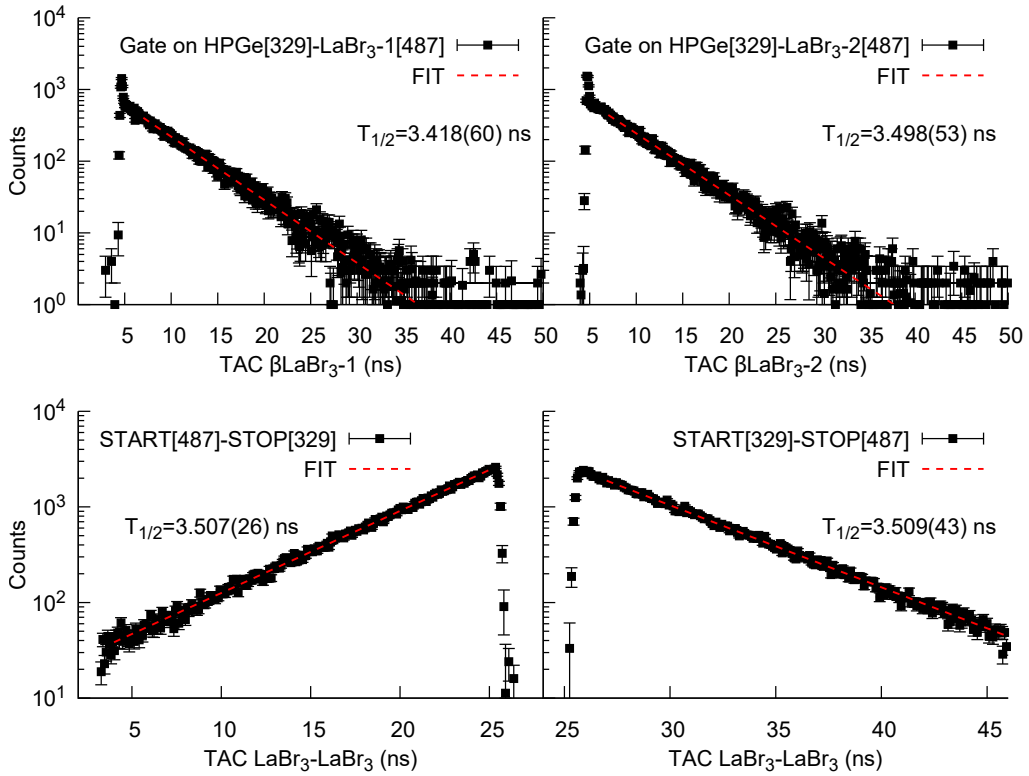

Figure 4.10: Half-life analysis of the 2083-keV level in ^{140}Ce. 2018 data set. Same than in Figure 4.9 but for the 2018 data set.

other particles such as γ-rays or neutrons can also interact with the plastic, contributing mostly to the low energy range of the spectrum. The sum of all these effects contribute to the β-energy spectrum. Figure 4.11 (Top) shows the β-energy spectrum for the decay of ^{131}In, after gating on the 2434-keV γ in the $LaBr_3$(Ce) detectors. The transmission peak can bee seen in the center of the spectrum.

The procedure to derive the *β-walk* curve for an specific decay is quite simple. Firstly, a prompt γ-ray is selected in the $LaBr_3$(Ce) detector. In addition a third coincident gate in the HPGe detector can also be set if there is enough statistics. Hereafter, the β-energy spectrum is divided in small sections, and projected to the TAC spectrum. The *β-walk* curve is built from the measured centroid position of the TAC spectrum for each portion of the β-spectrum. Figure 4.11 (bottom) shows the *β-walk* on the detector measured for the decay of ^{131}In. This curve was built using double β-$LaBr_3$(Ce) events,

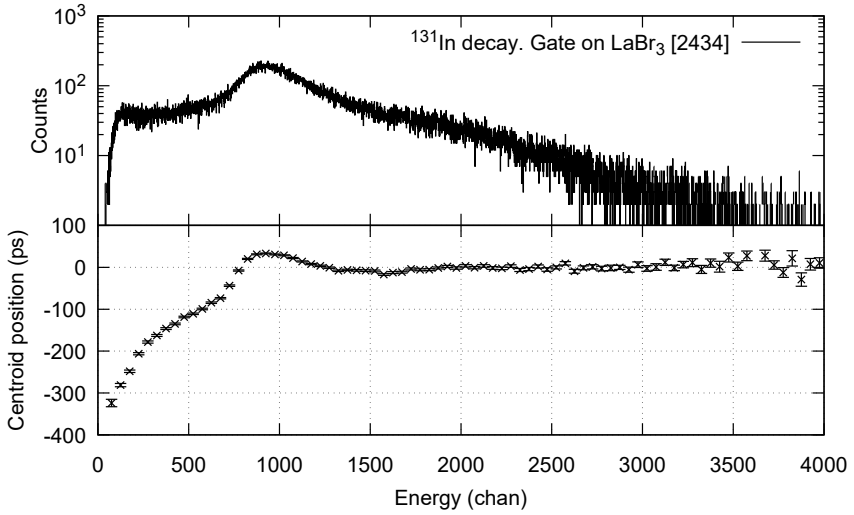

Figure 4.11: Example of β energy spectrum and $\beta - walk$ curve. These figures were generated using the data measured for the decay of ^{131}In.

setting a gate on the 2434-keV γ peak.

The β-walk curve shows a variation of more than 300 ps along the β energy range. The *β-walk* curve follows a smooth trend along the entire range, showing an abrupt change in its behaviour in the region of the transmission peak. Before starting with any lifetime analysis, the dependence of the time response with deposited β-energy needs to be corrected. This is done by shifting the TAC value by a certain number of channels, depending on the deposited energy. The resulting corrected TAC shows a constant *walk*. The correction is extracted directly from the measured *β-walk*, which depends strongly on the Q_β of the decay, and therefore needs to be performed independently for each studied decay.

4.4.2.1 Two component behaviour of the β-response.

The excellent time resolution of our detectors granted us the possibility of performing a fine analysis of the time response of the β-detector. A common feature observed in the decay of the indium isotopes, was the non-Gaussian shape of the $\beta\gamma$(t) time distributions. This anomalous behaviour was found to have a dependency on the energy of the β, and it can be observed only within a narrow range of energies at the middle of the β-spectrum. The analysis of the β-walk curves for these cases showed that this non-

Gaussian could be interpreted as the sum of two different Gaussian time distributions.

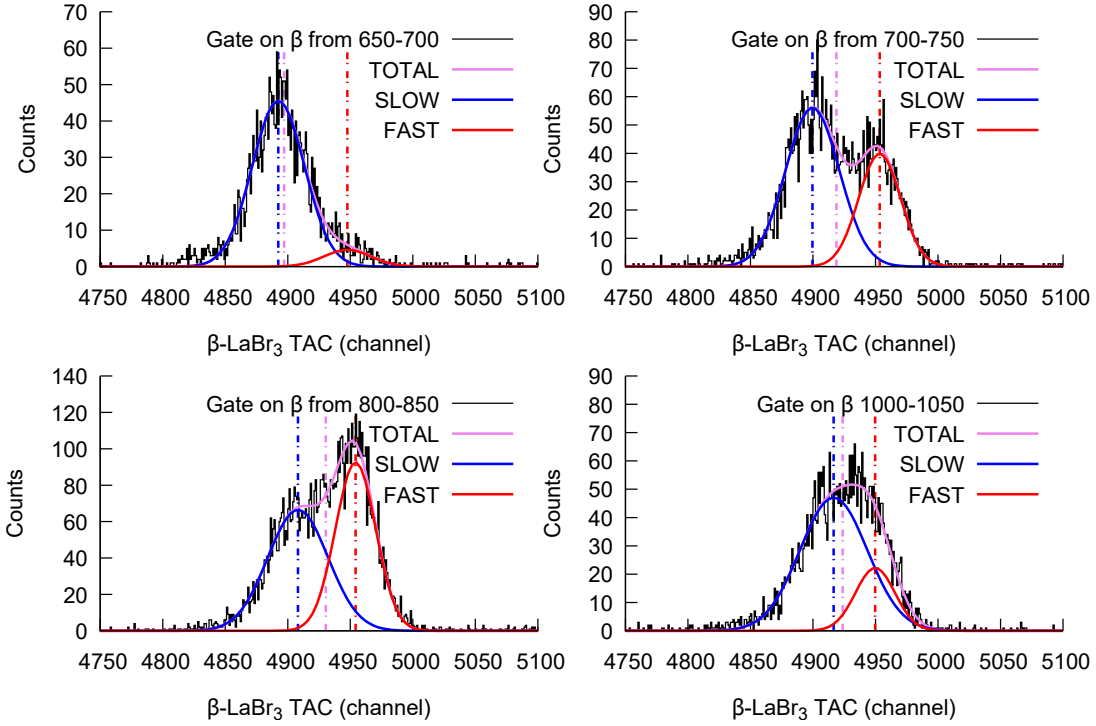

Figure 4.12: Analysis of the FAST and SLOW components of the β-$LaBr_3$(Ce) TAC spectra. Each TAC spectrum is derived using double $\beta\gamma$(t) coincidence events from the ^{131}In decay dataset. A gate on the 2434-keV transition is set on the $LaBr_3$(Ce) detector.

Figure 4.12 illustrates the analysis performed to disentangle the two components of the β energy spectrum for the decay of ^{131}In. Each subplot contains the TAC spectrum for the β-$LaBr_3$(Ce)[2434 keV] gated in a small 50 channel section of the β-energy spectrum. The TAC projections can be fitted to a two Gaussian component function. In this way, the centroid position and the area of each component can be estimated separately. From now on, we will call the left-hand and right-hand components as SLOW and FAST component respectively. This naming was chosen because a higher value of the TAC implies an earlier, or faster, start of the β detector and vice versa. This two-component behaviour is only observed in a small region of the spectrum in the center of β-energy range of about 400 ch. Outside this region, only the SLOW component can be observed. The FAST component shows a nearly constant behavior

with β-energy, when it is present. The SLOW component moves smoothly to the right-hand side of the spectrum until it becomes nearly constant in the high energy range.

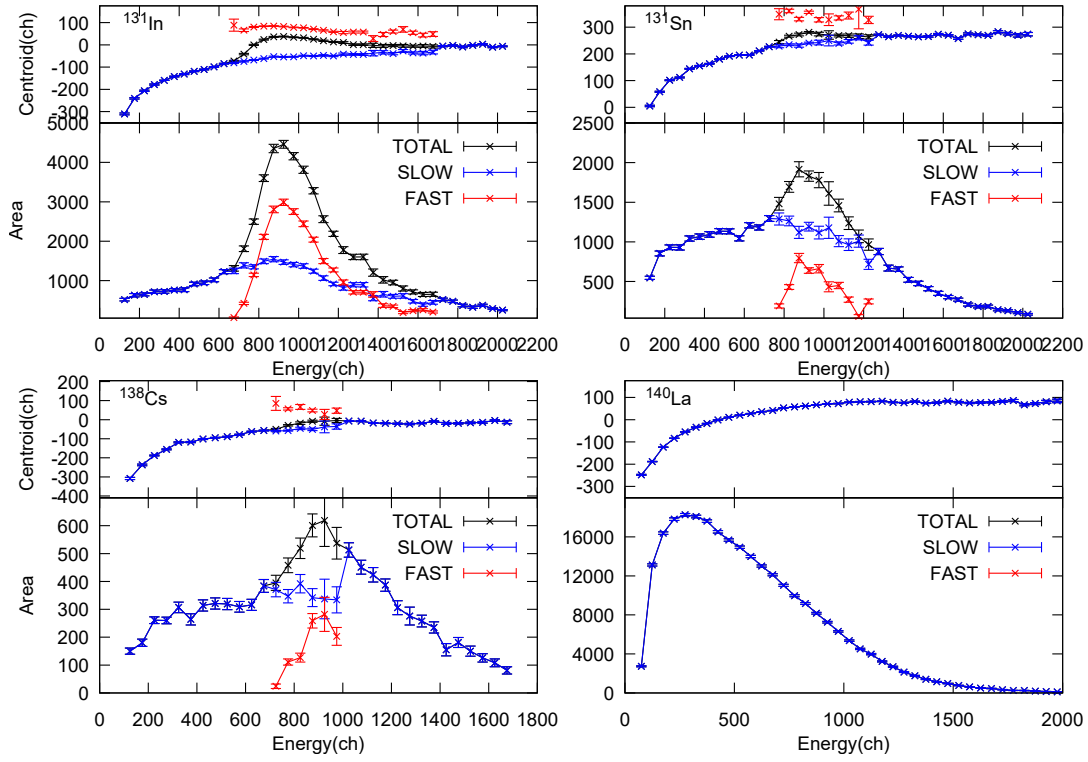

Figure 4.13: β-energy spectra and β-walk for the SLOW and FAST components. The energy spectra and time-walk curves are generate by plotting the area and centroid position derived for each component as a function of the deposited energy. (Top-left) ^{131g}In decay, gated on the 2434-keV γ-ray. (Top-right) ^{131}Sn decay, gated on the 798-keV γ-ray. (Bottom-left) ^{138}Cs decay, gated on the 1436-keV γ-ray. (Bottom-right) ^{140}La decay, gated on the 1596-keV γ-ray. See text for details.

By means of the analysis method described in Figure 4.12, it is possible to separate the deposited energy spectrum of each component, as well as their contribution to the *β-walk*. In Figure 4.13 there are depicted the area and centroid positions of the TAC for each component as a function of the deposited energy, for several decays measured our experiment. The resulting spectra show that the FAST component is produced by the peak that appears in the center of the β-spectra, while the SLOW component is produced by a much more continuous energy spectrum. This peak contributes to the *β-walk* by shifting it to the right of the TAC, (when it is present). The magnitude of

the shift depends on the relative ratio between the SLOW and FAST contributions. By comparing the energy spectrum and β-*walk* curves measured for the decay of other isotopes such as ^{131}Sb, ^{138}Cs and ^{140}La, we found that they show a similar two-component behaviour. However, the contribution of the FAST-component is much lower for ^{131}Sb and ^{138}Cs, and non-existent for the decay of ^{140}La. This indicates that the existence of this FAST-component is related to the presence of high-energy β-particles in the spectrum. On the other hand, the SLOW component is always present in all the isotopes, and even if the shape of the β-energy spectrum shows slight differences.

In conclusion, the β-spectra is made of two main components. The time-walk of each component does not change from one isotope to the other. However, the relative contribution from each components to the β-spectra depends strongly on the available energy for the β-particles. Hence, the change in the $\beta - walk$ observed for different isotopes, is produced by the varying contribution of each component to the β-energy spectrum, which is strongly related to the maximum energy of the β-electrons.

4.4.3 $LaBr_3$(Ce) FEP walk

The time response of the $LaBr_3$(Ce) detectors also shows a residual dependence on the energy deposited by γ-rays. The interaction of Compton events in $LaBr_3$(Ce) crystals differs from FEP events, and thus their time response is slightly different. The information on lifetimes is extracted from the time distributions of FEP events only, so we need to the characterize the time response of FEP events. This dependence with energy is given by the FEP *Walk* curve, which accounts for the energy dependence of the response of the system to γ-rays that leaves all the energy in the lanthanum crystals.

The construction of FEP *walk* curve is done by measuring the time centroid position of a set of prompt γ-rays of different energies. Transitions with short lifetimes can also be used, by correcting the centroid position by the lifetimes of the contributing levels. The FEP *walk* of the $LaBr_3$(Ce) detectors depends on several of factors, such as the shape of the crystal, the PMT and t CFD. All these features are the same for both detector, and hence their FEP-*walk* should be similar. Nevertheless, small differences could appear and thus they have to be calibrated separately.

For $\beta\gamma$(t) events we followed the methodology described in the previous section to clean the $LaBr_3$(Ce), as well as to account for contributions from the Compton that

are applied, see section 4.3.1. Two $\beta\gamma$(t) *walk* curves are constructed, one for each $LaBr_3$(Ce) detector.

For $\gamma\gamma$(t) events, two extra *walk* curves can be derived. One for the START detector and the other for the STOP detector. To build the *walk* curves using $\gamma\gamma$(t) we need to use a combination of γ-rays whose intermediate levels have a prompt lifetime. In this case it does not matter if there is a higher-lying level with a long-lifetime, since it does not affect the time distribution.

The two $LaBr_3$(Ce) detectors, as well as the signal processing, are the same for both $\gamma\gamma$(t) and $\beta\gamma$(t) coincidences events. Consequently, the *walk* curves derived from $\gamma\gamma$(t) events are related to those obtained from $\beta\gamma$(t). The *walk* curve from the STOP $LaBr_3$(Ce) detector in $\gamma\gamma$(t) is the same than the one derived from the same detector in $\beta\gamma$(t), except for an offset. On the other hand, the *walk* for the START $LaBr_3$(Ce) detector in $\gamma\gamma$(t) coincidence is also the same than in $\beta\gamma$(t), but in this case it appear inverted. Given these equivalencies, we can use the data points extracted from both kinds of events to build the walk curve from both detectors.

In order to obtain a precis characterization of the FEP-*walk* curves, a complete set of calibrations sources was used. It included a closed γ-ray sources, ^{140}Ba/^{140}La and ^{152}Eu as well as on-line sources, ^{138}Cs and ^{88}Rb. Additionally, several transitions in ^{132}Sb, are present in the decay chain of ^{132}In, were used as internal calibration. The list of γ-rays used for this calibration can be found in Table 4.2.

Table 4.2: List of γ-lines employed to measured the FEP-*walk* curves for both $LaBr_3$(Ce) detectors.

Nucleus	E_{level}(keV)	$T_{1/2}$ (ps)	E_γ (keV)	Method
^{140}Ce	2521.43	$\leq$2.4	2521.4	$\beta\gamma$(t)
			925.2	$\beta\gamma$(t), $\gamma\gamma$(t)
			109.4	$\beta\gamma$(t)
	2525.77	$\leq$2.5	919.55	$\beta\gamma$(t), $\gamma\gamma$(t)
			432.49	$\beta\gamma$(t)
	2525.77	$\leq$2.5	919.55	$\beta\gamma$(t), $\gamma\gamma$(t)
			432.49	$\beta\gamma$(t)
	2464.09		867.846	$\beta\gamma$(t), $\gamma\gamma$(t)
	2412.02	1.3(4)	815.772	$\beta\gamma$(t), $\gamma\gamma$(t)
		1.3(4)	328.762	$\beta\gamma$(t)
	2347.89	0.15(10)	751.637	$\beta\gamma$(t), $\gamma\gamma$(t)
	2083.26	3474(10)	487.021	$\gamma\gamma$(t)
	1596.24		1596.21	$\beta\gamma$(t)
^{138}Ba	2639.59		2639.59	$\beta\gamma$(t)
	2445.64	5(4)	1009.78	$\beta\gamma$(t), $\gamma\gamma$(t)
			546.990	$\beta\gamma$(t)
			227.76	$\beta\gamma$(t)
			138.08	$\beta\gamma$(t)
	2307.59	7(3)	871.72	$\beta\gamma$(t), $\gamma\gamma$(t)
			408.98	$\beta\gamma$(t)
	2218.0		2218.00	$\beta\gamma$(t)
	2090.6		191.96	$\beta\gamma$(t)
	1898.64	2160(11)	462.785	$\gamma\gamma$(t)
	1435.77		1435.77	$\beta\gamma$(t)
^{152}Sm	1371.721		1005.27	$\gamma\gamma$(t)
	1233.8626	$\leq$6	867.380	$\gamma\gamma$(t)
	810.453	7(5)	444.01	$\gamma\gamma$(t)
	366.4795	60(5)	244.6974	$\gamma\gamma$(t)
^{152}Gd	1643.421		1299.142	$\gamma\gamma$(t)
	1434.020		1089.737	$\gamma\gamma$(t)
	1123.1855		778.9045	$\gamma\gamma$(t)
	755.3960	7.3(4)	411.1165	$\gamma\gamma$(t)
^{88}Sr	2734.137	0.70(5)	898.042	$\beta\gamma$(t)
	1836.063	0.154(8)	1836.063	$\beta\gamma$(t)

Table 4.2: List of γ-lines employed to measured the FEP-*walk* curves for both $LaBr_3$(Ce) detectors.

Nucleus	E_{level}(keV)	$T_{1/2}$ (ps)	E_γ (keV)	Method
^{132}Sb	1325.15	$\leq$37	1239.63	$\beta\gamma$(t)
			899.04	$\beta\gamma$(t)
			246.87	$\beta\gamma$(t)
	1078.3	2.6(14)	1078.3	$\beta\gamma$(t)
			992.66	$\beta\gamma$(t)
			652.31	$\beta\gamma$(t)
			549.23	$\beta\gamma$(t)
	426.07	15.8(17)	340.53	$\beta\gamma$(t)

The walk curves for each source are shifted by an offset one from the other, providing a set of parallel curves. The global curve for each detector is obtained by applying an offset to match the ^{138}Ba $\beta\gamma$(t) points.

In Figures 4.14 and 4.15 the FEP *walk* curves derived for both detectors and experimental campaigns are shown. The curves show an excellent compatibility between the calibration points derived from all the calibration sources, as well as, between those derived from $\beta\gamma$(t) and $\gamma\gamma$(t) coincidence events.

The experimental data points have been fitted to the calibration function defined by 4.27.

$$FEP_{walk}[E_\gamma] = a_0 + \frac{a_1}{\sqrt{E_\gamma + a_2}} + a_3 \cdot E_\gamma + a_4 \cdot E_\gamma^2 \tag{4.27}$$

This is an empirical function that is used instead of interpolation, and avoids *adhoc* extrapolations at high energies. It was not possible to fit the whole energy range with the same curve. Thus, the data points are separated in two energy regions, with the boundary located at E_γ = 765 keV. The overall agreement between the fitted curves and experimental points was excellent with a $\sigma \sim 1$ ps for all the curves. Nonetheless, for the measurement of half-lives, we have incremented the uncertainty of the FEP-*walk* curves up to the more conservative 3σ value. This is the value that is propagated to the lifetime results.

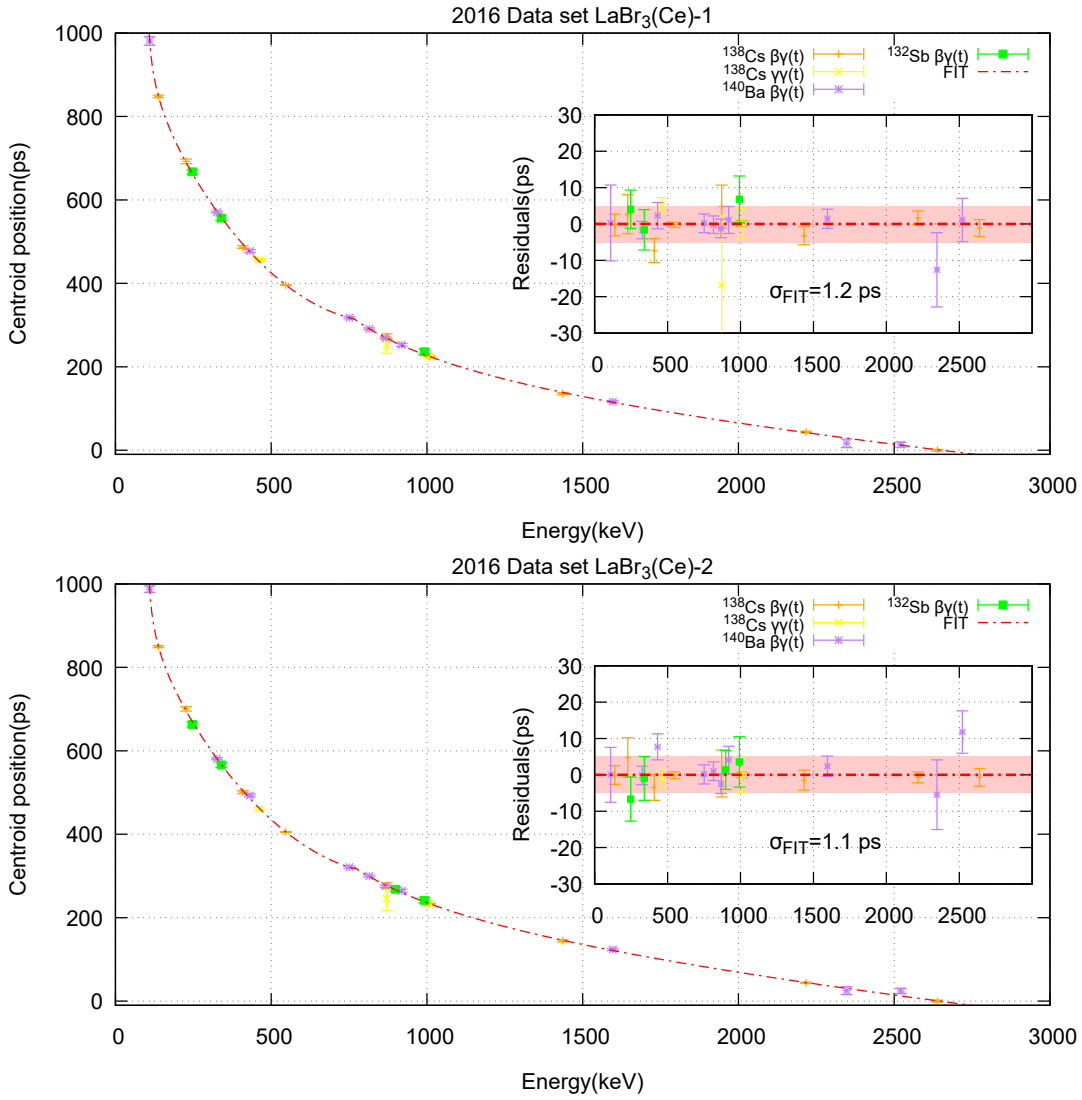

Figure 4.14: FEP walk curve for both $LaBr_3$(Ce) detectors for the 2016 measurements.

4.5 Conclusions

The fast-timing method is a well established electronic technique for the measurement of lifetimes of nuclear excited states. It is based on the use of delayed coincidence between fast-scintillator detectors. The use of fast scintillators opens the possibility of lifetime measurements in the range of tens of ns down to a few ps. Nowadays the standard type of detectors used in fast-timings experiments are $LaBr_3$(Ce) crystals as γ-ray detectors,

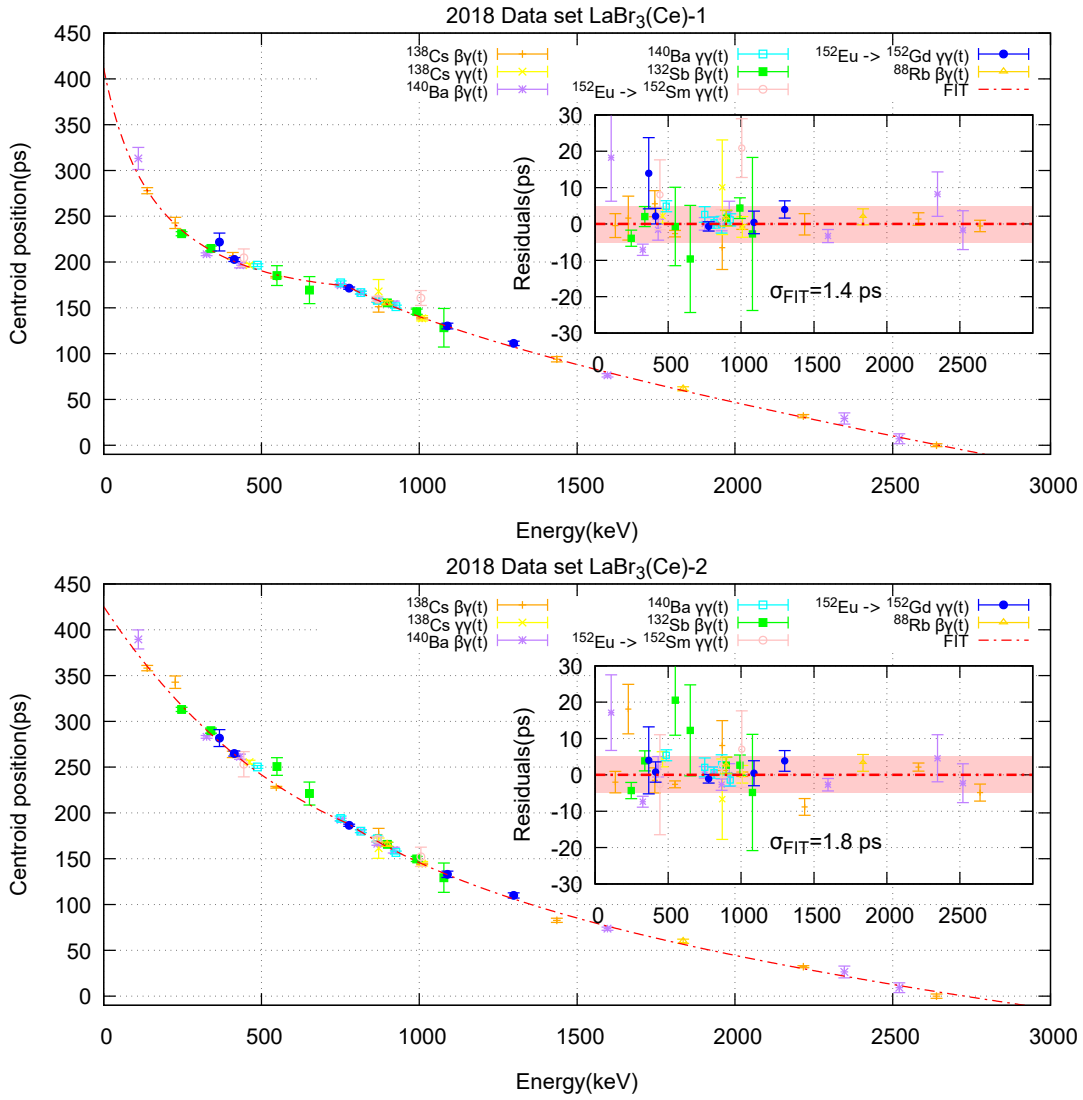

Figure 4.15: FEP walk curve for both $LaBr_3$(Ce) detectors for the 2018 measurements.

and ultra-fast thin plastics as β detectors. The two complementary methods to measure lifetime relies in the analysis of $\beta\gamma$(t) and $\gamma\gamma$(t) delayed coincidences. In certain cases either method will be more suited depending on the level under study and the decay level-scheme. In other cases the complementary use of both techniques may be possible to most populated levels, when statistics suffices.

One of the main difficulties in fast-timing experiments consists in dealing with complex γ-ray spectra and normally with a high level of Compton background. The most

Table 4.3: Calibration parameters for the FEP *walk* curves. The limit that separate the two fit regions is located at E_γ = 765 keV for the four combinations.

	2016			
	$LaBr_3$(Ce) 1		$LaBr_3$(Ce) 2	
	Region 1	Region 2	Region 1	Region 2
a_0	7.825×10^{2}	5.932×10^{3}	7.262×10^{2}	6.250×10^{3}
a_1	-9.719×10^{1}	-4.213×10^{2}	-9.903×10^{1}	-3.885×10^{2}
a_2	-1.503	-6.419×10^{-2}	-1.445	-6.969
a_3	9.167×10^{2}	4.454×10^{1}	9.174×10^{2}	5.286×10^{1}
a_4	8.853×10^{-4}	0	8.161×10^{-4}	0

	2018			
	$LaBr_3$(Ce) 1		$LaBr_3$(Ce) 2	
	Region 1	Region 2	Region 1	Region 2
a_0	5.164×10^{3}	3.711×10^{3}	1.079×10^{5}	7.309×10^{3}
a_1	1.257×10^{2}	-1.234×10^{2}	1.607×10^{3}	-8.001×10^{1}
a_2	6.507×10^{-2}	-5.405×10^{-2}	3.141×10^{-1}	-2.715×10^{-2}
a_3	-4.862×10^{1}	6.919×10^{1}	-2.265×10^{3}	-6.798×10^{1}
a_4	0	0	0	0

common strategy to get rid of this background consists in setting a third γ-ray coincidence in the HPGe detector. However, this approach may not be sufficient to deal with all the background of a complex spectra, and further corrections for the Compton background may be still required. In this PhD thesis, a set of new correction methodologies have been developed, in order to estimate and correct the contribution from Compton background events, see Section 4.3.

The time response of the fast-timing setup has been carefully calibrated. The relationship between TAC channels and time has been measured using a time calibrator module. This calibration has been cross-checked using the known 3.474(10) ns half-life of the 2083-keV state in ^{140}Ce [MF95]. On the other hand, the time walk of the β and $LaBr_3$(Ce) detectors were also derived. The analysis of the β-walk showed the existence of two different components in the β spectrum, a FAST component related to the transmission peak and a SLOW component related to a much wider energy spectrum. Our analysis indicated that the relative contribution of each component depends

strongly on the available energies for the β particles, gaining importance the fast component for high energy β. Consequently, the β-walk is strongly affected by the Q_β and decay-scheme, which producing non-Gaussian time distributions in decays with large Q_β energy spectrum.

The FEP-*walk* curves for both $LaBr_3$(Ce) detectors in each dataset were calibrated separately. A complete set of calibration sources was employed to cover a wide range of energies, from 100 keV up to 2.6 MeV. Taking into account that the same the $LaBr_3$(Ce) detectors are used for both $\beta\gamma$(t) and $\gamma\gamma$(t) events, the FEP-*walk* curves were built using points derived from both types of coincidence events.

5

Doubly Magic ^{132}Sn

In this Chapter we address the investigation of the excited structure of ^{132}Sn. As described in Chapter 1, this doubly-magic nucleus is of paramount importance to understand excitations across the $N = 82$ and $Z = 50$ shell gaps.

Due to its interest the excited structure of ^{132}Sn has been experimentally investigated since the 1970s. Beta decay experiments were carried out at OSIRIS [KHDGB73, FHJ$^+$94, FHJ$^+$95, MF95] and ISOLDE [BBB$^+$86, BGE$^+$80], as well as fission experiments performed at the JOSEF facility [KSB$^+$82, DLSS78] and the Argonne National Laboratory [BDZ$^+$01].

Beta decay is the ideal tool to investigate the excited structure of ^{132}Sn, both directly from ^{132}In (7^-) g.s. and via beta-delayed neutron emission from the ^{133}In ($9/2^+$) g.s. and the ($1/2^-$) 330-keV β-decaying isomer. This is due to the large energy window available for the decay, of $Q_\beta(^{132}\text{In}) = 14135(60)$ keV and $Q_{\beta n}(^{133}\text{In}) = 11010(200)$ keV [WAK$^+$17], respectively, and due to the high spin of the parent nuclei that makes it possible to populate many states in ^{132}Sn.

The most complete β-decay experiment was performed by Fogelberg *et al.* [FHJ$^+$94, FHJ$^+$95, MF95] at the OSIRIS facility in the 1990s, where the level scheme of ^{132}Sn was expanded to 21 excited levels, including negative and positive parity states up to the neutron separation energy. Proton particle-hole states were identified for the first time, and the 4352-keV $J^\pi = 3^-$ state was confirmed to have an octupole vibrational character. Lifetime measurements of the excited states down to the ps range were performed, and spin and parities assignments were made for the levels below 5 MeV.

Despite all the detailed studies on ^{132}Sn attained through the β-decay and fission experiments, many of the expected particle-hole multiplet states remain without experimental identification.

In this work we focus on the investigation of the excited structure of ^{132}Sn populated in β-decay of ^{132}In and β-n decay of ^{133}In. Taking advantage of the enhanced yield and selectivity the aim is to identify some of the missing particle-hole multiplet states, and to measure lifetimes of excited states in ^{132}Sn

Owing to the large difference in the β-decay half-lives of ^{132}In and ^{132}Sn, of 200(2) ms and 39.7(8) s [KRSS05], respectively, the time distribution relative to the arrival of the proton on target makes it possible to identify whether a γ ray has been emitted during the β decay of ^{132}In or from the daughters. A similar situation occurs for the β decay of ^{133}In. Apart from the time distribution, the identification of the γ-rays belonging to ^{132}Sn is based on γ-γ coincidences with previously-known transitions.

5.1 Beta decay of ^{132}In

The Q_β in ^{132}In is 14140(60) keV, while the neutron separation energy in ^{132}Sn is 7353(4) keV [WAK$^+$17], and therefore the feeding of excited states up to $\approx$ 7 MeV is possible in this decay. One has to bear in mind that the ^{132}In β decay is quite complex. The(7$^-$) of the parent [JGG$^+$16], favours the population of relative high spin (6-8) excited states in the energy range from 4 to 7 MeV, which can only de-excite to the ground state by means of γ-ray cascades of 3 or more transitions. As discussed in Chapter 1, due to the doubly magic nature of ^{132}Sn, the first excited state appears at a very high energy, 4041 keV. Therefore, new levels that can de-excite directly to the g.s. with an energy below 4 MeV are not expected.

In Figure 5.1, the shell model configuration of ^{132}In ground state is illustrated. The β-feeding intensity of states in ^{132}Sn is dictated by to the initial configuration. Both Gamow-Teller and first forbidden transitions are expected for that configuration. In the simplest scheme a dominant population of the $\nu f_{7/2} g_{7/2}^{-1}$ multiplet, caused by the GT $\nu g_{7/2} \rightarrow \pi g_{9/2}$ transition in the ^{132}In decay is expected. The remaining decays are mostly due to first forbidden transitions, feeding consequently states of the $\nu f_{7/2} h_{11/2}^{-1}$, $\pi g_{7/2} g_{9/2}^{-1}$ and $\pi d_{5/2} g_{9/2}^{-1}$ configurations. The f.f.$\nu f_{7/2} \rightarrow \pi g_{9/2}$ f.f. transition would populate the tin ground state, however, the large change in angular momenta between

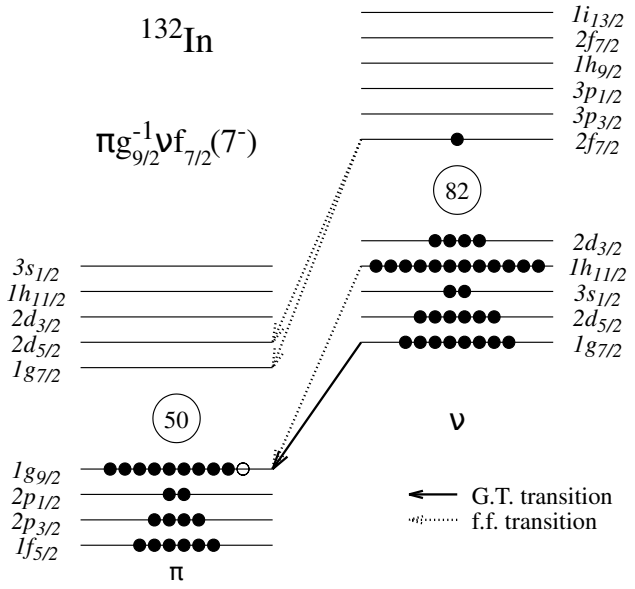

Figure 5.1: Shell model configuration of ^{132}In ground state. The arrows represent the expected Gamow-Teller (solid arrows) and first forbidden (doted arrows) transitions.

both ground states ΔJ=7 removes this possibility. The occurrence of GT transitions of neutrons below the N =82 shell gap into proton orbits above the Z = 50 gap can also be expected. Such transitions would most likely lead to the population of 2p2h configurations with energies above the neutron separation energy, which would decay via delayed neutron emission.

The energy spectrum recorded in the HPGe clover detectors, setting a time window of 30-530 ms after proton impact, is depicted in Figure 5.2. This condition was imposed in order to reduce the contribution of the different contaminants. The contribution of neutron-induced background coming from the target is suppressed by removing the first 30 ms of the time window. An upper limit of the time window at 530 ms was chosen to reduce the contribution of the long-lived daughters, while keeping most of the statistics.

5.1.1 Half-life of ^{132}In ground state

The half-life of ^{132}In was measured by fitting the time distribution of the 10 strongest γ rays labeled in Figure 5.2, except for the 4416 keV peaks, which was excluded because its relatively low intensity. In order to build the time distributions, the full statistics

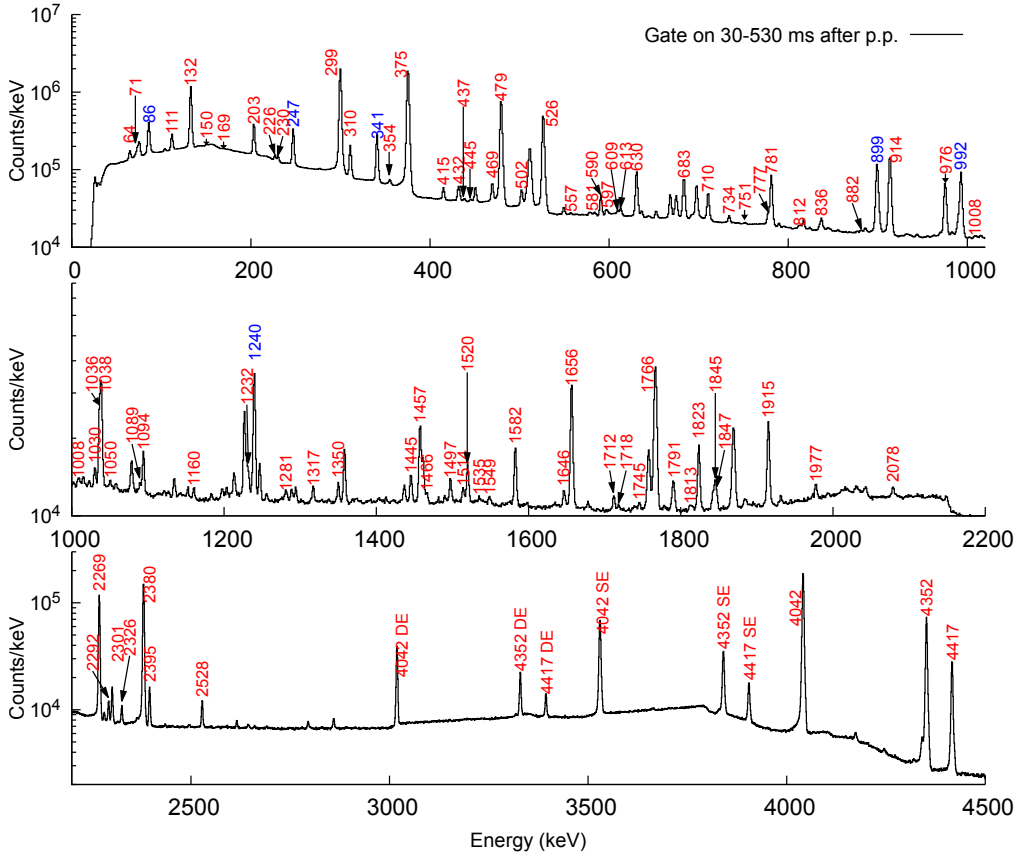

Figure 5.2: Singles γ-ray energy spectrum recorded in the HPGe detectors following the ^{132}In decay. This histogram was built using the events measured during the 30-530 ms time interval after proton impact. The strongest peaks observed in the spectra are labeled with their energies in keV. The SE and DE labels indicates single escape and double escape peaks.

recorded by the HPGe detectors was employed, no extra coincidence in other detectors required. Since the activity at the experimental station is pulsed by the proton beam structure and the release from the target, the time distribution is fitted to an exponential decay function with a constant background after the end of the implantation. The background contribution was estimated by analyzing the time range from 2400 to 3600 ms after proton impact.

Due to the high count rates, dead time effects are sizable, mainly during implantation, but also at the beginning of the decay. In each HPGe crystal an average count rate

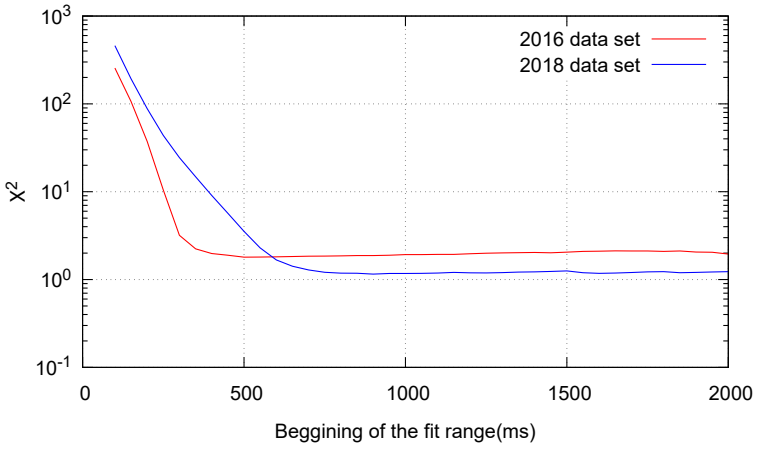

Figure 5.3: Dead-time characterization for the ^{131}In decay data set. χ^2 fit Test. The lines represent the measured χ^2 as a function of the starting point for the fit range. For the 2016 data set, exponential behaviour is recovered quickly after the end of the implantation. It can be seen that at 500 ms the χ^2 has already reached a minimum. For the 2018 distributions, it takes more time for the χ^2 to get closer to 1, but at 900 ms after it has already converged.

of 3×10^3 counts per seconds (cps) was observed, however, during the implantation time the count rate could rise up to 1.5×10^4 cps. To account for this effect the beginning of the fit range was shifted by a few half-lives towards higher times and a χ^2 fit test was performed to verify that the expected exponential decay behavior was recovered, see Figure 5.3. In this way a safe fit starting point was decided.

The lifetime measurement was performed independently for each of the two data sets of ^{132}In decay measured in the two experimental campaigns. The contribution of the Compton background under full-energy peaks was subtracted. This investigation furnishes 20 independent values for the ^{132}In, 10 from each data set, which are all statistically compatible with each other. The final value of the ^{132}In half-life was adopted as the weighted average of the measurements, yielding $T_{1/2}$=202.2(2) ms. The statistical uncertainty of the weighted average is calculated and increased by multiplying by the χ^2 obtained. No systematic error is included. This half-life is in agreement with, but more precise than, the value reported in the latest evaluation, $T_{1/2}$=200(2) ms [KRSS05]. In Figure 5.4 the decay curves for the 10 γ rays under consideration, from the 2016 and 2018 dataset, are shown.

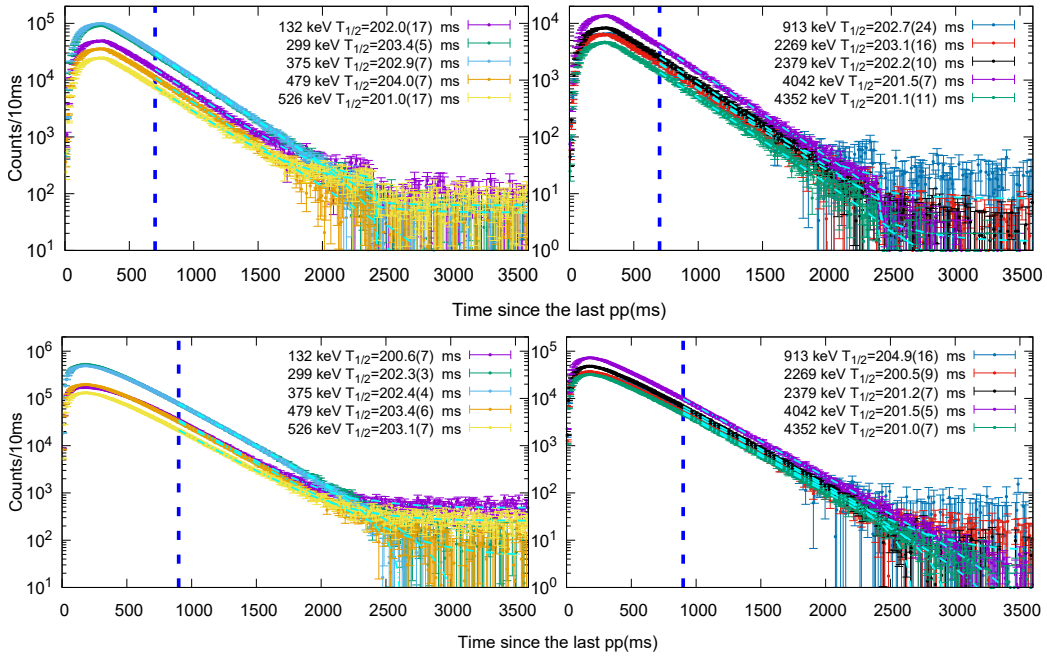

Figure 5.4: Decay curves of the ten most intense γ-rays form ^{132}In β decay recorded in singles in the HPGe detectors. The region considered for the fit goes from 700 ms, marked with a dark-blue dashed line, up to 2400 ms. This region has been adjusted in order to minimize dead-time effects.

5.1.2 Identification of new γ-rays in ^{132}Sn

The analysis of γ-γ coincidences was done using the full statistics independently for the two data sets from each campaign. The assignments were cross-checked by requiring coincidences with the β detector and/or a time range since proton impact from 30 to 530 ms.

There is a large number of levels that are populated directly during ^{132}In decay. However, there are only three observed levels, the 4042, 4352 and and 4417 keV, that are directly connected to the ground state via γ-rays. Thus, regardless of the level initially populated, the de-excitation path is bound to pass through one of these three states. Almost all the γ-rays in the ^{132}Sn level scheme can be found in the γ-γ coincidence spectra of the de-exciting γ-rays for those three levels.

The $4^+ \rightarrow 2^+$ 375 keV transition in ^{132}Sn is the most intense γ-ray in the spectra. It is the strongest transition that de-excites the 4417-kev level. Even though this level is not directly fed in the decay of ^{132}In, it is populated in $\sim$65% of the total indium

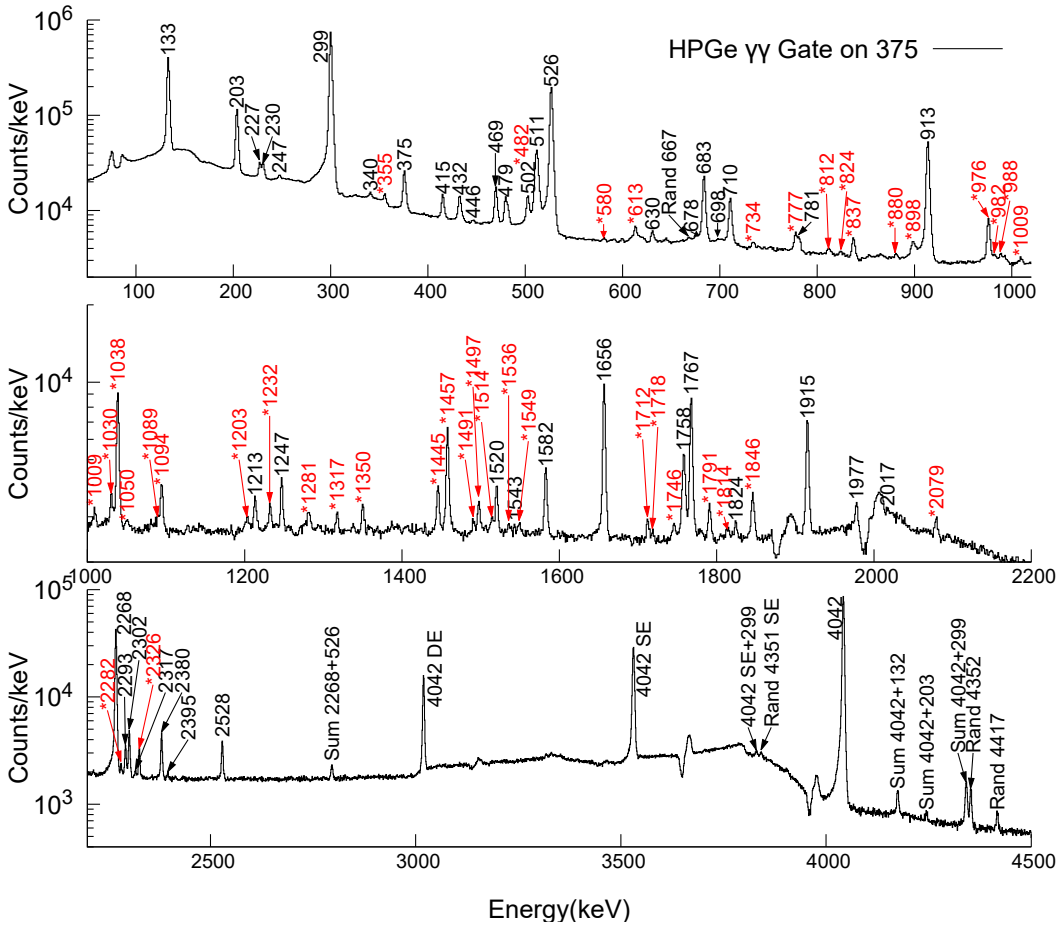

Figure 5.5: Compton-subtracted γ-γ energy spectra gated on the 375 keV $4^+ \rightarrow 2^+$ γ transitions in ^{132}Sn. The previously-known γ rays are labeled with their energies in black. New transitions identified in this work are labeled in red with an asterisk. The negative peaks in the spectrum arise from background subtraction, due to Compton scattering between two HPGe clover detectors. Due to the large counting ratio, several random coincidence peaks can be observed, they appear labeled with Rand. The peaks labeled with Sum correspond to summing peaks between two coincident γ-rays also in coincidences. They are a side effect of the addback correction for the strongest γ-lines

decay by γ-rays. It is connected to most of the positive parity levels, either directly or via the 299-keV γ-ray, and to the negative parity levels via the 526-keV transition. Consequently, mostly all the γ-rays in ^{132}Sn appear in coincidence with the 375-keV transition. Figure 5.5 shows the γ rays in coincidence with the 375-keV line. The spectrum illustrates the amount of statistics and the large amount of newly observed γ-rays that are revealed in this study. Their appearance in coincidence with the 375-keV

γ, strongly supports their assignment to the ^{132}Sn level scheme. However, a complete γ-γ investigation is required to correctly place them.

Figure 5.6 shows the coincidence spectra for the 299-keV (top), 132-keV (middle) and 682-keV (bottom) transitions. These three γ-rays belong to de-excitations from positive parity levels, which are populated by a large number of γ-rays. The 4715-keV 6^+ level is de-excited exclusively by the 299-keV γ-ray that connect it to the 4417-keV level. This state is populated also very intensely, $\sim$45% of the intensity, from which only a small fraction is directly fed in the β-decay. In the γ-γ-ray coincidence spectrum strong γ-lines at 132-, 203-, 683 and 913-keV, can be observed, these transition are the ones that provides to the 4715-keV the majority of the feeding. Besides them, there is a large number of weak γ-lines that can be observed in the same spectrum, most of them related to newly observed γ-rays.

In the bottom spectrum in Figure 5.6 the coincidence spectrum with the 683-keV transition the only one de-exciting the 5399-keV (6^+) state, is depicted. This level is populated only in a 2% of the total indium decays, and no noticeable direct feeding has been measured. Its population is due to a large number of γ-rays. The γ-γ spectrum gated on the 683-keV γ-line shows a lot of small γ-rays that have not been quoted in previous studies. In particular, it reveals the erroneous assignment of 1457-1038 keV γ cascade. This sequence had already been observed by Fogelberg *et al.* [FHJ$^+$94], however the order of the γ rays proposed was inverted, giving rise to an excited level at 6173 keV with suggested (6^+) spin-parity. This level has been ruled out in our analysis due to the finding of another γ-ray at 354 keV that de-excites the 5754-keV state, confirmed by γ-γ coincidences with the 683-keV and 1457-keV transitions.

The states located at 5766 and 5446 keV are observed in the β-delayed neutron emission of ^{133}In from our experiment [PKF$^+$19]. The assignment is confirmed in the analysis of the ^{132}In decay with the uncovering of new cascades in the ^{132}In decay involving both levels.

The 4848 8^+ level is populated in $\sim$23% of the decays. Direct β feeding provides only $\sim$15%, thus the remaining 8% due to γ-rays. The 4848 8^+ state is characterized by a long lifetime, $T_{1/2}$ =2.080(17) [KRSS05]. Henceforth, a modification of the default 200 ns coincidence time window was required to explore the γ-rays that populate this level. Figure 5.6 (center) shows the coincidence spectrum of γ-rays measured within a 0.5-2 μs before the detection of the 132-keV transition. This large time-window produce

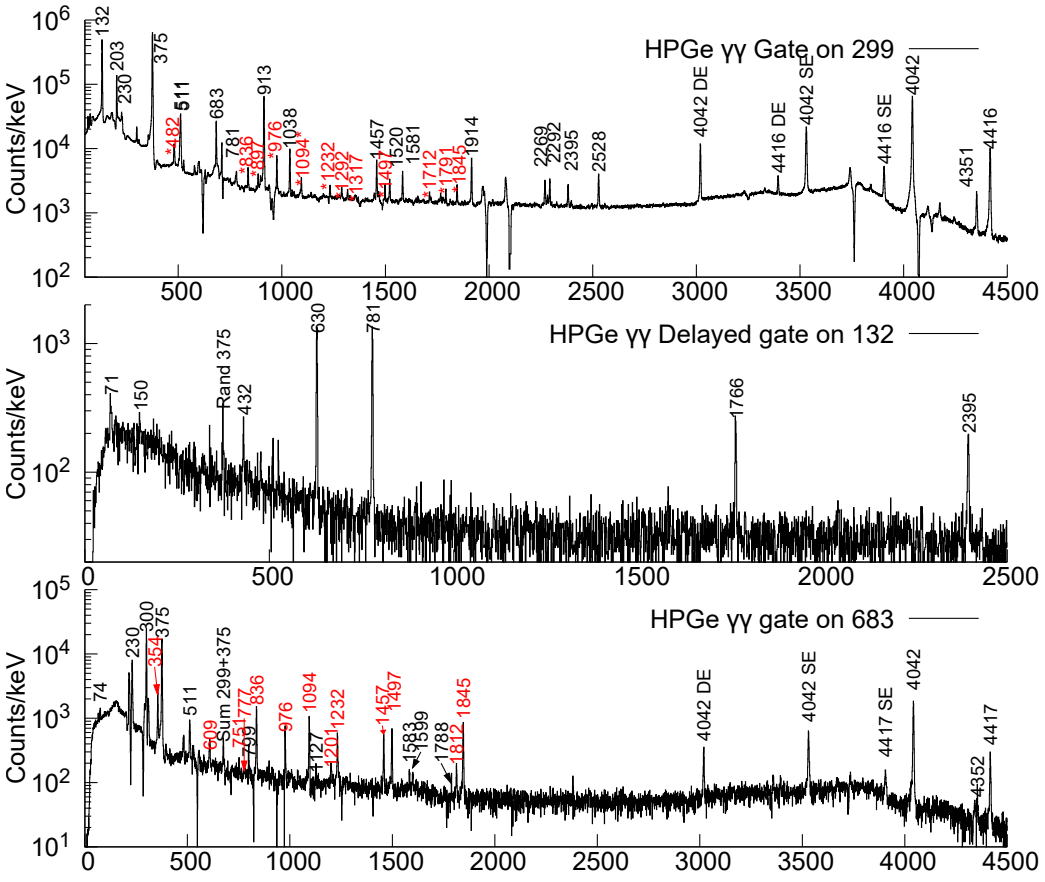

Figure 5.6: γ-γ coincident energy spectra for γ-rays from positive parity levels in ^{132}Sn. gated on the 299.3 keV (top), 132-keV (center) and 683-keV (bottom) γ transitions in ^{132}Sn. Due to the long-lifetime of the 4848-keV 8^+ level, For the spectrum gated on the 132-keV, only the γ rays measured within a coincidence window of 0.5-12 μs before the detection of the 132-keV γ-ray were used.

a large contribution of random coincidences. Thus a random background spectrum was also generated, using the γ-rays measured 0.5-2 μs after the detection of the 132-keV γ-ray, and subtracted from the other. Under these conditions only the γ-rays that feed the 4848-keV state appear in the spectrum. The observation of the de-exciting 432-keV transition in delayed coincidence with the 132-keV γ-ray, confirms the population of a 5280-keV level. This level was already reported in ^{248}Cm fission studies [BDZ+01], and tentatively identified as the (9^+) state that arises from the particle-hole $\nu f_{7/2} h^{-1}_{11/2}$ configuration.

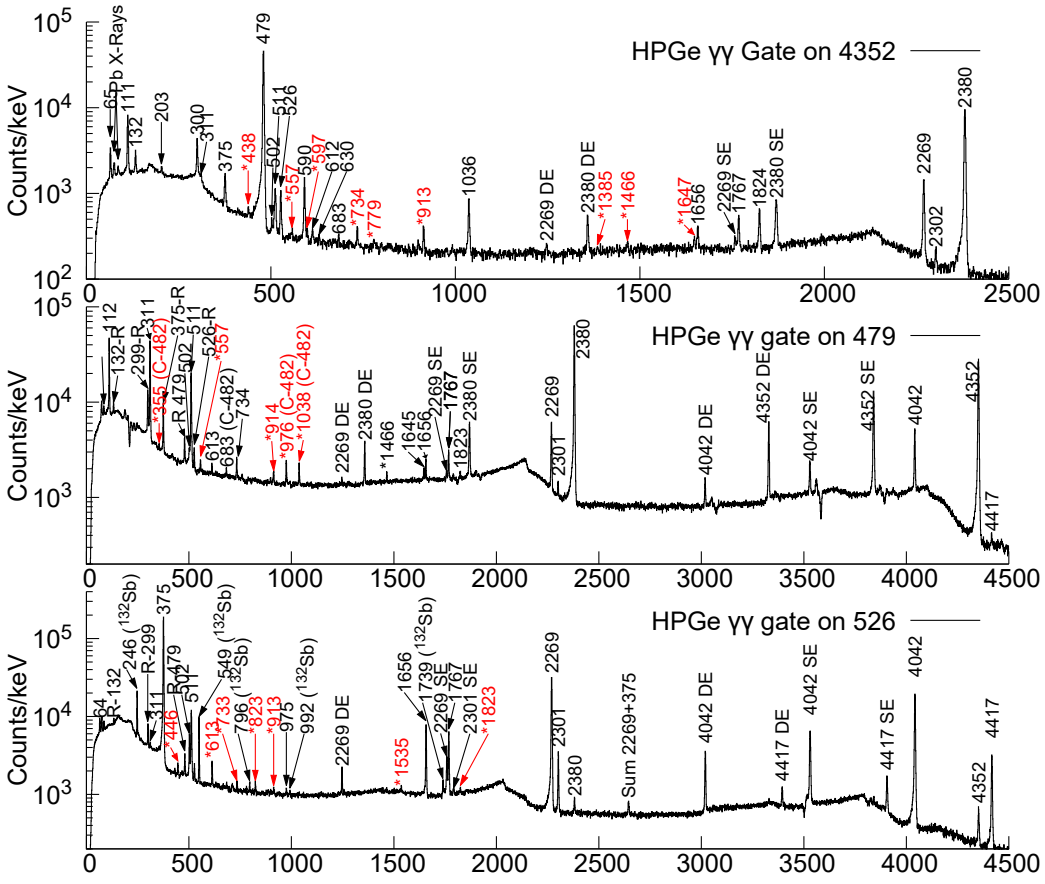

Figure 5.7: Compton-subtracted γ-γ energy spectra gated of the γ-rays de-exciting the low-lying negative-parity levels in ^{132}Sn. (Top) Gate on the 4352 keV transition from the 4352-keV 3^- level. (Center) Gate on the 479-keV γ-ray de-exciting the 4830-keV 4^- state. (Bottom) Gate on 526-keV transitions from the 4942-keV 5^- level.

Figure 5.7 shows the γ-γ coincidence spectra for the 4352-, 479- and 526-keV transitions, which de-excite the 4352-, 4830- and 4942-keV levels of spin-parity 3^-, 4^- and 5^- respectively. These three levels are not populated directly in the decay of ^{132}In, however they collect most of the γ-ray intensity from the higher-lying negative-parity levels. Therefore, the study of their coincidence γ-γ spectra is the best way to investigate the population of negative-parity states.

Three levels, at 4949, 6297 and 6476 keV excitation energy, were uncovered from the observance of new γ-rays in coincidence with the 4352-, 479- and 526-keV transitions. Besides them a good number of new γ-rays de-exciting the previously assigned negative

parity levels were found.

The γ-γ coincidence analysiscovers all previously known γ-rays in ^{132}Sn, and also to the new peaks found in from γ-γ coincidences. Given the high multiplicity cascades that dominate the decay, the new levels and γ-rays assigned are most of the time supported by coincidence with two or more transitions. The level scheme of ^{132}Sn has been greatly expanded with the addition of 57 new γ transitions and 11 new levels, observed following the direct ^{132}In β decay. The level scheme is shown in Figure 5.8. A list of the γ rays is provided in Table 5.1.

The direct β feeding to states in ^{132}Sn was determined from the balance between feeding and de-exciting γ rays to each level. The intensities of the γ rays were obtained from the measured HPGe singles with neither coincidence nor condition on the time from the impact of protons on target. Theoretical internal conversion coefficients have been taken from [KBT$^+$08] if required. The β feeding to the states should be understood as upper limits and the logft values as lower limits due to possible missing transitions.

Table 5.1: List of γ rays observed in the β decay of ^{132}In to ^{132}Sn, including transition energies and intensities. The initial and final levels for each connecting transition are also given.

E_i(keV)	J_i^Π	E_f(keV)	J_f^Π	E_γ (keV)	I_γ^a (%)
4041.6(3)	2^+	0	0^+	4041.6(3)	100(11)
4351.6(3)	3^-	0	0^+	4351.5(3)	43(5)
		4041.6(3)	2^+	310.5(3)	4.2(3)
4416.6(3)	4^+	0	0^+	4416.7(3)	16(2)
		4041.6(3)	2^+	374.9(3)	100
		4351.6(3)	3^-	64.4(3)	1.29(9)
4715.9(4)	6^+	4416.6(3)	4^+	299.3(3)	82(6)
4830.5(4)	4^-	4351.6(3)	3^-	478.9(3)	45(3)
		4416.6(3)	4^+	414.5(3)	0.79(6)
4848.3(5)	8^+	4715.9(4)	6^+	132.4(3)	26(2)
4885.7(5)	5^+	4416.6(3)	4^+	469.1(5)	2.5(2)
		4715.9(4)	6^+	169.5(4)	0.12(5)^b
4918.8(5)	7^+	4715.9(4)	6^+	202.9(3)	8.0(6)
		4848.3(5)	8^+	70.9(4)	1.2(2)^b
4942.4(4)	5^-	4351.6(3)	3^-	590.4(3)	1.07(8)
		4416.6(3)	4^+	525.9(3)	33(2)
		4715.9(4)	6^+	226.5(3)	0.67(5)
		4830.5(4)	4^-	111.3(3)	2.8(2)

4949.0(5)	(3^-)	4830.5(4)	4^-	117.9(5)	0.012(4)[b]
		4351.6(3)	3^-	597.4(6)	0.11(3)[b]
		4041.6(3)	2^+	908.2(4)	0.016(6)[b]
5280.0(6))	(9^+)	4848.3(5)	8^+	431.8(4)	0.63(6)[b]
5387.3(3)	(4^-)	4351.6(3)	3^-	1036.0(3)	1.29(11)
		4830.5(4)	4^-	557.1(4)	0.13(2)
		4942.4(4)	5^-	444.6(4)	0.23(3)
		4949.0(5)	(3^-)	437.2(4)	0.23(2)
5398.9(5)	(6^+)	4715.9(4)	6^+	683.0(3)	3.9(3)
5446.4(5)	(4^+)	4416.6(3)	4^+	1029.8(4)	0.26(3)
5478.4(6)	(8^+)	4848.3(5)	8^+	630.2(3)	4.6(3)
5628.9(3)	(7^+)	4715.9(4)	6^+	913.1(3)	12.2(10)
		4848.3(5)	8^+	780.6(3)	5.0(4)
		4918.8(5)	7^+	710.1(3)	2.0(2)
		5398.9(5)	(6^+)	229.8(3)	0.65(5)
		5478.4(6)	(8^+)	150.3(3)	0.29(3)[b]
5697.7(3)	(5^+)	4416.6(3)	4^+	1280.7(3)	0.134(13)
		4715.9(4)	6^+	982.2(5)	0.08(2)[b]
		4885.7(5)	5^+	812.4(6)	0.05(2)[b]
5753.9(4)	(6^+)	4715.9(4)	6^+	1038.2(3)	1.8(2)
		5398.9(5)	(6^+)	354.3(3)	0.58(4)
5766.3(3)	(5^+)	4416.6(3)	4^+	1349.6(3)	0.27(2)
		4715.9(4)	6^+	1050.3(4)	0.122(10)
		4885.7(5)	5^+	881.7(3)	0.114(14)
		4942.4(4)	5^-	823.2(7)	0.068(5)
6008.2(4)	(7^+)	4715.9(4)	6^+	1292.2(5)	0.042(7)[b]
		4848.3(5)	8^+	1160.1(3)	0.163(13)
		4918.8(5)	7^+	1089.1(4)	0.15(2)
		5398.9(5)	(6^+)	609.4(4)	0.37(5)
6235.5(3)	(7^+)	4715.9(4)	6^+	1519.6(3)	0.54(5)[b]
		4918.8(5)	7^+	1317.1(3)	0.31(3)
		5398.9(5)	(6^+)	836.3(4)	0.64(6)
		5753.9(4)	(6^+)	481.8(3)	0.53(6)
6296.6(5)	(5^-)	4830.5(4)	4^-	1466.1(3)	0.120(15)[b]
6434.2(3)	(5^+)	4715.9(4)	6^+	1718.3(4)	0.091(10)
		4885.7(5)	5^+	1548.5(4)	0.14(2)
		5446.4(5)	(4^+)	987.7(3)	0.14(4)[b]
6476.3(4)	(5^-)	4830.5(4)	4^-	1645.6(3)	0.40(7)
		4942.4(4)	5^-	1534.8(5)	0.085(9)
6492.8(3)	$(6,7^+)$	5398.9(5)	(6^+)	1093.9(3)	0.73(5)
6526.2(5)	$(6\text{-}8^+)$	5628.9(3)	(7^+)	897.3(3)	0.32(4)

6598.5(5)	(6^-)	4942.4(4)	5^-	1656.1(3)	4.0(3)
		5398.9(5)	(6^+)	1199.6(5)	0.036(10)[b]
6630.6(4)	(6^+)	4715.9(4)	6^+	1914.6(3)	2.5(2)
		4885.7(5)	5^+	1745.1(5)	0.23(5)
		4918.8(5)	7^+	1711.6(3)	0.24(2)
		5398.9(5)	(6^+)	1231.9(4)	0.27(3)[b]
6709.7(4)	(6^-)	4918.8(5)	7^+	1791.0(3)	0.42(4)
		4942.4(4)	5^-	1767.2(3)	3.2(3)[b]
6733.4(4)	(5^+)	4416.6(3)	4^+	2317.1(4)	0.098(10)
		4885.7(5)	5^+	1847.5(3)	0.12(2)[b]
6895.8(4)	(7^+)	4918.8(5)	7^+	1977.1(3)	0.31(3)
		5398.9(5)	(6^+)	1496.8(3)	0.37(3)
6997.1(3)	(7^+)	4715.9(4)	6^+	2281.0(3)	0.35(3)
		4918.8(5)	7^+	2078.3(3)	0.22(2)
		5478.4(6)	(8^+)	1519.2(5)	0.14(2)[b]
		5628.9(3)	(7^+)	1368.2(5)	0.43(5)[b]
7210.8(3)	6^-	4830.5(4)	4^-	2380.0(3)	38(3)
		4885.7(5)	5^+	2325.5(3)	0.85(6)
		4918.8(5)	7^+	2292.2(3)	1.04(10)
		4942.4(4)	5^-	2268.7(3)	27(2)
		5387.3(3)	(4^-)	1823.2(3)	1.41(10)
		5398.9(5)	(6^+)	1812.6(6)	0.12(1)
		5628.9(3)	(7^+)	1582.1(3)	1.16(9)
		5697.7(3)	(5^+)	1513.8(3)	0.34(3)
		5753.9(4)	(6^+)	1456.9(3)	1.44(11)
		5766.3(3)	(5^+)	1445.1(3)	0.49(4)
		6008.2(4)	(7^+)	1202.4(6)	0.024(7)[b]
		6235.5(3)	(7^+)	975.6(3)	1.4(2)[b]
		6296.6(5)	(5^-)	913.9(4)	0.121(14)[b]
		6434.2(3)	(5^+)	777.4(3)	0.15(2)[b]
		6476.3(4)	(5^-)	733.5(3)	0.38(3)
		6598.5(5)	(6^-)	612.6(3)	0.42(3)
		6709.7(4)	(6^-)	501.8(4)	1.7(4)
		6630.6(4)	(6^+)	580.8(5)	0.09(2)[b]
7244.0(3)	7^-	4715.9(4)	6^+	2527.9(3)	1.47(10)
		4848.3(5)	8^+	2395.4(3)	2.3(2)
		4942.4(4)	5^-	2301.3(3)	2.0(2)
		5398.9(5)	(6^+)	1845.3(3)	0.46(3)
		5478.4(6)	(8^+)	1766.2(3)	3.2(3)[b]
		5753.9(4)	(6^+)	1489.4(4)	0.084(11)
		6235.5(3)	(7^+)	1008.1(5)	0.11(2)
		6492.8(3)	$(6,7^+)$	751.3(3)	0.124(12)

[a] I_γ normalized to 100 units for the $4^+ \rightarrow 2^+$ 375-keV transition.
For intensity per 100 decays of the parent, multiply by 0.56(4).
[b] Intensity from γ-γ coincidences.

5.1.3 β-delayed neutron branches in ^{132}In

The β-delayed one neutron emission of ^{132}In has been confirmed by the observation of γ rays belonging to the excited structure of ^{131}Sn. Two transitions have been identified in this decay, specifically, the 2435.0(3) keV and 4273.6(5) keV with an absolute intensity of 0.11(1)% and 0.04(1)% respectively. The P_n value has been obtained from the analysis of the γ-ray intensities of the β and β-n branches, taking into account the β decay of the ^{132}Sn and ^{131}Sn daughters. For the ^{132}Sn $\rightarrow$ ^{132}Sb decay branch, the intensities of the 5 most intense γ rays were considered, these transition are listed in 5.2. The absolute intensities for those transitions were adopted from [SFW89]. Previous measurements of the ^{131}Sn $\rightarrow$ ^{131}Sb decay [HPRS81] were not able to disentangle the decay of the ^{131}In isomers. Besides, in our analysis we observed that the intensity of the γ rays emitted in this decay mainly originate from the population of levels with high spin (11/2, 13/2, 15/2). This indicates that the ^{132}In isotopes that decay by β-n mostly feed the $11/2^-$ isomer in ^{131}Sn directly, which is strongly favored against the $3/2^+$ g.s. due to the angular momentum difference.

The total intensity from ^{131}Sn $\rightarrow$ ^{131}Sb decay was calculated from the analysis of the γ rays from ^{131}Sb observed in this data set. An absolute intensity of 69(7)% has been estimated for the most intense transition, of 1226 keV. This value was obtained by making two assumptions: firstly that ^{132}In β-n decay mainly populates the $(11/2^-)$ isomer, which is consistent with our observations, and secondly that no direct intensity was lost due to direct population of ^{131}Sn to the ^{131}Sb g.s. This hypothesis is to be expected given the large spin difference ($11/2^- \rightarrow 7/2^+$ transition). The 7% uncertainty in the value takes into account these assumptions.

Finally, the number of decays calculated for each tin isotope was corrected to account for the movement of the tape at the end of each super-cycle. The correction factor was estimated taking into account the proton pulse pattern and the different half-lives of each isotope.for dead time effects. This calculation yielded that only the 36% of the ^{132}Sn decays and the 29% of ^{131m1}Sn decays can be measured due to the movement of the tape. From this analysis a P_n=12(2)% value was found for the ^{132}In β-n decay,

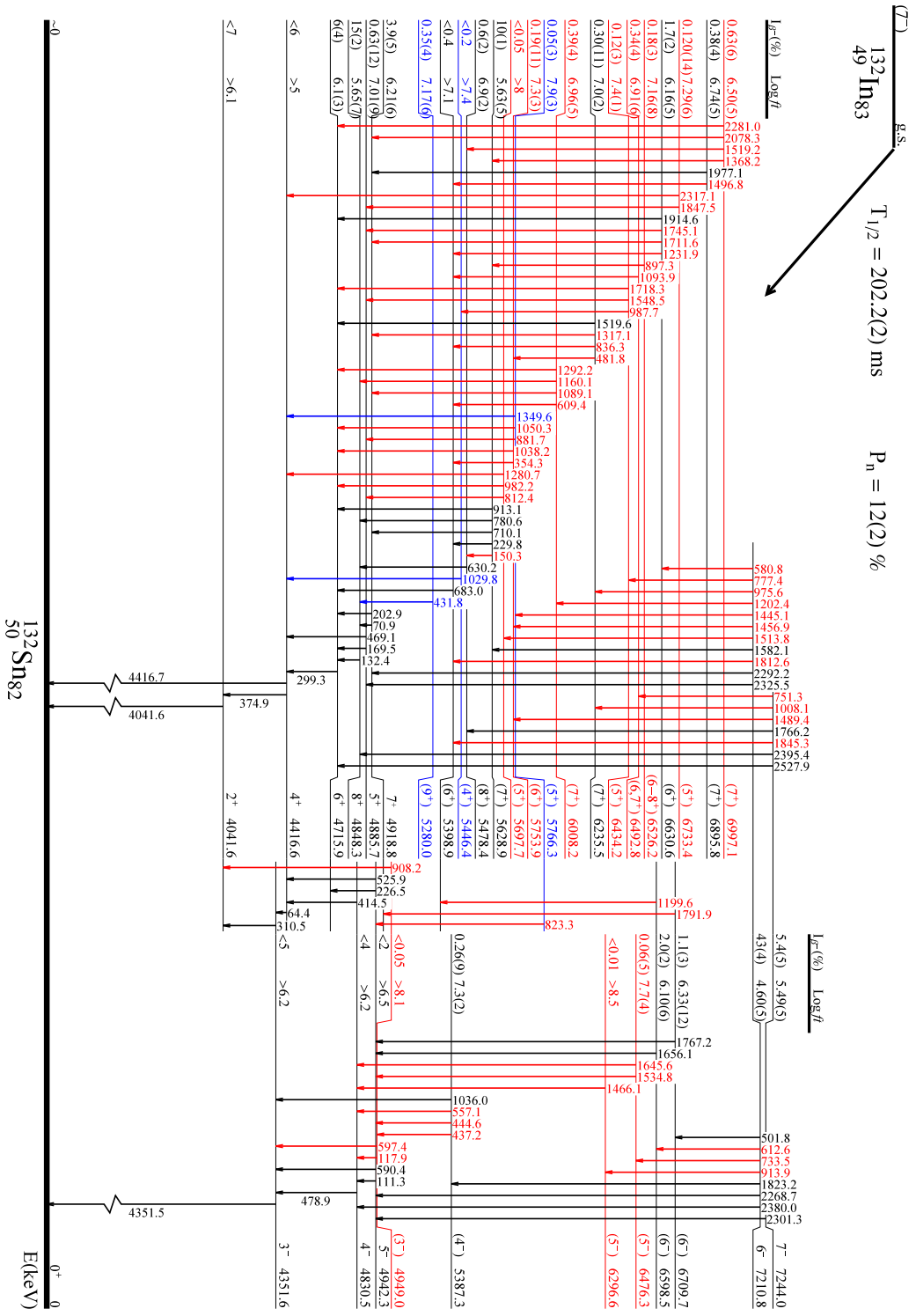

Figure 5.8: Level scheme of ^{132}Sn observed following the β decay of ^{132}In. Levels and transitions previously observed in this decay are colored in black, while those observed for the first time are highlighted in red. Levels previously-known from ^{248}Cm fission or from ^{133}In β-n decay and observed here in the β-decay of ^{132}In are colored in blue.

Table 5.2: Absolute γ-ray intensities for the decay of the ^{132}Sn g.s. and the ^{131m1}Sn ($11/2^-$) β-decaying isomer. The intensities for the decay of ^{132}Sn are taken from [SFW89], while the intensities in ^{131m1}Sn decay are deduced from our experiment.

^{132}Sn 0^+ β-decay		^{131m1}Sn ($11/2^-$) β-decay (This work)	
E_γ	I_γ(%)	E_γ	I_γ(%)
85	48(2)	1226	69(7)
247	42(2)	1230	17(2)
3407	49.0(12)	450	51(7)
899	45(3)	584	5.1(7)
993	37(2)	1932	6.0(8)

which is notably higher than the 6.8(14)% in [LHA$^+$80] but in good agreement with the 10.7(33)% from [RAS93].

Given the two-neutron separation energy in the ^{132}Sn $S_{2n}(^{132}\text{Sn})$=12557.0(27) keV [WAK$^+$17], there is a 1583 keV energy window, within $Q_\beta(^{132}\text{In})$, that makes the decay via a β-delayed two neutron branch possible. We have searched for γ rays belonging to the $A = 130$ mass chain. Nevertheless, no evidence has been found that would point to the existence of a β-2n decay branch in ^{132}In. This is consistent with expectations, since the only levels in ^{130}Sn that could be populated are the 0^+ g.s. and 2^+ at 1221 keV [Sin01]. Assuming a (7^-) spin-parity assignment for the ^{132}In g.s. [JGG$^+$16], this decay will be highly suppressed.

5.2 β-delayed neutron decay of ^{133}In

The large Q_β=13.4(2) MeV value along with the low neutron separation energy in ^{133}Sn, S_n=2.399(3) MeV [WAK$^+$17], favor the ^{133}In decay via β-delayed neutron emission to ^{132}Sn. The lower spin of the ^{133}In ($9/2^+$) ground state and ($1/2^-$) isomer, in comparison with ^{132}In (7^-), is expected to favor the population of low spin p-h excited states that are not fed in the β decay of ^{132}In due to the large spin of the parent (7^-). In the following section, we discuss on results of the β-n decay of ^{133}In to ^{132}Sn, tackle excited states in ^{132}Sn and report new transitions following the β-n decay branch of ^{133}In.

The indium beams for each isomer were separated taking advantage of the isomer selectivity provided by RILIS. However the separation was not complete, and the ^{133m}In

beam contained a contribution of ∼30% of ^{133g}In. The amount of ^{133m}In in the ^{133g}In beam is below 5%.

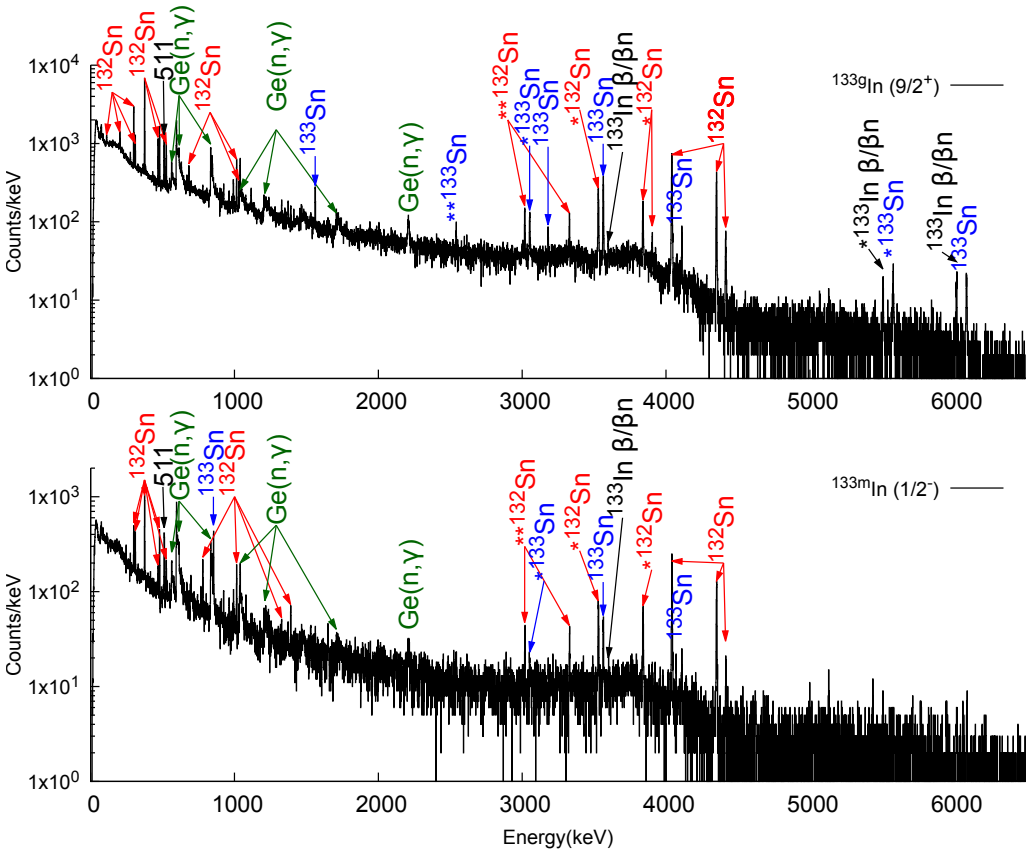

Figure 5.9: β-gated HPGe spectra measured following the β-decay of ^{133g}In (Top) and ^{133m}In (Bottom). Both spectra were generated with the γ-rays measured within the 50-550 ms after the arrival of the proton pulse. The long-lived activity from the background was removed by subtracting the spectra measured within the 700 to 1200 ms window. Mostly all the γ-rays can be related to transitions from either ^{133}Sn, ^{132}Sn and background induced by β-delayed neutrons from ^{133}In β-n decay in the HPGe detectors.

5.2.1 Feeding of excited states in ^{132}Sn

In Figure 5.9, two β-gated γ-ray spectra measured during ^{133}In decay are shown. They were measured using the narrow band RILIS configuration, to enhance the selective ionization of $9/2^+$ and $1/2^-$ ^{133}In isomers respectively. Gamma rays emitted after

the β decay of ^{133}In can be clearly distinguished from the background by their time distribution following the impact of protons on target. Nevertheless, the decay curve does not allow the separation of the transitions that belong to ^{132}Sn from those of ^{133}Sn, neither from the background induced by β-delayed neutrons from ^{133}In β-n decay.

Table 5.3: List of states in ^{132}Sn following the β-n decay of the ^{133}In $(9/2^+)$ g.s. (>95% pure), labeled ^{133g}In, and the beam with enhanced content of the $(1/2^-)$ isomeric state, with a contamination of ∼30% of ^{133g}In, labeled ^{133m}In.

E_i (keV)	J_i^Π	E_f (keV)	J_f^Π	E_γ (keV)	I^c_{rel} ^{133g}In	I^d_{rel} ^{133m}In
4041.6(3)	2^+	0	0^+	4041.6(3)	100	100
4351.6(3)	3^-	0	0^+	4351.5(3)	54(8)	70(11)
		4041.6(3)	2^+	310.5(3)	7.0(9)	12(2)
4416.6(3)	4^+	0	0^+	4416.7(3)	13(2)	9(2)
		4041.6(3)	2^+	374.9(3)	74(9)	39(6)
		4351.6(3)	3^-	64.4(3)	0.96(11)^b	0.51(7)^b
4715.9(4)	6^+	4416.6(3)	4^+	299.3(3)	31(4)	13(2)
4830.5(4)	4^-	4351.6(3)	3^-	478.9(3)	18(2)	18(2)
		4416.6(3)	4^+	414.5(3)	0.9(5)	0.21(8)^a
4848.3(5)	8^+	4715.9(4)	6^+	132.4(3)	4.0(6)	<2^a
4885.7(5)	5^+	4416.6(3)	4^+	469.1(5)	11.1(14)	7(2)
		4715.9(4)	6^+	169.5(4)	1.5(7)^a	<1.6^a
4918.8(5)	7^+	4715.9(4)	6^+	202.9(3)	5.4(8)	3(2)
		4848.3(5)	8^+	70.9(4)	0.8(1)^b	0.4(2)^b
4942.4(4)	5^-	4351.6(3)	3^-	590.4(3)	0.7(6)^a	0.22(3)^b
		4416.6(3)	4^+	525.9(3)	10.1(14)	6.6(10)
		4715.9(4)	6^+	226.5(3)	0.21(3)^b	0.14(2)^b
		4830.5(4)	4^-	111.3(3)	1.0(3)	0.56(9)^b
4949.0(5)	(3^-)	4830.5(4)	4^-	117.9(5)	1.4(4)	1.0(7)
		4351.6(3)	3^-	597.4(6)	8(2)^a	12(4)^a
		4041.6(3)	2^+	908.2(4)	1.5(3)	<8
4965.3(7)	(3^+)	4416.6(3)	4^+	549.0(4)	1.0(6)	1.9(8)^a
		4351.6(3)	3^-	613.5(5)	3.8(5)	13(5)^a
		4041.6(3)	2^+	923.8(7)	2.4(5)	3.2(12)
5131.2(6)	(2^-)	4351.6(3)	3^-	779.2(4)	2.3(4)	14(3)
		0	0^+	5131.9(8)	1.1(5)	4(3)
5387.3(3)	(4^-)	4351.6(3)	3^-	1036.0(3)	3.9(5)	3.9(12)
		4830.5(4)	4^-	557.1(4)	0.39(6)^b	0.39(13)^b
		4942.4(4)	5^-	444.6(4)	0.71(14)^b	0.7(2)^b
		4949.0(5)	(3^-)	437.2(4)	0.7(2)^b	0.7(2)^b
5398.9(5)	(6^+)	4715.9(4)	6^+	683.0(3)	4.7(7)	2.2(19)

5431.4(7)	(3)	4041.6(3)	2^+	1390.3(14)	2.0(7)	4.8(8)
		4351.6(3)	3^-	1078.9(7)	2.4(8)[a]	4(2)
		4416.6(3)	4^+	1015.4(10)	2.8(7)[a]	1.1(8)[a]
5446.4(5)	(4^+)	4416.6(3)	4^+	1029.8(4)	4.6(6)	2.9(12)
5478.4(6)	(8^+)	4848.3(5)	8^+	630.2(3)	3.2(7)	3.2(13)
5628.9(3)	(7^+)	4715.9(4)	6^+	913.1(3)	1.9(3)	<1[a]
		4848.3(5)	8^+	780.6(3)	0.79(13)[b]	<0.3[b]
		4918.8(5)	7^+	710.1(3)	0.31(5)[b]	<0.2[b]
		5398.9(5)	(6^+)	229.8(3)	0.10(2)[b]	<0.05[b]
		5478.4(6)	(8^+)	150.3(3)	0.047(8)[b]	<0.03[b]
5697.7(3)	(5^+)	4416.6(3)	4^+	1280.7(2)	0.8(3)	2.1(17)[b]
		4715.9(4)	6^+	982.2(3)	0.8(4)	1.3(9)[a]
		4885.7(5)	5^+	812.4(6)	0.5(4)[b]	0.7(7)[b]
5753.9(4)	(6^+)	4715.9(4)	6^+	1038.2(3)	2.0(6)[a]	0.8(7)[a]
		5398.9(5)	(6^+)	354.3(3)	0.6(2)[b]	0.3(2)[b]
5766.2(3)	(5^+)	4416.6(3)	4^+	1349.6(3)	1.4(10)	2.3(15)[a]
		4715.9(4)	6^+	1050.3(4)	0.9(4)[a]	0.46(7)
		4885.7(5)	5^+	881.7(3)	0.9(3)	0.24(6)
		4942.4(4)	5^-	823.2(7)	0.4(2)[b]	0.26(4)[a]
5790.4(6)	(4^+)	4416.6(3)	4^+	1373.9(4)	2.7(3)	3.3(13)[a]
		4351.6(3)	3^-	1438.5(4)	0.8(3)	1.0(6)
6296.6(5)	(5^-)	4830.5(4)	4^-	1466.1(3)	1.9(11)[a]	<0.5[a]
6476.3(4)	(5^-)	4830.5(4)	4^-	1645.6(3)	1.6(10)[a]	<0.5[a]
		4942.4(4)	5^-	1534.8(5)	0.3(2)[b]	<0.1[b]

[a] Intensity obtained from γ-γ coincidences.
[b] Not observed in this decay, intensity calculated from ^{132}In decay data.
[c] Relative γ intensities normalized to 100 units for the 4042-keV transition. For intensity per 100 decays multiply by 0.049(5).
[d] Relative γ intensities normalized to 100 units for the 4042-keV transition. For intensity per 100 decays multiply by 0.043(5).

The identification of new γ rays that belong to ^{132}Sn is based on γ-γ coincidences. It is not expected to find excited levels with excitation energies below 4 MeV, thus γ-rays with lower energies are always a part of a cascade since they cannot directly feed the g.s. The analysis allows to identify several levels and γ rays in ^{132}Sn that are not observed in the ^{132}In decay. Likewise in the analysis of ^{132}In decay, mostly all the new transitions can be observed in coincidence with the γ-rays from low-lying levels. Figure 5.10 contains the γ-γ coincidence spectra got after gating on the 4042-, 375- and 299-keV transitions. The γ-lines identified in those spectra indicate the population of excited levels in ^{132}Sn up to 6.6 MeV. New γ-lines, that were not quoted present at

^{132}In spectra, can be also found.

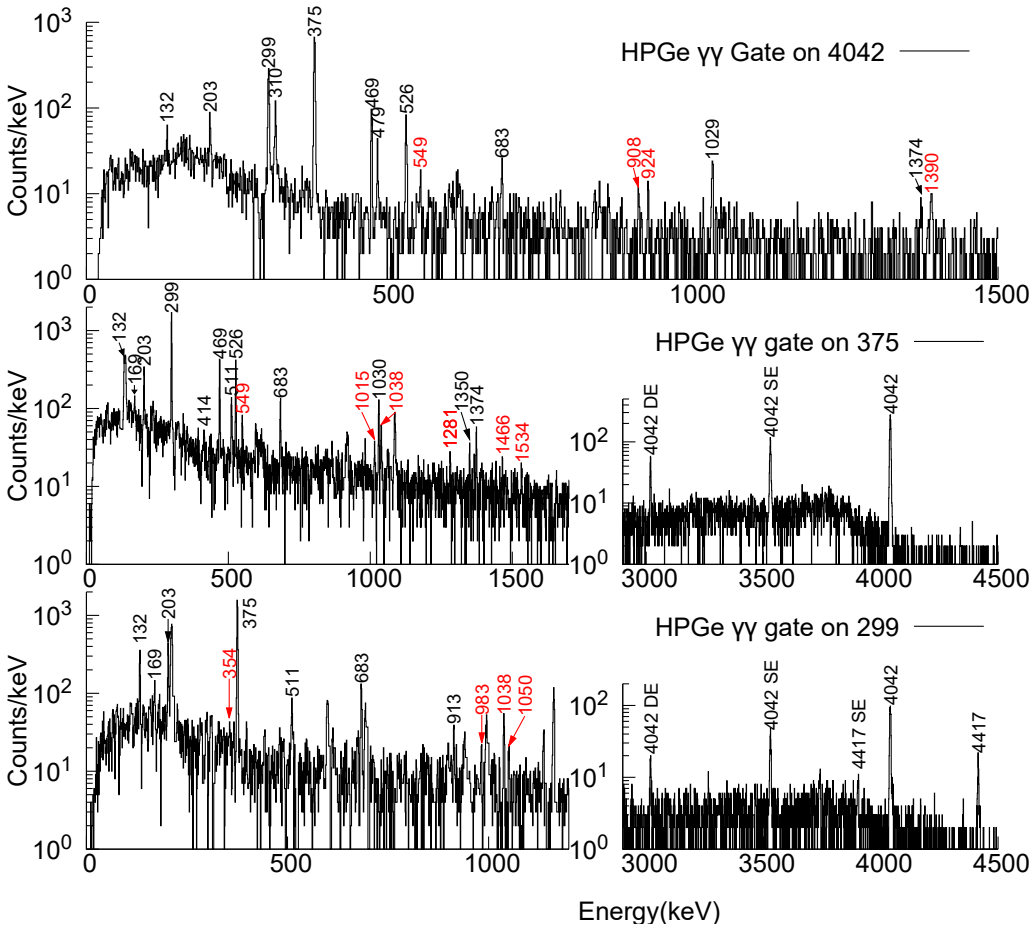

Figure 5.10: γ-γ coincident spectra corresponding to the γ-rays that de-excite the low-lying positive parity levels in ^{132}Sn, populate in the β decay of ^{133}In. (Top) Gated on the 4042-keV transition from the 4042-keV 2^+ level. (Center) Gated on the 375-keV transition from the 4416-keV 4^+ level. (Bottom) Gated on the 299-keV transition from the 4715-keV 6^+ level.

This information is completed by γ-γ analysis for the γ-rays from the low-lying negative parity states, Figure 5.11. New γ-lines that cannot be related to the transitions quoted in the ^{132}In decay can also be identified here. This study leads us to confirm the presence of states at 4965, 5131, 5431 and 5790 keV, that are populated only in the decay of ^{133}In β-decaying states.

The low spin of the states to which they can de-excite suggests a low spin value (2-4) for these levels, which makes them good candidates for the remaining low spin

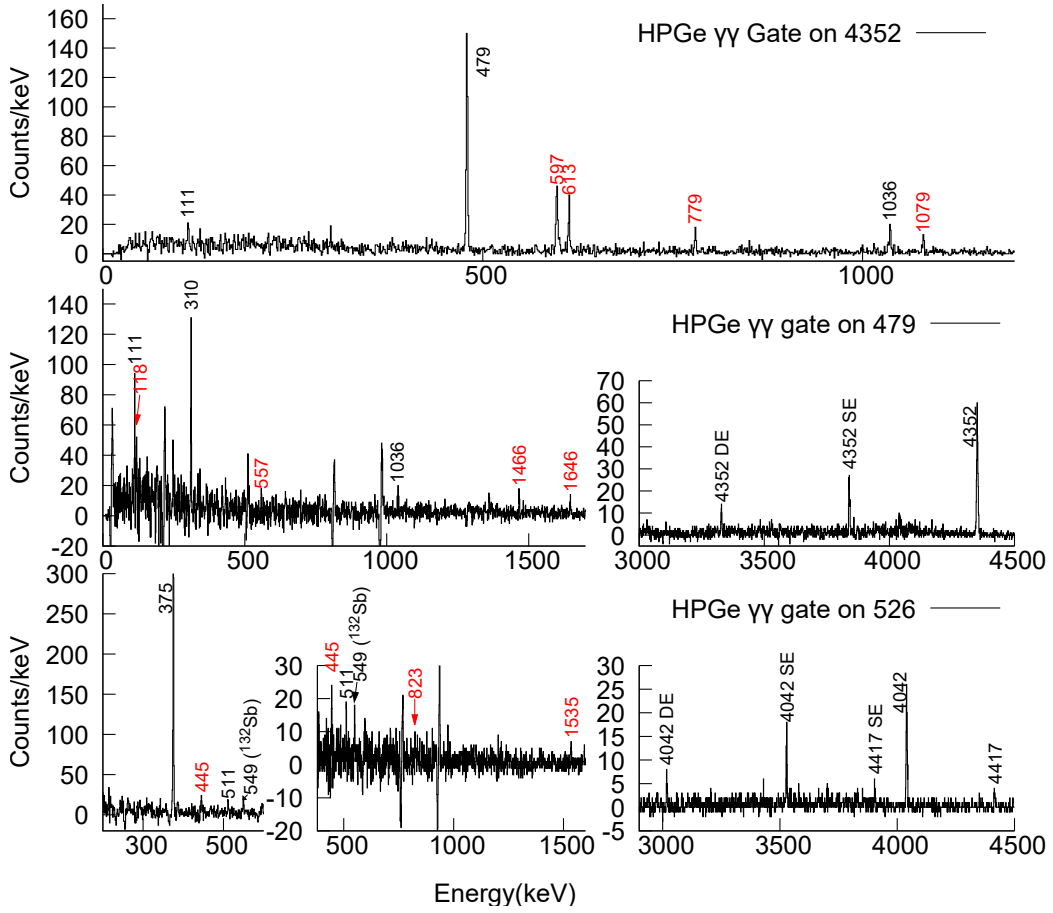

Figure 5.11: γ-γ spectrum observed in the β decay of ^{133}In, gated on the 4352-keV transition in ^{132}Sn. The contribution from Compton events beneath the 4352-keV peak has been subtracted. Newly-observed γ transitions are labeled in red with an asterisk.

particle-hole states expected in this energy range. In Figure 5.12 the β-n decay scheme of ^{133}In to ^{132}Sn is depicted. The direct feeding to each level ($I_{\beta-n}$) is measured by analyzing the γ-ray intensities calculated separately for each isomer.The total feeding has been calculated using the intensities of the γ-rays emitted by the daughters. The observed states in ^{132}Sn following the β-n decay of the ^{133}In $(9/2^+)$ g.s. and $(1/2^-)$ isomeric state are listed in Table 5.3.

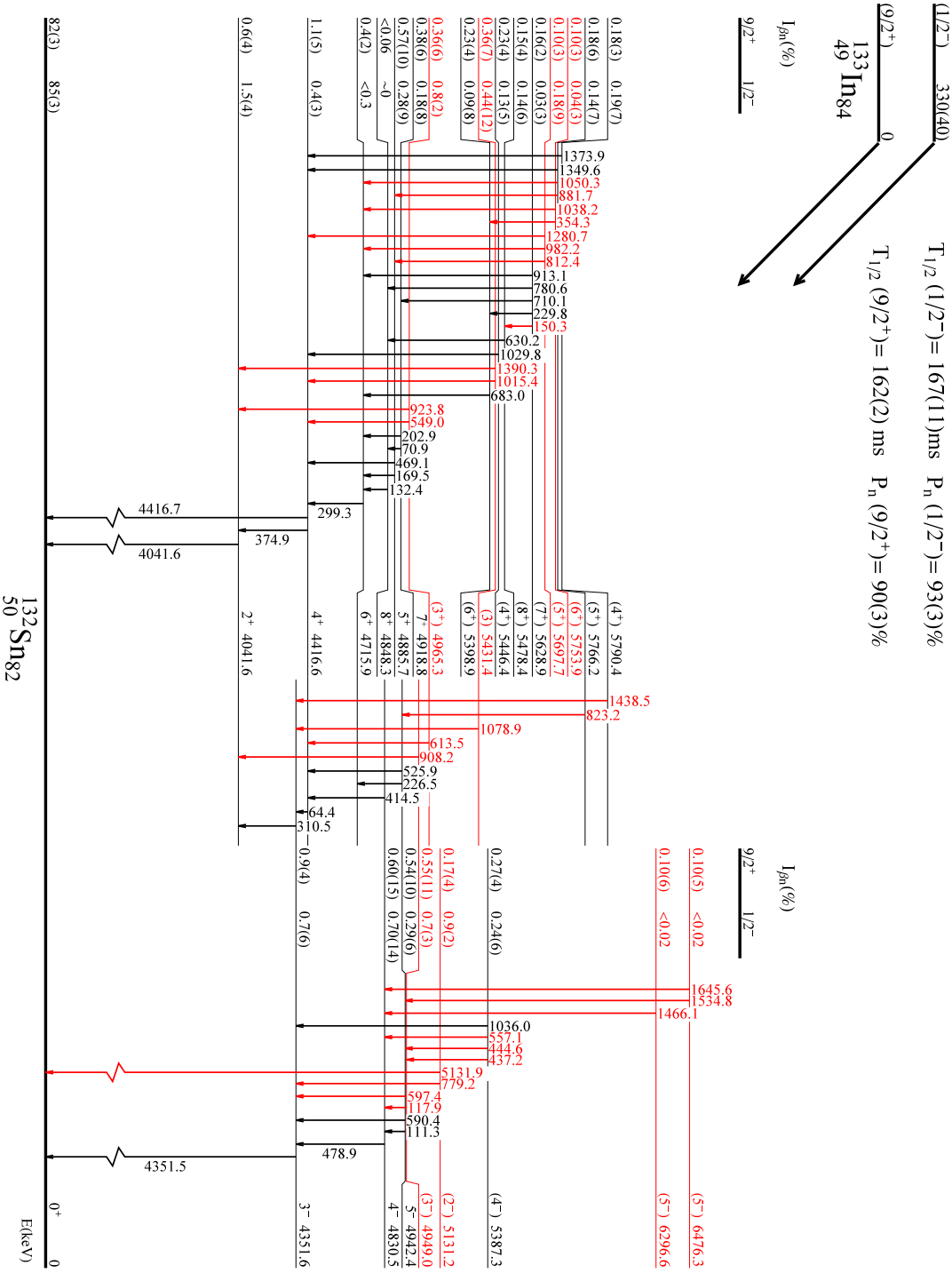

Figure 5.12: Level scheme of ^{132}Sn observed following the β-n decay of the ^{133}In $(9/2^+)$ ground state and $(1/2^-)$ isomer.

5.2.2 High energy γ-rays

Another interesting feature observed in the β-decay of ^{133}In is the presence of several γ rays of energies above 5 MeV, with a time behavior compatible with the decay of ^{133g,m}In.

The high energy γ lines observed in the ^{133g,m}In decays are shown in Figure 5.13. The peaks observed in the spectra differ notably depending on the selected β-decaying indium state. In the decay of the ^{133g}In $(9/2^+)$ g.s. there are two predominant γ-rays. The 6089-keV is thought to belong to ^{133}Sn, see Chapter 7 or [PKF$^+$19]. Another one appears at 6019 keV. Although it has the same energy as a transition in ^{57}Fe produced by a neutron reaction background as discussed in [PKF$^+$19, BFK$^+$20] its intensity is only a small fraction of the total γ-ray intensity from the excited 7647-keV level in ^{57}Fe, while the other, more intense transitions, are not observed. Therefore the 6019-keV transition is likely to be emitted following the β-decay of ^{133}In, and predominantly from the $(9/2^+)$ g.s.

The bottom plot of Figure 5.13 shows the β-gated γ-ray spectrum measured for the RILIS $1/2^-$ settings. The intensity of 6088- and 6019-keV transitions are reduced in this spectrum, and they are most likely produced by the ^{133g}In contaminant in the beam.

In the decay of the ^{133m}In $(1/2^-)$, the 6088- and 6019-keV transitions are suppressed, but several other peaks, which are absent in the decay of the ^{133g}In, can be identified. They appear at the energies of 5440, 5712, 5770, 5952, and 6067 keV. Two more tentative peaks, at the detection limit of the HPGe detectors, are seen at 6220 and 6463 keV. Some of these γ lines may be compatible with escape peaks from other γ rays (for instance single and double escape peaks from the 6463 keV γ-ray), but it is not possible to make a consistent identification for all of the energies. It is interesting to observe transitions having this energy from the decay of the $(1/2^-)$ isomer, as there are unidentified members of particle-hole multiplets in ^{132}Sn, such as $\nu p_{3/2}d^{-1}_{3/2}$, $\pi g_{7/2}g^{-1}_{9/2}$ and $\nu p_{3/2}s^{-1}_{1/2}$, that can give rise to low spin levels. It is very unlikely to populate them in the decay of ^{132}In with (7^-). However, the feeding of such levels would be strongly favored in the β-n decay of the $(1/2^-)$ state in ^{133m}In. All of this points towards these transitions likely originating from the de-excitation of such p-h multiplet states.

It is worth mentioning that a 5131-keV peak can be seen in both the ^{133g}In and ^{133m}In decays. This γ ray has been firmly identified to belong to ^{132}Sn since its energy

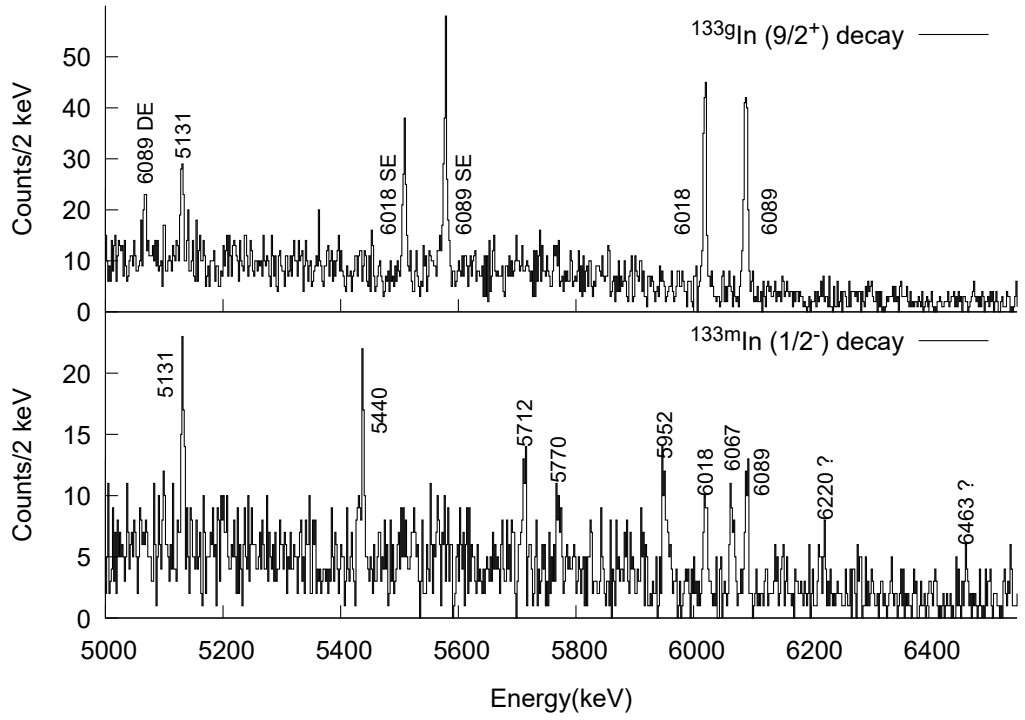

Figure 5.13: Beta-gated γ-ray spectra from the β decay of ^{133}In isomers highlighting the energy range above 5 MeV. Only the events recorded in the time window from 10 to 600 ms since the arrival of the proton pulse are used.

perfectly matches the de-excitation of the new 5131-keV level proposed in this work. In addition, the existence of a transition to the 0^+ g.s. supports the tentative assignment of this level to the 2^- state of the $\nu f_{7/2}d_{3/2}^{-1}$ multiplet.

For the sake of completeness, the γ-rays observed in the ^{133}In decay that have not been assigned to any decay branch are listed in Table 5.4.

5.2.3 β-delayed neutron emission from ^{133}In

We have used the same procedure described in section 5.1.3 for ^{132}In to determine the β-delayed neutron emission probabilities from the ^{133}In $(9/2^+)$ ground state and $(1/2^-)$ isomer. The most intense γ rays have been considered in the analysis. For the ^{133}Sn $\rightarrow$ ^{133}Sb decay, the absolute intensity of 12(2)% for the 962-keV transition was adopted from [BKF83], while for the ^{132}Sn $\rightarrow$ ^{132}Sb we used the same transitions ans intensities employed in ^{132}In decay, summarized in Table 5.2. The relative decay

Table 5.4: Gamma rays observed in the ^{133}In decay that could not been assigned to any specific decay branch. Intensities are given relative to the 4042-keV in ^{132}Sn γ-ray intensity. The label ^{133g}In refers to the ^{133}In $(9/2^+)$ g.s., with an estimated purity above 95%, while the label ^{133m}In is used for the beam with enhanced content of the $(1/2^-)$ isomeric state, with a contamination of $\sim$30% of ^{133g}In.

E_γ (keV)	I^a_{rel} ^{133g}In $(9/2^+)$	I^b_{rel} ^{133m}In $(1/2^-)$
1116(2)	2.5(4)	4.6(8)
1529.7(7)	-	2.6(7)
1649.9(4)	-	7(1)
4110.8(3)	8(1)	8(2)
5439.6(4)[d]	-	4(2)
5711.6(9)[e]	-	3.7(12)[c]
5770(1)	-	3.8(12)[c]
5952.5(6)[d]	-	6(2)[c]
6018(2)	4.7(9)	6(2)[c]
6067(2)	-	3.9(13)[c]
6220(2)	-	2.6(10)[c]
6463(3)	-	2.0(9)[c]

[a]For I_{abs} multiply by 0.049(5).
[b]For I_{abs} multiply by 0.043(5).
[c]Intensity obtained from β-gated spectrum.
[d]Energy compatible with the escape peaks from the tentative 6463-keV γ-ray.
[e]Energy compatible with the single escape peak from the tentative 6220-keV γ-ray.

activity of the tin daughter nuclei was corrected for the tape movement. In particular, the supercycle structure of the proton beam has to be considered for the evaluation of the unobserved activity. Our analysis yields P_n=90(3)% for the decay of the ^{133}In $9/2^+$ g.s., and P_n=93(3)% for the decay of the $(1/2^-)$ isomer. The re-evaluated results are in agreement with the P_n=85(10)% value in [HBH$^+$96]. Slightly lower values are given in [PKF$^+$19] where the proton pulse correction of the tape movement have not been fully implemented.

5.3 Lifetime measurements

Lifetimes of excited levels in ^{132}Sn have been investigated by means of fast-timing methods, see Chapter 4, using the time differences between the fast β and $LaBr_3(Ce)$ detectors. A coincidence condition on the HPGe detectors is applied. The HPGe detectors do not participate in the timing information, but are essential in this complex level scheme due to their energy resolution to obtain the required γ-ray selectivity. The use of two different $LaBr_3(Ce)$ detectors gives us the possibility to obtain two independent measurements for the same lifetime, one per β-$LaBr_3(Ce)$ combination. In addition, $\gamma\gamma(t)$ time differences between the two $LaBr_3(Ce)$ detectors are used when possible. Figure 5.14 shows the β-gated energy spectra measured in the HPGe and $LaBr_3(Ce)$ detectors for the decay of ^{132}In. Due to the large number of γ-ray peaks at overlapping energies observed in this decay it is necessary the use of triple $\beta\gamma\gamma(t)$ events to obtain the required selectivity.

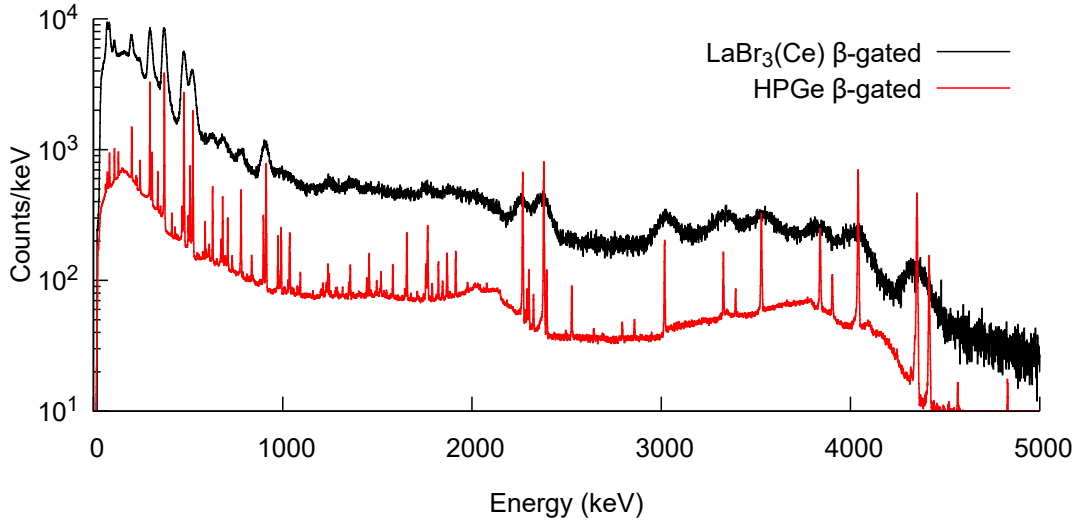

Figure 5.14: Beta-gated $LaBr_3(Ce)$ and HPGe energy spectra observed in the β-decay of ^{132}In. A large number of the γ-rays can be observed in the HPGe β-gated spectrum (red). Therefore, the use of triple $\beta\gamma\gamma(t)$ events is required to obtain the selectivity in $LaBr_3(Ce)$ detectors required for lifetime measurements.

5.3.1 Choice of a prompt-reference for ^{132}In decay.

To measure half-lives of states using the centroid shift method, the choice of a reliable prompt γ-ray to be used as reference is required. For the case of ^{132}Sn the most suitable γ-rays are those emitted by the 7210-keV level, for which a lifetime below the ps range is expected. This level is intensely populated, receiving $\sim$42% of the total feeding, and it has a large number of de-exciting γ-rays. However, only the 2269-keV and 2380-keV de-exciting γ-rays have sufficient statistics, to precisely determine the centroid position of their $\beta\gamma$(t) time-delayed distributions.

The time distributions from the 2269 and 2380 keV transitions have been obtained using triple $\beta\gamma\gamma$(t) coincidences. In Figure 5.15 there are depicted the energy spectra measured in one $LaBr_3$(Ce) detectors after selecting another γ-ray in the HPGe detectors. Both 2268 and 2380 γ-rays can be selected in coincidence with three different γ-rays each. For each spectrum the colored regions indicate the selected energy gates set in the $LaBr_3$(Ce) to produce the time spectra from the peak, as well as to estimate the contribution from the Compton background in lanthanum detectors.

In the bottom part of Figure 5.15 the time-delayed spectra derived after applying all the different gates and corrections described in Figure 5.15 are plotted. Thus, the lifetime of the levels measured by the centroid-shift method are obtained by measuring the shift from the curve to the centroid position after subtracting this offset derived from the 2268 and 2380 keV prompt γ-rays. The offset is obtained for the 2 γ-rays by minimizing the shift to the FEP curve, see Figure 5.16. The error bars from the prompt centroid have been added to the uncertainty of the FEP walk curve, and they are also included in the uncertainty of the lifetimes measured by centroid shift from of ^{132}Sn. This analysis has been extended to the four $LaBr_3$(Ce) and data-set combinations, deriving a different offset for each case.

5.3.2 Half-lives in the $\nu f_{7/2}h^{-1}_{11/2}$ particle hole multiplet

5.3.2.1 Lifetime of the 4416-keV 4^+state

The 4416-keV 4^+ level does not have a noticeable direct feeding in the ^{132}In decay, being populated in its totality by γ rays from higher-lying levels. It de-excites mainly by the 375-keV γ-ray, which carries $\sim$85% of the total intensity. The two strongest transitions that feed this state are the 299-keV and 526-keV γ-rays.

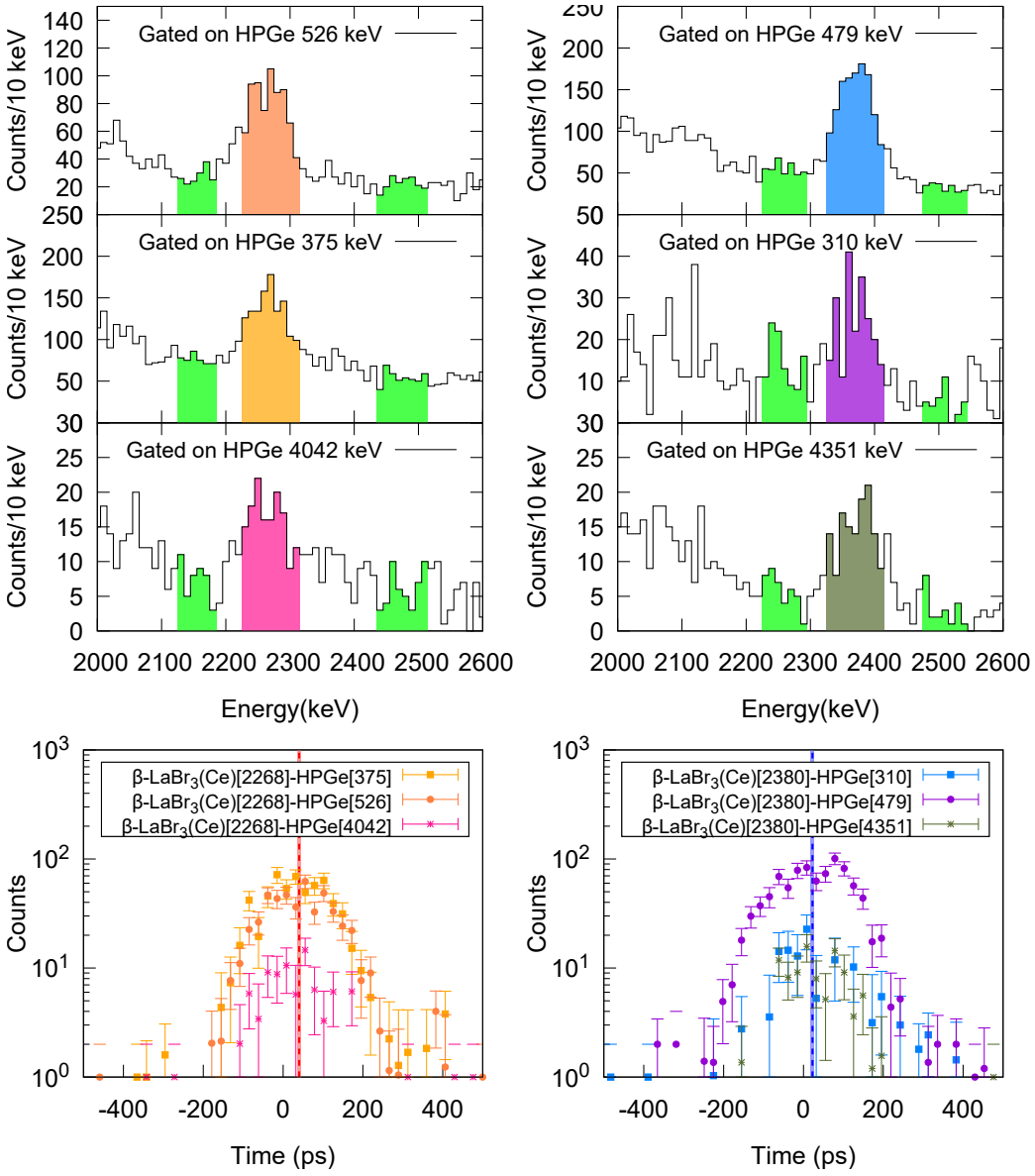

Figure 5.15: HPGe gated $LaBr_3$(Ce) Energy spectra for 2268 keV and 2380 keV prompt γ. The energy spectra are built by gating on the designed peak on the HPGe detector, and subtracting the contributions from the Compton background. The coloured areas mark the selected gates in the $LaBr_3$(Ce) to generate the time distribution of the peaks, the green areas indicates the selected region from the $LaBr_3$(Ce) background for the estimation of the Compton background contribution, (Bottom) $\beta\gamma\gamma$(t) Time delay spectra for the 2269 and 2380 prompt γ-rays. All the contributions coming from the various background have been subtracted. The final centroid position is adopted from the weighted average of the centroid position corresponding to each HPGe gate.

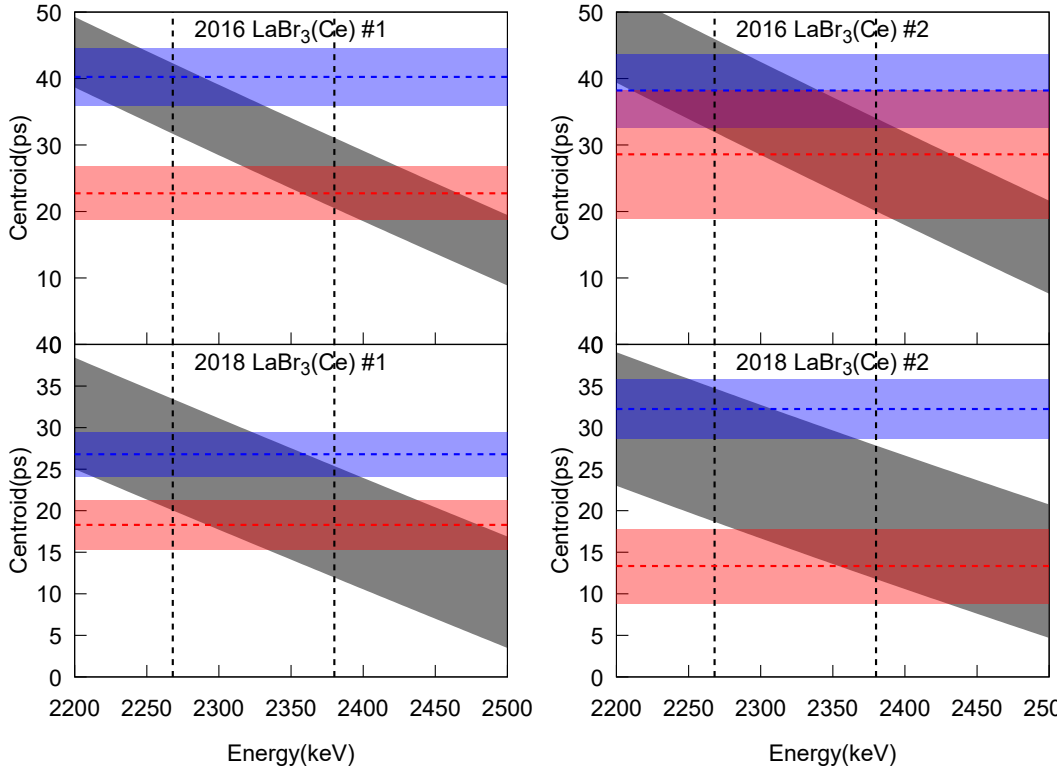

Figure 5.16: Centroid position of prompt γ-rays vs the FEP walk curve measured for each data set and $LaBr_3$(Ce) pair. The offset in the time distribution is obtained by simultaneously minimizing the difference between both centroid positions and the FEP walk curve.

This lifetime can either be measured by the $\gamma\gamma$(t) and $\beta\gamma$(t) time-delayed coincidence method, depending on the combination of γ-rays considered in the analysis.

To measure the 4416-keV 4^+ level half-life using $\beta\gamma\gamma$(t) events a time distribution was generated by selecting the 526- and 375-keV transitions in the HPGe and $LaBr_3$(Ce) detectors respectively. This combination of γ rays allows us to select cleanly the 375−keV peak in the $LaBr_3$(Ce) detectors, and at the same time avoid the contribution of long lifetimes from higher-lying levels. In Figure 5.17 the spectrum obtained in one of the $LaBr_3$(ce) detectors after gating on the HPGe detectors is show. The contribution of Compton backgrounds have been corrected using the methodologies described in Section 4.4 from Chapter 4. The colored regions indicates the energy gates used in the analysis.

The time distributions derived for each of the four $LaBr_3$(Ce) detectors and dataset

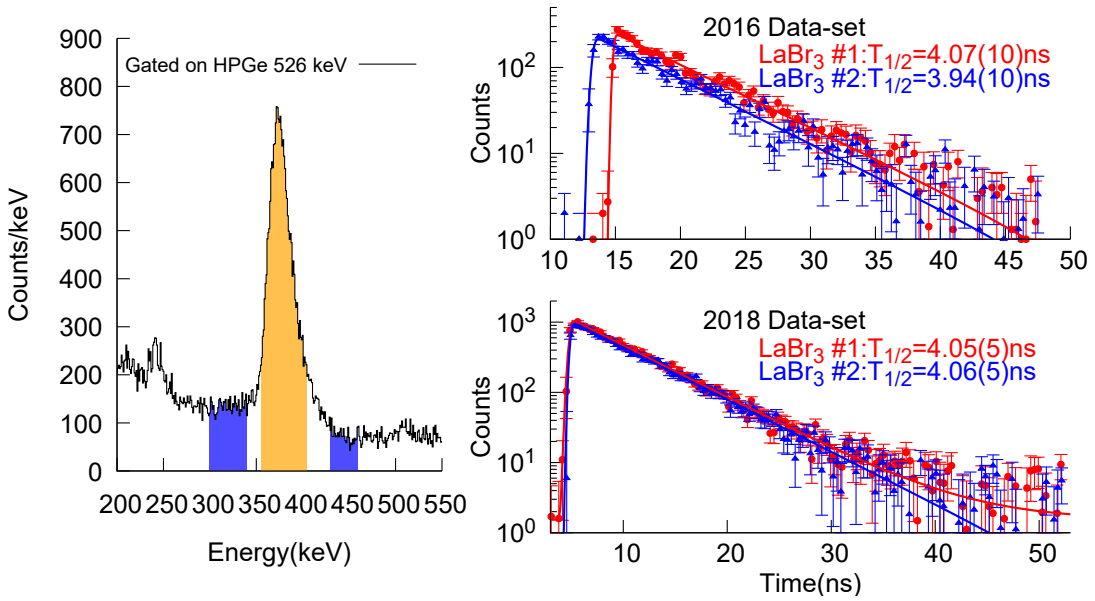

Figure 5.17: **$\beta\gamma\gamma$(t) half-life analysis of the 4416-keV level.** (Right) β-gated $LaBr_3$(Ce) energy spectrum in coincidence with the 526-keV transition on the HPGe detectors. (Right) Time-delayed distributions for the β-HPGe[526]-$LaBr_3$[375].

combination are drawn in the right-hand side of Figure 5.17. The gate on the 526-keV transition ensure that the time distribution is free from the contributions of lonf-lifetimes from higher lying states. Each time distibution was fitted separately to an exponential decay function convoluted with a Gaussian function plus a constant background to account for the random background.

This lifetime can also be derived form the analysis of $\gamma\gamma$(t) events, by analyzing the time distributions of the 299-375-keV coincident peak between the two $LaBr_3$(Ce) detectors. By using this combination of γ-rays the influence of other lifetimes is removed. In Figure 5.18 (Left) the $LaBr_3$(Ce)-$LaBr_3$(Ce) coincidence energy matrix is shown, along with the energy gates selected for the analysis of the peak and background contributions. Here no extra gate in the HPGe energies is needed thanks to the good peak to background ratio. To reduce the background from the daughters decays, only the events measured in a time window from 50 to 800 ms after the proton pulse were selected for this analysis. The resulting time delay distributions are depicted in the right-hand side of Figure 5.18. The lifetime is measured from the fitting of time-difference distributions with the direct and reversed energy selection on the $LaBr_3$(Ce) detectors, giving two

independent measurements for each of the two data sets.

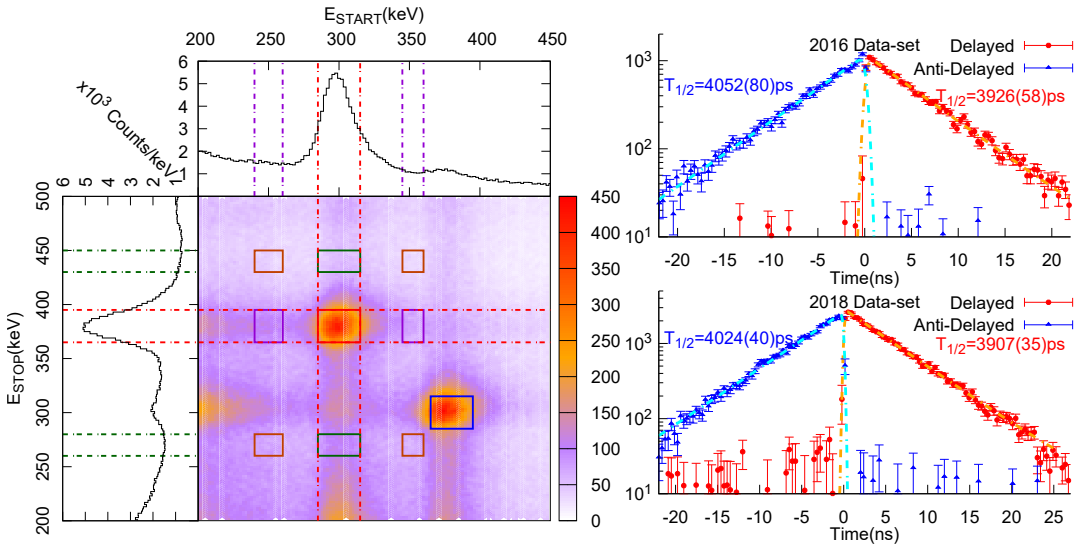

Figure 5.18: Time delayed $\gamma\gamma$(t) analysis of the 299-375-keV coincidence. (Left) Coincidence energy matrix measured in the $LaBr_3$(Ce) detectors. The adjacent spectra are the projections of the matrix within the red lines. The delayed and anti-delayed coincidence peak appear enclosed within the red and blue boxes respectively. (Right) Compton-subtracted time distributions of the 299-375 coincidence for both data-sets. from the right show the projections for each axis corresponding to the gates of the delayed peak. See text for details

Table 5.5: Summary of $T_{1/2}$ values derived for the half-life of 4416-keV 4^+ state.

Dataset	Method	$T_{1/2}$(ns)
2016	$\beta\gamma\gamma$(t) $LaBr_3$(Ce)-1	4.07(10)
	$\beta\gamma\gamma$(t) $LaBr_3$(Ce)-2	3.94(10)
	$\gamma\gamma$(t) Delayed	3.93(6)
	$\gamma\gamma$(t) Anti-delayed	4.05(8)
2018	$\beta\gamma\gamma$(t) $LaBr_3$(Ce)-1	4.05(5)
	$\beta\gamma\gamma$(t) $LaBr_3$(Ce)-2	4.06(5)
	$\gamma\gamma$(t) Delayed	3.90(4)
	$\gamma\gamma$(t) Anti-delayed	4.02(4)
Final value	Weighted average	3.99(2)

All the values derived from this analysis are summarized in 5.5. The final value is

obtained from the weighted average from these measurements, yielding a final value of 3.99(2) ns, which is in good agreement with the 3.95(13) ns reported by Fogelberg *et al.* [FHJ$^+$95].

5.3.2.2 Lifetime of the 4715-keV 6^+ state

The lifetime of the 4715-keV is longer, at the limit of the fast-timing range. The best method to measure it would be from the $\gamma\gamma$(t) delayed coincidence between the 132- and 299-keV γ-rays in the $LaBr_3$(Ce) detectors. Unfortunately the TAC range is too short, and the value obtained is too unreliable. On the other hand, this half-life is below the time resolution limit of a HPGe detector, so it cannot be measured from either the fit of the β-HPGe(t) time-delayed events. The only viable alternative for obtaining this half-life is via $\beta\gamma\gamma$(t) with the $LaBr_3$(Ce) detectors, whose time range is almost twice the time window available in for the $\gamma\gamma$(t) events.

In order to build the $\beta\gamma$(t) time delay distribution of the 299-keV, an extra coincidence needs to be set in the HPGe detector to remove the influence of the long lifetime of the 4848-keV level, due to the feeding by the 132-keV transition. The best candidate to do so is by gating at the 913-keV transition since this combination provides the highest amount of statistics. In Figure 5.19 the energy spectra measured in one of the $LaBr_3$(Ce) detectors, in coincidence with the 913-keV peak is shown. The gates set in the $LaBr_3$(Ce) energy are also depicted.

The time distribution for each pair of $LaBr_3$(Ce) detectors and data sets are drawn in Figure 5.19. They were obtained after selecting the HPGe[913]-$LaBr_3$(Ce)[299] events, and correcting for the contribution of the Compton background. The four time distributions show a very long exponential tail. The limited time range is insufficient to observe the full decay of the 4715-keV level, nevertheless there is still enough time for about two half-lives. The time spectra have been fitted separately to an exponential decay function. Due to the limited range, the accuracy of the fit is reduced. Nonetheless the uncertainty of the 4 values is lower than 5%, being all of them compatible to each other. For the final value we adopted the weighted average of the four measurements, which yielded a $T_{1/2}$=21.3(5) ns half-life. This new measurement is in agreement within two σ with the 20.1(5) ns value reported by Fogelberg *et al.* [FHJ$^+$94].

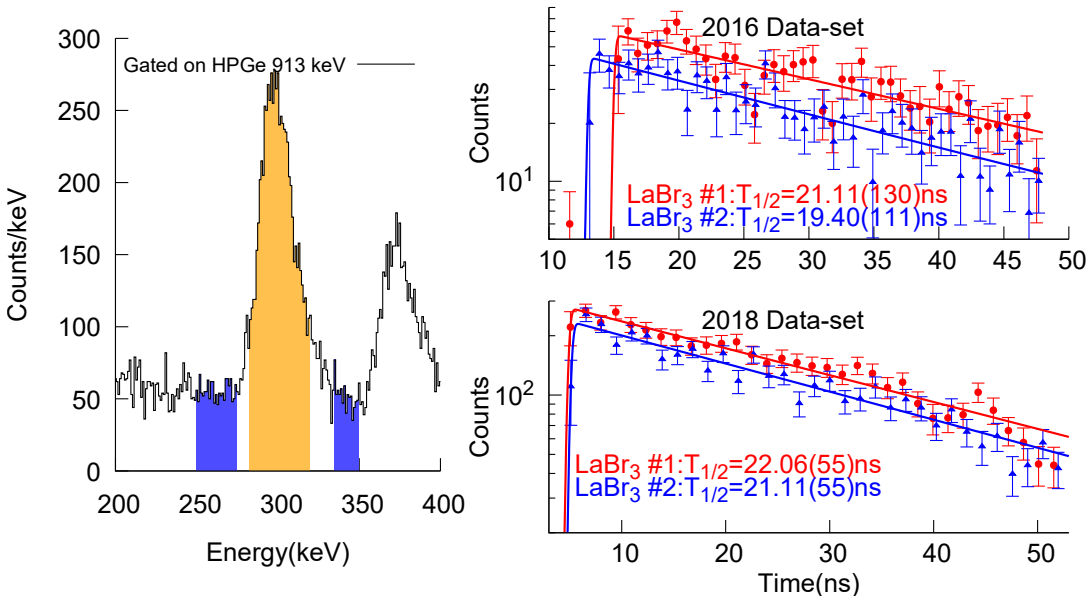

Figure 5.19: $\beta\gamma\gamma$(t) analysis for the half-life of 4715-keV 6^+ state. A coincidence with the 913-keV peak on the HPGe detectors was required. The contribution of events in coincidence with the background beneath the 913-keV peak have been subtracted. (Left) Energy $LaBr_3$(Ce) spectrum and energy regions for the peak (orange) and background (blue) time distributions.(Right) Derived $\beta\gamma\gamma$(t) time-delay spectra for the 299-keV γ-ray after applying all the corrections for the background. The half-life is estimated from a χ^2 fit of the slope.

5.3.2.3 Lifetime of the 4848-keV 8^+ state

The lifetime of the 4848-keV 8^+ level is too long for the fast-timing range, but it can be investigated using $\beta\gamma$(t) coincidences between the plastic scintillator and the HPGe detectors. Three β-HPGe(t) time differences spectra were obtained by selecting the 132-, 299- and 375-keV γ rays, respectively. The resulting time delay distributions are shown in Figure 5.20. No extra coincidence was required.

The half-life was measured by fitting the delayed slope of the three time spectra in a long time range of $\sim$30 μs. Due to the large coincidence window required, the amount of random coincidences is quite large. The random contribution has been carefully taken into account by analysing the expected random background measured for the prompt 526-keV γ-ray. For the final value, the weighted average of the six values furnished by this analysis was adopted. This yielded a $T_{1/2}$=2.108(14) μs for the 4848-keV 8^+ level

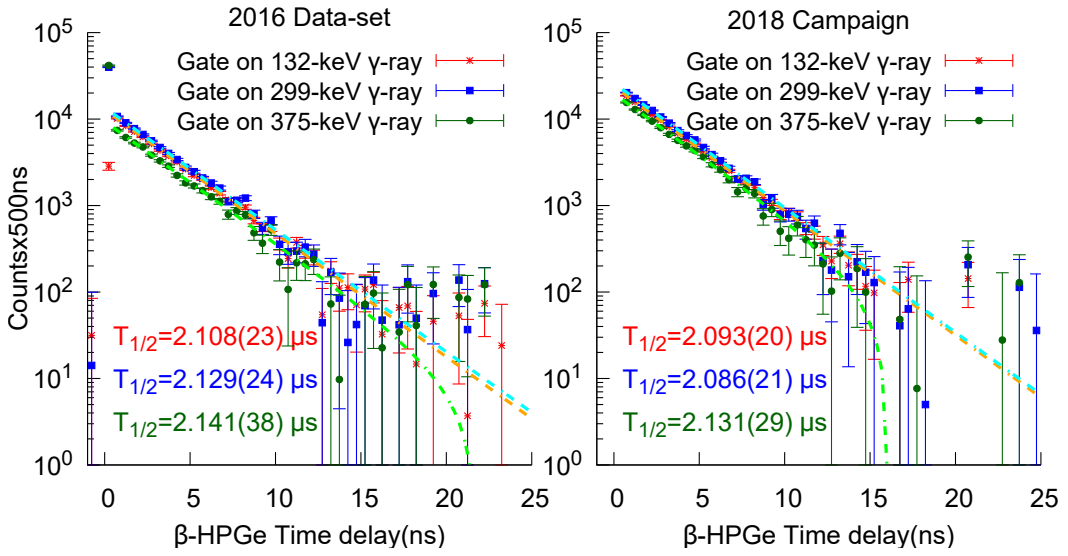

Figure 5.20: .Time delay spectra between the β and each of the HPGe detectors for the 132-keV, 299-keV and 375-keV γ-rays.

in agreement with the value of 2.080(17) μs reported in the latest evaluation [KRSS05].

5.3.2.4 Lifetime of the 4886-keV 5^+ state

For the 4886-keV 5^+ level, it is a quite difficult task to measure its mean-life. Since the level is not strongly populated in the ^{132}In decay, the only combination of γ-rays that provides enough statistics is the HPGe[375]-$LaBr_3$(Ce)[469], but is still not possible a clean selection of the 469-keV γ-ray in the $LaBr_3$(Ce) detector. The energy spectrum measured in one of the $LaBr_3$(Ce) detector in coincidence with the 375-keV peak in the HPGe is depicted in Figure 5.21. The 469-keV peak is weak and overlaps slightly with the 511-keV peak.

The Compton corrected, time distribution of the 469-keV γ-ray is shown on the bottom of Figure 5.22. The centroid shift analysis indicates a short τ=27(14) ps value. This analysis have been extended to the four $LaBr_3$(Ce) and data-set combination, yielding similar values for all cases. The weighted average of the four values give a $T_{1/2}$ = 18(6) ps for the (5^+) level. Nonetheless, given the low peak to background ratio, as well the potential contribution from the 526-keV and 511-keV peaks to the time distribution, this value is not completly reliable. Therefore, we have adopted a more conservative $T_{1/2} < 30$ ps upper limit for the lifetime of the 4885-keV level.

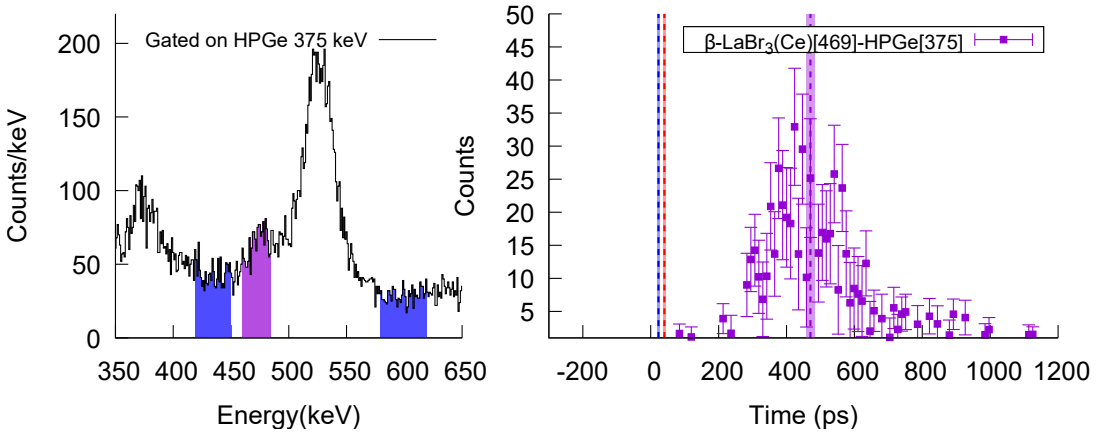

Figure 5.21: Lifetime Analysis of the 4885-keV 5^+ state.(Left) Energy spectrum recorded in $\beta\gamma\gamma$ on of the $LaBr_3$(Ce) after gating on the 375-keV γ-ray in the HPGe detectors. (Right) $\beta\gamma\gamma$(t) Time delay distribution of the 469-keV transition in $LaBr_3$(Ce) detector.

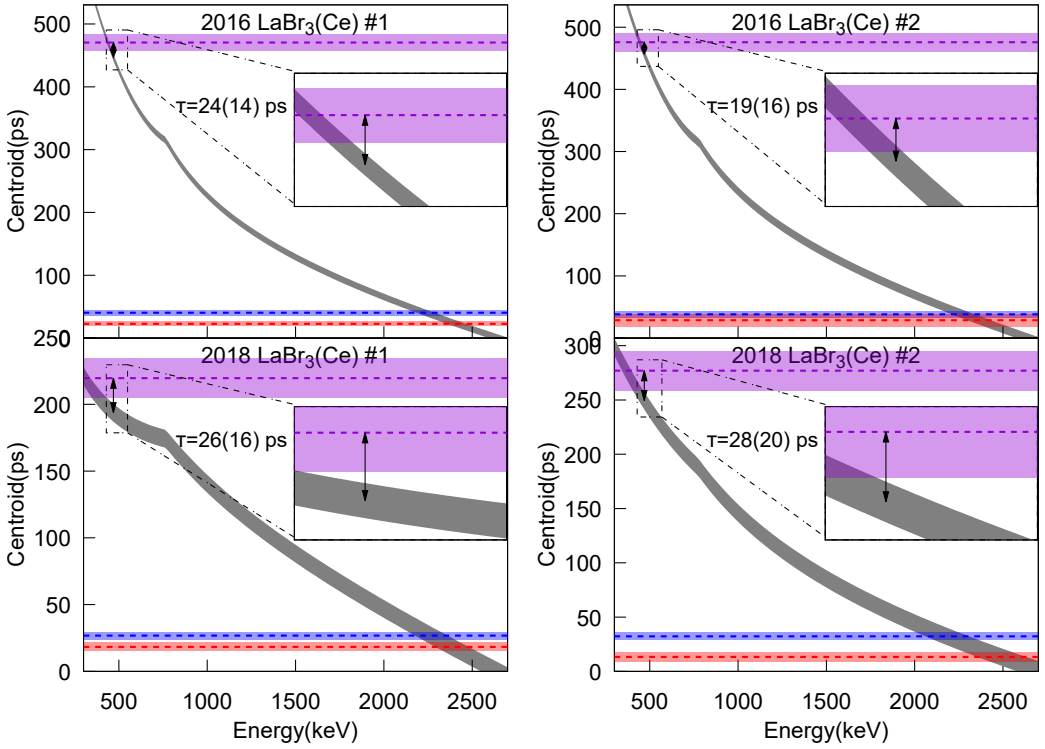

Figure 5.22: $\beta\gamma\gamma$(t) centroid shift analysis for the 4886-keV 5^+ state.

5.3.2.5 Lifetime of the 4919-keV 7^+ state

The lifetime of the 4919-keV 7^+ state state has been measured by analyzing the time distribution of the 203-keV de-exciting γ-ray. To cleanly select this peak in the $LaBr_3$(Ce) spectra three γ-rays can be used as coincidence gate on the HPGe detectors, the 299-, 375- and 710-keV transitions. In Figure 5.23 the β $LaBr_3$(Ce) energy spectra measured in HPGe coincidence wiht these three γ-rays are shown.

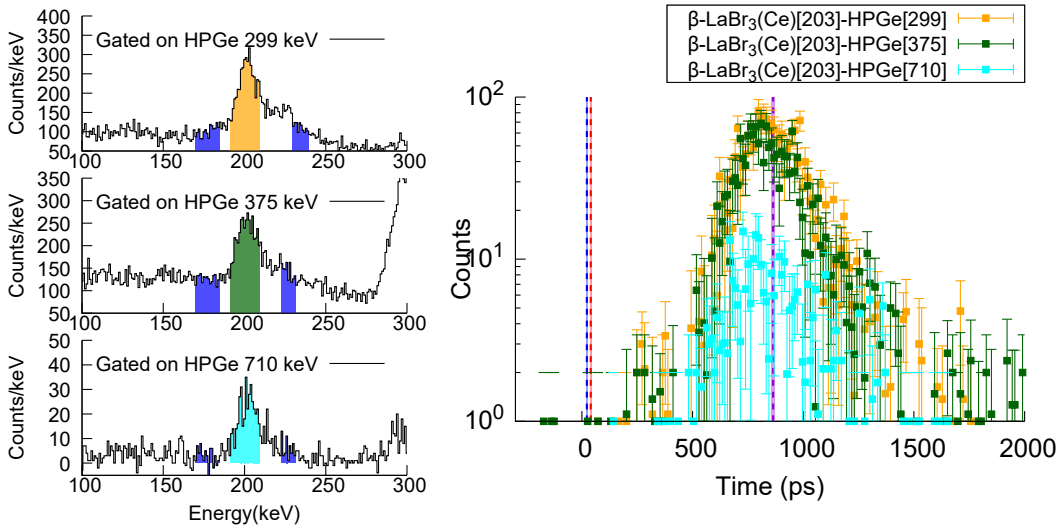

Figure 5.23: $\beta\gamma\gamma$(t) analysis for the 203-keV peak observed in $LaBr_3$(Ce) energy spectra. The γ-rays employed as gates in the HPGe detector are the the 299-, 375-keV transitions from below, and 710-keV γ-ray from above.

The 203-keV transition can be clearly observed in the three spectra. The HPGe[299]-$LaBr_3$(Ce)[203] and HPGe[375]-$LaBr_3$(Ce)[203] comibnations have an amount of statistic 10 time higher than the HPGe[710]-$LaBr_3$(Ce)[203] combination. Nonetheless the contribution of Compton background over which the 203-keV sits on in the $LaBr_3$(Ce) spectra is much higher for the 375- and 299-keV HPGe gates. Corrections were applied to subtract the contribution of this Copmton background, nevertheless, the low ~ 0.5 peak to background increase the uncertainty over the centroid position in those peaks. Thus the centroid position of the 203-keV time spectra has been estimated as the weighted average of the three centroids obtained for each time HPGe gate, see Figure 5.24.

Another source of uncertainty for this lifetime is the contribution of other half-lifes from upper levels. The 4919-keV level is populated directly in 60% of all β-decays, however in the remaining 40% it is populated by γ-rays from upper levels, that can contribute to measured shift of the centroid. From all the upper levels that populates it, only the 5629-keV has a measured mean-life of $\tau = 13(4)$ ps, For the remaining levels, there are no measurements available. However it is not expected for those levels, to have half-lifes longer than few ps. Therefore, considering the fraction populated from above, we estimate a shift no longer than 2 ps for the centroid position due to these contributions. However this situation changes for the HPGe[710]-$LaBr_3$(Ce)[203] time distribution which should appear shifted by the whole 13 ps from 5629-keV lifetime. Hence, before averaging the centroid position of the 203-keV peak of the three HPGe gates, we have subtracted the expected contribution of upper levels in each case..

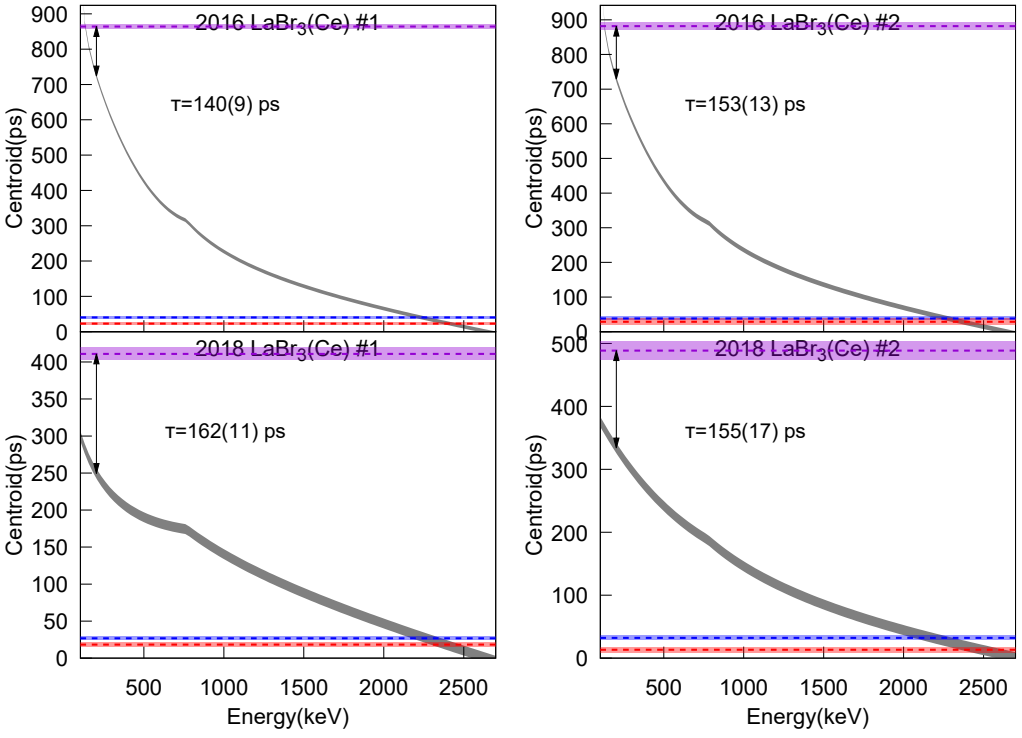

Figure 5.24: $\beta\gamma$(t) Centroid shift analysis for the 4919-keV (7^+). The four dataset-detector combinations yields similar values for the mean-life of this level. The final value was adopted as the weighted average of these 4 values.

The weighted average of the four measurements yield a $\tau = 150(5)$ ps for this level,

or $T_{1/2}$ = 104(4) ps. This new measurement provides a notably longer value than the $T_{1/2}$ = 62(7) ps reported in previous investigations [FHJ+94]. The reason of this difference might be that it was measured using BaF_2 scintillators by Fogelberg *et al.* [FHJ+94]. Since in their work this level could only be measured by analyzing the time distribution of the 203-keV γ-ray, where the contribution of Compton background is very important, the difference may stem from time corrections in this difficult energy range.

5.3.3 Half-lives in the $\nu f_{7/2} d_{3/2}^{-1}$ particle hole multiplet

The 4830-keV 4^- and 4949-keV 5^- levels are identified as members of the $\nu f_{7/2} d_{3/2}^{-1}$ particle-hole multiplet. These levels are not populated with noticeable intensity in the β-decay of ^{132}In. Nevertheless they receive a strong population via γ-rays, mainly from the de-excitation from the Gammow-Teller-fed 7210-keV 6^- level. The measured γ-ray intensities indicates that, after the β-decay of ^{132}In, the tin isotope de-excites in $\sim$25% of the cases via the 4830-keV level, and $\sim$21% goes through the 4942-keV state. Therefore, both levels emit γ-rays of strong intensity, which makes them very suitable to explore their lifetimes via the fast-timing technique.

5.3.3.1 Lifetime of the 4830-keV 4^- state

The half-life of the 4830-keV level can be measured by means of both the $\beta\gamma\gamma$(t) and $\gamma\gamma$(t) fast-timing methods.

In the $\beta\gamma\gamma$(t) delayed coincidence, the mean-life is derived from the centroid shift measured in the time distribution of the 479-keV γ that de-excites the 4830-keV level. Three different coincidence gates on the HPGe detectors can be used to cleanly select the 479-keV peak on the $LaBr_3$(Ce) spectra, these are the 2380-, 310- and 4352-keV transitions. Figure 5.25 (left) shows the three $LaBr_3$(Ce) spectra measured in coincidence with these three γ-rays.

The centroid shift analysis of the $\beta\gamma\gamma$(t) events for one of the β-$LaBr_3$(Ce) pairs in the 2016 data set, is depicted in 5.26. A mean life of 32(6) ps was derived for this pair. This analysis has been extended to all four β-$LaBr_3$(Ce) and data sets combinations providing a total of four independent measurements which turn out to be, all of them compatible between each other within their error bar.

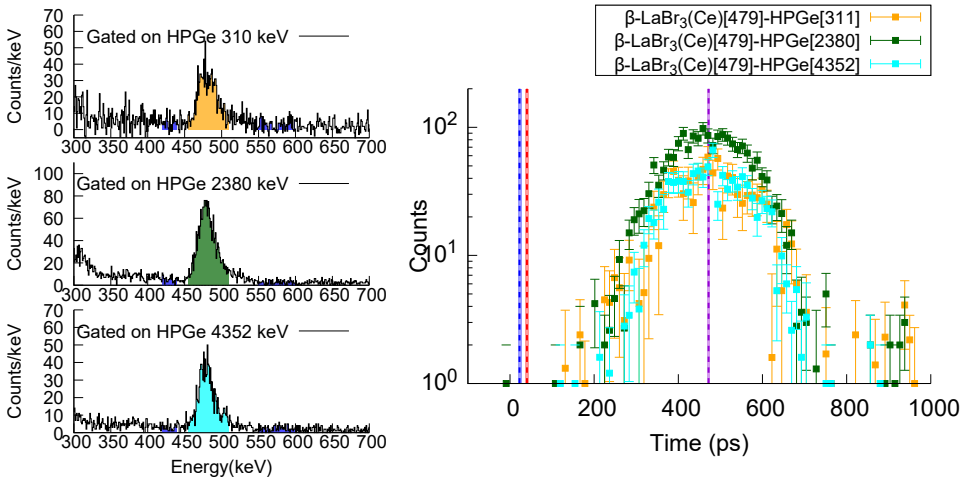

Figure 5.25: Energy spectra measured in the $LaBr_3$(Ce) gated by the 310-keV, 479-keV and 4351-keV γ-rays in HPGe detectors. All three coincidence γ-rays achieve a high selectivity of the 479-keV γ-ray in the $LaBr_3$(Ce) detector. The highest statistics is provided by the 2380-keV germanium gate.

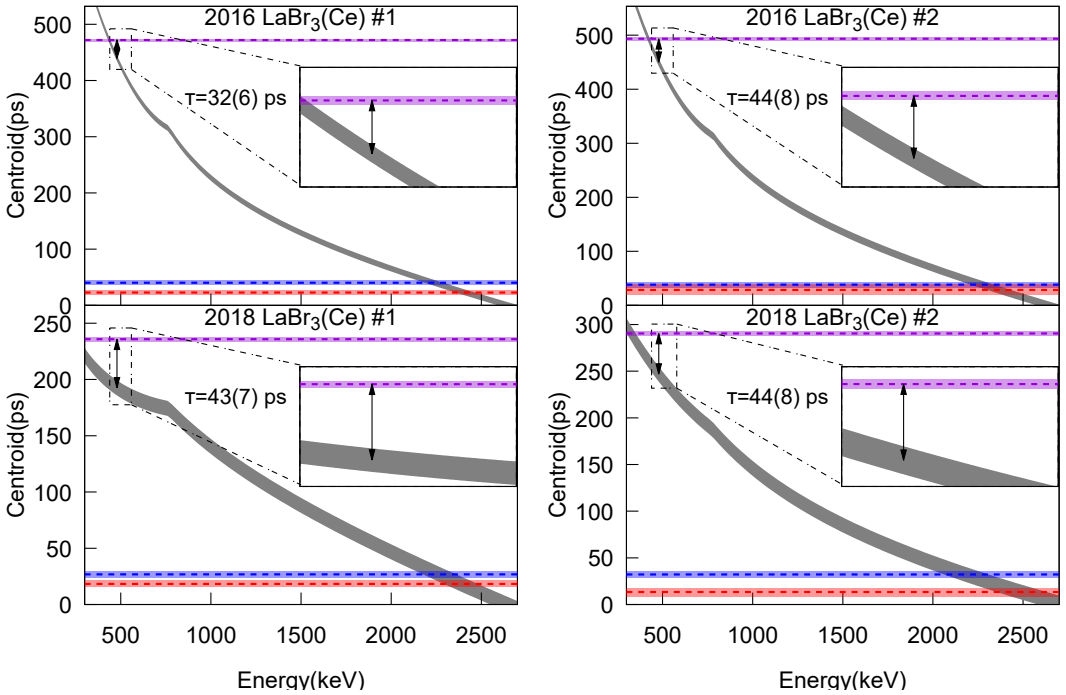

Figure 5.26: $\beta\gamma\gamma$(t) Centroid shift analysis for the 4830-keV 5^- level.

This same half-life can also be measured using the $\gamma\gamma$(t) method. Figure 5.27 shows the energy region of the $LaBr_3$(Ce) coincidence matrix where the 2380-479-keV delayed coincidence peak is observed. The statistic is insufficient to require a third coincidence in the HPGE detector, and consequently the contribution from Compton events is sizable. Only 1/3 of the events within the selected gates are FEP-FEP events, hence corrections of the Compton background are of upmost importance here. Figure 5.27 (left) depicts the energy region around the 2380-479-keV coincidence peak, along with the energy gates used to select the coincidence peak and the Compton background contributions. The same analysis was applied to the anti-delayed coincidence peak. Figure 5.27 (right) shows the $\gamma\gamma$(t) time distributions for the delayed and anti-delayed 2380-479-keV coincidence peak, separately for both datasets. The mean-life is obtained from the centroid-shift between the two time distributions. The two values that are derived are compatible between each other and also with those measured from $\beta\gamma$(t) events.

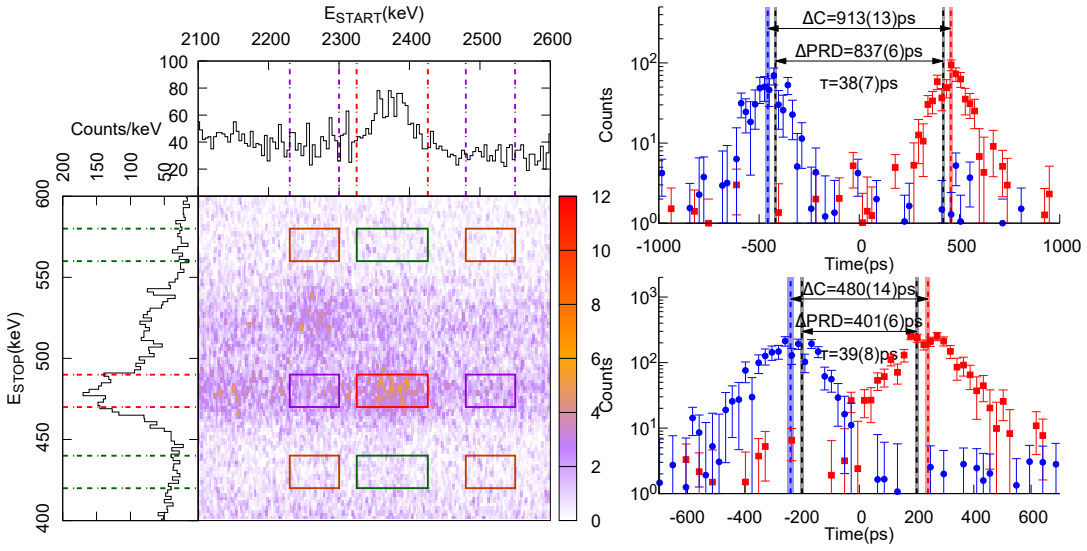

Figure 5.27: $\gamma\gamma$(t) analysis for the half-life of the 4830-keV level. (Left) $LaBr_3$(Ce)-$LaBr_3$(Ce) energy matrix in the region around the 2380-479-keV delayed coincidence peak. (Right) Delayed and anti-delayed $\gamma\gamma$(t) time distributions and centroid shift analysis for the 2380-479-keV cascade.

Summarizing the analysis has been done for both $LaBr_3$(Ce) detectors and both data sets, including also the $\gamma\gamma$(t) method, yielding six independent values for the 4830-keV 5^- level mean-life that are shown in Table 5.6. The weighted average of τ= 39(3) ps

Table 5.6: Summary of $T_{1/2}$ values derived for the half-life of 4830-keV 4^- state.

Dataset	Method	τ (ps)
2016	$\beta\gamma\gamma$(t) $LaBr_3$(Ce)-1	32(6)
	$\beta\gamma\gamma$(t) $LaBr_3$(Ce)-2	44(8)
	$\gamma\gamma$(t)	38(7)
2018	$\beta\gamma\gamma$(t) $LaBr_3$(Ce)-1	43(7)
	$\beta\gamma\gamma$(t) $LaBr_3$(Ce)-2	44(8)
	$\gamma\gamma$(t)	39(8)
Final value	Weighted average	39(3)

or $T_{1/2}$=28(2) ps is adopted as the final result. The half-life is in very good agreement with the 26(5) ps reported by Fogelberg *et al.* [FHJ+95].

5.3.3.2 Lifetime of the 4942-keV 5^- state

The procedure to measure the half-life of the 4942-keV 5^- level is almost identical to that performed for the 4830-keV 4^- level. It can both be measured by using the $\beta\gamma\gamma$(t) and $\gamma\gamma$(t) methods, representing six independent measurements for the lifetime. In this case the analysis focused on the time distributions for the 526-keV γ-rays which carries $\sim$85% of the total de-excitation of the 4942-keV level.

The time delay distribution of the 526-keV γ-ray in the $LaBr_3$(Ce), were built separately requiring a coincidence in the HPGe with the 375-, 2269- and 4042-keV γ-rays. The β-$LaBr_3$(Ce) spectra measured in coincidence with those peaks are shown in Figure 5.28, all three HPGe gates provide high enough selectivity for the 526-keV γ-ray.

The time delay spectra of the 526-keV γ-ray for the three HPGe gates and one of the $LaBr_3$(Ce) detectors, are shown in Figure 5.29. The measured shift of the centroid position relative to the estimated prompt position indicates a τ=33(5) ps value. This analysis was extended to the remaining three data-sets, yielding three similar values for this mean life.

Another two measurements for this lifetime were provided by the analysis of the 2269-526-keV $\gamma\gamma$(t) delayed coincidence. Figure 5.30 contains the $LaBr_3$(Ce)-$LaBr_3$(Ce) coincidences energy-matrix for the energy region where the 2269-526 delayed coincidence peak appears. The energy gates set in the spectra to built the time delayed distribution are depicted in the same plot. Similar to the 4830-keV level case, the contributions from

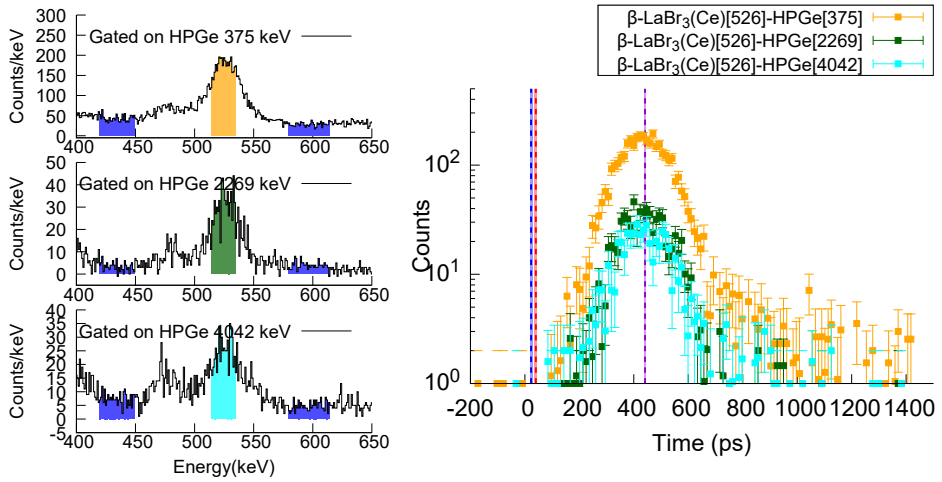

Figure 5.28: $\beta\gamma\gamma$(t) analysis for the 4942-keV 5$^-$ level. (Left) β-gated $LaBr_3$(Ce) spectra measured in coincidence with the 375-, 2269-, and 4042-keV transitions on the HPGe detectors. .All three coincidence γ-rays provides a high selectivity of the 526-keV γ-ray in the $LaBr_3$(Ce) detector. The larger statistics is provided by the 375-keV HPGe gate. (Right) Compton corrected $\beta\gamma\gamma$(t) Time-delayed distributions for the three combinations.

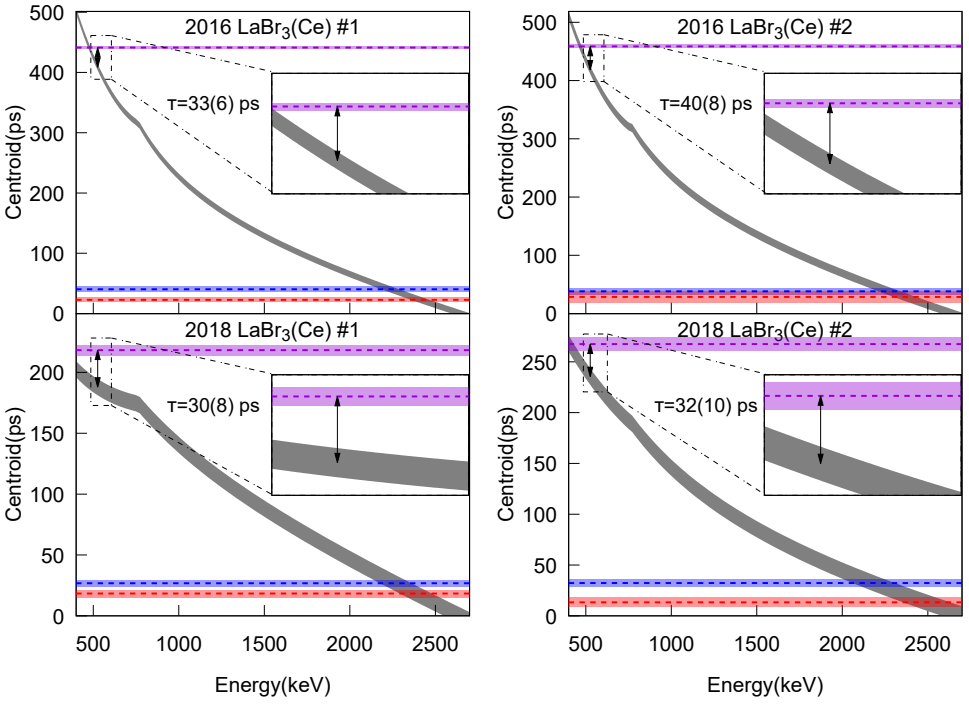

Figure 5.29: $\beta\gamma\gamma$(t) Centroid shift analysis for the 4942-keV 5$^-$ level.

the Compton background beneath the peaks provides 2/3 of the total area within the energy gates. Thus correction for the background contributions are necessary in this case. The corresponding energy gates set in the nearby background are also drawn in the plot.

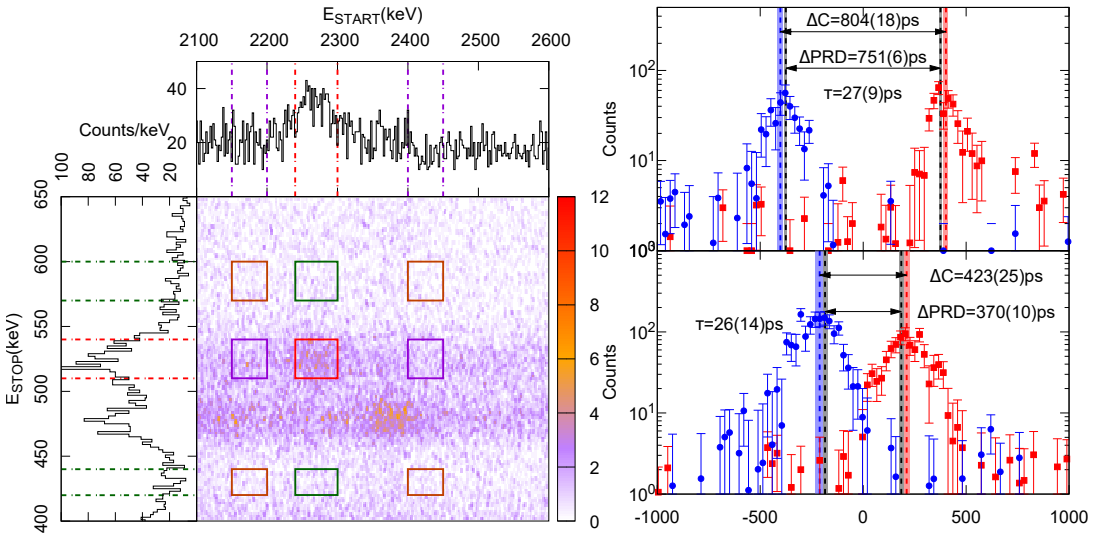

Figure 5.30: $\gamma\gamma$(t) analysis for the half-life of the 4942-keV level. (Left) $LaBr_3$(Ce)-$LaBr_3$(Ce) energy matrix in the region around the 2269-526-keV delayed coincidence peak. (Right) Delayed and anti-delayed $\gamma\gamma$(t) time distributions and centroid shift analysis for the 2269-526-keV cascade.

In Figure 5.30 the lifetime analysis using $\gamma\gamma$(t) events for this level is depicted. The centroid shift measurement yielded two new values for the mean-life, both of them compatible between each other and with those derived from $\beta\gamma\gamma(t)$ events.

Table 5.7: Summary of $T_{1/2}$ values derived for the half-life of 4942-keV 5^- state.

Dataset	Method	τ (ps)
2016	$\beta\gamma\gamma$(t) $LaBr_3$(Ce)-1	33(6)
	$\beta\gamma\gamma$(t) $LaBr_3$(Ce)-2	40(8)
	$\gamma\gamma$(t)	27(9)
2018	$\beta\gamma\gamma$(t) $LaBr_3$(Ce)-1	30(8)
	$\beta\gamma\gamma$(t) $LaBr_3$(Ce)-2	32(10)
	$\gamma\gamma$(t)	26(14)
Final value	Weighted average	33(3)

The six values obtained for this lifetime are compiled in 5.7. All of them in agreement between each other, hence we adopted the value derived as a weighted average of these six measurements, which yielded a τ=33(3) ps or $T_{1/2}$=23(2) ps. This new value is compatible,within the error bars with the $T_{1/2}$=17(5) ps measured in[FHJ^{+}94].

5.3.4 Lifetimes in the $\pi g_{7/2} g_{9/2}^{-1}$ particle hole multiplet

Among the excited levels in ^{132}Sn, some of the positive parity states, located in the 5-6 MeV region, are related with the $\pi g_{7/2} g_{9/2}^{-1}$ proton particle-hole multiplet.

5.3.4.1 Lifetime of 5399 (6^{+}) state

The lifetime of the 5399-keV state, can only be extracted from the $\beta\gamma$(t) coincidences for the 683-keV transition. Unfortunately this γ-ray cannot be selected alone in the $LaBr_3$(Ce) via triple coincidences. Only the 299 or 375 keV peaks in the HPGe detectors provide enough statistics for the 683-keV. However, in both cases the 683-keV peak overlaps with the 710-keV γ-ray with a similar intensity. Hence, due to the narrow gates that need to be set to reduce the influence of the 710-keV peak along with the low $\sim$ 0.8 peak to background ratio, the centroid position of the time distribution cannot be determined with precision. The centroid shift analysis of the β-$LaBr_3$(Ce)[682]-HPGe[299] time delay distribution, were carried out for the four $\beta\gamma$(t) combinations. This result of the four combinations is compatible with 0. The average of the errors sets an upper limit for this lifetime of $T_{1/2} < 17$ ps.

5.3.4.2 Half-life of 5478 (8^{+}) state

The half-life of the 5478-level was measured from the centroid shift in the $\beta\gamma$(t) distribution of the 630-keV transition in the $LaBr_3$(Ce). The events were selected with a coincidence in the HPGe detectors on the 1766-keV γ-ray that populates this level. This analysis could only be carried out for the data measured in 2018, since the statistics measured in 2016 was insufficient. The centroid shift measured in both $LaBr_3$(Ce) detectors indicates a half-life compatible with a prompt transition. Hence, an upper limit of $T_{1/2} < 14$ was adopted as the average of the errors provided by each measurement.

5.3.4.3 Half-life of 5629 (7^+) state

The half-life of the 5629-keV can be measured by analyzing the $\beta\gamma$(t) time distribution of the 913-keV γ, the strongest transition that de-excite the level.

The 5629-keV state has 5 γ-rays de-exciting it, however only the 913-keV has enough statistics in triple coincidence to perform a reliable analysis. This level is very weakly populated by γ-rays, for this reason, the 299-keV and 375-keV from lower-lying levels were used as coincident HPGe transitions in this case.

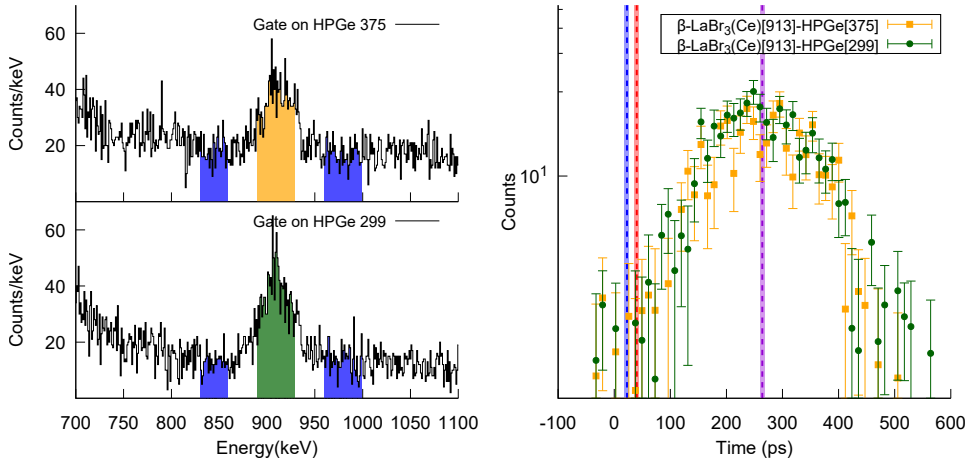

Figure 5.31: $\beta\gamma\gamma$(t) Centroid shift analysis for the lifetime of 5629-keV (7^+) level.

Both HPGe coincident γ-rays provide enough $\beta\gamma\gamma$ statistic for the analysis, and allow a clean selection of the 913-keV peak in the $LaBr_3$(Ce). In Figure 5.31 there are depicted the energy spectra measured for each germanium gate, along with the time distribution derived for each combination of gates after subtracting the Compton contributions. The centroid position for the 913-keV peak was estimated averaging the centroid of both time spectra.

Figure 5.32 shows the centroid-shift estimation of τ for each measurement. The four measurements provide a short lifetime, in agreement between each other. A final value of τ =13(4) ps or $T_{1/2}$=9(3) ps was adopted from the weighted average of the 4 measurements. This new value is in good agreement with the $T_{1/2}$=13(4) ps measured in [FHJ+94].

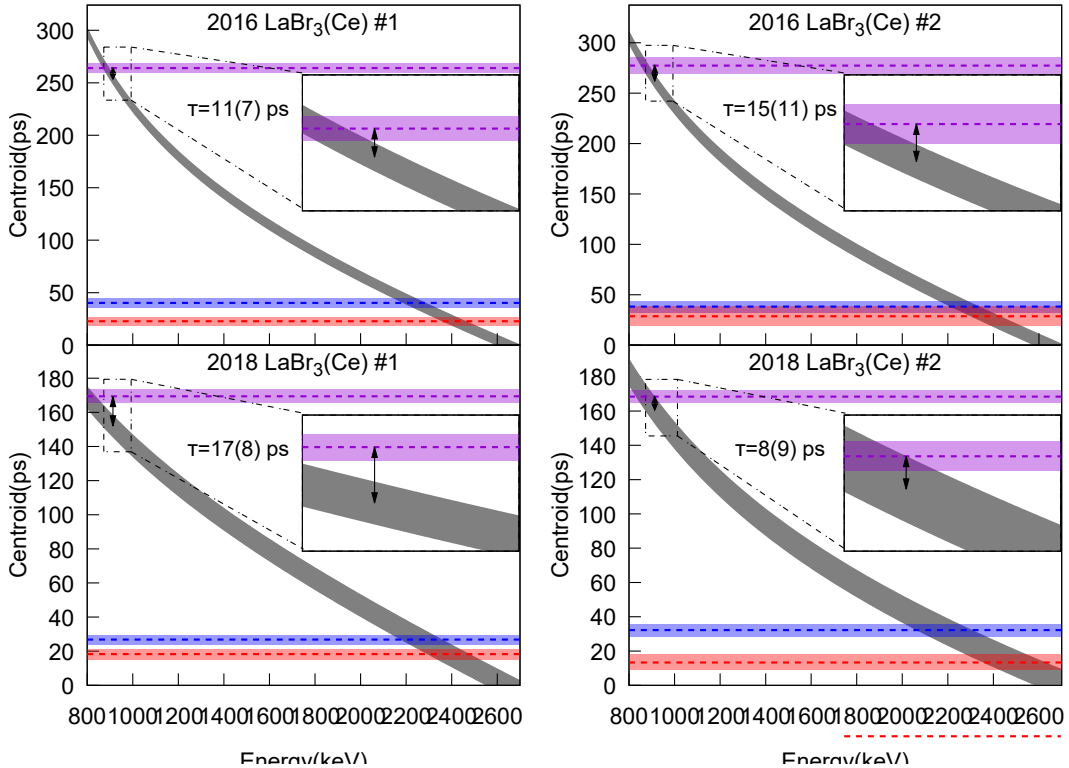

Figure 5.32: $\beta\gamma\gamma$**(t) centroid shift analysis for the lifetime of 5629-keV (7$^+$) level.**

5.3.5 $T_{1/2}$ upper limits for the high-lying energy levels.

The analysis was extended to the remaining levels. Although the statistics was insufficient it was possible to determine upper limits for the half-life of additional 7 levels in ^{132}Sn. The adopted limits are compiled in 5.8

5.3.6 Reduced transition probabilities

The corresponding B(Xλ) values have been derived from the lifetimes and branching ratios obtained in this work, as well as the theoretical internal conversion coefficients, calculated using Bricc [KBT$^+$08]. Transition rates have been calculated assuming a pure multipolarity character of the transitions, using the assignments from [FHJ$^+$94]. For those levels where no previous assignment had been made, the B(Xλ) values corresponding to the most likely multipolarities are presented. These results are summarized in Table 5.9.

Table 5.8: Measured $T_{1/2}$ Upper limits for states in ^{132}Sn.

E_{level} (keV)	J^π	Gate on HPGe	Gate on $LaBr_3$(Ce)	Prompt ref. γ	$T_{1/2}$ (ps)
4351	3^-	479	310	479-keV	$\leq$5
5387	(4^-)	1823	1036	2380- and 2269-keV	$\leq$17
5754	(6^-)	1457	1038	2380- and 2269-keV	$\leq$17
6235	(7^+)	975	1766	2380- and 2269-keV	$\leq$10
6710	(7^-)	502	1766 1823	2380- and 2269-keV	$\leq$20

Table 5.9: State half-lives and reduced transition probabilities in ^{132}Sn. See text for details.

E_i(keV)	Config$_i$	E_f(keV)	Config$_f$	J_f^Π	E_γ(keV)	Xλ	B(λL) (W.u.)
4351.6	Oct. Vibr	0	g.s.	0^+	4351.5	E3[c]	$\geq$7.1
$J_i^\Pi = 3^-$		4041.6	$\nu f_{7/2} h_{11/2}^{-1}$	2^+	310.5	E1[c]	$\geq 1.2\times10^{-4}$
$T_{1/2} \leq$5 ps							
$\leq$5 ps [FHJ+94]							
$=3.4(^{+20}_{-9})$ ps[b]							
4416.6	$\nu f_{7/2} h_{11/2}^{-1}$	0	g.s.	0^+	4416.7	E4	7.7(4)
$J_i^\Pi = 4^+$		4041.6	$\nu f_{7/2} h_{11/2}^{-1}$	2^+	374.9	E2[c]	0.40(2)
$T_{1/2}$ =3.99(2) ns		4351.6	Oct. Vibr	3^-	64.4	E1	$2.57(13)\times10^{-6}$
=3.95(13) ns [FHJ+94]							
4715.9	$\nu f_{7/2} h_{11/2}^{-1}$	4416.6	$\nu f_{7/2} h_{11/2}^{-1}$	4^+	299.3	E2[c]	0.268(6)
$J_i^\Pi = 6^+$							
$T_{1/2}$ = 21.3(4) ns							
=20.1(5) ns [FHJ+94]							
4830.5	$\nu f_{7/2} d_{3/2}^{-1}$	4351.6	Oct. Vibr	3^-	478.9	M1[c]	$7.3(5)\times10^{-3}$
$J_i^\Pi = 4^-$		4416.6	$\nu f_{7/2} h_{11/2}^{-1}$	4^+	414.5	E1	$2.3(3)\times10^{-6}$
$T_{1/2}$ =27(2) ps							
=6(5) ps [FHJ+94][a]							
4848.3	$\nu f_{7/2} h_{11/2}^{-1}$	4715.9	$\nu f_{7/2} h_{11/2}^{-1}$	6^+	132.4	E2[c]	0.1039(14)
$J_i^\Pi = 8^+$							
$T_{1/2}$ =2.108(14) μs							
=2.080(17) μs [KRSS05]							
4885.7	$\nu f_{7/2} h_{11/2}^{-1}$	4416.6	$\nu f_{7/2} h_{11/2}^{-1}$	4^+	469.1	M1	$\geq 6.5\times10^{-3}$
$J_i^\Pi = 5^+$						E2	$\geq$19
$T_{1/2} \leq$30 ps		4715.9	$\nu f_{7/2} h_{11/2}^{-1}$	6^+	169.5	M1	$\geq 4.6\times10^{-3}$
$\leq$40 ps [FHJ+94]						E2	$\geq$94

Table 5.9: (Continued)

E_i(keV)	Config$_i$	E_f(keV)	Config$_f$	J_f^Π	E_γ(keV)	Xλ	B(λL) (W.u.)
4918.8	$\nu f_{7/2}h_{11/2}^{-1}$	4715.9	$\nu f_{7/2}h_{11/2}^{-1}$	6^+	202.9	M1	$1.74(9)\times10^{-2}$
$J_i^\Pi = 7^+$		4848.3	$\nu f_{7/2}h_{11/2}^{-1}$	8^+	70.9	M1	$6.0(7)\times10^{-2}$
$T_{1/2}$ =104(4) ps							
=62(7) ps [FHJ$^+$94]^a							
4942.4	$\nu f_{7/2}d_{3/2}^{-1}$	4351.6	Oct. vibr.	3^-	590.4	E2	0.24(3)
$J_i^\Pi = 5^-$		4416.6	$\nu f_{7/2}h_{11/2}^{-1}$	4^+	525.9	E1^c	$6.7(7)\times10^{-5}$
$T_{1/2}$ =23(2) ps		4715.9	$\nu f_{7/2}h_{11/2}^{-1}$	6^+	226.5	E1	$1.7(2)\times10^{-5}$
=17(5) ps [FHJ$^+$94]^a		4830.5	$\nu p_{3/2}h_{11/2}^{-1}$	4^-	111.3	M1	$5.2(7)\times10^{-2}$
5387.3	$(\nu f_{7/2}s_{1/2}^{-1})$	4416.6	$\nu f_{7/2}h_{11/2}^{-1}$	4^+	299.3	E2^c	0.268(6)
J_i^Π =(4^-)		4351.6	Oct. vibr.	3^-	1036.0	M1	$\geq0.8\times10^{-3}$
$T_{1/2}\leq$17 ps						E2	$\geq$0.5
		4830.5	$\nu f_{7/2}d_{3/2}^{-1}$	4^-	557.1	M1	$\geq4.5\times10^{-4}$
						E2	$\geq$0.9
		4942.4	$\nu f_{7/2}d_{3/2}^{-1}$	5^-	444.6	M1	$\geq1.5\times10^{-3}$
						E2	$\geq$5.1
		4949.0	$\nu f_{7/2}d_{3/2}^{-1}$	(3^-)	437.2	M1	$\geq1.7\times10^{-3}$
						E2	$\geq$5.6
5478.4	$(\pi g_{7/2}g_{9/2}^{-1})$	4848.3	$\nu f_{7/2}h_{11/2}^{-1}$	8^+	630.2	M1	$\geq6.4\times10^{-3}$
J_i^Π =(8^+)						E2	$\geq$10
$T_{1/2}\leq$14 ps							
5628.9	$(\pi g_{7/2}g_{9/2}^{-1})$	4715.9	$\nu f_{7/2}h_{11/2}^{-1}$	6^+	913.1	M1	$2.0(^{+9}_{-5})\times10^{-3}$
J_i^Π =(7^+)						E2	$1.5(^{+7}_{-4})$
$T_{1/2}$=9(3) ps						E2	$\geq$0.5
=13(4) ps[FHJ$^+$94]^a		4830.5	$\nu f_{7/2}d_{3/2}^{-1}$	4^-	557.1	M1	$\geq4.5\times10^{-4}$
		4848.3	$\nu f_{7/2}h_{11/2}^{-1}$	8^+	780.6	M1	$1.3(^{+6}_{-3})\times10^{-3}$
						E2	$1.4(^{+6}_{-3})$
		4918.8	$\nu f_{7/2}h_{11/2}^{-1}$	7^+	710.1	M1	$7(^{+3}_{-2})\times10^{-4}$
						E2	$0.9(^{+4}_{-2})$
		5398.9	$(\pi g_{7/2}g_{9/2}^{-1})$	(6^+)	229.8	M1	$6(^{+3}_{-2})\times10^{-3}$
						E2	$76(^{+34}_{-19})$
		5478.4	$(\pi g_{7/2}g_{9/2}^{-1})$	(8^+)	150.3	M1	$9(^{+4}_{-2})\times10^{-3}$
						E2	$215(^{+95}_{-54})$
5753.9	$(\nu p_{3/2}h_{11/2}^{-1})$	4715.9	$\nu f_{7/2}h_{11/2}^{-1}$	6^+	1038.2	M1	$\geq7.1\times10^{-4}$
J_i^Π =(6^+)						E2	$\geq$0.4
$T_{1/2}\leq$20 ps		5398.9	$(\pi g_{7/2}g_{9/2}^{-1})$	(6^+)	354.3	M1	$\geq5.5\times10^{-3}$
						E2	$\geq$28

Table 5.9: (Continued)

E_i(keV)	Config$_i$	E_f(keV)	Config$_f$	J_f^Π	E_γ(keV)	Xλ	B(λL) (W.u.)
6235.5		4715.9	$\nu f_{7/2} h_{11/2}^{-1}$	6^+	1519.6	M1	$\geq 1.6\times10^{-4}$
$J_i^\Pi = (7^+)$						E2	≥ 0.04
$T_{1/2} \leq 10$ ps		4918.8	$\nu f_{7/2} h_{11/2}^{-1}$	7^+	1317.1	M1	$\geq 1.4\times10^{-4}$
						E2	≥ 0.05
		5398.9	$(\pi g_{7/2} g_{9/2}^{-1})$	(6^+)	836.3	M1	$\geq 1.1\times10^{-3}$
						E2	≥ 1.0
		5753.9	$(\nu p_{3/2} h_{11/2}^{-1})$	(6^+)	481.8	M1	$\geq 4.8\times10^{-3}$
						E2	≥ 13
6709.7		4918.8	$\nu f_{7/2} h_{11/2}^{-1}$	7^+	1791.0	E1	$\geq 3.6\times10^{-7}$
$J_i^\Pi = (7^-)$		4942.4	$\nu f_{7/2} d_{3/2}^{-1}$	5^-	1767.2	E2	$\geq 6\times10^{-2}$
$T_{1/2} \leq 13$ ps							

[a] The uncertainties are taken from [FHJ+95] since those in [FHJ+94].
contain several typographical errors [Mac14].
[b] Calculated from the B(E3) rate measured in Coulomb excitation [RSR+18]
[c] Assigned multipolarity in [FHJ+94]

5.4 Discussion

All the new levels in ^{132}Sn observed in this investigation are candidates for the remaining unidentified states within the particle-hole multiplets. In Figure 5.33 the energies for the 24 particle-hole multiplets in ^{132}Sn expected to appear below the neutron separation energy are represented. The energies and the splitting of the different levels for the same multiplet are estimated by taking into account the single particle energies from neighboring nuclei, and the analogous particle-hole states in ^{208}Pb, taken from [MFH+95, FHJ+95, Blo98], introducing a $A^{-1/3}$ scale to take into account the change in the nuclear potential depth. These empirical calculations provide guidance for the location of the p-h states, which allows to propose spin-parity assignments to the new levels found in this work.

Another piece of information is provided by the vast number of new transitions which connect the new states to known levels. Assuming that the transitions are predominantly of dipole character (mainly of M1 multipolarity) and using the electromagnetic selection rules it is possible to make tentative spin-parity assignments of the newly-identified levels. The transition rates obtained from the measured lifetimes and lifetime limits of the new levels provide additional constraints. Together with the information

from the systematics of p-h states, tentative configurations for the new levels are proposed. In the level schemes presented in Figures 5.8 and 5.12, the tentative spin and parity assignments are already shown.

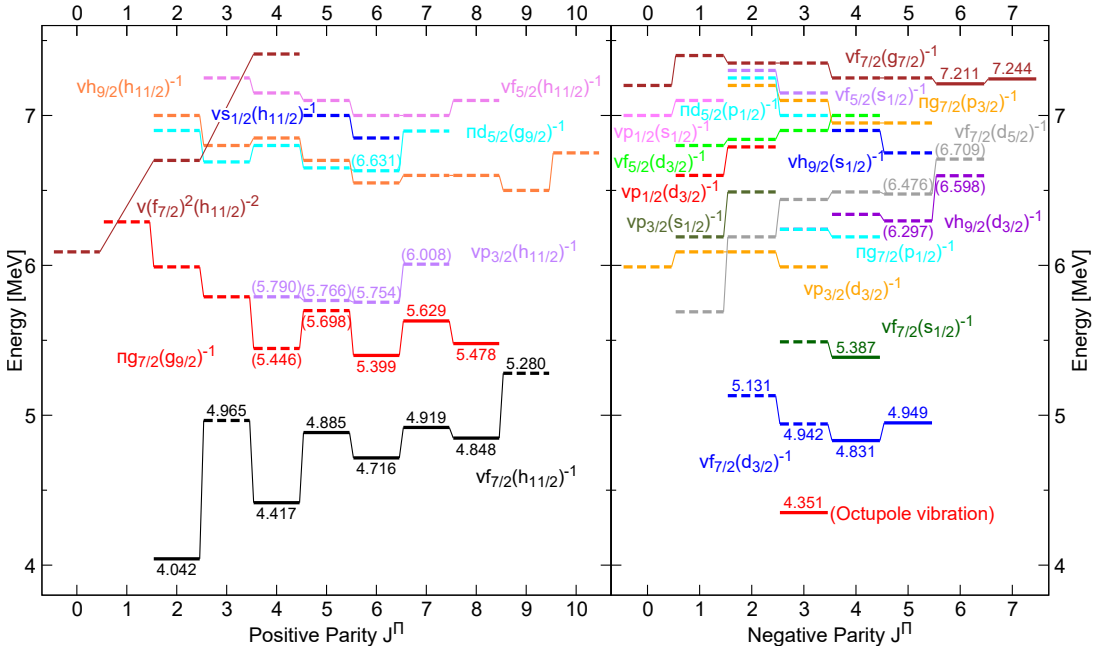

Figure 5.33: Calculated energies for the different particle-hole multiplet states in ^{132}Sn, adopted from J. Blomqvist [Blo98, MFH^{+}95]. The energies and energy splitting within a given multiplet are estimated by scaling the analogous particle-hole states in ^{208}Pb and taking into account single particle energies from neighboring nuclei. Previously identified levels are plotted with continuous lines. The experimental energies from our work are shown for the newly identified states. The levels whose energies appear between brackets correspond to tentative assignments.

5.4.1 Low energy neutron particle-hole states

Given the large number of states that may arise from all the possible particle-hole multiplets, it is very complex to do an unique identification of the observed levels. The interpretation of the levels has been done following the same methodology employed in previous β-decay studies [FHJ^{+}94, BBB^{+}86]. The assignments has been done by comparison of the ^{132}In $[(\pi g_{9/2})^{-1}\nu f_{7/2}]$ β-decay with those observed for the β-decay of its two neighboring ^{131g}In $[\pi g_{9/2}^{-1}]$ and ^{133}Sn $[\nu f_{7/2}]$ isotopes.

The strongest transition in ^{131g}In decay corresponds to the Gamow-Teller connection between the $\pi g_{9/2}^{-1}$ and $\nu g_{7/2}^{-1}$ states, see subsection 6.6 in Chapter 6. The equivalent transition in the ^{132}In β decay corresponds to the strong β-feeding intensity observed for the 6^- and 7^- levels above 7 MeV. This is the reason why these two levels are attributed as part of the $\nu f_{7/2} g_{7/2}^{-1}$ configuration. The second most intense β transition in the ^{131g}In decay is the $\pi g_{9/2}^{-1} \rightarrow \nu h_{11/2}^{-1}$ first-forbidden transition that feeds the $(11/2^-)$ state. Its equivalent transition in ^{132}In decay would populate states from the $\nu f_{7/2} h_{11/2}^{-1}$ multiplet, and thus the low-lying positive parity states can be assigned to this configuration.

Following the analogy with the ^{131g}In β-decay, the strongest γ-ray is at 2434-keV, which corresponds to the $\nu g_{7/2}^{-1} \rightarrow \nu d_{3/2}^{-1}$ between single hole states. An equivalence can be traced back between the 2434-keV transition and the 2380-keV and 2268-keV γ-rays in ^{132}Sn. This strongly suggest the identification of the 4^- and 5^- populated by those transitions as members of the $\nu f_{7/2} d_{3/2}^{-1}$ p-h multiplet.

Among the states that can be built from the low lying $\nu f_{7/2} h_{11/2}^{-1}$ and $\nu f_{7/2} d_{3/2}^{-1}$ configurations, there are several levels which lack experimental identification. In the $\nu f_{7/2} h_{11/2}^{-1}$ p-h multiplet, the 3^+ and 8^+ states remains missing. A level at 5280 keV, which was observed in a previous ^{248}Cm spontaneous fission experiment [BDZ+01], was proposed as the 9^+ state. In this work, we have measured a small feeding to this level in ^{132}In β-decay. This level, for which only one γ-ray transition to the 4848-keV 8^+ has been measured, present a very large apparent logft value $\approx$7.2. All these features supports the assignment of the 5280 keV level as the 9^+ state in $\nu f_{7/2} h_{11/2}^{-1}$ multiplet.

Within this same energy range, there are predicted the 2^- and 3^- states from the $\nu f_{7/2} d_{3/2}^{-1}$ configuration. Including the missing 3^+ state from the $\nu f_{7/2} h_{11/2}^{-1}$ multiplet, there are a total of 3 states in this energy range. This number match the number of new states that have been identified in this region, the 4949-, 4965- and 5131-keV states. These three levels are only fed directly in the ^{133g,m}In β-n decay. Of these only the 4949-keV level can be observed in ^{132}In decay, fed via a γ-ray transition from the 5387 keV (4^-) level. This suggests a low spin for the three states, indicating that these three levels are indeed the three aforementioned unidentified states. On the other hand, the slightly favored population of the 5131-keV state in the β-n decay of the $(1/2^-)$ ^{133m}In isomer, and the 5131-keV transition that connect that level to the 0^+ g.s., suggest that the 5131-keV level is most likely the 2^- state from $\nu f_{7/2} d_{3/2}^{-1}$ multiplet. Regarding the 4949- and 4965-keV states, their γ-ray indicate a J=3 assignment for both of them.

Several similarities can be drawn between the 4949-keV level and the 5^- 4942-keV state from the $\nu f_{7/2}d_{3/2}^{-1}$ multiplet. Firstly, the 5387-keV state, identified as $\nu f_{7/2}s_{1/2}^{-1}$ (4^-), populates both levels via a γ-ray transition. Secondly, both levels have two transitions that de-excite them into the 4352-keV 3^- and the $\nu f_{7/2}d_{3/2}^{-1}$ 4^- states, being the intensity ratio between the two transitions of 10:1 in both cases. Taking into account these similarities, we can assume that the 4949-keV state is indeed the 3^- level from the $\nu f_{7/2}d_{3/2}^{-1}$ multiplet. Consequently, by elimination the 3^+ state of the $\nu f_{7/2}h_{11/2}^{-1}$ p-h multiplet corresponds to the 4965-keV state. The new assignments are shown in Figure 5.33.

5.4.2 Particle-hole states from 5 to 6 MeV

In the β-decay of ^{133}Sn, the dominant decay transition corresponds to the $\nu f_{7/2} \rightarrow \pi g_{7/2}$ f.f. transition. In ^{132}In decay, the analogous transition would populate states belonging to the proton $\pi g_{7/2}g_{9/2}^{-1}$ p-h configuration. Taking into account this analogy, Fogelberg *et al.* proposed the 5399-keV (6^+), 5629-keV (7^+) and 5478-keV $(8^+)$to be states from this proton p-h multiplet [FHJ$^+$95, FHJ$^+$94]. This assignment was based on the intense feeding measured for the 5629 keV (7^+) level, which would be analogous to the f.f. transition in ^{133}Sn decay.

In addition to the states from the proton $\pi g_{7/2}g_{9/2}^{-1}$ configuration, the $\nu p_{3/2}h_{11/2}^{-1}$ and $\nu f_{7/2}s_{1/2}^{-1}$ p-h multiplets are also expected to produce levels in the 5-6 MeV energy range. In this work, 7 new states have been observed at these energies, whose γ-ray transitions suggest a relatively high angular moment for them, J =3-8. These new levels are very likely built on those configurations. Nonetheless, given the limited information that is available, as well as the possibility of configuration mixing, it become very difficult to do an unambiguous identification of those levels. Nevertheless several conclusions about them can be drawn.

Regarding the 5431-keV state, which was only populated in ^{133}In decay, a $J = 3$ was suggested based on the transitions connected to this level. There are two possible configurations for this state, the 3^+ from the proton $\pi g_{7/2}g_{9/2}^{-1}$ configuration or the 3^- from the $\nu f_{7/2}s_{1/2}^{-1}$ configuration.

In this energy range two levels with a $J^\pi = (4^+)$ are expected. They are built on the $\pi g_{7/2}g_{9/2}^{-1}$ and $\nu p_{3/2}h_{11/2}^{-1}$ configurations. In this work, two states have been identified whose transitions points towards a angular momenta compatible with 4. The 5446-keV

level has an expected $J^{\pi} = (4^{+})$value. This state is populated either indirectly via γ-rays in ^{132}In decay, or directly in the ^{133g,m}In β-n decay. Hence, this level can be associated to the 4^{+} member of the two aforementioned configurations. The 5790-keV is only observed in the ^{133g,m}In β-n decay. Taking into account the γ-rays de.exciting it we suggest an angular momenta between 3 and 4. Thus this level is also a good candidate as 4^{+} member of both configurations. However, it is also compatible with the 3^{+} state from $\pi g_{7/2} g_{9/2}^{-1}$ configuration.

Two 5^{+} state can be built on the $\pi g_{7/2} g_{9/2}^{-1}$ and the $\nu p_{3/2} h_{11/2}^{-1}$ respectively. Those levels can be related with the 5698- and 5766-keV states, which are observed in the decay of both ^{132}In and ^{133}In isotopes, and their transitions suggest a J^{π}=(5^{+}) for both of them.

The last two newly identified levels are the 5754-keV (6^{+}) and the 6008-keV (7^{+}) states. Taking into consideration the assignment of the 5399-keV (6^{+}), 5629-keV (7^{+}) to the $\pi g_{7/2} g_{9/2}^{-1}$ proposed by Fogelberg *et al* [FHJ^{+}95, FHJ^{+}94], we suggest that the 5754-keV and the 6008-keV states are the (6^{+}) and the (7^{+}) of the $\nu p_{3/2} h_{11/2}^{-1}$ p-h multiplet.

These tentative assignments are reflected in Figure 5.33.

5.4.3 States from 6 to 7 MeV

An unique identification of the observed states with their respective p-h multiplets, becomes even more difficult for levels with excitation energies above 6 MeV. The reason is the large number of expected p-h multiplets at these energies and the possibility of configuration mixing. Most of these levels are populated exclusively in the decay of ^{132}In (7^{-}), thus several conclusions can be drawn relying on the selective character of the β-decay.

Regarding the configurations with negative parity, there are two states at 6598- and 6709-keV, which are populated exclusively in ^{132}In decay. Their γ-rays transitions indicate a (6^{-}) assignment for both levels. Only the $\nu h_{9/2} d_{3/2}^{-1}$ and $\nu f_{7/2} d_{5/2}^{-1}$ configurations predict a 6^{-} state at this energy range, hence the 6598- and 6709-keV levels are most likely built on those two configurations. On the other hand, The 6297- and 6476-keV states are assumed to be (5^{-}) states. Taking into consideration the γ-rays connected to those levels,one can conclude that these two states are built on the 5^{-} states of the $\nu h_{9/2} d_{3/2}^{-1}$ and $\nu f_{7/2} d_{5/2}^{-1}$ configurations also.

Regarding the positive parity states, the number of expected multiplets is even larger. A total of 8 states with expected positive parity have been observed. All of them are populated only in the decay of ^{132}In. The γ-rays connected to these levels suggest a spin between 5 and 8 for those 8 states. There are a total of 4 p-h multiplets that can produce positive parity states with J=5-8, the $\nu h_{9/2}h_{11/2}^{-1}$, $\nu f_{5/2}h_{11/2}^{-1}$, $\nu p_{3/2}h_{11/2}^{-1}$) and $\pi d_{5/2}g_{9/2}^{-1}$ configuration. Each of these 8 states are most likely members from one of those 4 configurations. However, given the large number of possibilities it is not possible to do an unique identification.

Among these levels, only the 6631-keV stands out slightly from the rest. It shows an enhanced β-feeding in comparison with the rest, receiving around 1% intensity with a logft=6.4 value (Figure 5.8). We can interpret this enhanced feeding using the equivalency between ^{132}In and ^{133}Sn decays. The strongest transition in ^{133}Sn decay corresponds to the $\nu f_{7/2} \rightarrow \pi g_{7/2}$ transition that populates the g.s..This transition takes of 86% of the total β intensity, which corresponds to a log$ft \approx 5.5$ [SVFM^{+}99]. The remaining β intensity mainly proceeds via the $\nu f_{7/2} \rightarrow \pi d_{5/2}$ transition, I$_\beta$ ≈11%, which corresponds to log$ft \approx 6.1$ [SVFM^{+}99]. In the case of ^{132}In decay, these two transition populate states in the $\pi g_{7/2}g_{9/2}^{-1}$ and $\pi d_{5/2}g_{9/2}^{-1}$ configurations respectively. Comparing the feeding of the 5629 keV state in ^{132}In decay, identified as the (7^+) member the $\pi g_{7/2}g_{9/2}^{-1}$ multiplet, with the feeding to the 6631-keV state, a 8:1 ratio is obtained. This ratio is very similar to that observed for the ^{133}Sn decay transitions. This similarity indicates that the 6631 keV (6^+) state might be predominantly built on the $\pi d_{5/2}g_{9/2}^{-1}$ configuration.

5.5 Conclusions

Experimental information about the ^{132}Sn structure plays a crucial role in the shell-model interpretation of nuclei around $N = 82$, because it provides direct knowledge about the particle-hole couplings for both protons and neutrons. In this chapter the properties of excited states in ^{132}Sn have been studied from the β decay of ^{132}In. By taking advantage of the isomer selectivity capabilities of the ISOLDE RILIS, independent investigations of the β-decay of the ^{133g}In $(9/2^+)$ g.s. and the ^{133m}In $(1/2^-)$ isomer were performed as well. Thanks to the use of both decay modes, the knowledge of the ^{132}Sn structure has been largely expanded in this work. A total of 17 new levels

and 68 new γ-transitions have been added to the level-scheme (including those already quoted in the previous publication [PKF$^+$19] derived from the same experiment). A complete fast-timing investigation of the excited levels in ^{132}Sn has been performed as well, confirming and extending previous results.

An interpretation of the level structure is provided in terms of particle-hole configurations arising from core breaking states across the gap, both from the $N = 82$ and $Z = 50$ shells . The interpretation is based on empirical calculations [MFH$^+$95, FHJ$^+$95, Blo98] leading to positive and negative parity particle-hole multiplets, where the energies are obtained from the single-particle energies from neighboring nuclei and from the analogous particle-hole states in ^{208}Pb. These empirical calculations, together with the experimental information on the β and β-n feeding, the level lifetimes and the γ decay branching ratios provide guidance for the identification of the levels as members of the proton-hole multiplets, facilitating tentative spin-parity assignments to the new levels.

The number of states is consistent with the one calculated from the angular momentum couplings. An identification of all remaining missing levels from the $\nu f_{7/2} h^{-1}_{11/2}$ and $\nu f_{7/2} d^{-1}_{3/2}$ neutron-hole configurations has been obtained. A tentative interpretation has been provided for the rest of observed states, where we have been able to observe most of the expected p-h levels with angular momenta close to 7.

Most of the missing information is related to the anticipated low spin states, which are very unlikely to be populated in the ^{132}In (7^-) β-decay. However, the identification of many γ-rays around 7 MeV from the ^{133g,m}In β-decay strongly suggests feeding of those missing low-spin multiplet states. Enhanced statistics for this decay in future measurements could provide more firm assignments.

In conclusion the knowledge about states in the doubly magic ^{132}Sn has been largely expanded by the investigation of the β-decay of ^{132}In and β-n decay of ^{133}In performed at the ISOLDE facility at CERN. The identification of particle-hole multiplets both for protons and neutrons and the transition rates connecting different p-h configurations and states within multiplets provide new input for the two-body matrix elements and single particle states in this region. The new data challenges the theoretical description of ^{132}Sn, which is relevant for the understanding of nuclear structure in the region.

6

The structure of the single neutron-hole nucleus ^{131}Sn

6.1 Introduction

The nucleus ^{131}Sn, with $N = 81$ and $Z = 50$, having one neutron less than the doubly-magic ^{132}Sn, is specifically relevant from the point of view of nuclear structure. From its investigation, several key observables can be extracted and particularly the ESPEs of the single-hole states, and transition probabilities, which are employed as the main ingredient in large scale shell model calculations. This is the reason why ^{131}Sn has been investigated repeatedly since the 1980s.

The main tool employed to gain access to the excited structure of ^{131}Sn has been the β decay of ^{131}In. Three β-decaying indium states have been identified for this mass: the ^{131g}In ground state, and two higher lying isomers. The $J^\pi = 9/2^+$ ground state ^{131g}In, corresponds to the proton hole configuration $\pi g_{9/2}^{-1}$. The low lying isomer ^{131m1}In is found at 302(32) keV [FGM$^+$04a] with $J^\pi = 1/2^-$, which can be related to the proton hole configuration $\pi s_{1/2}^{-1}$. Lastly, a third isomer is also found at a very high energy 3764(88) keV [FGM$^+$04a], for which a high angular momenta of $J^\pi = (21/2^+)$ is assumed and can be identified as a member of the core-excited $\pi g_{9/2}^{-1}\nu h_{11/2}^{-1} f_{7/2}$ 1-particle 2-hole (1p2h) configuration. This complex set of isomers with such diverse angular momenta gives the opportunity of populating a large range of excited state in ^{131}Sn, when the selection rules of β decay are considered.

The first investigation of ^{131}Sn was carried at OSIRIS by De Geer *et al.* [DGH80],

where the population of excited levels in ^{131}Sn through the β decay of ^{131}In was observed for the first time. This investigation led to the first identification of the $\nu g_{7/2}^{-1}$ and $\nu s_{1/2}^{-1}$ neutron-hole states. Further studies performed at OSIRIS [FB84, FGM^{+}04a], expanded notably the knowledge of the level scheme. The observation of the $\nu d_{5/2}^{-1}$ state was reported in those studies, as well as the population of a large set of core-excited states located at high energies, around 4 MeV. A set of levels populated in the β decay of the high-spin ^{131m2}In isomer were also identified. The excited levels populated in the decay of this isomer showed a strong resemblance to the decay of ^{132}In. The populated levels were de-excited in cascades with two or more steps until they reach the $11/2^{-}$ isomeric state of ^{131}Sn, which is associated to the $\nu h_{11/2}^{-1}$ configuration.

In spite of the experimental information about ^{131}Sn being rather complete there is a key piece of information that remains missing, namely the energy of the single-hole $\nu h_{11/2}^{-1}$. It was mentioned before, that in the decay of the ^{131m2}In isomer, several high-energy core-excited levels are populated, which de-excite to the $\nu h_{11/2}^{-1}$ state. However, no transition connecting the levels populated in the decay of ^{131m2}In with those populated in the decay of other two indium isomers has been observed so far. This is to be expected due to the large angular momenta difference between the ^{131m2}In and the other two. The large difference in spin between the $11/2^{-}$ isomer, with an expected excitation energy om 69(14) keV [FGM^{+}04a], and the $3/2^{+}$ ground state, would require a highly forbidden direct M4 γ transition. Due to the lack of γ rays that could provide the precise energy of the $\nu h_{11/2}^{-1}$ SPE, in Fogelberg *et al.* [FGM^{+}04a] the position of this level was determined by measuring the differences in the Q_{β} from the decay of the ^{131}Sn isomers. A more precise value of 65.1 keV was also proposed by Fogelberg *et al.* [FGM^{+}04a] based in the assignment of a 2369-keV M2 γ-ray connecting the 2434-keV $\nu g_{7/2}^{-1}$ level to the $\nu h_{11/2}^{-1}$ isomer. However, this assignment has been never confirmed by $\gamma\gamma$ coincidences, and nowadays remains as a tentative value, awaiting for an experimental confirmation.

The understanding of the ^{131}Sn excited structure has been recently expanded. In the early 2000s, this tin isotope was investigated at Argonne National Laboratory, where the excited levels in ^{131}Sn were populated in the spontaneous fission of ^{248}Cm. The results derived from this work were published by Bhattacharyya *et al.* [BDZ^{+}01], and led to a better understanding of the yrast excitations in ^{131}Sn, providing also a rather complete interpretation of the high-spin states, in terms of (1p2h) configurations.

Two β-decay studies of ^{131}In populating ^{131}Sn have been recently performed. One of them is the subject of this PhD thesis. The other one was performed at TRIUMF and the results are published in [DSA$^+$19]. That investigation further expanded the known excited states in ^{131}Sn, specially on the high-spin excited levels populated in the decay of ^{131m2}In. In addition to the new spectroscopic information on ^{131}Sn, measurements were provided for the lifetimes of the indium β-decaying states, as well a new value for the 300-ns high-spin isomer in ^{131}Sn.

6.2 Investigation of ^{131}In decay at ISOLDE

In spite of the existing literature, there are still relevant pieces of information that remain missing. One of the most important ones is the aforementioned lack of confirmation of the position of the $\nu h^{-1}_{11/2}$ state. Despite all the complementary studies carried out at the ANL [BDZ$^+$01], and TRIUMF [DSA$^+$19], the 65.1 keV energy of has not been confirmed by $\gamma\gamma$ coincidences. In addition, there is scarce information about level lifetimes and transition rates in this nucleus, which could shed light on the structure of excited states.

The structure if ^{131}Sn was investigated again in the framework of the IS610 campaign with the aim of addressing these issues. The method employed to populate the excited levels in ^{131}Sn was the β decay of indium. A great advantage of this new β-decay experiment is the use of RILIS in a narrow band mode to ionize the indium isotopes. This setup made it possible to study the decay of ^{131}In isomers independently. The measurements of ^{131}In decay were carried out using three different RILIS configurations. For the first two configurations the ionizing lasers were configured in a narrow-band mode. The laser was set at the optimal wavelength for the ionization of the ^{131g}In and ^{131m1}In isomers respectively. In Figure 6.1 the high selectivity achieved in the ionization of the ground state and the first isomer can be appreciated. For the optimal ^{131g}In wavelength (Figure 6.1 top), the 2434-keV γ-ray emitted in ^{131g}In decay is the strongest one, while the 332-keV γ-ray from ^{131m1}In decay is highly suppressed. On the other hand, when the lasers are set at the optimal ^{131m1}In wavelength (Figure 6.1 Center), the 2434-keV line has almost disappeared, while the 332-keV γ becomes the dominant transition in the spectrum. The third RILIS configuration used to ionize indium was a broad band mode. By using this configuration the total ionization efficiency is higher,

however is not possible to select a specific isomer. In the bottom of Figure 6.1, the β-gated spectrum measured with the broad band configuration is depicted. In this case, the γ rays emitted by all three isomers show up with similar intensity. The figure highlights one of the advantages of the study performed at ISOLDE.

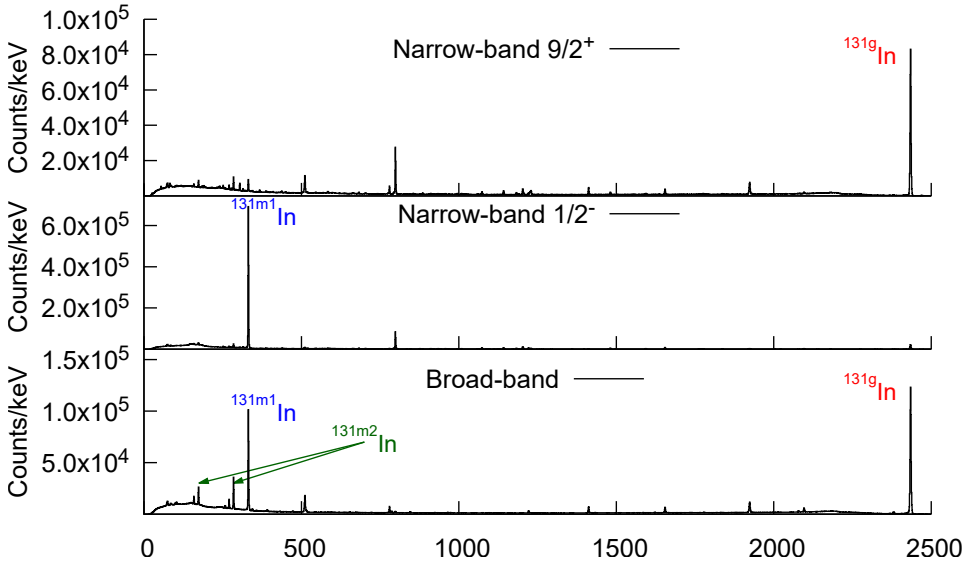

Figure 6.1: β-gated HPGe energy spectra recorded for each RILIS configuration. Measured β-gated spectra for the β decay of ^{131}In. (Top) RILIS lasers are set in narrow-band mode, with the optimal wavelength for the ionization of the ^{131g}In isomer. (Center) Narrow-band mode with the optimal wavelength for the ionization of the ^{131m1}In isomer. (Bottom) RILIS lasers are set in broad band mode, where maximum ionization efficiency is attained.

The selectivity achieved for the ^{131g}In and ^{131m1}In isomers was very high. On the other hand the ^{131m2}In isomer could not be separated, and one needs to resort to γ spectroscopy. Since there are three separate measurements, each with a different isomer composition of the beam, it is possible to use the γ intensity ratios to compare the measurements and deduce the states populated in the decay. The previous β-decay studies [FB84, FGM$^+$04a, DSA$^+$19], did not have this capability to distinguish the β emitting isomer and hence, the distinction was solely based on $\gamma\gamma$ coincidences with the most intense γ lines from each decay. Although this approach showed to be quite effective, the transitions from levels that only decay to the ground or isomeric state may suffer from wrong allocation.

The decay of ^{131}In was measured in both the 2016 and 2018 experimental campaigns. During the first data-taking campaign measurements were carried out by using the three laser configuration aforementioned, while during the second one, the data for this mass was collected using the broad band configuration to enhance the statistics.

Another asset of this new β-decay study is the use of the complementary fast-timing setup. The information on the lifetimes of the excited levels is very scarce. So far, only the half-life of the 300 ns high-spin isomer from ^{131}Sn has been measured. Thanks to the fast-timing setup, the lifetimes of the excited states down to the ps range will be accessible in this work.

6.3 Half-life measurement of the ^{131}In β-decaying states.

The lifetimes of all three ^{131}In β-decaying states have been measured by analyzing the time distribution of events with respect to the time of proton impact on the target. For this analysis we have used the events recorded in the HPGe clover detectors without applying any extra condition. The events have been selected by using the narrow-band RILIS data set when available, and by choosing the strongest γ rays emitted after the decay of each state. The choice of γ-rays in itself grants a high selectivity of the isomer under study. Given the large differences in angular momentum of the parent indium isomers in this mass, $J = (9/2, 1/2, 21/2)$, it is not expected to observe states in ^{131}Sn that can be populated in the decay of more than one isomer.

Due to the large count rates sustained for this mass, a noticeable dead-time effect is observed. The large count rates were partly caused by yields achieved for the lower masses, and partly by the short lifetimes of the indium, of the value of 300 ms for $A = 131$. In the 2018 data-taking campaign, for only one HPGe crystal a nominal intensity of 10^4 counts per second (cps) was registered during the implantation time. However, 1.5 s after closing of the beam gate the count rate dropped down to 300 cps. Hence, the impact of the dead time due to these sizable rates is mainly located during the implantation time and for a couple of indium half-lives of ms after it. For the 2016 campaign the count rates achieved were a factor of 10 times lower, therefore the dead time for this dataset was significantly lower in comparison with the 2018 dataset.

For the purpose of measuring the ^{131}In β-decay lifetimes, the decay curves of each isomer needs to be analyzed. However, this analysis might be hampered by the afore-

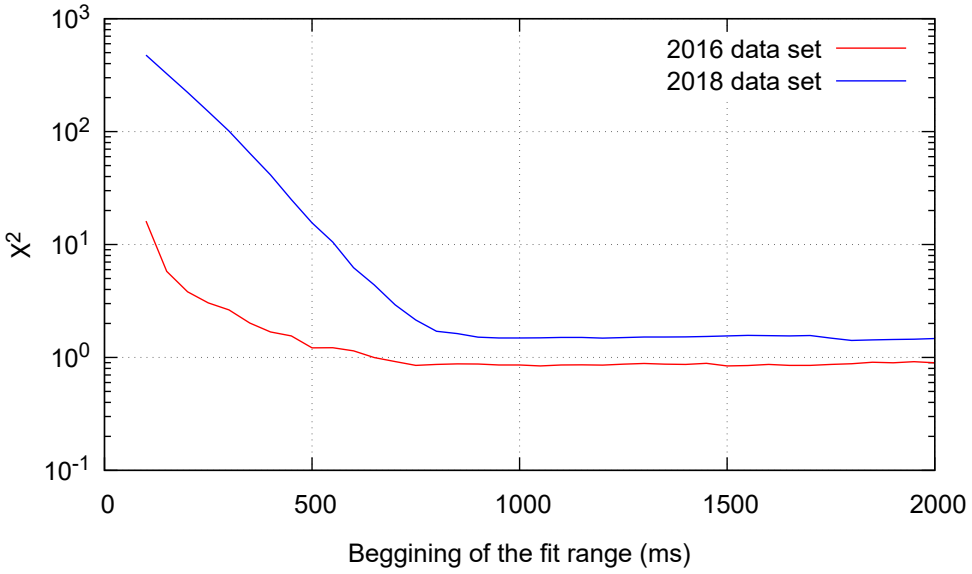

Figure 6.2: Dead time characterization for the ^{131}In decay. Obtained χ^2 from the fit of the 2434-keV γ-ray time distribution. The lines represent the measured χ^2 as a function of the starting point of the fit range. For the 2016 data set, exponential behaviour is quickly recovered after the end of the implantation, it can be seen that at 500 ms the χ^2 reaches a minimum. For the 2018 dataset, it takes longer the χ^2 to converge to 1, but 1 second after the start of the implantation the χ^2 has already been reached a minimum.

mentioned dead-time data loss. In order to avoid this unwanted effect we move forward the range considered for the fit of the decay curve, until the dead time has disappeared. In order to select the optimal fit range of the analysis, a χ^2 fit test has been performed. This test was done using the time distribution of the 2434-keV transition, the strongest γ-ray in the ^{131g}In decay. The time distribution has been fitted to an exponential decay, changing the starting point of the range considered in the fit. The results from his analysis are depicted in Figure 6.2. It can be appreciated that for the 2016 data set the exponential decay behavior is quickly recovered after the end of the implantation, and 500 ms after the proton pulse, the χ^2 is already minimized. For the 2018 case it takes longer for the χ^2 to converge, but 1 second after the pulse the exponential decay behaviour has already been recovered.

Decay of the ^{131g}In $9/2^+$ g.s.

For the analysis of the ground-state half-life, the 2434-, 3990- and 4487-keV have

been selected. Those three transitions were chosen because they are identified to be populated only by the decay of the ^{131g}In[FGM^{+}04a], identification confirmed by their enhanced intensity in the narrow-band [$9/2^{+}$] spectra. As it was mentioned in the previous section, the ^{131}In decay has been measured in the two IS610 experimental campaigns. These means that there are two different datasets, which give us the possibility of perform the same analysis independently in for each measurement, and so this study has furnished 6 different values. The time distributions employed for this analysis were generated by gating on the corresponding peaks for three aforementioned transitions, the contribution of the Compton background under the FEP was estimated by at the background located at both sides of the peak, and subtracted from time distribution. The time distributions from 2016, were generated employing only the measurements carried out using the narrow band mode with the wavelength tuned to the $9/2^{+}$ isomer. The broad band mode measurements in 2016 were designed with the tape moving with the arrival of every proton pulse, and therefore they are not included in the analysis.

The time distributions were fitted to a single exponential with a constant component. In Figure 6.3 the decay curves for the 3 γ-rays considered in this analysis in both datasets are shown. The six values obtained for this half-life are statistically compatible between each other. As a final value the weighted average of these six measurements has been adopted, yielding $T_{1/2}$=261.8(4) ms. This new value is in agreement with, but with a much higher precision, than the 280(30) ms value reported in the last evaluation [KMR06]. This new value is fully consistent also with the values reported by other two recent measurements, the 261(3) ms half-life by Lorusso *et al.* [LNX^{+}15], and the value of 265(8) ms reported by Dunlop *et al.* [DSA^{+}19].

Decay of the ^{131m1}In $1/2^{-}$ isomer

Similarly to the ground state case, the half-life for the ^{131}In first isomer has been measured by the analysis of the most intense γ rays emitted after β decay. The 332-, 3578- and 4430-keV γ-rays have been chosen. The 332-keV transition is emitted from the quasi single-particle $1/2^{+}$ state, which could be indirectly fed also in the β decay of the ^{131}In g.s. However the effect is very small since the population is minimal. To verify this we take advantage of the data set from the 2016 campaign employed in this analysis, where a narrow band laser was employed maximizing the ionization of the ^{131m}In isomer while minimizing the ^{131g}In one. The other two high energy transitions

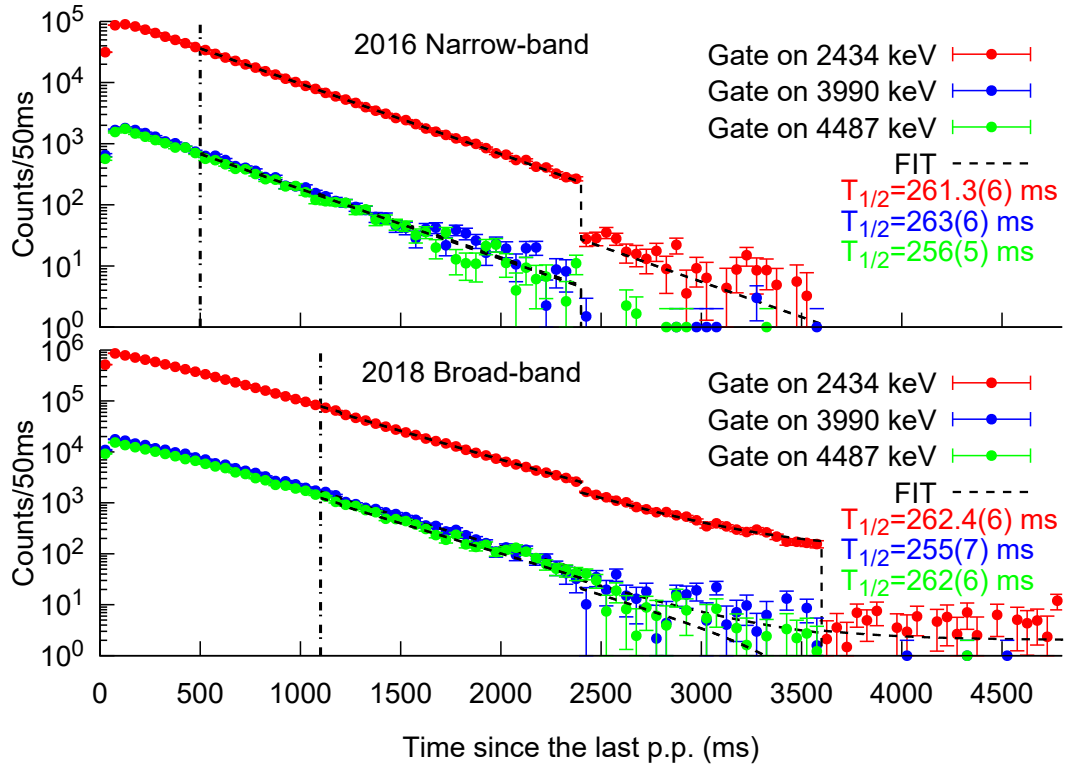

Figure 6.3: Time distribution analysis of the ^{131g}In lifetime. Time distributions relative to the arrival of the last proton pulse and exponential decay fit curves. The top panel represent the analysis for the 2016 dataset measured with the RILIS Narrow-band $[9/2^+]$ enhanced configuration, while the bottom panel shows the same analysis but using the dataset measured in the 2018 campaign with the RILIS Broad-band settings.

are much weaker, and can only be distinguished from the background in the 2016 spectra measured with RILIS in narrow band mode. From the 2016 narrow-band data set, the lifetime can be independently extracted from the three aforementioned γ-rays. Besides those three, an extra measurement can be obtained from the 332-keV time distribution, by using the data recorded in 2018 with the broad band configuration of RILIS.

The time distributions analyzed in this section are shown in Figure 6.4. This analysed have furnished 4 independent values for the half-life of ^{131m1}In isomer, all of them in good agreement between each other, within their uncertainties. The adopted final value for the half-life proposed in this work is $T_{1/2}$=335.7(6) ms, which was obtained as the weighted average of the 4 values from Figure 6.4. This new measurement in in full agreement with the 350(50) ms value reported in the last evaluation [KMR06], and

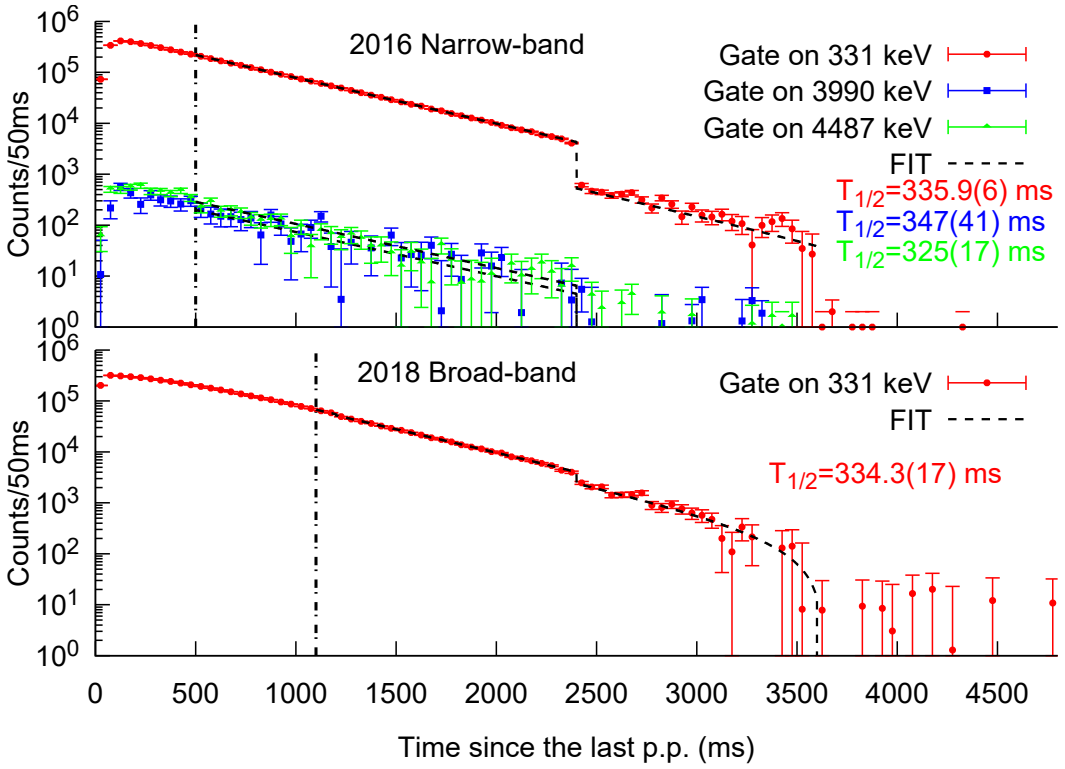

Figure 6.4: Time distribution analysis of the ^{131m1}In lifetime. ^{131m1}In decay curves for the narrow-band ($1/2^-$) configuration (Top) and broad-band (Bottom) selected by the 332-, 3990 and 4487-keV γ-rays. The fit curves are shown with dashed lines.

with the newer 328(15) ms half-life value reported by Dunlop *et al.* [DSA+19].

Decay of ^{131m2}In $21/2^+$ isomer

To conclude this subsection, the results derived from the analysis applied to the γ rays emitted after the β decay of the high spin isomer in ^{131}In will be discussed. In the decay of the ^{131m2}In isomer, excited levels are populated in a wide range of energy, up to 7 MeV. The decay is quite complex, with a good number of transitions emitted cascades of two or more γ-rays, with energies ranging from 100 keV up to 4 MeV. Therefore, there are a lot of transitions which carry the time distribution of ^{131m2}In decay. We have selected the 4 the strongest ones for this analysis. As it mentioned before, the production of ^{131m2}In could not be separated from the others isomers by using narrow-band laser ionization. Thus, for this analysis three different data have been used, the two of 2016 campaign with the narrow band laser configuration, as well

as the data set from 2018 in broad band. The 2016 in broad-band cannot be employed due to the fast tape movement mentioned before.

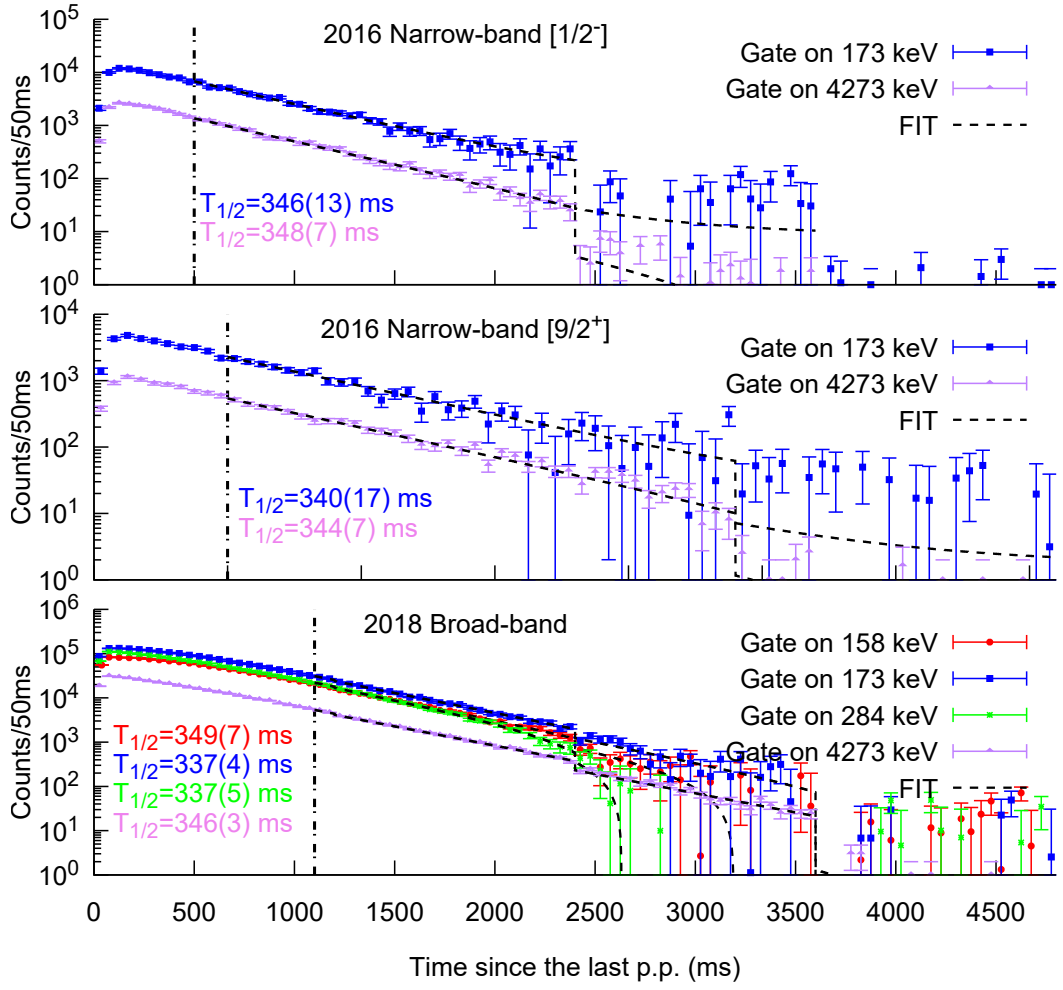

Figure 6.5: Time distribution analysis of the ^{131m2}In lifetime. (Middle) ^{131m2}In decay curves for the narrow band ($9/2^+$) configuration. (Top) ^{131m2}In decay curves for the narrow band ($1/2^-$) configuration. (Bottom) Decay curves measured for the broad band configuration during the 2018 measurements.

The lifetime analysis is shown in Figure 6.5 for the different data sets and γ rays altogether. The final value we have adopted is the weighted average of all these measurements, which yields $T_{1/2}$= 343(2) ms. This new measurement is in complete agreement, and with a notably higher precision, with the reported value in the last evaluation $T_{1/2}$= 320(60) ms [KMR06], and also with the new measurement in the latest β decay

experiment $T_{1/2}$= 323(55) ms [DSA$^+$19].

6.4 Structure of ^{131}Sn populated in the β-decay of ^{131}In

In this section, the analysis of the γ-ray spectra measured for the decay of ^{131}In isomers will be discussed. Determining the origin of all the different γ-lines that show up in the spectra is a complex task. The γ-ray identification was carried out by three different methods. Firstly, the analysis of the time distribution of the events relative to the arrival of the last proton pulse on target makes it possible to assign the γ-rays that have been emitted to the β decay of indium isotopes, and to separate them from those emitted after the β decay of tin daughter isotopes. Secondly, the identification the γ rays based on γ-γ coincidences with previously known transitions provides unambiguous assignment of new ones. Lastly, the comparison between the spectra measured with different ionization configurations in RILIS, offers the possibility of identifying the ^{131}In isomer from which the γ rays have been emitted.

Apart from the γ-rays emitted after the β decay of the indium isomers, there are different types of background radiation that may appear in our spectra. The main contribution to the background is due to the decay products of ^{131}Sn. The tape system described in Chapter 3.2, was employed to remove most of the activity of the long-lived daughters from the spectra. However, most of the measurements for $A = 131$ mas were performed with the tape moving only once every super-cycle, roughly every 40-50 s. For the β decay of ^{131}Sn, the ground state and isomer have a 56 s and 58 s half-life respectively [KMR06], thus around 22% of the implanted isotopes have already decayed to ^{131}Sb when they are removed by the tape movement, and only We estimate that only a 0.2% manged to decay to ^{131}Te before the end of the super-cycle, so a noticeable contribution to the spectra from the remaining isotopes of the decay chain is not expected.

Another source of background are surface ionization contaminants. Alkali elements such as caesium are heavily produced and easily surface ionized, and they can travel through the mass separator and reach the experimental station, since the mass resolution is insufficient to reject the elements with the same A. Nonetheless, for this mass the contaminant would be ^{131}Cs, which is an isotope that decays via electron capture and does not emit γ rays. Other kinds of backgrounds, such as the laboratory background, or

neutron-capture induced γ-rays can also be observed in the singles spectra, however they can be easily removed by imposing conditions in the time, or by requiring a coincidence with the β detector.

The Q_β of ^{131}In is 9240(5) keV [WAK$^+$17], This large β-decay energy window opens up the possibility of populating states in ^{131}Sn up to that high energy. The one-neutron separation energy in ^{131}Sn is 5204(4) keV [WAK$^+$17]. Normally, excited levels is populated above the neutron separation energy predominantly decay by the emission of a neutron. However, recent studies in this and others regions have reported the phenomena of competition between the emission of neutrons and γ-rays from unbound states [VJD$^+$17, PKF$^+$19]. This feature is also present in ^{131}Sn, where γ-emitting excited levels above the neutron separation energy are already reported in previous studies [FGM$^+$04b]. In the latest published β-decay study [DSA$^+$19], the knowledge about those levels was expanded with the identification of a good number of γ-decaying levels above the neutron separation energy. They were populated through the β decay of the high spin isomer ^{131m2}In $(21/2^+)$ and are characterized by an expected large angular momentum ($\approx 21/2$). Some of them are located 1 MeV above the neutron separation energy.

Our analysis is illustrated in Figures 6.6, 6.7 and 6.8 showing the β-gated spectra recorded for mass A=131. The black spectrum drawn in these figures corresponds to the full statistics measured in the 2016 campaign. In the three complementary spectra the same data set is drawn, but with the three different RILIS ionization conditions employed in the measurement, the narrow-band enhanced $[9/2^+]$ (red spectra), the narrow-band enhanced $[1/2^-]$ (Blue spectra) and the broad band (brown spectra). A partial identification of the peaks is also included. The classification of the peaks has been carried out on the basis of γ-γ coincidences, the time distribution, and the intensity ratios between each ionization laser condition. The γ lines are labeled with their energy in keV along with the parent isotope.

In Figure 6.6 the HPGe spectra from up to 1 MeV is depicted. Within this energy range there are two peaks that stand out. One of them is the 332-keV γ-line due to the $1/2^+ \rightarrow 3/2^+$ transition from the first excited level to the ground state in ^{131}Sn. This level is populated only in ^{131m1}In decay with sizable intensity, thus it is mainly seen in the narrow band $[1/2^-]$ and the broad band spectra. The other one is the 798-keV peak corresponding to the transition from the first excited level in ^{131}Sb to the ground state.

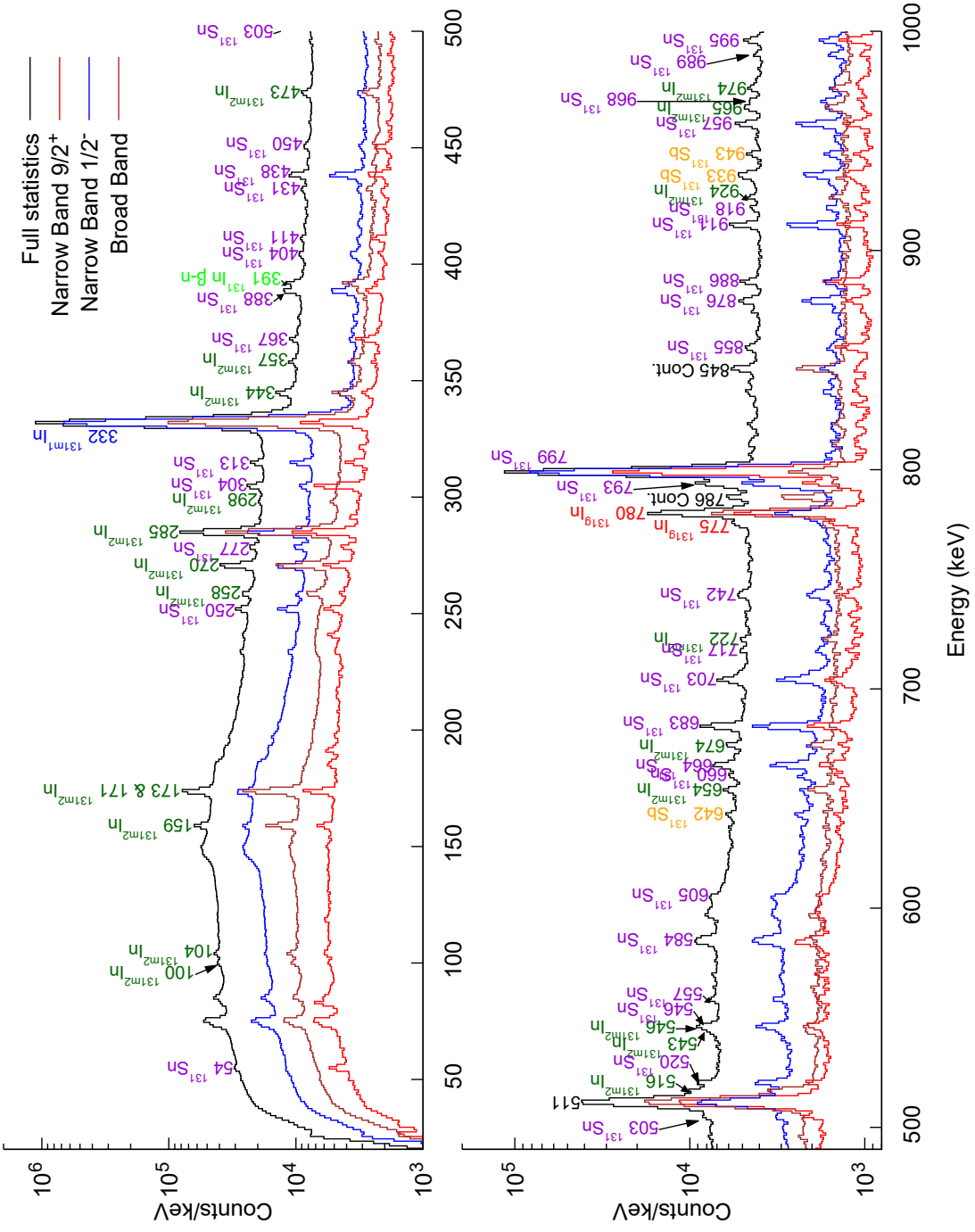

Figure 6.6: Beta-gate HPGe-spectra recorded for ^{131}In decay up to 1 MeV. Gamma lines are labeled with their respective energy and the assumed isotope from which they have been emitted. The strongest lines in this energy region is the $(1/2^+ \rightarrow 3/2^+)$ 332-keV transition in ^{131}Sn, and the $(5/2^+ \rightarrow 7/2^+)$ 798-keV in ^{131}Sb.

This γ-ray appears with similar intensity in all the spectra, except for the one measured with broad-band RILIS. The cause of this suppression for the daughter activity is that the tape was set to move after every proton pulse for those particular measurements. A large number of weaker transitions appears also in this energy region. Many of these peaks are mainly due to γ-rays produced in ^{131m2}In decay, such as the 158-, 173- and 284-keV lines which are related to transitions between high-spin levels located around 4 MeV in ^{131}Sn. The remaining peaks mostly belong to transitions in ^{131}Sb, except for the 391-keV transition, which has been identified as a γ-ray from ^{130}Sn emitted in the β-delayed neutron decay of ^{131}In.

Within the energy region from 1 to 2.5 MeV, Figure 6.7, the strongest γ-line corresponds to the $7/2^+ \rightarrow 3/2^+$ 2434-keV transition, together with its two escape peaks, between single-hole $\nu g_{7/2}^{-1}$ and $p_{3/2}^{-1}$ states in ^{131}Sn. Another strong peak is the 1655-keV line that has its origin in a transition between single-hole states in ^{131}Sn, $\nu d_{5/2}^{-1} \rightarrow p_{3/2}^{-1}$. Regarding the other peaks in the spectra, most of them can be ascribed to γ-rays emitted either from the ^{131}Sn or ^{131m2}In decays. Another peak that stands out notably in this region is the one originating from the 1221-keV transition from the β-delayed neutron decay branch in ^{131}In, that seems to be strengthened in the narrow band $[1/2^-]$ spectrum.

Gamma-rays can be observed up to very high energies in the HPGe spectrum, up to the detection limit around 7 MeV. Due to the energy available in the ^{131}Sn decay Q_β = 4717(4) keV [WGK$^+$17], the γ-lines from this decay do not appear in this energy range. Luckily almost all of them arise from the decay of ^{131}In. The analysis of the spectra becomes more complex from this point onwards, due to the presence of the escape peaks. Most of the peaks are due to the de-population of high-energy core-excited levels that decay directly to the ground state or to the $11/2^-$ isomer in ^{131}Sn.

In this region γ-rays from the decay of the three indium isomers can be observed. However the situation changes above the neutron separation energy of ^{131}Sn, S_n =5204(4) keV [KMR06]. A large number of γ-rays emitted with the time distribution of indium can still be found. A remarkable fact is that all these transitions are emitted only by the decay of the ground state, ^{131g}In.

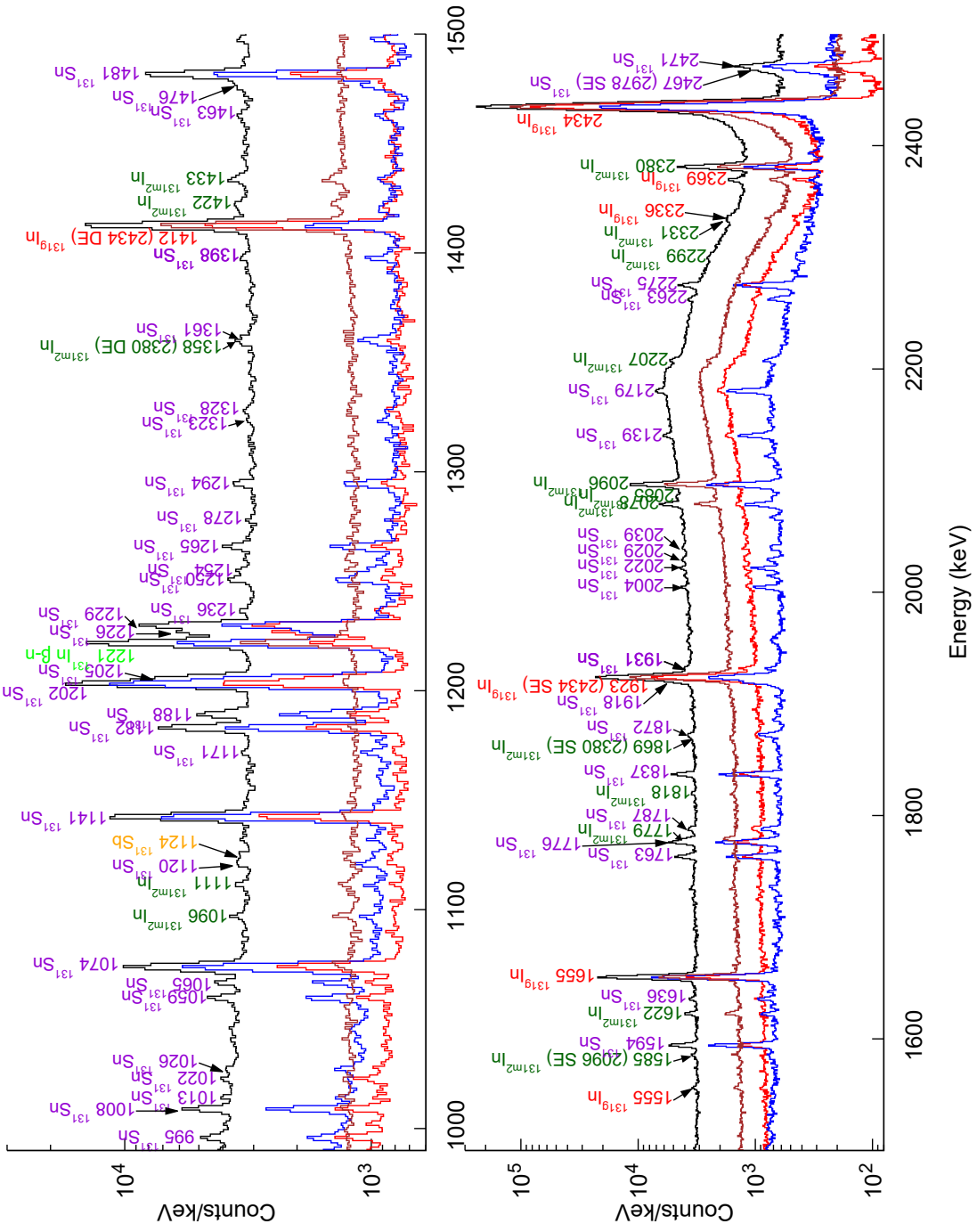

Figure 6.7: Beta-gate HPGe-spectra recorded for ^{131}In decay, in the 1-2.5 MeV range. The strongest peak corresponds to the 2434-keV γ-ray, along with its escape peaks, which arise from to the $7/2^+ \rightarrow 3/2^+$ transition between single-hole states in ^{131}Sn.

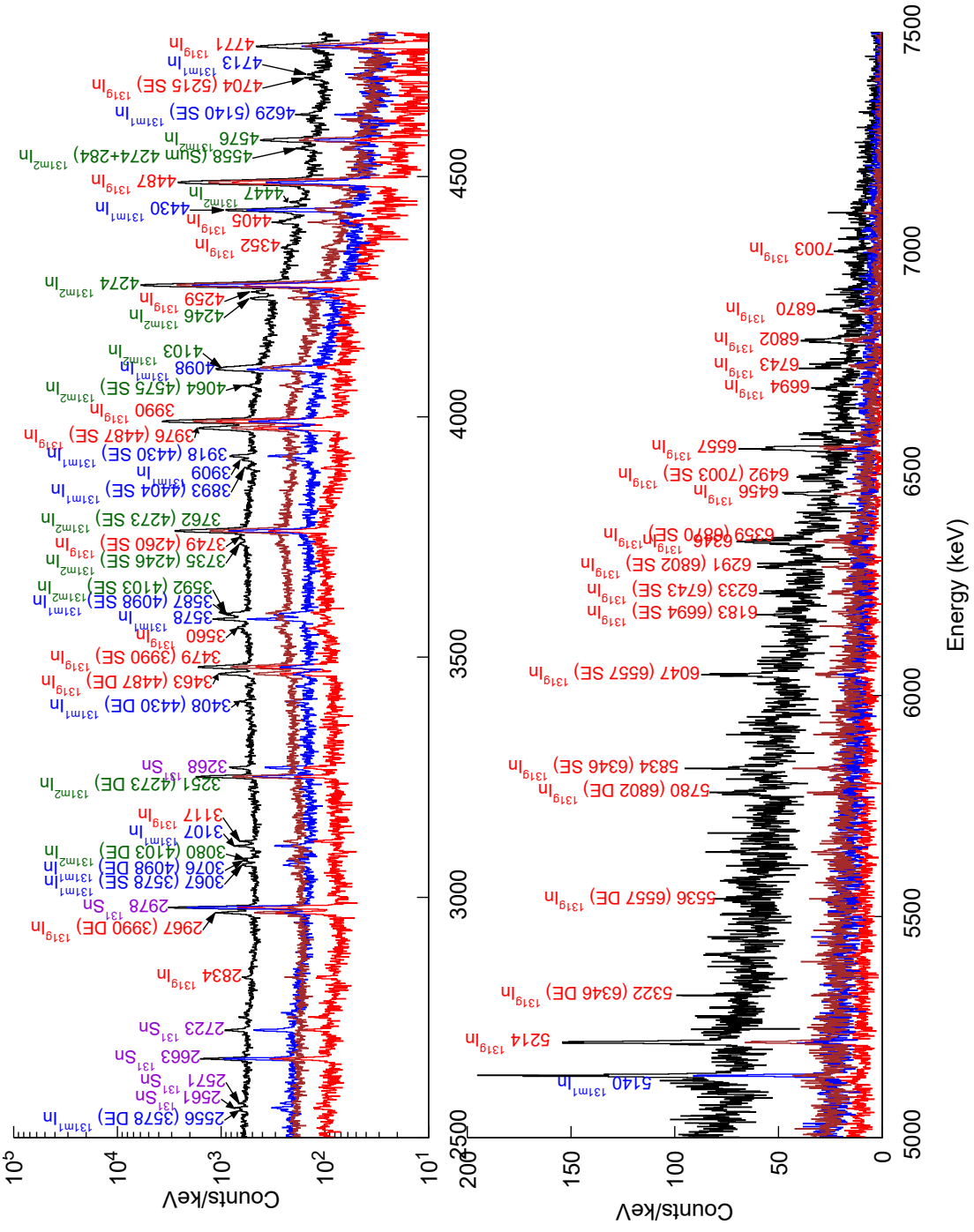

Figure 6.8: Beta-gate HPGe-spectra recorded for ^{131}In decay, in the 2.5-7 MeV range. Mostly all the transitions observed at this high energy have been identified as γ-rays from the decay of ^{131}In, owing to the agreement between their time distributions with the short lifetime of indium isomers. These γ rays can be related to the transitions from high-lying core-excited levels to either the ground state or the $11/2^-$ isomer.

6.5 Level scheme of ^{131}Sn populated in the ^{131m1}In decay.

In this subsection the population of excited levels in ^{131}Sn through the β decay of the ^{131m1}In isomer with $J^{\pi} = (1/2^{-})$ will be discussed. The ^{131}In isotope, with $Z = 49$ and $N = 82$, has one proton less than the doubly magic ^{132}Sn. Similar to the ^{131}Sn case, its structure can be interpreted as the coupling of a hole to the closed ^{132}Sn, but in this case a proton hole in the $Z = 50$ shell. From this interpretation, two types of states are expected. The first one concerns single particle levels at low excitation energy. They correspond to the proton orbitals close to the Fermi energy where a proton hole can be created (see Figure 1.3 in Chapter 1). The second kind of states are the core-excited levels that appear at much higher excitation energies, above 3.5 MeV. Those levels are generated by excitations of the core, where one nucleon, either a proton or a neutron, is promoted across the shell gap. The $(1/2^{-})$ isomer is the first-excited state of ^{131}In, located at 302(32) keV [FGM^{+}04b]. Due to the large difference in angular momentum with the ground state $(9/2^{+})$ the γ transition between these two states is highly forbidden. An M4 multipolarity would be required for a direct transition, thus β decay becomes the dominant decay process for this level.

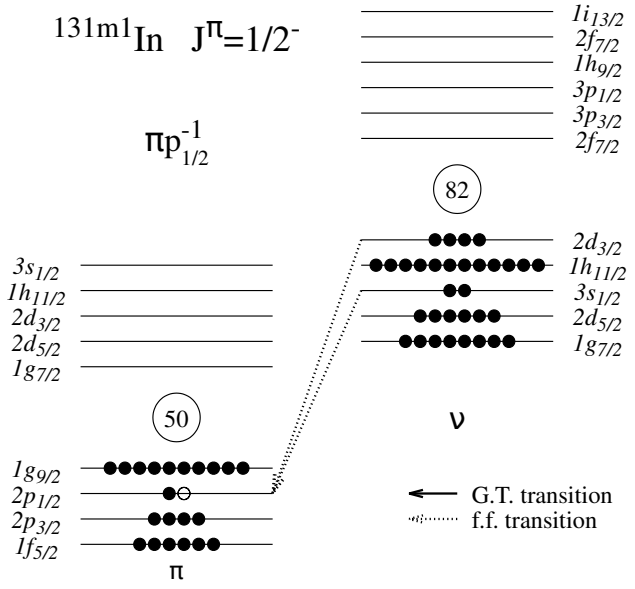

Figure 6.9: Shell model configuration for ^{131m1}In.

In the extreme shell model, the $(1/2^-)$ isomer is identified with the $\pi p_{1/2}^{-1}$ single particle hole configuration, see Figure 6.9. The β decay of this isomer leads to two first forbidden transitions, $\nu s_{1/2} \rightarrow \pi p_{1/2}$ and $\nu d_{3/2} \rightarrow \pi p_{1/2}$. Therefore, the $1/2^+$ first excited level and the $3/2^+$ ground state of ^{131}Sn are expected to be predominantly populated during this decay. The direct population of the remaining single particle levels, would require forbidden transitions, of second or higher grade, and thus is not expected to populate those states in this decay. However, the large Q_β = 9240(5) keV [WAK$^+$17] opens the possibility of populating levels at high excitation energy such as core excited levels, for which a low angular momentum of J = (1/2,3/2) would be expected given β-decay selection rules.

The γ-rays emitted after the β-decay of the ^{131m1}In isomer have been identified as those γ lines whose intensity is enhanced in the RILIS $[1/2^-]$ spectrum, but suppressed in the RILIS $[9/2^+]$ one, as is illustrated in Figures 6.6, 6.7 and 6.8. The strongest γ line associated with ^{131m1}In decay is the 332-keV γ-ray. In addition to this this peak, a total of 8 transitions emitted by the de-excitation of 7 different excited levels, have been confirmed in this work. In the previous β-decay studies [FGM$^+$04a, DSA$^+$19], the only transitions that were associated with this level were those confirmed by γ-γ coincidences with the 332-keV γ-ray. In this work all those assignments were confirmed (see coincident spectrum in Figure 6.10), with the exception of the 1322-keV γ-ray from the 1654→332 keV transition, which was not observed in the 332-keV coincident spectrum. Nevertheless the population of the 1655-keV $(5/2^+)$ single particle level was confirmed in ^{131m1}In decay by the comparison of its relative intensity in the RILIS $[9/2^+]$ spectra. In addition, two new high-energy γ-rays at 4712.6 keV and 5139.9 keV were assigned to this decay (supported by their relative increase in intensity observed in the RILIS $[1/2^-]$ γ-ray spectra compared to the RILIS $[9/2^+]$ γ-ray spectra), see Figure 6.8.

The observed decay-scheme from ^{131m1}In populating both ^{131}Sn and ^{130}Sn is depicted in Figure 6.11, and the γ-rays in ^{131}Sn with their relative intensity are listed in Table 6.1. The intensities for the direct β-feeding was determined from the balance between the populating and de-exciting transitions to each level. The direct ground state feeding to ^{131}Sn and ^{130}Sn, was estimated from the balance between the γ-ray feeding and the total decays intensity of each tin isotope. The total number of ^{131}Sn→^{131}Sb decays was estimated from the γ-ray intensities in ^{131}Sn. The previous measurements for

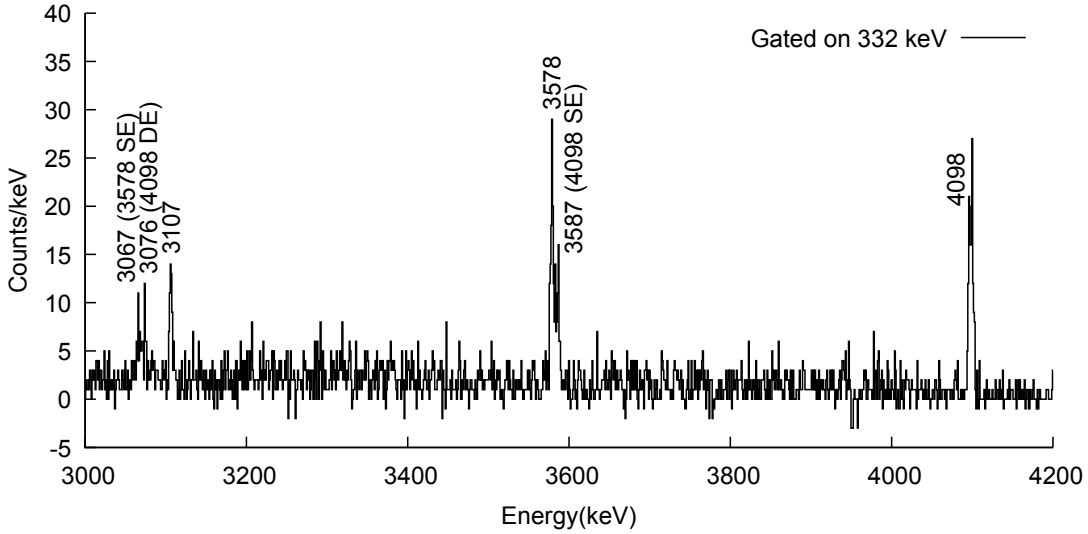

Figure 6.10: Compton subtracted $\beta\gamma\gamma$ energy spectrum gated on the 332-keV $\nu s_{1/2} \rightarrow \nu d_{3/2}$ transition. Within this energy range it can be found the 3107-, 3578- and 4098-keV γ-rays can be found.

Table 6.1: γ-ray intensities from ^{131m1}In$\rightarrow^{131}$Sn β decay

E_i (keV)	J_i^π	E_f (keV)	J_f^π	E_γ (keV)	I_γ^a (%)
331.6(3)	$(1/2^+)$	0.0	$(3/2^+)$	331.6(3)	100
1654.7(3)	$(5/2^+)$	0.0	$(3/2^+)$	1654.7(3)	3.7(4)
3438.4(4)	$(3/2^-)$	331.6(3)	$(1/2^+)$	3106.8(4)	0.20(4)
3910.0(3)	(1/2,3/2)	331.6(3)	$(1/2^+)$	3578.4(3)	0.65(8)
4429.6(3)	(1/2,3/2)	0.0	$(3/2^+)$	4429.8(3)	1.2(2)
		331.6(3)	$(1/2^+)$	4097.9(4)	0.8(1)
4712.6(5)	(1/2,3/2)	0.0	$(3/2^+)$	4712.6(5)	0.11(3)^b
5139.9(4)	(1/2,3/2)	0.0	$(3/2^+)$	5139.9(4)	0.21(4)^b

^{a} Relative γ intensities normalized to 100 units for the 332-keV $1/2^+ \rightarrow 3/2^-$ transition.
For intensity per 100 decays of the parent ^{131m1}In, multiply by 0.42(12).

^{b} Intensity derived from β-gated spectrum.

^{131}Sn decay did not decouple the β-decay of the $(3/2^+)$ and $(11/2^-)$ isomers [HPRS81]. However, in the decay of the $(1/2^-)$ ^{131}In isomer it is not expected to populate the $(11/2^-)$ ^{131}Sn isomer due to the large spin difference. Thus, the absolute intensity of

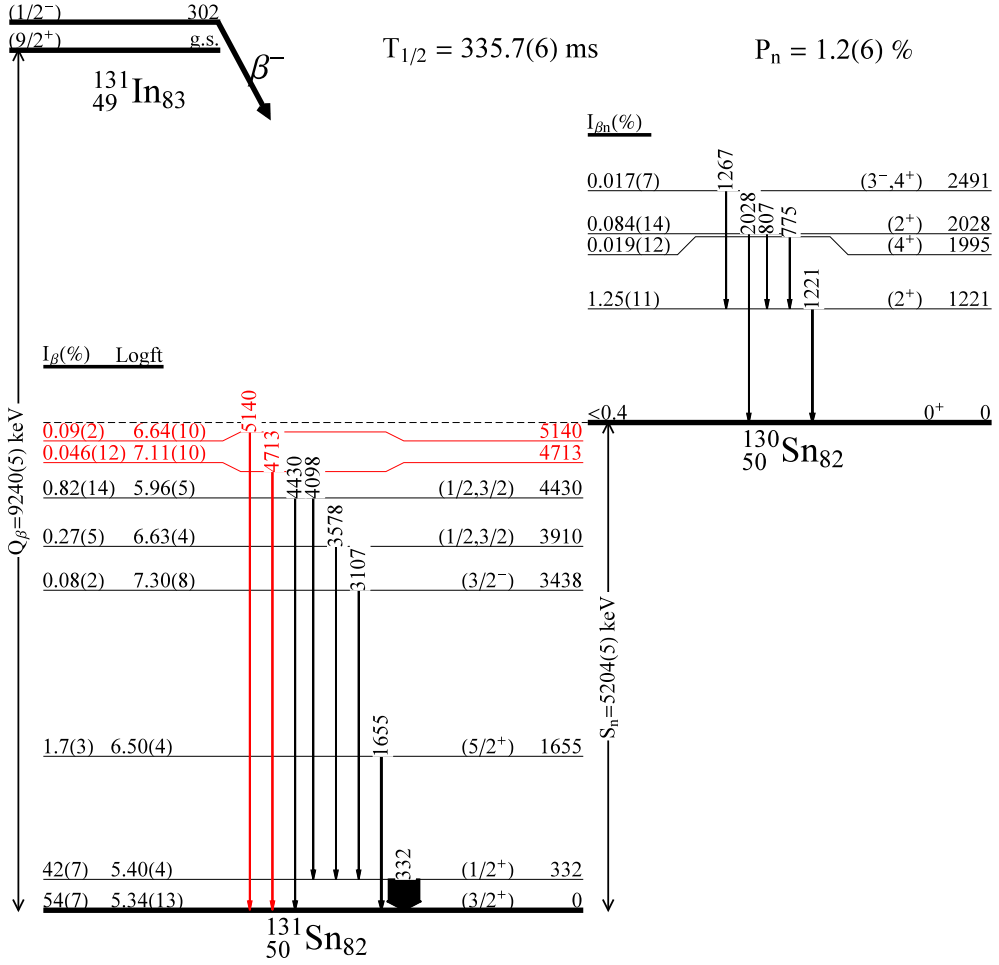

Figure 6.11: Decay scheme of ^{131m1}In $(1/2^-)$ to ^{131}Sn and ^{130}Sn.

the ^{131}Sn $(3/2^+)$ $\rightarrow$^{131}Sb decay has been calculated from the analysis of the γ-ray intensities in the RILIS $[1/2^-]$ spectra. In particular, an absolute intensity of 57(3)% was estimated for the 798-keV γ-ray, the most intense transition in the β-decay of the ^{131}Sn ground state. On the other side, the total intensity of ^{130}Sn decay was estimated using the absolute intensities from [Sto87]. In this case only the transitions coming from the 0^+ ground state were considered, since it is not expected either that the ^{130}Sn (7^-) isomer is populated in the ^{131m1}In decay.

In order to compare the number decays measured for the ^{131}Sn and ^{130}Sn daughters, it is necessary to correct by the fraction of decays that are not observed due to the movement of the tape at the end of the super-cycle. This fraction has been calculated

from Bateman equations, where the indium implantation pattern has been taken into account. It is defined by the proton pulse structure from the super-cycle, and the lifetimes of the In parent and Sn daughter considered in each case. Due to the short half-life of ^{131m1}In 335.7(6) ms, it is estimated that that only 1% of the total decays are not observed. The ^{131}Sn isotopes have a much longer lifetime, $T_{1/2}$=54.0(6) s [KMR06], and our calculation yielded that only 20% of the implanted indium isotopes have already decayed into ^{131}Sb. For the β-n decay branch the half-life of ^{130}Sn is even longer, $T_{1/2}$ = 3.72(7) min [KMR06], thus the measured intensity fraction is only a 6% in this case. These factors have been taken into account for the estimation of the total number of Sn decays. They have been used to normalize the feeding intensity and to calculate the ground state feeding.

Considering the ^{131}Sn decay intensities, it was estimated that the ^{131}Sn $(3/2^+)$ g.s. receives 54(7)% of the β feeding, while the 332-keV $(1/2^+)$ state receives a 42(7)%. These results differ significantly from the 68.1(22)% and 27.8(7) % values reported in [DSA$^+$19] or the 95% and 3.5(9)% reported in [FGM$^+$04a]. These difference seems to be motivated by the inability of these previous studies to separate the production of each indium isomer. Because this limitation, an important fraction of the $\nu g_{9/2}^{-1} \rightarrow \nu h_{11/2}^{-1}$ transition intensity in ^{131g}In decay was erroneously assigned to the g.s. feeding in the ^{131m1}In. Using the β-feeding derived in this work, two similar logft values of 5.34(5) and 5.40(4) were obtained for the $(3/2^+)$ and $(1/2^+)$ states respectively. These values are coherent with the expected f.f. behaviour of the $\nu p_{1/2}^{-1} \rightarrow \nu d_{3/2}^{-1}$ and $\nu p_{1/2}^{-1} \rightarrow \nu s_{3/2}^{-1}$ transition.

6.5.1 β-delayed neutron decay of ^{131m1}In decay

Apart from the excited levels in ^{131}Sn, we have studied also the population of the excited levels in ^{130}Sn via the β-delayed neutron emission from ^{131m1}In. The emission of γ-rays was already reported in [DSA$^+$19], however it was not possible to distinguish which levels were populated from which isomer. Thanks to the isomer selectivity, in our work it is now possible to study β-n branches for each isomer separately. In the decay of ^{131m1}Sn, the most intense γ-ray from the β-n branch observed is the 1221-keV peak, which corresponds to the de-excitation of the first excited (2^+) in ^{130}Sn. Besides this level, the population of the levels 1995 keV (4^+), 2028 (2^+) and 2491 $(3^-,4^+)$ was also confirmed by γ-γ coincidences with the 1221-keV transition.The small 96- and 396-keV

γ-peaks arise from the contaminant for the others two isomers in the RILIS [$1/2^-$] indium decay spectrum. Taking into account the estimated g.s. feedings the β-delayed one neutron emission can be estimated. From this calculation a small P_n=1.2(6)% value was derived for this decay, where only the decay intensity of the ^{131g}Sn ($3/2^+$) and ^{130g}Sn 0^+ ground states have been considered.

6.6 Decay scheme of the ^{131g}In to ^{131}Sn.

In this subsection, the excited structure populated in the β-decay of ^{131g}In ($9/2^+$) will be discussed. The ground state in ^{131}In ($9/2^+$), similarly the ($1/2^-$) isomer, is built from the $\pi g_{9/2}^{-1}$ proton hole configuration (see Figure 6.12). Given this interpretation, the most favorable decay-path for this state is the Gamow-Teller (GT) $\nu g_{7/2} \rightarrow \pi g_{9/2}$ allowed transition. This GT transition would feed the $\nu g_{7/2}^{-1}$ level in ^{131}Sn, which is identified with the 2434-keV ($7/2^+$) level. The second strongest transition would be the first forbidden (f.f.) $\nu h_{11/2} \rightarrow \pi g_{9/2}$ transition, where the ($11/2^-$) isomer in ^{131}Sn is directly populated. This interpretation is coherent with the experimental results obtained by previous works, where the ($7/2^+$) and ($11/2^-$) states, were estimated to receive 90% and 5% of the total decay intensity respectively [DSA$^+$19]. Apart from these two single particle states, is not expected to observe a direct population to the remaining states due to the higher degree of forbiddeness. Besides the single particle levels at low energy, the large Q_β from indium decay makes it possible to populate high energy states above 4 MeV, which are built from the coupling of a neutron hole to excitations of the ^{132}Sn core.

The investigation of γ-rays emitted in this decay has been performed following the same methodology than for the ^{131m1}In ($1/2^-$) decay. The transitions in ^{131}Sn have been identified by the compatibility of their time distributions with the decay of indium. We have assigned to the decay of the ground state those transitions whose intensities are strengthened in the RILIS [$9/2^+$] spectra but suppressed in the RILIS [$1/2^-$] (Figures 6.6, 6.7 and 6.8), and the γ-rays from ^{131}Sn with their relative intensity are listed in Table 6.2. The strongest γ-lines in the spectrum, assigned to ($9/2^+$) decay, are the 2434-, 780-, 1655-keV peaks, which arise from transitions connecting the GT fed ($7/2^+$) state to the $5/2^+$ and $3/2^+$ single particle states. There are two peaks at 3990 and 4487 keV with sizeable intensity, which can be assigned to this decay. They are interpreted as

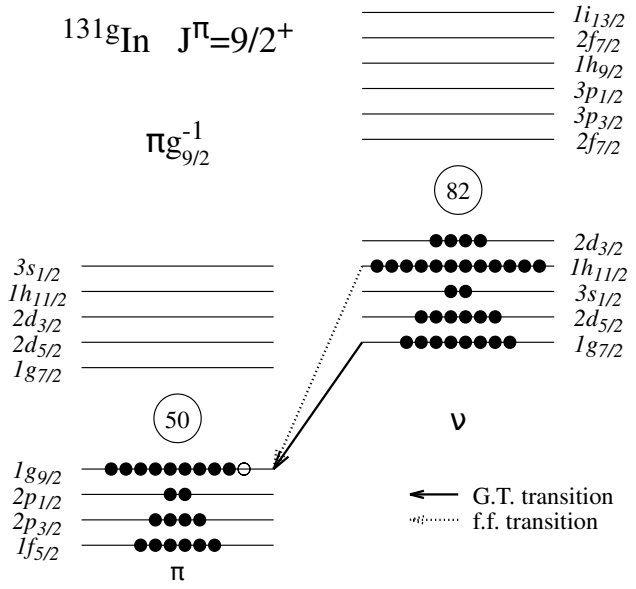

Figure 6.12: Shell model configuration for the ^{131g}In to ^{131}Sn decay.

transitions from core-excited states to the $(3/2^+)$ ground state. Along with them, there is a good number of states from 3.5 to 5 MeV with a small feeding, which de-excite via transitions to the $(3/2^+$, $5/2^+$ and $7/2^+)$ single particle levels.

Table 6.2: γ-ray intensities from ^{131g}Inβ decay

E_i (keV)	J_i^π	E_f (keV)	J_f^π	E_γ (keV)	I_γ^a (%)
1654.7(6)	$(5/2^+)$	0.0	$(3/2^+)$	1654.7(6)	2.4(4)
2434.1(6)		0.0	$(3/2^+)$	2434.1(6)	100
	$(7/2^+)$	65.1(5)	$(11/2^-)$	2368.7(7)	0.20(4)
	$(7/2^+)$	1654.7(6)	$(5/2^+)$	779.6(7)	2.2(4)
3989.6(6)	$(7/2^+)$	0.0	$(3/2^+)$	3989.6(7)	3.7(6)
	$(7/2^+)$	1654.7(6)	$(5/2^+)$	2335.9(8)	0.12(3)
	$(7/2^+)$	2434.1(6)	$(7/2^+)$	1555.4(7)	0.15(4)
4259.1(10)	0	0.0	$(3/2^+)$	4259.1(10)	0.15(4)
4352.4(10)	0	0.0	$(3/2^+)$	4352.4(10)	0.06(3)
4404.5(5)	$(7/2^+)$	0.0	$(3/2^+)$	4404.6(8)	0.15(4)
	$(7/2^+)$	1654.7(6)	$(5/2^+)$	2750.6(8)	0.08(2)
	$(7/2^+)$	2434.1(6)	$(7/2^+)$	1969.4(8)	0.08(2)
4486.8(6)	$(7/2^+)$	0.0	$(3/2^+)$	4486.7(7)	3.6(7)
	$(7/2^+)$	1654.7(6)	$(5/2^+)$	2833.8(7)	0.19(4)
	$(7/2^+)$	2434.1(6)	$(7/2^+)$	2053.0(7)	0.10(2)

E_i (keV)	J_i^π	E_f (keV)	J_f^π	E_γ (keV)	I_γ^a (%)
4771.1(8)		0.0	0	4770.9(7)	0.28(6)
		1654.7(6)	$(7/2^+)$	3116.8(8)	0.12(3)
5110.3(11)		2434.1(6)	$(5/2^+)$	2676.2(9)	0.08(4)
5214.3(6)		0.0	$(3/2^+)$	5214.0(8)	0.19(5)
		1654.7(6)	$(5/2^+)$	3560.0(8)	0.12(3)
5412.7(10)		0.0	$(3/2^+)$	5412.7(10)	0.07(3)
		2434.1(6)	$(7/2^+)$	2978.4(6)	<0.1
5594.7(13)		1654.7(6)	$(5/2^+)$	3940.1(12)	0.12(3)[b]
5646.6(11)		0.0	$(5/2^+)$	5646.5(11)	0.07(2)[c]
		1654.7(6)	$(5/2^+)$	3993.5(8)	0.004(2)[c]
6193.6(7)+y		y		6193.6(7)	0.026(6)[c]
6321.7(8)+y		y		6321.7(8)	0.041(10)[c]
6345.8(7)+y		y		6345.8(7)	0.12(2)[c]
6457.0(7)+y		y		6457.0(7)	0.065(14)[c]
6557.3(7)+y		y		6557.3(7)	0.12(2)[c]
6591.2(8)+y		y		6591.2(8)	0.024(7)[c]
6694.1(7)+y		y		6694.1(7)	0.035(8)[c]
6743.3(7)+y		y		6743.3(7)	0.08(2)[c]
6800.0(8)+y		y		6800.0(8)	0.058(14)[c]
6806.0(11)+y		y		6806.0(11)	0.028(9)[c]
6870.2(7)+y		y		6870.2(7)	0.068(14)[c]
7003.3(9)+y		y		7003.3(9)	0.023(8)[c]
7090.9(10)+y		y		7090.9(10)	0.028(10)[c]

[a] Relative γ intensities normalized to 100 units for the 2434-keV $7/2^+ \rightarrow 3/2^-$ transition. For intensity per 100 decays of the parent ^{131g}In, multiply by 0.65(11).
[b] Intensity derived from $\gamma\gamma$ coincidences.
[c] Intensity derived from β-gated spectrum.

6.6.1 Feeding to β-decaying states and β-delayed neutron decay branch.

The direct ground state feeding to ^{131}Sn and ^{130}Sn, was estimated from the balance between the γ-ray feeding and the total decays intensity of each tin isotope. In the case of ^{130g}In decay it is possible to populate both the two β-decaying states in ^{131}Sn, as well as the 0^+ and (7^-) β-decaying states in ^{130}Sn. The total number of decays for each decay have been derived from the γ-ray intensities. However, the previous studies on ^{131}Sn did not disentangle the decay of the two β-decaying states. Hence, the absolute intensities for the γ-rays from ^{131}Sn $(3/2^+)$ and $(11/2^-)$ states, have been obtained from our data. In particular, the absolute intensity for ^{131}Sn $(3/2^+)$ decay is taken from the ^{131m1}In decay dataset, while the intensities from ^{131}Sn $(11/2^-)$ have been measured

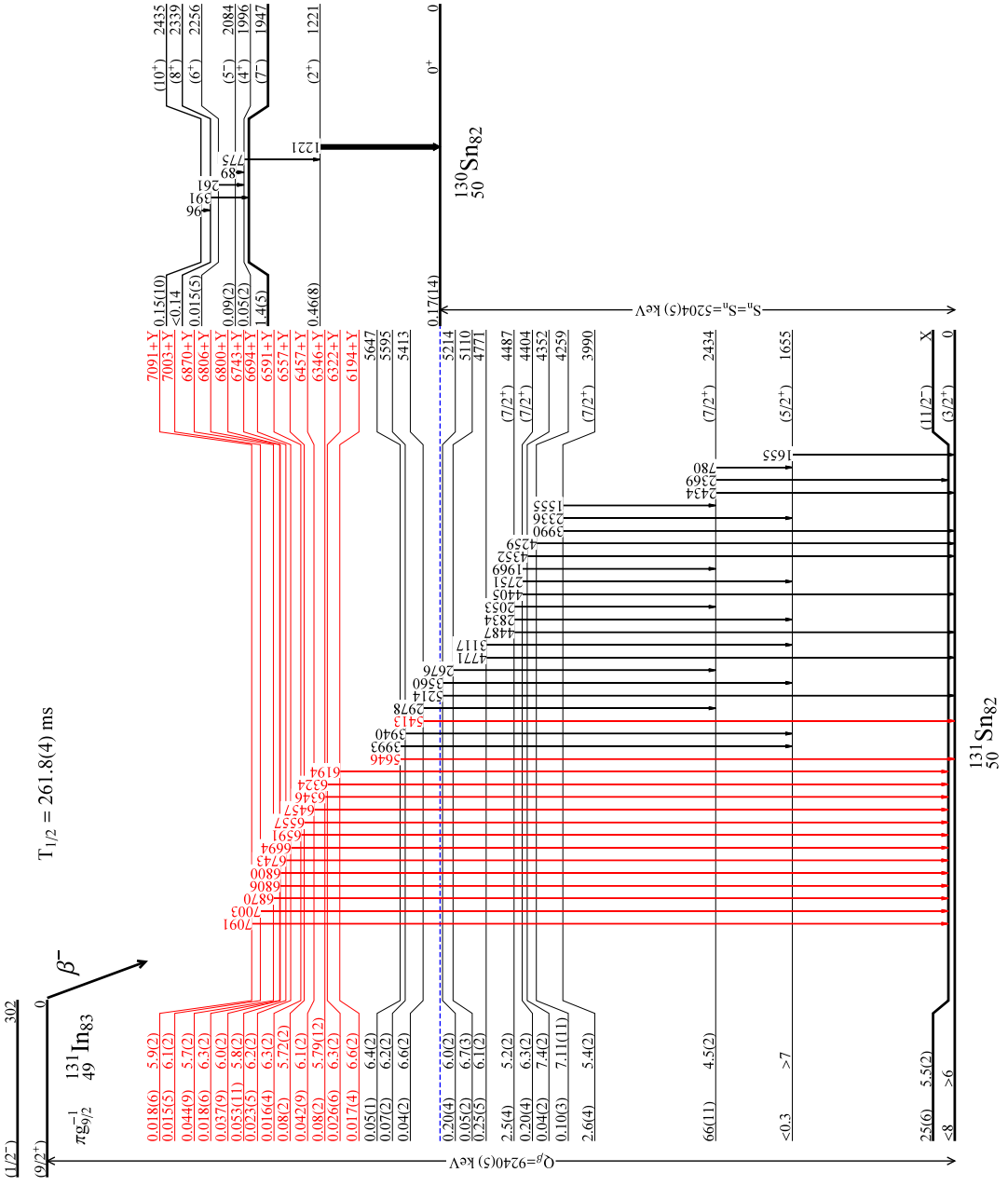

Figure 6.13: Level scheme in ^{131}Sn populated in the decay of ^{131g}In $9/2^+$ isomer.

from the ^{132}In (7^-) decay. For the β-n branch, the γ-rays absolute intensities for both 0^+ and 7^- states have been taken from [Sto87].

Our analysis yields a negligible population to the ($3/2^+$) ^{130}Sn and (0^+) ^{130}Sn levels. This result was to be expected due to the spin difference with the ^{131g}In ($9/2^+$) initial state. The ($11/2^-$) state receives a 26(6)% of the total feeding. This value contrast notably with the 5^{15}_{-5}% β-feeding reported in [DSA$^+$19]. As mentioned in the ^{131m1}In decay subsection, an important part of the ($11/2^-$) state feeding was erroneously assigned to the g.s. feeding in ^{131m1}In, resulting in a reduced apparent feeding to ($11/2-$) state. However, the 1226-keV γ-ray from ^{131m1}Sn ($11/2^-$) decay is notably enhanced the narrow-band [$9/2^+$] spectrum. This indicates a non-negligible population of the ($11/2^-$) state in ^{131g}In decay. This new value indicates a logft=5.6(1) value for the first forbidden $\nu g^{-1}_{9/2} \rightarrow \nu h^{-1}_{11/2}$ transition, which is compatible with the other two f.f. transitions measured in ^{131m1}In decay. Taking into account the estimated g.s. feeding from this work we have calculated a P_n=2.4(6)% value for the ^{131g}In decay.

6.6.2 High-energy γ-rays emission in ^{131g}In decay

An interesting feature observed in this decay is the presence of a large number of γ lines of very high energy, up to 7 MeV, see Figure 6.8. These γ-lines appears in the β-gated spectra and show a time distribution compatible with the decay of indium, thus we can assign them to the decay of ^{131}In. The presence of such γ-rays is already reported in [DSA$^+$19], but without assignment to the decay of any specific isomer. Thanks to the isomer selectivity provided by RILIS, we were able to confirm that almost all of them belong only to the decay of the ^{131g}In ($9/2^+$) ground state. A certain inconsistency has emerged between the energy of the high-energy γ-rays reported in [DSA$^+$19], and those measured in this work. Actually, it was not possible to identify any of the γ-rays at the energy values that were reported in the work by Dunlop *et al.* The energy calibration in our work has been cross-checked using neutron capture γ-lines in ^{56}Fe (from the set-up frame) and ^{73}Ge (from the detectors). These lines are produced by the neutrons emitted from the target area during irradiation. Thanks to this, we have γ-lines available up to 7.6 MeV in the same indium decay data set, which can be used for internal calibration. This makes us confident of our calibration.

The analysis of this energy region is complex due to the low FEP efficiency and the large number of escape peaks. To distinguish the escape from the full-energy ones, the

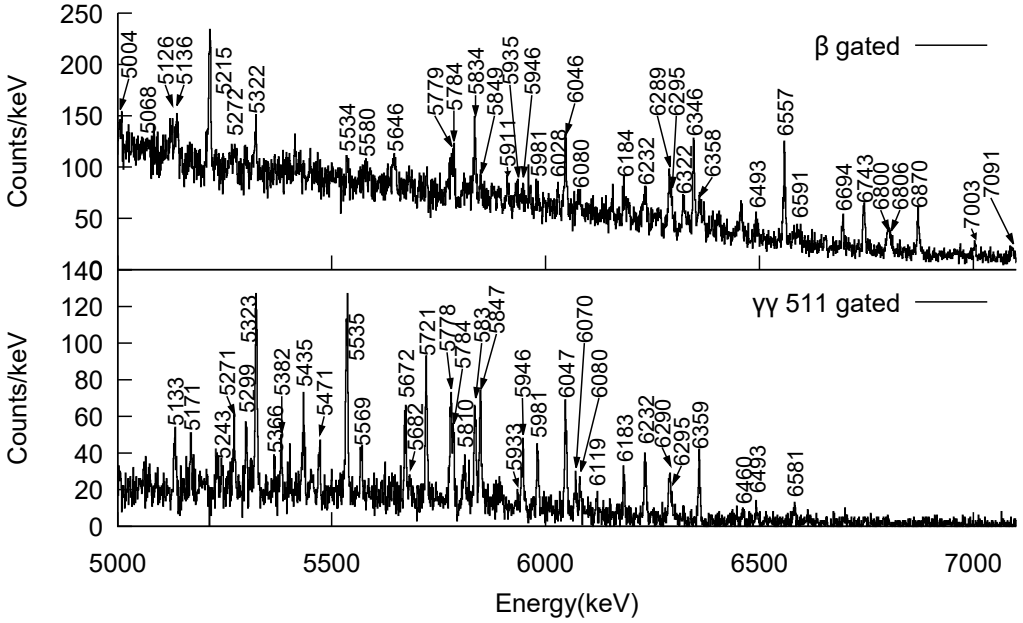

Figure 6.14: High energy γ-rays emitted in ^{131g}In decay. (Top) Beta-gated energy spectrum recorded following the decay of ^{131}In. (Bottom) $\gamma\gamma$ coincidence spectrum, gated on the 511-keV peak.

$\gamma\gamma$ coincidence spectrum with a gating on the 511-keV peak has been analyzed (Figure 6.14 (Bottom)). This spectrum was built without applying add-back correction, in order to avoid losing efficiency for the escape peaks Therefore, we have confirmed these γ-rays for which the full-energy peak in the β-gate spectrum, along with their two corresponding escape peaks in the $\gamma\gamma$ 511-gated one, has been identified

Another uncertainty of these high energy γ-rays is where their position in the level-scheme is. None of them show any detectable coincidence, so they must be directly populated in the β decay of indium and they de-excite directly to either the $(3/2^+)$ g.s. or the $(11/2^-)$ isomer. Given the expected $J^\pi = (9/2^+)$ from the parent isomer, it is safe to assume that these levels will have an angular momentum within one unit from that of the parent, J =(7/2−11/2). Given those possibilities, only these levels with $J^\pi = (7/2^+)$ would rather decay via an E2 γ transition, the remaining ones $(7/2^-$,9/2,11/2) would decay predominantly to the $11/2^-$ isomer via E2,M1 and E1 transitions. Having this into consideration, we can assume that most of those transitions are connected to the $11/2^-$ isomer, since only the $7/2^+$ states would rather decay to the ground state.

However, the lack of confirmation by $\gamma\gamma$ coincidences does not allow us to rule out any of the two possibilities for any state. To conclude, we have included those γ-rays to the level-scheme (see Figure 6.13, de-exciting level whose energy has been labeled as E_γ+Y, where Y can be either 0 or X (the energy of the $11/2^-$), but not necessarily the same for all levels.

An striking feature of these levels is that they appear at very high energies above the neutron separation energy S_n =5204(4) keV [KMR06], which means that they are particle unbound, and that γ-ray emission is a competitive process to the neutron emission. There is a large amount of states and they carry $\sim$0.5% of the β population from the $9/2^+$ state. In the level-scheme shown in Figure 6.13, it can be noted that among these levels that exist above the energy of ^{130}Sn g.s., a large number of them placed above the 6425(4) keV limit corresponding to the energy of the first-excited 1221-keV (2^+) level in ^{130}Sn. However, there are no γ-rays from excited levels above 7.1 MeV. This might be caused by the insufficient efficiency of the HPGe detectors at that energy. It should be also noticed that the energy at which these unbound levels are no longer present, corresponds to the energy at which the (7^-) isomer in ^{130}Sn, along with other excited high-spin levels, starts to appear. One may hypothesize that the presence of those high spin levels reduces the possibility of decay by γ emission. Above that energy, the unbound levels would have below them a lot of levels in ^{130}Sn with a low difference in angular momentum, thus they will rather decay via neutron emission with low l. However, for the unbound levels below the energy of the (7^-) isomer, the only possibility to decay via neutron emission are the 2^+ and 0^+ levels in ^{130}Sn. Therefore, the levels populated in the ^{131g}In decay for which a J = (7/2-11/2) is expected, would require a large change in angular momentum for some cases Δl =1$-$5. Hence, neutron emission would be suppressed.

6.6.3 Analysis of $\gamma\gamma$ coincidences.

To conclude the study of the γ-rays emitted in the decay of ^{131g}In ($9/2^+$), the $\gamma\gamma$ coincidence spectra for the two strongest transitions from this decay, the 1655- and 2434-keV γ-lines have been analyzed. In Figure 6.15 (Top) the coincidence spectrum for both transitions is shown. The strongest coincident transition is the 779-keV γ-ray which belongs to the $(7/2^+)\rightarrow(5/2^+)$ transition that de-excites the single particle 2434-keV level. Besides, there is a number of smaller peaks which arise at higher energies.

They arise from by transitions from high-energy core-excited levels, which de-excite via the 1655-keV level. There are no new transitions identified besides those quoted in [FGM$^+$04a, DSA$^+$19].

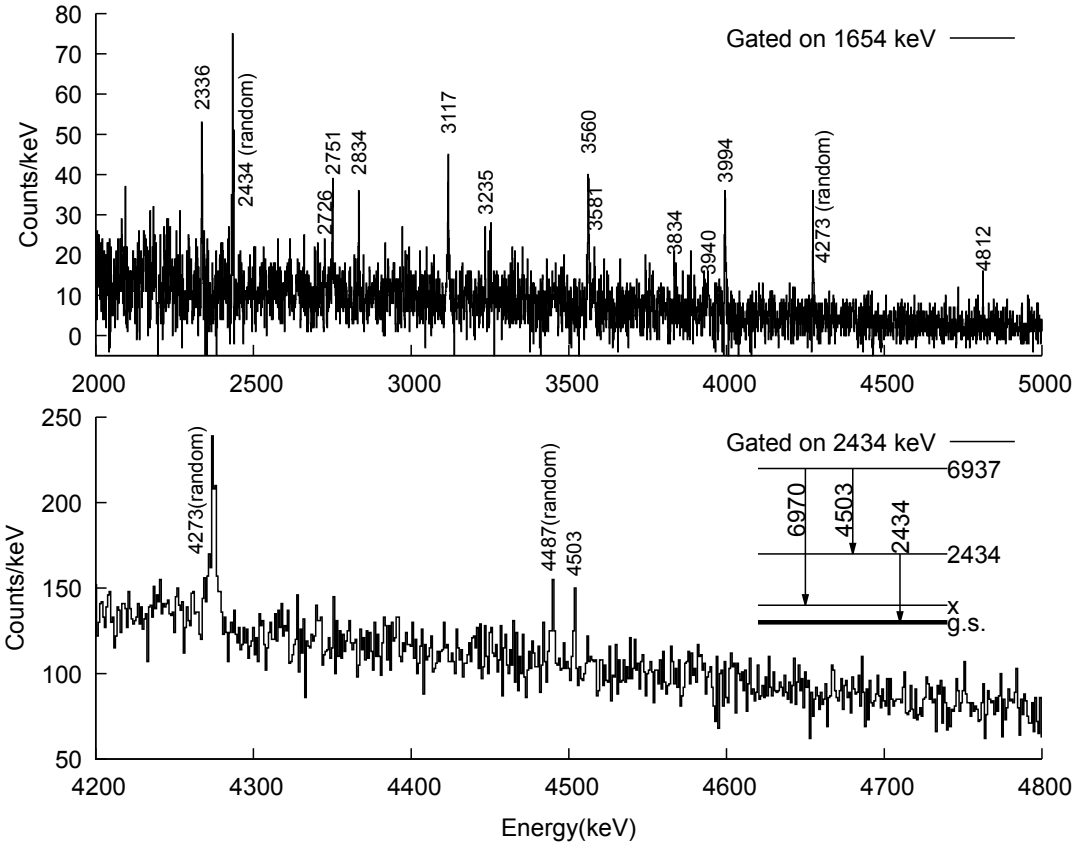

Figure 6.15: Compton subtracted $\gamma\gamma$ energy spectrum gated on the 1655-keV transition $\nu d_{5/2}^{-1} \rightarrow \nu d_{3/2}^{-1}$. (Top) Compton subtracted $\gamma\gamma$ energy spectrum gated on the 1655-keV transition $\nu d_{5/2} \rightarrow \nu d_{3/2}$. (Bottom) Compton subtracted $\gamma\gamma$ energy spectrum gated on the 2434-keV transition $\nu g_{7/2}^{-1} \rightarrow \nu d_{3/2}^{-1}$.

The coincident spectra for the 2434-keV transition has been also studied, see Figure 6.15 (Bottom). However, the very weak feeding to this level by γ rays made it very difficult to identify new peaks. This large background is mainly produced by the detection of high energy β-particles in the HPGe-detectors, and by a small contribution of random coincidences. The β background from the HPGe clover detectors can be removed by requiring an extra coincidence with the β-detector. However, the amount

of statistics of γ-rays that feed the 2434-keV level is very low, thus in the $\beta\gamma\gamma$ spectra for 2434-keV there is not enough statistics to identify new peaks.

6.6.4 Search for the $\nu h_{11/2}$ single-hole state.

As discussed above, a precise determination of the energy of the $\nu h_{11/2}$ single hole state in ^{131}Sn is still lacking. One of the aims of the present work is to find its position via $\gamma\gamma$ coincidences. In the work of Fogelberg *et al.* [FGM$^+$04a] an energy of 69(14) keV was reported, derived from the measurement of the Q_β. In addition, a more precise 65.1 keV value was also proposed by Fogelberg *et al.* on the basis of the assignment of a 2369-keV as a M2 γ-transition between the 2434-keV $(7/2^+)$ and the $(11/2^-)$ isomer. Nevertheless this assignment has never been confirmed by $\gamma\gamma$ coincidences, thus it remains tentative.

The 2369-keV γ-line can also be observed in the spectra recorded in this experiment. It is emitted with the time distribution of indium decay. In addition, its intensity is stronger in the RILIS $[9/2^+]$ spectrum while it is reduced in the RILIS $[1/2^-]$ configuration, see Figure 6.7. Both features indicate that the 2369-keV transition is emitted in the ^{131g}In $(9/2^+)$ decay. However, it has not been possible to confirm its placement in the level-scheme via $\gamma\gamma$ coincidences. In fact, no $\gamma\gamma$ coincidence has been observed with the 2369-keV transition. Given the low intensity of the γ-rays feeding the 2434-keV level, see Figure 6.15 (bottom), it would be very unlikely to observe any coincidence with the 2369-keV γ-ray, whose immensity is 0.2% of the 2434-keV transition. Thus the lack of coincidences for the 2369-keV line does not rule out its placement in the level-scheme. Nevertheless, it was not possible to confirm its placement in the level-scheme.

We have attempted a different approach to confirm the energy of the $(11/2^-)$ isomer. By searching for a level that de-excites both into the $(11/2^-)$ and into one of the other single particle levels, whose energies are known. The difference in J^π between the $(11/2^-)$ isomer and the $(3/2^+)$ g.s. would require a competition between an M2 and a E2, in the best case, in order to directly feed both levels. For the 2434-keV level, which receives almost the entire β-feeding, it may seen reasonable to observe a M2 2369-keV transition competing with a 0.2% of relative intensity with the E2 2434-keV γ-transition. However, this is not possible for any other transition, since they are much weaker. Another option would be that a level could de-excite into both the $(7/2^+)$ and the $(11/2^-)$ states. For example, a level with hypothetical $J^\pi = (7/2^-\ 9/2^-$ or $11/2^-)$ would be able to de-excite via M1 or E2 transitions to the $(11/2^-)$ isomer, but also

to the 2434-keV ($7/2^+$) level (and 1655-keV ($5/2^+$) state in the $7/2^-$ case) by means of an E1 γ-transition. In those cases the energy difference would help to balance the competition between both decay branches. The population of high-energy levels with those J^π values is only expected in the decay of the ^{131g}In ($9/2^+$) ground state. As pointed out earlier, in this work the existence of a large amount of high-energy levels populated from the ^{131g}In ($9/2^+$) g.s. has been observed. Thus, it is likely that some of those levels de-excite both to the ($11/2^-$) and the ($7/2^+$) or ($5/2^+$) single particle states.

This possibility has been exhaustively investigated by comparing the γ-rays that are emitted in the decay (Table 6.2), with those observed in coincidence with the 1655-keV and 2434-keV transitions. Unfortunately, this analysis did not bring any definitive conclusion, primarily due to the low intensity of γ-rays feeding the 2434-keV level. Nonetheless, a possible combination of γ-rays that fulfill the required condition has been found. There is a small peak at 4503 keV, in coincidence with the 2434-keV γ-ray, that has been observed in the spectrum from Figure 6.15 (bottom). Its intensity is weak, but it clearly stands out from the background. If we assume that peak is real, it would lead to the assignment of a level at 6937 keV. This tentative energy was compared with the list of high energy γ-rays observed in this decay, Table 6.14. If we assume that these transitions populate the ($11/2^-$) state, together with the 65.1 keV energy suggested by Fogelberg *et al.* [FGM$^+$04a], the 6872 keV γ-ray would also fit a level at 6937 keV. Nonetheless, given the unclear 2434-4503-keV coincidence, along with the absence of some other possible levels like this one, it is not possible to draw a definitive conclusion from this analysis.

6.7 Level scheme of ^{131}Sn populated in ^{131m2}In decay.

This last subsection devoted to the decay of the second isomer ^{131m2}In with tentative spin-parity assignment ($21/2^+$) isomer. Unlike the other two β-decaying single-particle states in ^{131}In, is assumed to be built from a three particle configuration $\pi g_{9/2}^{-1}\nu f_{7/2}h_{11/2}^{-1}$, see Figure 6.16. This second isomer, which appears at a very high excitation energy of 3764(88) keV [FGM$^+$04a], decays by β emission due to the lack of a de-excitation path that connects it with any of the two other β-decaying single particle states in

^{131}In. Similarly to the decay of the two other isomers, the dominant β transitions can be interpreted as transitions between single particle configurations.

From the expected $J = (21/2^+)$ [FGM$^+$04a], the allowed transitions would feed directly states with $J = (19/2{-}23/2)$. Given the shell model interpretation, the $\nu g_{7/2} \rightarrow \pi g_{9/2}$ GT transitions would be allowed. Therefore it is expected to observe a strong population to states built on the $\nu g_{7/2}^{-1} h_{11/2}^{-1} f_{7/2}$ multiplet. In a second level of intensity first forbidden transitions are foreseeable. As shown in Figure 6.16, there are two possible first forbidden transitions in this decay. Firstly the $\nu f_{7/2} \rightarrow \pi g_{7/2}$ one, which feeds states from the $\pi g_{7/2} g_{9/2}^{-1} \nu h_{11/2}^{-1}$ multiplet, mainly of proton nature. The second one is the $\nu h_{11/2} \rightarrow \pi g_{9/2}$ transition, which populates levels built on the $\nu f_{7/2} h_{11/2}^{-2}$ multiplet.

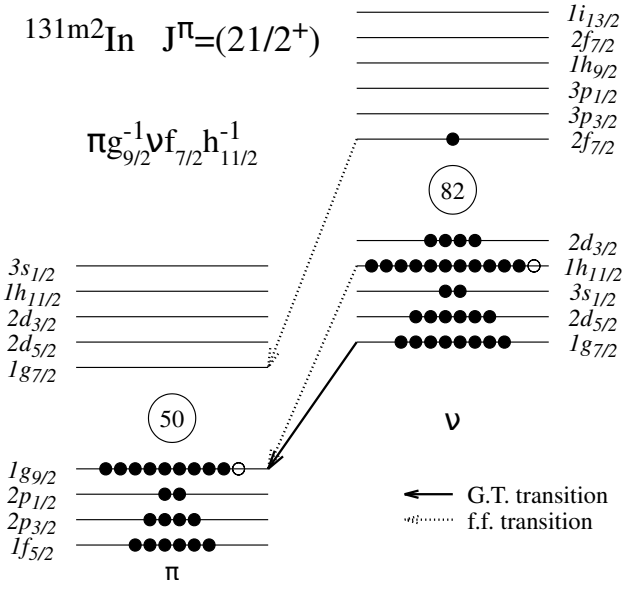

Figure 6.16: Shell model configuration for ^{131m2}In.

There is also a possibility of decays via GT transitions from the N=82 shell to their equivalent proton shell. However, such transitions would populate states involving one neutron and one proton above their respective shell gaps, together with one proton and two neutron holes. Such core-excited configurations are expected at very high energies, and the levels based on them will give rise to unbound states.

6.7.1 Identification of new γ-transitions in ^{131}Sn.

For ^{131m2}In decay, there was no isomerically purified measurement. Its γ-rays are present in the spectra measured for all RILIS settings with a similar intensity. A 2% ^{131m2}In beam composition for both narrow-band configurations, and around 5% in the broad-band mode, has been estimated. The transitions can be distinguished from those emitted by the other two states by analyzing their relative intensities. However it is not so straight forward in this case. The population of states with spin (19/2−23/2) in the β-decay of (21/2$^+$) ^{131m2}In does not allow direct feeding of the (11/2$^-$) isomer. Consequently they are de-excited by cascades of two or more γ-rays. Thus, the identification of the ^{131m2}In γ-rays, has been carried out based on $\gamma\gamma$ coincidences. The high spin of the populated levels, forbids de-excitation to any other of the states populated in the decay of ^{131g}In and ^{131m1}, except for the (11/2)$^-$ isomer with a yet unconfirmed excitation energy. For this reason, the energy of the levels are written relative to the excitation energy (X)f of the (11/2)$^-$ isomer.

The strongest γ-ray emitted in the ^{131m2}In decay corresponds to the 4274-keV transition. This γ-line is identified with the direct de-excitation of the 4274+X-keV level to the 11/2$^-$ isomeric state. The 4274+X-keV state is assumed to have a (17/2$^+$) assignment and would would arise from of the coupling of the $\nu h^{-1}_{11/2}$ hole to the 3$^-$ octupole vibration of the ^{132}Sn core. Its analogous state in ^{132}Sn is the 4351-keV 3$^-$ level, with less than 100 keV energy difference between them. This level does not receive measurable direct β-feeding from indium, but it is very intensely populated by γ-rays from higher-lying levels. In fact, around 84% of the total decays de-excite via the 4274-X keV level, which is de-excited almost entirely by the 4274 keV γ-ray. Hence this level is key to investigate $\gamma\gamma$ coincidences, since most of the γ-rays emitted from the high-lying levels should be visible. The HPGe energy spectrum measured in coincidence with the 4274-keV line is depicted in Figure 6.17. Within this spectra there is a good number of strong transitions that can be clearly identified. Among them the 173-, 284-, 302- and 2380- keV transitions, which directly populate the 4274+X keV state. The remaining peaks correspond to transitions between higher levels. It is possible to identify almost all the new γ-rays observed in this study. However, none of them populates directly the 4274-keV level. Hence, their placement in the level scheme has been deduced by the analysis of their $\gamma\gamma$ coincidences with other transitions in the spectrum.

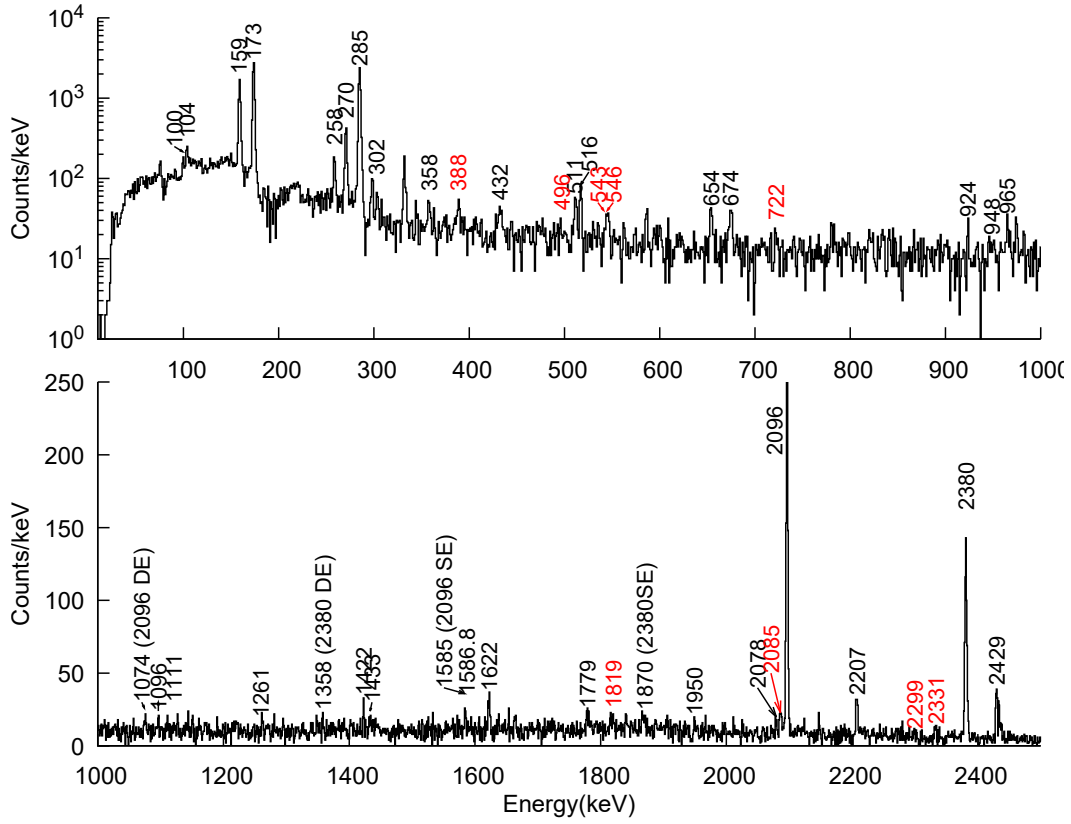

Figure 6.17: Compton subtracted $\gamma\gamma$ coincidence spectrrum gated on the 4274 keV $(17/2^+)\rightarrow (11/2^-)$ transition The previously known γ-rays are labeled in black. The new transitions identified in this work for the first time are labeled in red.

In figure 6.18, the γ-ray spectrum measured in coincidence with the 284-keV transition is plotted. This transition de-excites a level at 4558+X keV to the 4274+X keV level. This state was assumed to be a $(19/2^+)$ state, member of the $\nu h^{-1}_{11/2} f_{7/2} d^{-1}_{3/2}$ multiplet. It is mainly populated by γ-rays owing to its participation in the 2096-284-4273 cascades which de-excite the 6654+X keV $(21/2^+)$level, member of the $\nu g^{-1}_{7/2} h^{-1}_{11/2} f_{7/2}$ multiplet. Besides, the 4458+X-keV level is also fed by transitions from a good number of other levels, with a suspected positive parity. In the spectrum several new transitions, not reported in previous works, are observed. Specifically, weaker γ lines has been found at 496, 2085, 2298 and 2332 keV, which point out to the existence of new levels at 5053+X, 6644+X, 6857+X and 6890+X keV respectively.

Another important excited level in this decay is the $(19/2^-)$ 4447-X state, which

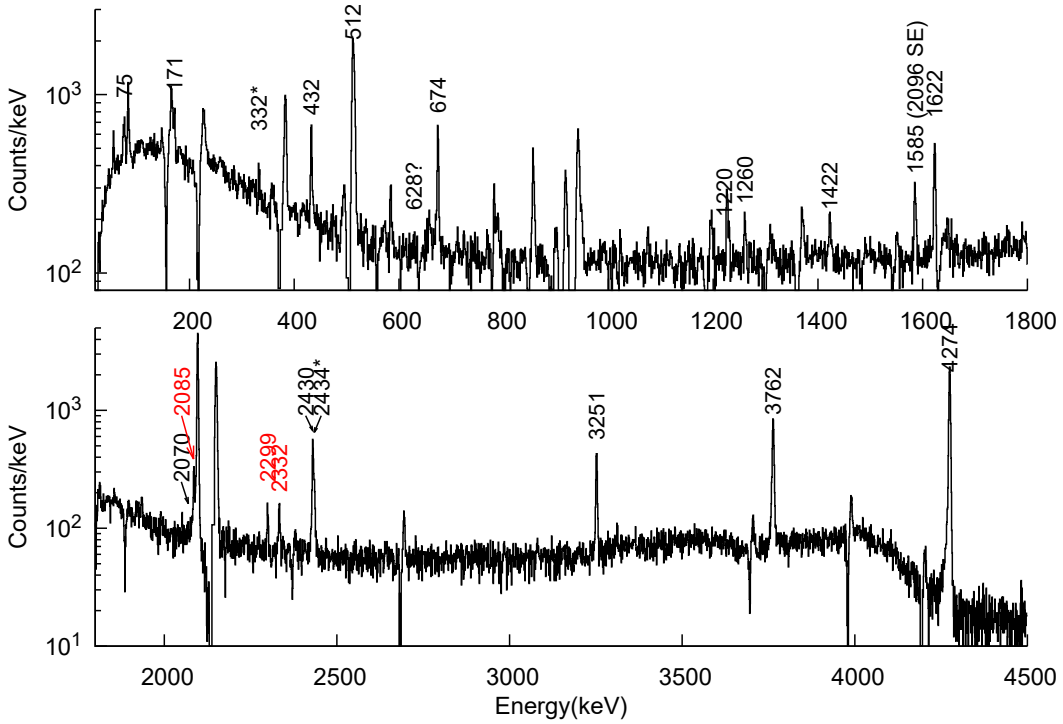

Figure 6.18: Compton background subtracted $\gamma\gamma$ coincidence spectrum gated on the 284 keV $(19/2^+)\rightarrow (17/2^+)$ transition The previously known γ-rays are labeled in black. The new transitions identified in this work are labeled in red.

is assumed to be a member of the $\nu f_{7/2}h^{-2}_{11/2}$ multiplet [FB84, FGM$^+$04a, BDZ$^+$01]. Although this level is not populated directly in β decay either, around 50% of the decays proceed through it. There are three de-exciting. The most intense one is the 173-keV E1 transition that which connects it to the 4274+X keV $(17/2^+)$ level. The two other γ-rays are the E2 transition of 344 keV, which connects it with the $(17/2^-)$ 4103+X-keV state, and the 4447-keV E4 transition to the $(11/2^-)$ isomer. An analogy can be drawn between the 4447+X level and the 4416-keV 4^+ state in ^{132}Sn. In the ^{132}Sn the 4416-keV level is also de-excited by three transitions, an E1 γ of 64 keV to the (3^-) 4351-keV level, an E2 of 375 keV to the 2^+ 4042 keV level and an E4 transition of 4416 keV to the 0^+. However, in the ^{132}Sn of the strongest de-exciting transition is the E2 to the 2^- transition, probably due to the lower energy (64 keV) for the E1 transition in ^{132}Sn.

In Figure 6.19 the $\gamma\gamma$ coincidence spectrum gated on the 173-keV peak is shown.

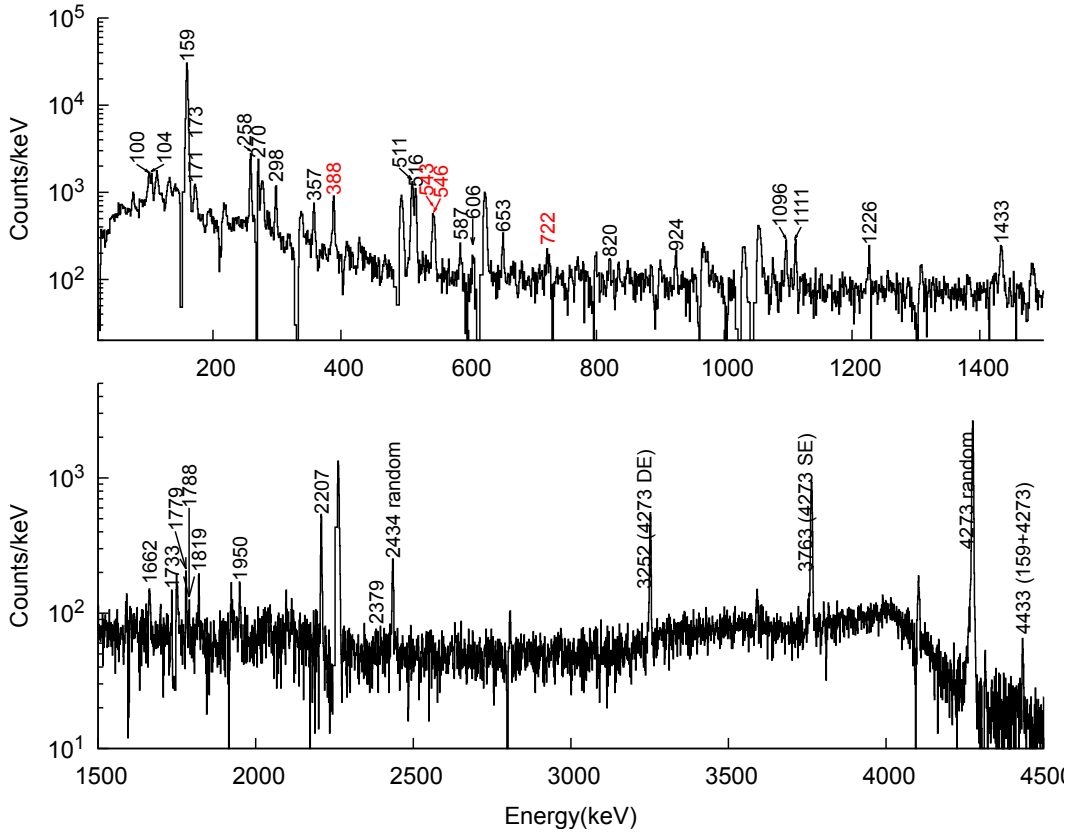

Figure 6.19: Compton background subtracted $\gamma\gamma$ coincidence spectrum gated on the 173 keV $(19/2^-)\rightarrow (17/2^+)$ transition The previously known γ-rays are labeled in black. The new transitions identified in this work are labeled in red.

The strongest peak arises from the 158 keV γ-ray that de-excites the 4606+X-keV level. Such level is assumed to be the $(23/2^-)$ member of $\nu f_{7/2}h^{-2}_{11/2}$ configuration, and it would be the analog state to the 4715-keV 6^+ level in the ^{132}Sn core, coming from the $\nu f_{7/2}h^{-1}_{11/2}$ multiplet. Half of the peaks that appear in coincidence with the 173-keV line are connected to it through the 158-keV transition. The remaining ones feed directly the 4447+X-keV state, which corresponds to transitions from levels from 4.8 to 6 MeV. Sticking to the ^{132}Sn analogy, those levels can be related to the members of the $\nu f_{7/2}h^{-2}_{11/2}$, $\nu d_{3/2}h^{-2}_{11/2}$ and $\pi g_{7/2}g^{-1}_{9/2}\nu h^{-1}_{11/2}$ configurations. However due to the large number of options, altogether with the lack of extra information, the assignment to a specific configuration is not possible. From the s.tudy, four γ-rays are identified to directly populate the 4447+X-keV level the 388-, 543-, 546- and 722-keV γ-rays. These

peaks show the existence of three new levels at 4836, 4993 and 5328 keV above the $(11/2^-)$ isomer energy.

At 4606+X keV a high-spin isomer of ^{131}Sn, with a measured half-life of 300 ns [KMR06], exists. Figure 6.20 shows the detected delayed coincidence spectrum with the 158-keV de-exciting γ-ray. Due to the long lifetime of this level, the standard coincidence time window of 200 ns needs to be modified in order to measure the true coincidences. We have used a time window of 200 to 1000 ms in order to observe the feeding transition to the 4606+X-keV level. The strongest γ-lines in the spectrum are the 100-, 104- and 270-keV ones that originate from the de-excitation of the 4706+X-, 4710+X- and 4876+X-keV levels. Several new γ-rays have bee found revealing to transitions and levels in ^{131}Sn, not observed in previously. In some cases these γ-rays are not directly feeding the 4605+X-keV level, hence, their placement in the level scheme has been confirmed by $\gamma\gamma$-coincidences. A small but clear peak at 75 keV appears in delayed coincidence with the 158-keV transition. This γ-ray might point out to the existence of an excited level at 4680+X keV. This level would be a good candidate for another possible long-lived high-spin isomer, which corresponds to a predicted $(27/2^-)$ state from the $\nu d_{3/2}h^{-2}_{11/2}$ multiplet. However, there are no further $\gamma\gamma$ coincidences that support this assignment, and its energy overlaps with the lead X-rays energies. Thus, the existence of this level remains very tentative. The intensity if¡¡of this γ-ray suggest a 2.8(8)% feeding to this state, however this intensity has not been taken into account for the other levels, due to the uncertainty of the assignment.

Apart from the $\gamma\gamma$ spectra discussed in this section, a systematic investigation of the coincidences shown by all γ-rays identified in ^{131}Sn has been performed. The results from this work are condensed in the new level-scheme, shown in Figure 6.21, and in the transitions listed in Table 6.3. The β intensities have been obtained from the balance between the γ-rays that feed and de-excite each level. Due to large amount of low energy γ-rays branches, special care was taken to account for electron conversion. The internal conversion coefficients were calculated using the Bricc tool [KBT$^+$08], assuming the most likely transition multipolarities.

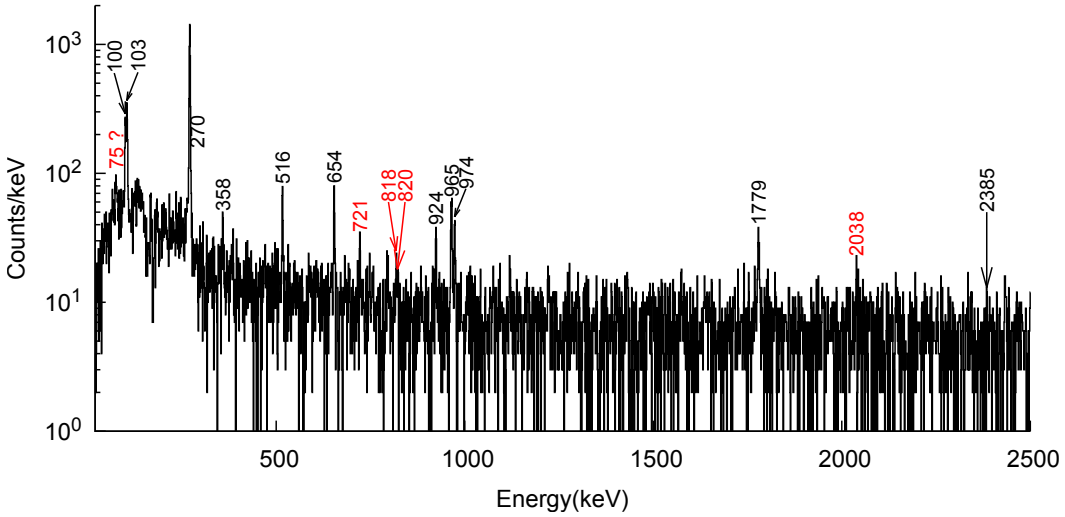

Figure 6.20: $\gamma\gamma$ measured with a delayed time window of 20-1000 ns before the detection of the 158-keV $(19/2^-)\rightarrow (19/2^-)$ transition The previously known γ-rays are labeled in black. The new transitions identified in this work are labeled in red.

Table 6.3: γ-ray intensities in the ^{131m2}Inβ decay

E_i (keV)	J_i^π	E_f (keV)	J_f^π	E_γ (keV)	I_γ^a (%)
4102.7(6)	$(15/2^-)$	0.0	$(11/2^-)$	4102.7(6)	11(2)
4246.2(5)	$(15/2^+)$	0.0	$(11/2^-)$	4245.6(5)	3.2(6)
4273.9(3)	$(17/2^+)$	0.0	$(11/2^-)$	4273.3(3)	100
		4102.7(6)	$(15/2^-)$	171.2(3)	1.2(3)^b
4422.2(13)	$(15/2^+)$	0.0	$(11/2^-)$	4421.5(13)	0.5(2)
4447.2(3)	$(19/2^-)$	0.0	$(11/2^-)$	4446.8(5)	2.7(5)
		4102.7(6)	$(15/2^-)$	344.4(2)	6.6(8)
		4273.9(3)	$(17/2^+)$	173.4(2)	42(5)
4510.9(7)	$(15/2^+)$	4102.7(6)	$(15/2^-)$	408.2(4)	0.36(11)
4558.4(4)	$(19/2^+)$	4273.9(3)	$(17/2^+)$	284.6(2)	43(5)
4575.7(4)	$(17/2^+)$	0.0	$(11/2^-)$	4574.7(6)	4(1)^b
		4102.7(6)	$(15/2^-)$	473.4(2)	1.8(3)
		4246.2(5)	$(15/2^+)$	329.6(3)	3.6(10)^b
		4273.9(3)	$(17/2^+)$	302.0(3)	0.7(2)^b
		4422.2(13)	$(15/2^+)$	153.3(5)	0.7(4)^b
4605.8(4)	$(23/2^-)$	4447.2(3)	$(19/2^-)$	158.7(2)	28(3)
4680.8(6)	$(27/2^-)$	4605.8(4)	$(23/2^-)$	75.1(5)	0.7(2)^b
4705.3(3)	$(21/2^-)$	4447.2(3)	$(19/2^-)$	258.2(2)	3.2(4)
		4605.8(4)	$(23/2^-)$	99.7(3)	1.9(2)
4709.3(4)		4605.8(4)	$(23/2^-)$	103.6(2)	2.4(3)

E_i (keV)	J_i^π	E_f (keV)	J_f^π	E_γ (keV)	I_γ^a (%)
4744.9(4)	$(21/2^-)$	4447.2(3)	$(19/2^-)$	297.8(3)	1.0(2)
4835.3(4)	$(15/2^+)$	4447.2(3)	$(19/2^-)$	388.2(3)	1.7(2)
4875.8(4)		4605.8(4)	$(23/2^-)$	270.2(2)	14(2)
		4705.3(3)	$(21/2^-)$	168.3(3)	$<2^b$
4990.4(3)	$(21/2^+)$	4558.4(4)	$(19/2^+)$	432.0(3)	0.8(2)
		4447.2(3)	$(19/2^-)$	543.3(3)	0.82(14)
4992.8(3)		4447.2(3)	$(19/2^-)$	545.9(3)	1.0(2)
		4705.3(3)	$(21/2^-)$	287.4(5)	$0.7(4)^b$
5054.6(4)		4558.4(4)	$(19/2^+)$	496.2(3)	1.2(2)
5221.2(5)		4705.3(3)	$(21/2^-)$	515.9(4)	4.5(10)
5232.5(4)		4558.4(4)	$(19/2^+)$	674.0(2)	1.4(2)
5328.0(4)	$(15/2^+)$	4605.8(4)	$(17/2^+)$	722.2(3)	0.64(10)
5529.6(3)		4605.8(4)	$(23/2^-)$	923.9(3)	1.3(2)
		4709.3(4)		820.4(3)	0.66(10)
		4875.8(4)		653.6(2)	1.17(15)
5543.5(4)		4447.2(3)	$(19/2^-)$	1096.3(3)	0.96(14)
5579.0(4)		4605.8(4)	$(23/2^-)$	973.8(2)	1.3(2)
		5221.2(5)		357.2(3)	1.1(2)
5674.1(5)		4709.3(4)		964.8(2)	2.7(3)
6109.8(4)		4447.2(3)	$(19/2^-)$	1662.4(3)	$0.5(2)^b$
6180.6(4)		4558.4(4)	$(19/2^+)$	1622.0(2)	3.0(4)
6266.6(4)		4447.2(3)	$(19/2^-)$	1819.3(3)	$0.6(2)^b$
6493.8(6)		5232.5(4)		1261.2(4)	0.48(9)
6644.0(5)		4558.4(4)	$(19/2^+)$	2085.3(4)	1.5(2)
6654.5(2)	$(21/2^+)$	4273.9(3)	$(17/2^+)$	2380.4(3)	17(2)
		4447.2(3)	$(19/2^-)$	2207.4(3)	2.4(3)
		4558.4(4)	$(19/2^+)$	2095.9(2)	32(4)
		4575.7(4)	$(17/2^+)$	2078.3(3)	10.0(12)
		4705.3(3)	$(21/2^-)$	1949.7(4)	0.7(3)
		4835.3(4)	$(15/2^+)$	1818.5(6)	1.0(4)
		4875.8(4)		1778.6(3)	2.9(4)
		5221.2(5)		1432.9(3)	1.5(2)
		5232.5(4)		1422.3(4)	0.6(2)
		5543.5(4)		1111.3(3)	0.9(2)
6857.6(5)		4558.4(4)	$(19/2^+)$	2298.8(3)	0.44(7)
6890.1(6)		4558.4(4)	$(19/2^+)$	2331.4(5)	0.7(1)
6987.6(4)		4558.4(4)	$(19/2^+)$	2429.4(3)	$4.0(7)^b$
		4605.8(4)	$(23/2^-)$	2379.3(6)	$1.1(6)^b$

[a] Relative γ intensities normalized to 100 units for the 4273-keV $17/2^+ \rightarrow 11/2^-$ transition. For intensity per 100 decays of the parent ^{131m2}In, multiply by 0.75(6).
[b] Intensity derived from $\gamma\gamma$ coincidences.

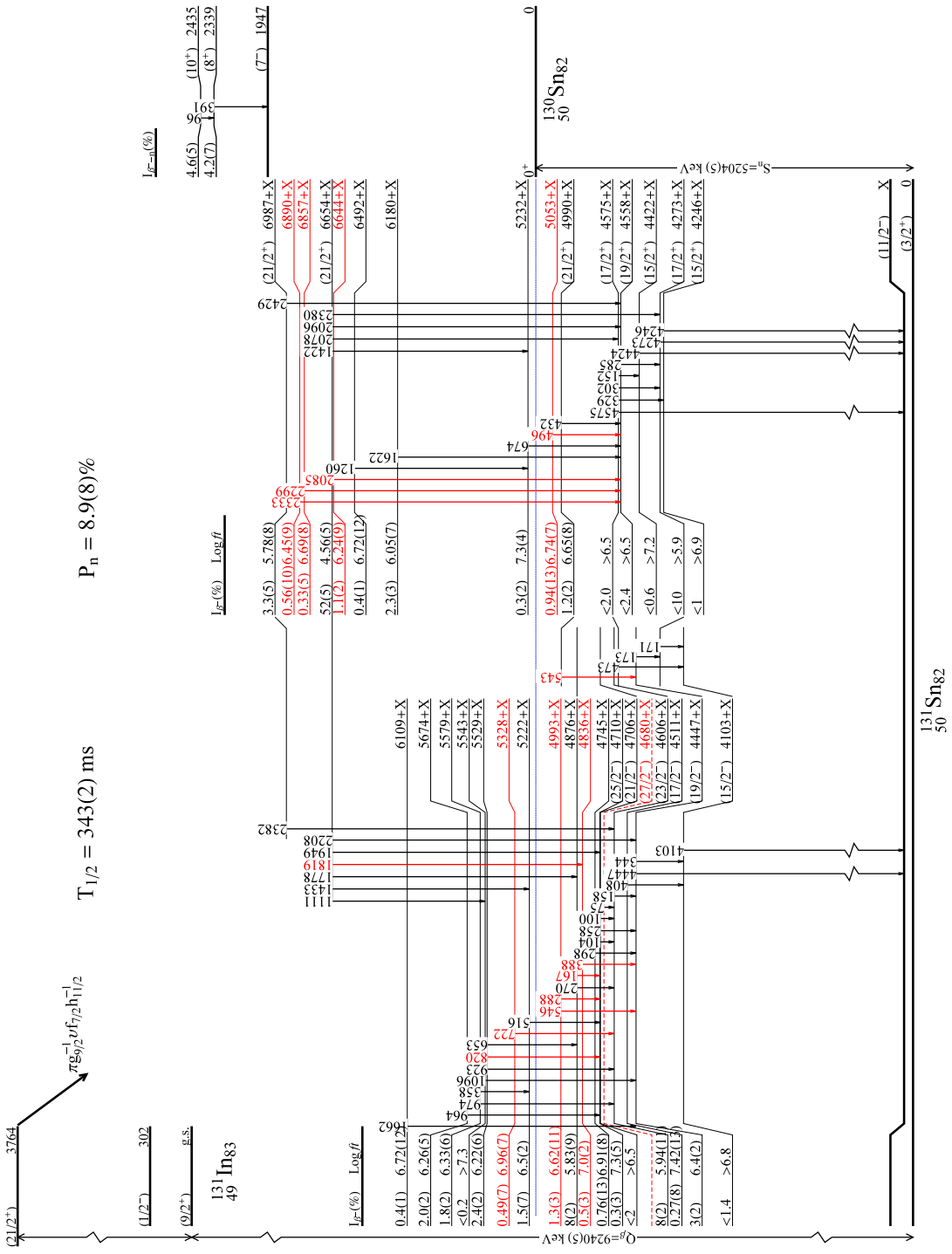

Figure 6.21: Level scheme in ^{131}Sn populated in the decay of ^{131m2}In $(21/2^+)$ isomer.

It should be noted that the decay of ^{131m2}In β-decay populates a lot of states lying above the neutron separation energy, which de-excite by γ-ray emission. These levels, contrary to those populated in the decay of the ground state, are de-excited by cascades of two, three or even more γ-rays. They give rise in some cases to transitions between unbound levels, which shows the weak competition of the neutron emission process for those levels. Once again, excited levels are found also above the energy of the (2^+) state in ^{130}Sn. Similar to the ^{131g}In decay, no levels has been identified above the 7^- isomeric state. Given the large multiplicity of the γ-ray cascades that dominate the decay, the detector efficiency should not be a problem to detect the presence of levels above 7 MeV. However, none have been seen with energies above the location of the (7^-) isomer in ^{130}Sn. This clearly shows that the neutron-emission competition is strongly influenced by the available ^{130}Sn states to decay via neutron emission with a low orbital angular momentum.

6.7.2 β-n delayed branch.

The population of levels in ^{130}Sn via β-delayed neutron emission, seems to be also possible in this decay. This is suggested by the observation of γ-rays from high-spin states in ^{130}Sn, observed in the spectra measured with the RILIS $[1/2^-]$ configuration. In the decay of ^{131m2}In $(21/2^+)$, is not expected to observe population the ^{131}Sn $(3/2^+)$ nor the ^{130}Sn 0^+ in the β-n decay branch, neither directly or by γ-rays. Hence, the P_n values can be derived by comparing the decay intensities from ^{131m1}Sn $(11/2^-)$ and ^{130m1}Sn (7^-) isomeric states. By comparing the relative γ-ray intensities emitted after the decay of these two states, measured in the RILIS $[1/2^-]$ spectra, a P_n=7(4)% is derived. A more precise value can be measured if we assume that the direct β feeding of ^{131}Sn $(11/2^-)$ and the ^{130}Sn (7^-) can be neglected. Thus, the whole ^{131m2}In intensity can be obtained directly from the γ-rays intensities emitted in this decay. Using this approach, a P_n=8.9(8)% is derived for this decay, which is perfectly consistent with the one derived from activity of the daughters. This value is notably larger than those obtained for the other two β-decaying ^{131}In states, and it is very similar to the P_n=12(3)% measured for the ^{132}In decay

6.7.3 Similarity to the decay of ^{132}In (7^-)

An interesting feature of the ^{131m2}In ($21/2^+$) decay is the high resemblance with the ^{132}In decay-scheme. It has been mentioned before that, except for the single-hole levels, the reaming ones are built by coupling single-particle states in ^{131}Sn to core-excited levels in ^{132}Sn. Even though this connection has been already pointed out, the similarities of the high-spin indium isomer decay and the decay of ^{132}In are worth to underline. In Figure 6.22, the ^{131}Sn states, that are populated in ^{131m2}In decay, are drawn along with p-h multiplets in ^{132}Sn, only the most intensely fed in ^{132}In decay.

The cause probably lies in the fact that the $(\pi g_{9/2}^{-1}\nu f_{7/2}h_{11/2}^{-1})$ ^{131m2}In shell model configuration arise from the coupling of a $\nu h_{11/2}^{-1}$ neutron hole to the ^{132}In ground state $(\pi g_{9/2}^{-1}\nu f_{7/2})$ configuration. This suggests that the p-h configurations of the ^{131}Sn states populated in the ^{131m2}In β-decay would be the same than those in ^{132}Sn populated from ^{132}In, but coupled to the $\nu h_{11/2}^{-1}$ neutron hole component.

Continuing with this analogy, the configurations populated in the decay of the ^{131}Sn ($11/2^-$) state should be found. However, this would lead to the population of 2p-3h states in ^{131}Sn also, including excitation across both neutron and proton shell gaps. Such states would be characterized by very high energies and they would be probably neutron unbound. Therefore, it is not expected to observe strong contribution from the decay of the $\nu h_{11/2}^{-1}$ neutron-hole component.

Another factor that favours the similarity to the ^{132}In decay is the high-spin of the ^{131m2}In ($21/2^+$) isomer. The selective feeding of β decay leads to the population of high-spin levels, which can only be built by including at least a hole in the $\nu h_{11/2}$ orbital. Hence, the number of possible combinations that can give rise to states with large angular momentum is reduced. In addition, the difference in angular momentum between the parent isotope and the final level in the daughter nuclei for the A=131 case, ^{131m2}In ($21/2^+$) $\rightarrow$ ^{131}Sn ($11/2^-$) ΔJ =6 and $\Delta\pi$ =yes, is very similar to the A=132 case, ^{132}In (7^-) $\rightarrow$ ^{132}Sn 0^+ ΔJ =7 and $\Delta\pi$ =yes. Therefore, the number of γ-rays that the populated levels in ^{131m1}Sn need to emit to reach the $11/2^-$ isomer are also similar to those required in the ^{132}In decay to reach the ^{132}Sn ground state.

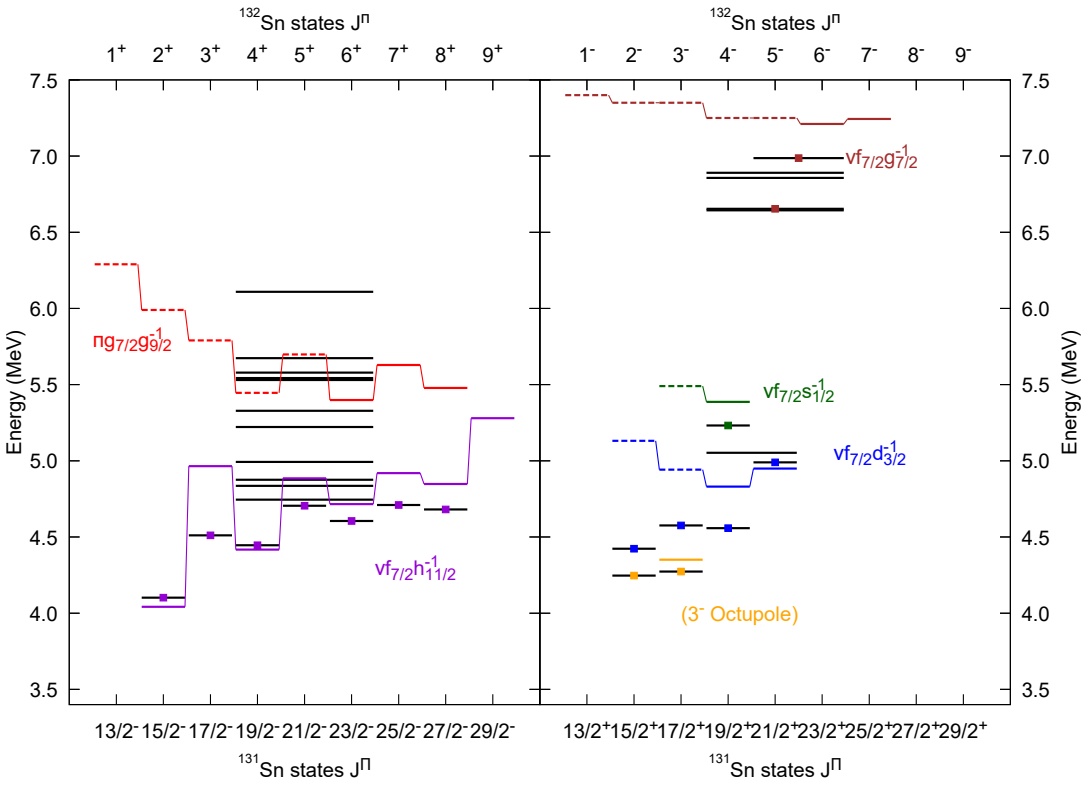

Figure 6.22: Comparison between the p-h multiplets in ^{132}Sn and the core-breaking states mmore intensely populated in ^{131m2}In decay. The p-h multiplets in ^{132}Sn are illustrated with colored lines, labeled with their configuration. Their spin and parity correspond to their position in the upper horizontal axis. The core-breaking levels in ^{131}Sn are drawn with black lines. Their spin and parity correspond to their position in the bottom axis.

6.8 Gamma emitting neutron unbound states in ^{131}Sn

One of the most interesting results observed in this mass, is the large amount of γ-rays at very high energies, above the one-neutron separation energy. The presence of high-energy γ-rays is reported in the results from TRIUMF [DSA$^+$19], however, they did not allocate them to the β-decay of any specific ^{131}In state. An unambiguous assignment of these new high energy γ-rays to the decay of ^{131g}In is done in our work thanks to the isomer selective RILIS ionization. This result indicates a very different decay pattern for each indium isomer. In Figure 6.23, the lowest lying states of ^{130}Sn are represented as well. If we compare the energies of ^{130}Sn levels and the upper limit of the high-energy γ-emitting levels in ^{131}In, we can find a clear correlation. The phenomenon of competition of γ-ray emission with neutron emission is attributed to a large hindrance due to by the large l required for the neutron emission. The states above S_n populated in the ^{131m1}Sn $(1/2^-)$ decay can be connected to the 0^+ g.s. or 2^+ first-excited state in ^{130}Sn with a low orbital momentum l=0,1, hence, they can freely decay by neutron emission. Consequently there are no γ-rays emitted from excited levels above the S_n from ^{131m1}Sn cay. On the other hand, in the decay of ^{131g}In $(9/2^+)$ and ^{131m2}In $(21/2^+)$, the levels have a much larger spin, $J \geq 7/2$, and thus neutron needs to carry an large orbital angular momentum, $l \geq 3$. Neutron emission, even though is energetically possible for these levels, is highly forbidden due to the large l. Hence, the threshold between γ-emitting and neutron-emitting levels is shifted upwards 2 MeV from the S_n. At these energies, states in ^{130}Sn with a high-spin begin to appear. They can be reached by neutrons emitted with low l, even by the unbound levels populated in ^{131g}In and ^{131m2}In.

In the ^{131m1}In $(1/2^-)$ β-decay, the population of high-energy levels up to the one-neutron separation energy is observed. Beyond that energy, no γ-ray emitting states are observed. The levels that are populated in the decay of ^{131m1}In, de-excite directly to either the $(3/2^+)$ g.s. or the $1/2^+$ 332-keV single particle states. In the decay of the ^{131g}In $(9/2^+)$ g.s., there are strongly populated $\nu g_{7/2}^{-1}$, $\nu g_{7/2}^{-1}$, $\nu h_{11/2}^{-1}$ and $\nu d_{3/2}^{-1}$ single-particle states. Besides, γ-emitting core-excited levels are populated from 4 to 7 MeV, with energies significantly higher than the neutron separation energy S_n =5204(4) keV. They are commonly de-excited by high-energy transition that connect them directly

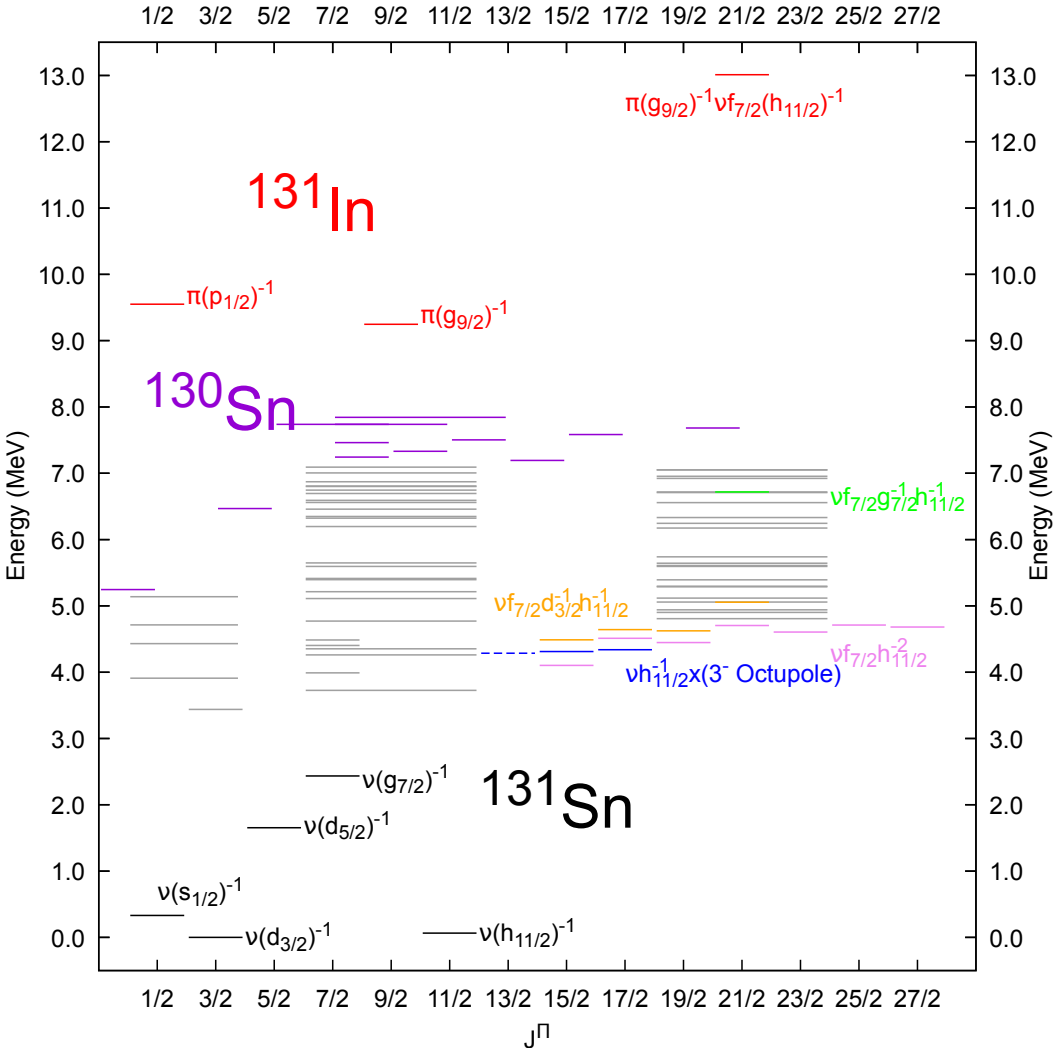

Figure 6.23: Global level-scheme of ^{131}Sn populated in the β decay of the three ^{131}In β-decaying states. In this figure, all the identified levels in ^{131}Sn are plotted. In the low energy region the single-hole states depicted in black, while the core-excited levels appear in the energy region from 3 to 7 MeV. Additionally, the β-decaying states in ^{131}In (red) and the lowest lying states from ^{130}Sn (violet) are shown.

with the $3/2^+$ g.s. and the $11/2^-$ isomer states, and in some case with the $7/2^+$ 2434-keV and $5/2^+$ 1655-keV single particle levels.

Finally, in the decay of ^{131m2}In, the population of γ-emitting excited levels above S_n up to 7 MeV is observed. In this case, there are core-excited levels from 4 to 7 MeV,

which cannot de-excite directly to any of the single-particle states due to the large spin difference. Therefore, they usually undergo a series of consecutive transitions, ans sometimes several low-energy γ-rays connecting the levels in the 4-5 MeV region. Once the spin is sufficiently reduced, they decay to the $11/2^-$ isomer via a 4 to 5 MeV γ-ray.

As can be observed in Figure 6.23, the levels ^{131}Sn can be separated in two regions. The low energy region below 3 MeV, characterized by a small density of levels, which can be identified with single-hole neutron states from the N=50-82 shell. In the high energy region, above 3 MeV, there is a high density of states covering a wide range of spins. These high energy levels are identified as core-excited states, which are mostly built from 1p-2h configurations. In the β-decay of each indium isomer, a large number of states with a similar angular momenta to that of the parent isomer are populated, respectively. Several gaps can be found in the regions in between the states populated by each of them. These gaps of missing levels are caused by the low probability in β-decay studies of populate directly levels with J= 5/2 and 13/2 to 17/2.

6.9 Lifetimes of excited states in ^{131}Sn

An important part of our investigation of the structure of ^{131}Sn is the measurement of excited-state lifetimes. The information available prior to this work regarding the lifetimes of the excited levels in ^{131}Sn is very scarce. Only a $T_{1/2}$=316(5) ns for the high-spin $(23/2^-)$ 4605+X isomer has been reported [DSA$^+$19]. The reason behind this lack of information is that none of the previous investigations have been directed to the lifetime measurements in a shorter range. The use of the fast-timing set of detectors in the IS610 experimental campaign carried out at ISOLDE, offers the possibility of measuring lifetimes down to the ps range. In this section the fast-timing analysis for the ^{131}In decay will be discussed.

6.9.1 The *l*-forbidden $\nu 3s_{1/2}^{-1} \rightarrow 2d_{3/2}^{-1}$ M1 transition

All the single -particle states of ^{131}Sn are intensely populated in the β-decay of ^{131}In, either directly or by γ-rays. Only the 332-keV $(1/2^+)$ level, attributed to the $\nu s_{1/2}^{-1}$ single-particle configuration, is expected to have a half-life in the range of the fast-timing technique. All the other levels, are expected to show lifetimes below the ps range, below the time resolution of the technique.

The lifetimes of single-particle state are of key importance for the shell-model interpretation of the nuclear structure. The lifetime measurement of the 332 keV $(1/2^+)$ level in ^{131}Sn provides a direct measurement of the electromagnetic transition strength between the single particle states $\nu 3s_{1/2}^{-1} \rightarrow \nu 3d_{3/2}^{-1}$. Sticking to the shell model interpretation, the dipole magnetic transition between them would be l-forbidden transition due to the $\Delta l = 2$ change required. However, the experimental measurements shows that most of the transitions classified as magnetic dipole transitions do not satisfy the $\Delta l = 0$ rule. They are l-forbidden, and usually imply much larger lifetimes than for levels de-exciting by allowed M1 transitions. These l-forbidden transitions are explained by considering configuration mixing from [AHS57], and/or by the re normalization of the free M1 operator, induced by core-excitations. Given the single particle nature of the low energy levels in ^{131}Sn, configuration mixing between is not expected, therefore the enhancement of the M1 operator would be produced by core-polarization effects. Other possibility is electric quadruple transition. In the shell model interpretation, the E2 transition would be allowed. In this case, given the single particle nature of those level we could assume an B(E2) strength of 1 W.u. which would led to a lifetime of 3.5 ns.

6.9.1.1 Fast-Timing Analysis

The 332-keV level is only populated with sufficient intensity in the decay of the ^{131m1}In $(1/2^-)$ isomer. The preliminary analysis of $\beta\gamma$(t) events shows that the lifetime is short, and needs to be analyzed via the centroid shift methods. In this decay the 332-keV γ-ray is the only intense one. The rest of the transitions are weak, and cannot be used as prompt references, nor to select the 332-keV peak in triple $\beta\gamma\gamma$(t) events. For this reason, the analysis was done using the 2434-keV transition from ^{131g}In as reference using double $\beta\gamma$(t) coincidence events.

In Figure 6.24 the β-gated $LaBr_3$(Ce) and HPGe energy spectra for the RILIS broad-band settings are depicted. Both the 2434-keV and the 332-keV dominate the spectrum without overlapping peaks. Under these conditions it is possible to select both peaks in the $\beta\gamma$(t) safely, without the need to employ a third coincidence in the clover detectors.

Another possibility is to use the 798-keV transition in ^{131}Sb as prompt reference. However, this option was discarded due to the dependence of the response of the β detector on the energy of the electrons, see section 4.4.2. The energy of the β particles

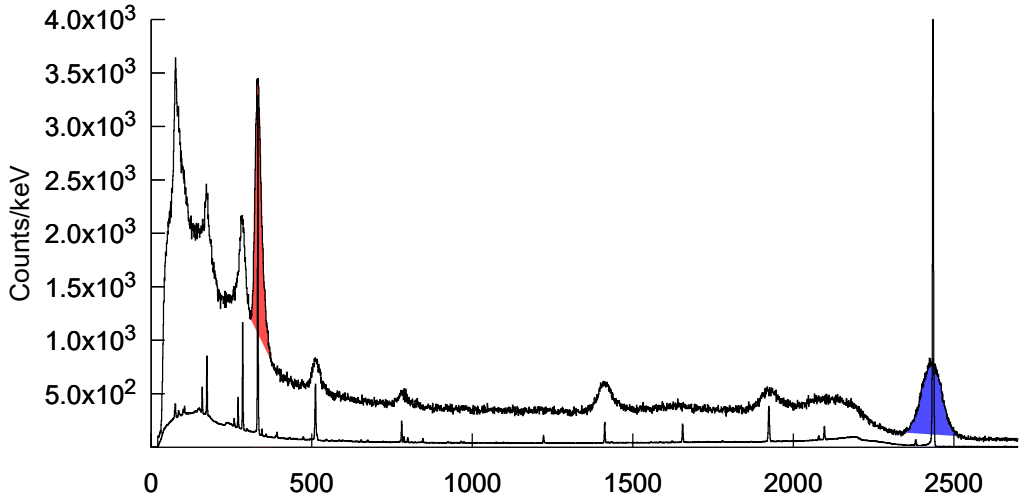

Figure 6.24: Beta-gated γ-ray energy spectra recorded by the $LaBr_3$(Ce)(Top) and HPGe detectors (Bottom). These spectra were built using the data set measured with RILIS set in the broad-band configuration, and the tape moving at every pulse. These conditions offer us the possibility of measuring both 332- and 2434-keV transitions at the same time, with a very high suppression of the long-lived contaminants.

emitted in ^{131}In decay, Q_β (^{131}In)= 9240(5) keV [WAK$^+$17], is much higher than the maximum energy of the β emitted in ^{131}Sn decay, Q_β (^{131}Sn)= 4717(4) keV [WAK$^+$17]. This difference becomes more prominent taking into account that the 798-keV state in ^{131}Sb receives around half of the feeding from higher lying levels close to 3 MeV. Hence, the average energy of β particles in ^{131}Sn decay is much lower than in ^{131}In decay, resulting in sizeable difference in the time response. Thus the 798-keV transition is not valid as prompt reference.

There is also a difference in the energy of the β particle that populates the 2434-keV level. The maximum energy of the β particles that feed it is 6.8 MeV but for the 332-keV level the maximum energy can reach up to 9.2 MeV. The reliability of the 2434-keV γ-ray as a good prompt reference has been verified by comparing the β time-walk with γ-ray gates. The result of this analysis can bee seen in Figure 6.25. We may conclude that there is no noticeable difference in the time response of the beta detector between the ^{131g}In and ^{131m1}In decay, thus the 2434-keV can be used as a prompt γ-ray reference. On the other hand, the time response of the β detector for the 798-keV γ-rays shows a slightly shifted curve, therefore it cannot be employed, as discussed above.

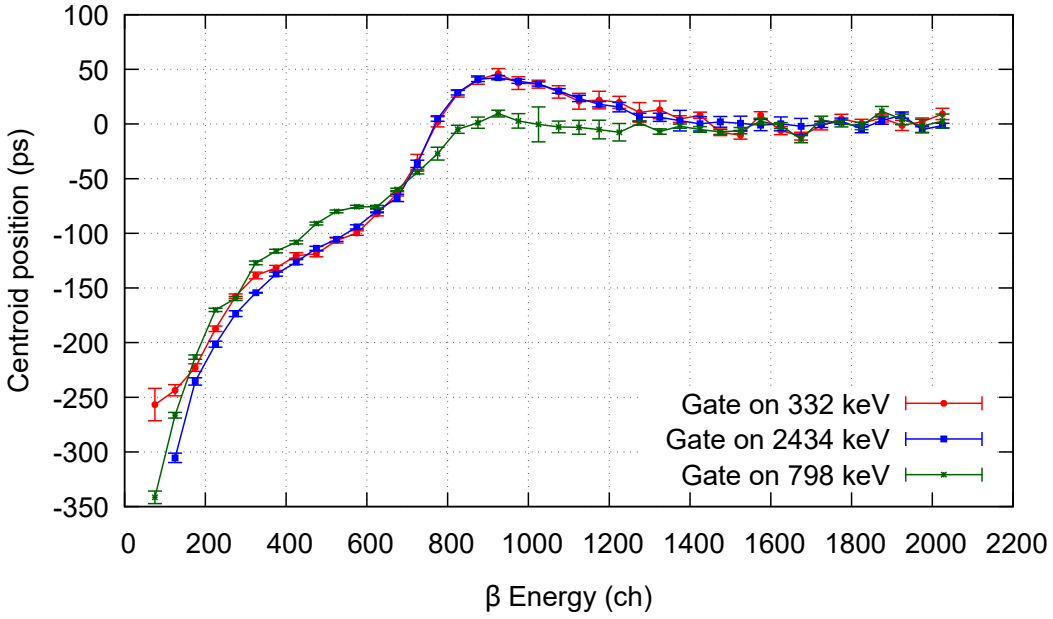

Figure 6.25: Beta-walk curves gating on the most intense γ-rays observed for mass $A = 131$ The blue spectrum depicts the time distribution used as prompt reference.

By using $\beta\gamma$(t) events the statistics for both transition is very high. On the contrary, the contributions from the Compton background are sizable for both. The FEP:Compton ratio is 2:1 for the 332-keV peak and 5:1 for the 2434-keV, in the 2016 dataset. Narrow energy windows have been set for both peaks. Nonetheless, the contribution from the Compton background is still significant. The contribution of the Compton background has been subtracted from the peak time distribution, using the correction method described in section 4.3.1 of Chapter 4.

This analysis was done separately for all the $LaBr_3$(Ce) detector and dataset combinations, resulting in four independent measurements for this lifetime. The centroid shift analysis for one of them is illustrated in Figure 6.27. The four resulting values are compatible with each other, with the exception of the one obtained for the first $LaBr_3$(Ce) from the 2018 dataset, which is 2σ away from the other ones. The reason behind these differences might be an underestimation of the error propagated from the Compton background correction. This is specially the case for the 332-keV peak, which sits on top of a non-constant background, which is very difficult to estimate with precision. For the final value, we have adopted the weighted average of the 4 measurements

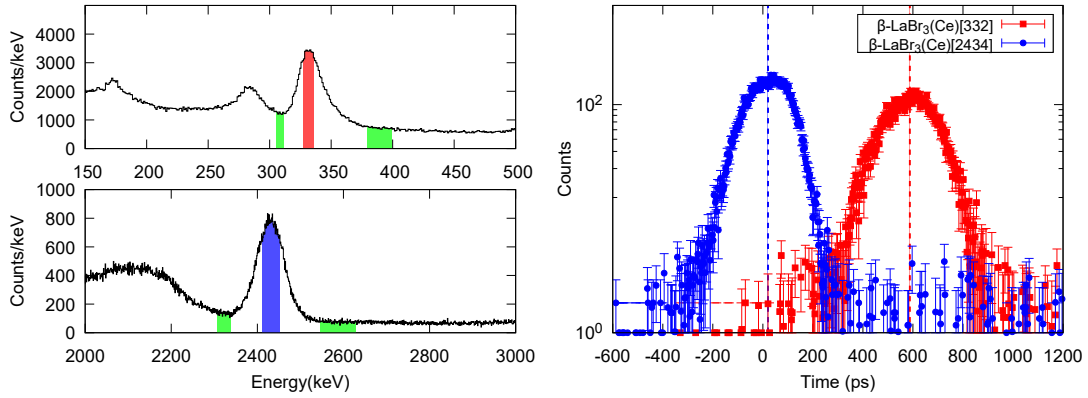

Figure 6.26: Energy gates and time spectra for the 332-keV and 2434-keV transitions. (Left) β gated $LaBr_3(Ce)$ energy spectrum, measured in one of the two lanthanum detectors during the 2016 campaing. The colored areas illustrate the selected regions to estimate the peak and background contributions. (Right) Derived time distributions for the 332-keV and 2434-keV peaks. The corresponding background contribution have been removed from both time spectra. The vertical lines represent the centroid positions.

assuming a 2σ for each value to deal with the variance of the values. Hence, a τ =26(5) ps or $T_{1/2}$ = 18(4) ps for the 332-keV state is obtained.

From this $T_{1/2}$ = 18(4) ps we can derive the reduced transition probabilities for the 332-keV transition. Assuming a pure M1 character, the half-life yields a B(M1) = 0.059(12) μ_N^2 or B(M1) = 0.033(7) W.u. for this transition. On the other hand, by assuming a pure E2 multipolarity it leads to a very unrealistic B(E2) = 195(42) W.u. or B(E2) = $8(2)\cdot10^3$ e^2fm^4 value. The M1/E2 mixing ratio for the 332-keV transition is unknown, hence those values should be understood as upper limits, but in the view of the B(E2) value, the E2 branch should be negligible.

6.9.1.2 Comparison to ^{129}Sn.

The $T_{1/2}$ = 18(4) ps in ^{131}Sn compares very well with the $T_{1/2}$ = 19(10) ps for the $(1/2^-)$ 315-keV level in ^{129}Sn [LMF+16]. In the work Lica *et al.*, realistic shell model calculations were performed in order to explain the, also unexpected, short lifetime. The calculations yield a large enhancement of the M1 matrix element by taking into consideration microscopically the effect of core excitations. The calculations also showed that the E2 operator did not substantially change by considering the same microscopic

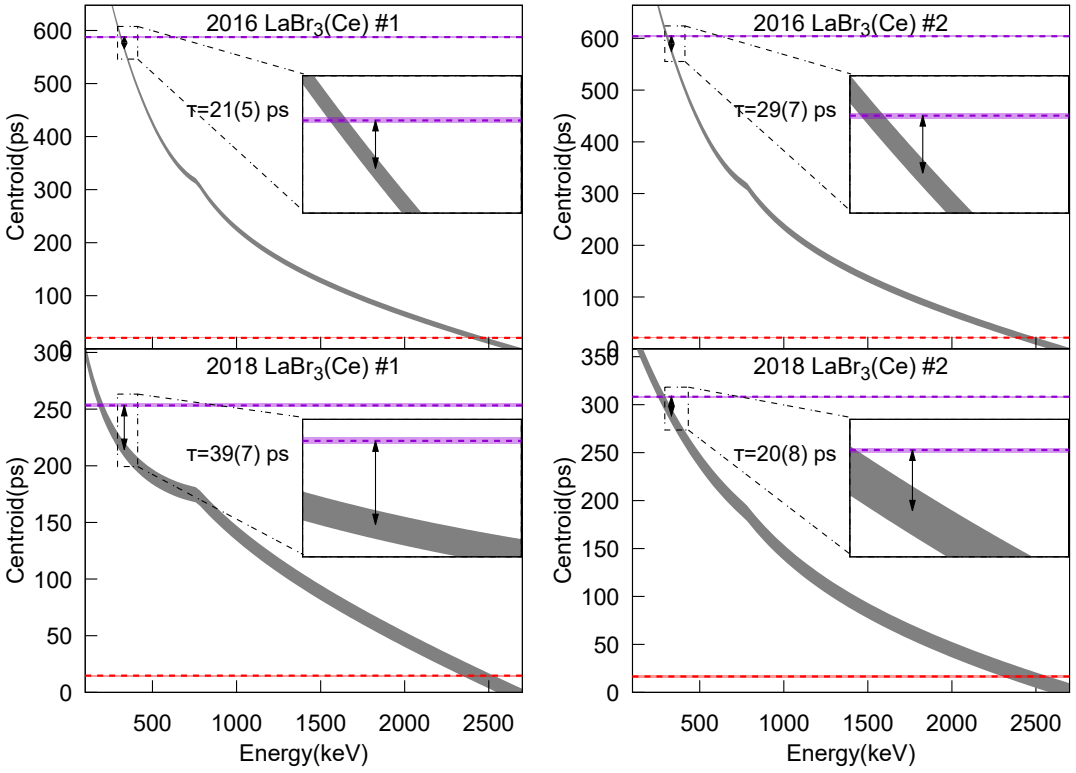

Figure 6.27: $\beta\gamma$(t) Centroid shift analysis and mean life of the 332 keV ($1/2^+$) state. Each plot correspond to the centroid shift analysis done for each of the four detector and dataset combination.

framework, concluding that the 315-keV transition was mainly of M1 nature. Nevertheless, the estimated enhancement for the l-forbidden M1 transition did no manage to fully reproduce the short lifetime of the 315-keV level, accounting only for a lifetime of about an order of magnitude larger. The conclusion was that the re-normalization of the M1 operator was strongly influenced by core-polarization effects, and their inability to reproduce the experimental result was probably due to by higher-order diagrams not included in the calculations [LMF$^+$16].

We can expect a very similar situation in ^{131}Sn with the expectancy that the single-particle nature of the state is even purer in our case. The remarkable similarity between both lifetime, seems to indicate that reason behind is the same in both cases. It should be noted that in ^{131}Sn there is only one neutron hole in the shell, thus the effect produced by excitations of the core requires requires that proton or neutrons are excited across

the shell gap. Therefore, this might indicate that the excitations of the ^{132}Sn core, plays a major role in the re normalization of the effective electromagnetic M1 operator.

6.9.1.3 Comparison to the ^{208}Pb region.

It is also worthwhile to compare these results to the information available for transition rates near ^{208}Pb. The measured B(M1) = 0.033(7) W.u. upper limit, derived from the 332-keV lifetime in ^{131}Sn, is totally consistent with the B(M1) l-forbidden M1 transitions from the lead region, (see Table 6.4), specially with those measured for the neutron hole ^{207}Pb (which would be the equivalent) and proton-hole ^{207}Tl nucleus. On the other hand, the allowed E2 transitions near ^{208}Pb, are not compatible with the B(E2) = 195(42) W.u. derived pure E2 multipolarity of the 332-keV γ-ray.

Table 6.4: Experimental B(Xλ) for the l-forbidden M1 transitions and allowed E2 transitions in the ^{208}Pb region

Nucleus	$j_i \rightarrow j_f$	B(M1) W.u.[a]
^{207}Pb	$\nu 3p^{-1}_{3/2} \rightarrow \nu 2f^{-1}_{5/2}$	0.028(5)
^{207}Tl	$\pi 3p^{-1}_{3/2} \rightarrow \pi 2f^{-1}_{5/2}$	0.013(3)
^{209}Pb	$\nu 1i_{11/2} \rightarrow \nu 2g_{9/2}$	0.0055(6)
^{209}Bi	$\pi 2f_{7/2} \rightarrow \pi 1h_{9/2}$	0.0026(5)

Nucleus	$j_i \rightarrow j_f$	B(E2) W.u.
^{207}Pb	$\nu 2f^{-1}_{5/2} \rightarrow \nu 3p^{-1}_{1/2}$	0.972(6)
	$\nu 3p^{-1}_{3/2} \rightarrow \nu 3p^{-1}_{1/2}$	0.92(22)
^{207}Tl	$\pi 3p^{-1}_{3/2} \rightarrow \pi 2f^{-1}_{5/2}$	2.7(7)
^{209}Pb	$\nu 3d_{5/2} \rightarrow \nu 2g_{9/2}$	2.7(7)
	$\nu 4s_{1/2} \rightarrow \nu 3d_{5/2}$	2.13(8)
^{209}Bi	$\pi 2f_{7/2} \rightarrow \pi 1h_{9/2}$	0.44(9)

[a] Values taken from [KL11] or [CK15]

Therefore, we can conclude that the single particle $\nu 3s^{-1}_{1/2} \rightarrow \nu 3d^{-1}_{3/2}$ 332-keV γ transition is predominantly of l-forbidden M1 character, with a negligible E2 contribution. Its enhanced B(M1) strength may be produced by the influence of core-excitations across the shell gap. However, there are no shell-model calculations that fully reproduce this enhancement. The large value for the B(M1) transition rate is consistent with the

reported strength for others l-forbidden M1 transitions between single particle levels in the ^{208}Pb region.

6.9.2 Lifetimes of high-spin levels populated in the ^{131m2}In decay

Apart from the single particle $(1/2^+)$ 332-keV level, there is also a set of core-excited levels, populated in both the decay of the high spin ^{131m2}In isomer, whose lifetimes were accessible for the first time in our analysis. For the high energy levels above 4 MeV is quite uncommon to observe lifetimes longer than picoseconds. In this decay, there is a lot excited levels with a very large angular momentum $J = (19/2,21/2,23/2)$. Due to the large spin difference with the $(11/2^-)$ state in ^{131}Sn, they usually lack a low-multipolarity transition that could connect them and, there are no intermediate levels available either. Thus those levels can only de-excite by reducing their spin step by step via emission several low energy γ-rays until they reach a level that can decay to the $(11/2^-)$ state. This situation is analog to the observed in the ^{132}In decay-scheme. A clear example of this situation the 4607+X-keV $(23/2^-)$ level, it can only be de-excited into the 4607+X-keV $(19/2^-)$ via a E2 158-keV γ-ray, giving rise to a long half-life of 315(6) ns [DSA$^+$19]. In ^{131m2}In the $(17/2^+)$ 4273+X keV level is the one that collects most of the de-excitations from the higher-lying levels, and connects them with the $(11/2^-)$ state via the 4273-keV E3 transition.

6.9.2.1 Half-life of the 4447+X $(19/2^-)$ level

The 4447+X-keV level in ^{131}Sn is strongly populated in the β-decay of ^{131m2}In, ($\sim$42% of the decays). However, it is not directly populated, but indirectly γ-rays from "upper" levels. The strongest feeding is due to the 159-keV transition from the 4606+X $(23/2^-)$ state, which accounts for $\sim$30% of the 42% total intensity. The level de-excites by three γ-transitions, the strongest one is the 173-keV γ-ray which has 80% of the branching ratio. Given this situation, the best method to measure the lifetime of the 4447+X level is to analyse the time distribution of the 159-173-keV $\gamma\gamma$(t) coincidences measured by the $LaBr_3$(Ce) detectors.

Figure 6.28 shows the $\gamma\gamma$(t) coincidences energy matrix measured by the $LaBr_3$(Ce) detectors for A = 131. The 158-173-keV coincidence peak can be clearly observed, as it stands out from the background. Given the proximity of the energies of both transitions, the peaks arising from delayed and anti-delayed events appear very close to

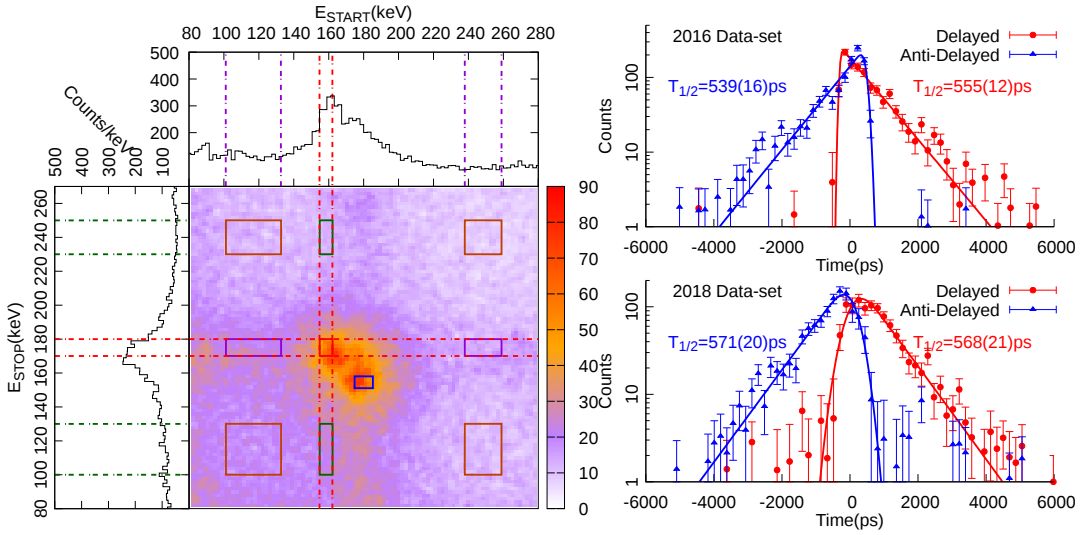

Figure 6.28: 4446+X $\gamma\gamma$(t) fast-timing analysis. Time distributions measured for the 158-173-keV $\gamma\gamma$ coincidences. The red circles correspond to delayed coincidence events, the anti-delayed events that show an inverted time-distribution are depicted in blue triangles. Along with the time distribution the fit curves are represented, with the derived $T_{1/2}$.

each other, slightly overlapping. The energy gates employed to get the time distributions are also drawn. The contribution from Compton events to the time distributions has been estimated from the nearby backgrounds regions and subtracted. The final time distributions used to extract the lifetimes are depicted in Figure 6.28. The analysis provides 4 different time spectra, corresponding to the delayed and anti-delayed time distributions from the two data sets. The half-life was extracted by fitting the time distribution to an exponential decay convoluted with a Gaussian function to account for the limited time resolution of the system. A constant was also included in the fit, to account for possible random background contributions. The fit and half-life results are shown in the plots.

The four values obtained are compatible with each other. Thus the final value was adopted as the weighted average of the 4 measurements, yielding a $T_{1/2}$ = 555(8) ps.

6.9.2.2 Half-life of the 4558+X (19/2$^+$) level

The 4558+X keV (19/2$^+$) is very strongly populated in the β^- ^{131m2}In decay, around 37% of the total decays go through this level. The main feeding is provided by γ-rays from higher-lying levels, being the 2096-keV γ-ray from the 6654+X keV level the

strongest one, which contributes with ∼26% of the 36% of the feeding. On the other hand, the 4558+X keV level only decays by a 284-keV γ-ray that connects it to the 4274+X keV. This level level was identified in [BDZ$^+$01] as a $(19/2^+)$ member of the $\nu f_{7/2} d_{3/2}^{-1} h_{11/2}^{-1}$ configuration, which would be analogous to the 4830 keV 4^- state in ^{132}Sn from the $\nu f_{7/2} d_{3/2}^{-1}$ particle-hole multiplet.

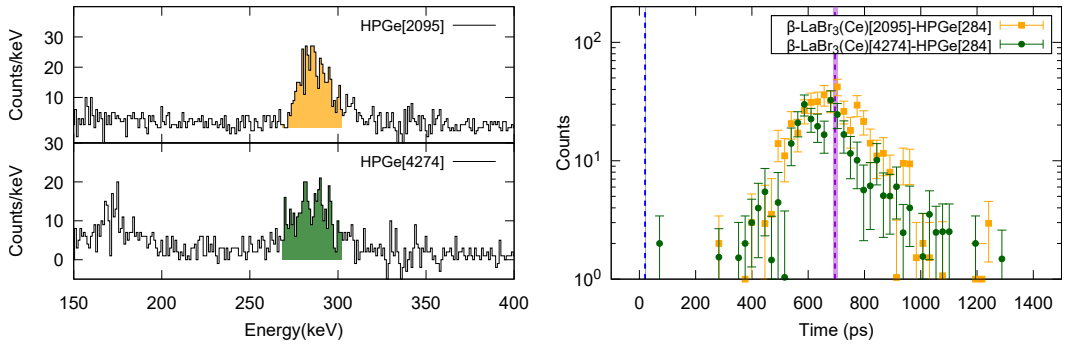

Figure 6.29: $\beta\gamma\gamma$ Energy spectrum for one of the LaBr$_3$(Ce) detectors gated on the HPGe detectors by the 2096-keV (top) and by the 4273-keV (bottom) transitions. The spectra hava been generated by applying gates in the HPGe detectors in the designed γ-rays. The contribution from the Compton background underneath the peaks in the HPGe detectors has been subtracted. The coloured bins in the spectra depict the selected events to built the time distributions used to measure the lifetime of the 4558+X−keV level.

The lifetime of this level has been measured by analysis of the $\beta\gamma$(t) time difference distributions of the 284−keV γ-rays measured in the LaBr$_3$(Ce) detectors. Since the 284 keV peak cannot be selected cleanly in the double coincidence β-LaBr$_3$(Ce) spectra by itself, a third coincidence in the HPGe detectors has been required in order to clean the spectra. There are two γ-rays that can be used to achieve a clean selection of the 284-keV peak in the LaBr$_3$(Ce) energy spectra, one is the 2096-keV feeding transition, while the other one is the 4274-keV γ-ray that follows the 284-keV emission. The remaining transitions have not been considered due to the insufficient amount of statistics. Figure 6.29 shows the spectra in one of the LaBr$_3$(Ce) detectors after gating on these two γ-rays respectively. Both conditions provide a similar amount of statistics for the coincidences and a clean selection of the peaks. Hence both time distributions have been analyzed.

The centroid shift analysis is depicted in Figures 6.30, together with the derived mean life value n each case. This analysis produces, four measurements for the half-life,

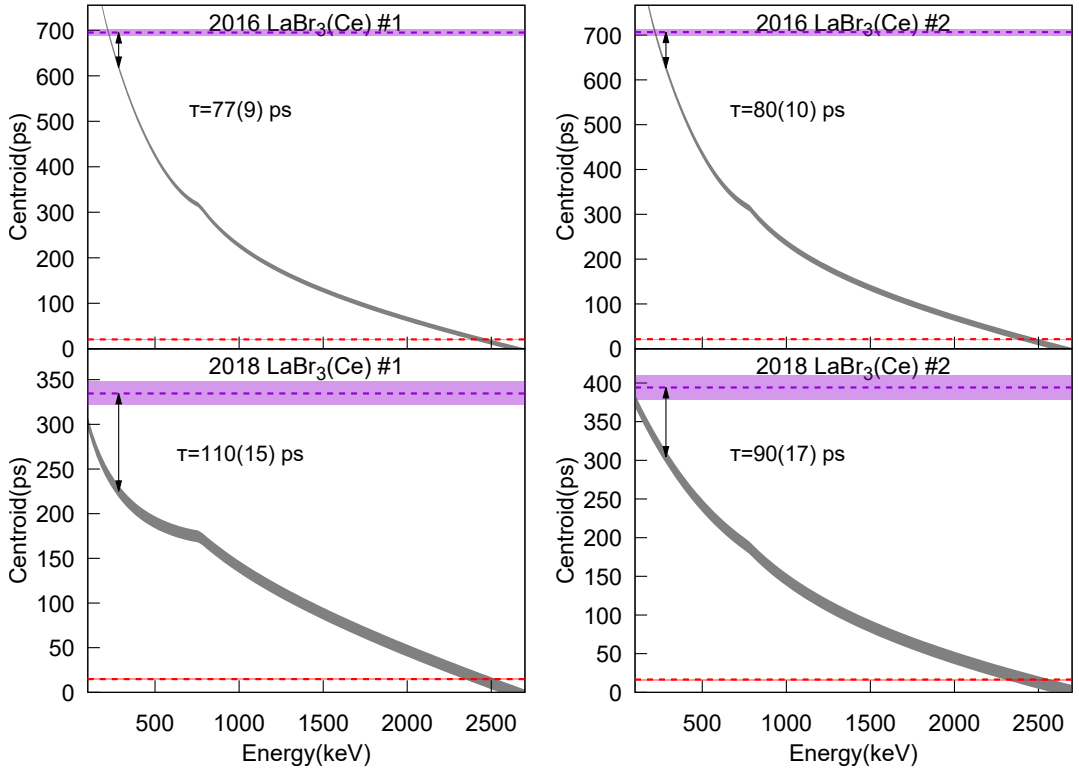

Figure 6.30: Centroid shift analysis for the lifetime of the 4558+X keV ($19/2^+$) level. (Left) β-$LaBr_3$(Ce) time difference distributions for the 284-keV γ-ray gated on the 2096-keV (violet) and 4274-keV (orange) transitions in the HPGe detectors. The blue spectrum corresponds to the time distribution of the 2434-keV measured in double β-$LaBr_3$(Ce) coincidences, which was used as a prompt reference. The centroid position for the 284-keV time spectra was adopted as the weighted average of both distributions. (Right) Comparison of the measured centroid shift with the expected shift due to the energy dependence of the time response in $LaBr_3$(Ce) detectors.

consistent with each other. The centroid position for the 284-keV γ-ray is derived from the weighted average centroid from the time distribution corresponding to both HPGe gate conditions. For the prompt reference, the time distribution of the 2434-keV γ-rays was used also for this lifetime, due to the lack of a intense prompt transition in this decay. The final value was adopted as the weighted average of the 4 measurements, which yielded a $T_{1/2}$=58(4) ps value for the 4558+X-keV level.

6.9.2.3 Half-life of the 4606+X ($23/2^-$) level

The 4606+X keV level in ^{131}Sn was proposed as the $(23/2^-)$ member of the $\nu f_{7/2}h^{-2}_{11/2}$ configuration [BDZ+01]. The lifetime of this level has been measured before in previous β-decay experiments, the most recent value being $T_{1/2} = 315(6)$ ns [DSA+19]. In our work a new measurement of this half-life has been performed, by analyzing the β-HPGe time-difference spectra for the de-exciting γ-rays. The 159-keV transition is the only one that de-excites the 4606+X keV, connecting it to the 4447+X level. Due to the long lifetime all the γ-rays emitted from the 4447+X keV level, carry the same time distribution of the 159-keV γ-ray. For that reason, we have analyzed the time distributions of the 159-, 173- and 4274-keV transitions.

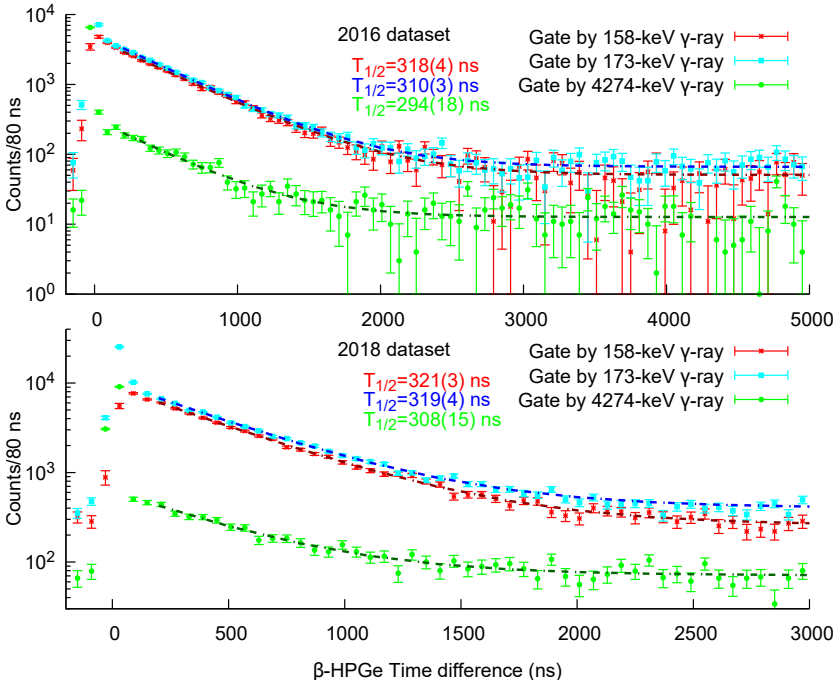

Figure 6.31: β-HPGe Time difference distribution for the 159-, 173-, 4274-keV γ-rays. (Top) 2016 campaign. (Bottom) 2018 campaign. The time distributions have been built by selecting each of the treee γ-rays separately. The contributions from the Compton background, over which these peaks sit on have been estimated from the nearby background, and subtracted from the time spectrum. The lifetime is obtained by an χ^2 fit of each time distribution to a exponential decay, plus a constant, to account for the background distribution of random coincidences.

The time distributions for the trio of γ-rays from each data set are depicted in Figure

Table 6.5: Reduced transition probabilities of the 4447.2+X in ^{131}Sn. The B(λL) were calculated assuming a pure multipolarity for the transitions.

E_i(keV)	Config$_i$	E_f(keV)	Config$_f$	J_f^Π	E_γ(keV)	Xλ	B(λL) (W.u.)
331.6	$(\nu s_{1/2}^{-1})$	g.s	$(\nu d_{3/2}^{-1})$	$(3/2^+)$	331.6	M1	0.033(7)
$J_i^\Pi = (1/2^+)$							
$T_{1/2}$ = 18(4) ps							
4447.2+X	$(\nu f_{7/2}h_{11/2}^{-2})$	X	$(\nu h_{11/2}^{-1})$	$(11/2^-)$	4447.2	E4	19.7(3)
$J_i^\Pi = (19/2^-)$		4102.7+X	$(\nu f_{7/2}h_{11/2}^{-2})$	$(15/2^-)$	344.3	E2	0.655(9)
$T_{1/2}$ = 555(8) ps		4273.9+X	$\nu h_{11/2}^{-1}\otimes$(Oct. Vibr.)	$(17/2^+)$	173.3	E1	$6.9(10)\times10^{-5}$
4558.4+X	$\nu f_{7/2}d_{3/2}^{-1}h_{11/2}^{-1}$	4273.9+X	$\nu h_{11/2}^{-1}\otimes$(Oct. Vibr.)	$(17/2^+)$	284.6	M1	$1.59(12)\cdot10^{-2}$
$J_i^\Pi = (19/2^+)$							
$T_{1/2}$ = 58(4) ps							
4606+X	$(\nu f_{7/2}h_{11/2}^{-2})$	4447.2+X	$(\nu f_{7/2}h_{11/2}^{-2})$	$(19/2^-)$	132	E2	0.340(3)
$J_i^\Pi = (21/2^-)$							
$T_{1/2}$ = 316(2) ns							

6.31. The analysis of each time spectrum furnished an independent measurement for this lifetime. The half-life was extracted by fitting each time distribution to an exponential decay function plus a constant background. The first 300 ns from the spectra were removed to reduce the influence of the prompt γ-events. We adopted the weighted average of the six measurements, $T_{1/2}$ = 316(2) ns as the final value. This new value is in perfect agreement with the 315(6) ns reported by Dunlop *et al.* [DSA$^+$19].

6.9.3 B(Xλ) values

Using the lifetimes derived in this work, the reduced transition probabilities for the most likely multipolarities have been determined. The values are summarized in Table 6.5.

The lifetime of the 4447+X-keV $(19/2^-)$ state, $T_{1/2}$ = 555(8) ps, is much shorter than the $T_{1/2}$ = 3.99(2) ns measured for its analog 4417-keV state in ^{132}Sn. From this value, and the relative γ-ray branching ratios (Table 6.3), the B(Xλ) reduced transition probabilities for the three transitions that de-excite it have been obtained. The E2 and E4 transitions are very consistent, the E2 being of the same order of magnitude and the E4 being stronger by a factor of 2.5 in ^{131}Sn. On the contrary, the E1 transition that connects this level to the octupole vibrational state is enormously enhanced in ^{131}Sn, having 40 times larger B(E1) for this mass than in ^{132}Sn.

This value is similar to the $T_{1/2}$ = 27(2) ps of its analog 4830.5-keV (4^-) state in

^{132}Sn. In the doubly magic tin, the 4830.5-keV de-excites also only to the octupole vibrational state by a 478.9-keV γ-ray, which was assumed of predominantly M1 character. Assuming also in ^{131}Sn M1 multipolarity for the 285-keV transition, the B(M1) rate has been calculated. Using the the theoretical internal conversion coefficients [KBT^{+}08], a B(M1) = 0.028(2) μ_N^2 or B(M1) = 15.9(12)$\times 10^{-3}$ W.u. was obtained. This value compares well with the B(M1) = 7.3(5)$\times 10^{-3}$ W.u. measured for the 478.9-keV transition in ^{132}Sn.

The 4606+X keV state is assumed to be the $(23/2^{-})$ member of the $\nu f_{7/2} h_{11/2}^{-2}$ configuration, whose equivalent in ^{132}Sn would be the 4716-keV (4^{+}) state from the $\nu f_{7/2} h_{11/2}^{-1}$ p-h multiplet. The 4716-keV level has a $T_{1/2}$ = 21.3(4) ns half-life, being de-excited only by a 299-keV γ-ray of E2 multipolarity. Assuming a pure E2 multipolarity also for the 159-keV transition, a B(E2) = 13.44(10) e^2fm^4 or B(E2) = 0.340(3) W.u. transition strength is derived. This value compares well to the 0.268(2) W.u. measured for the 299-keV transition in ^{132}Sn.

6.10 Conclusions

The excited structure of the neutron single-hole ^{131}Sn has been investigated in detail at ISOLDE, where the ^{131}Sn excited levels were populated in the β-decay of ^{131}In. The results obtained in this work have been discussed in this chapter. They can be summarized as follows:

- The half-lives of the three β-decaying states in ^{131}In have been newly measured with increased precision compared to previous values, Section 6.3. These three new values, $T_1/2[^{131g}\text{In}]$ = 261.8(4) ms, $T_1/2[^{131m1}\text{In}]$ = 335.7(6) ms and $T_{1/2}[^{131m2}\text{In}]$ = 343(2) ms, are in good agreement with the previous measurements.

- The level-scheme of ^{131}Sn has been notably expanded in the framework of this thesis with the addition of 28 new γ-lines and 22 new excited levels. The decay schemes of the three β-decaying states of ^{131g}In, ^{131m1}In and ^{131m2}In, are depicted in Figures 6.13, 6.11 and 6.21 separately.

- The population of a μs isomeric state in ^{131}Sn at 4680+X-keV has been suggested, based on the analysis of the γ-γ delayed coincidences with the 158-keV transition.

This level would correspond to the $27/2^-$ member of the $\nu d_{3/2}h_{11/2}^{-2}$ multiplet. A more detailed measurement is required to confirm this tentative assignment.

- An exhaustive analysis have been carried out to confirm the energy position $\nu h_{11/2}^{-1}$ single-hole state in ^{131}Sn, via $\gamma-\gamma$ coincidences. Evidences that supports the 65.1 keV assignment proposed in [FGM$^+$04a] were found in our analysis. Nevertheless, there is no definitive confirmation yet. Our analysis suggests that a more detailed investigation off the high-lying excited levels that are populated in ^{131g}In decay will likely shed light on the position of the $(11/2^-)$, via the identification of several levels that de-excite to both the 2434-keV $(7/2^+)$ state and the $(11/2^-)$ state of unknown energy.

- The direct feeding to the β-decaying levels in ^{131}Sn has been derived in this work from the daughter decay intensities. The isomer selectivity allowed us to separate the contributions from the β-decay of the ^{131g}In, ^{131m1}In and ^{131m2}In states. As result, a strong revision of the values with regard to previously reported ones is proposed. This revision has a sizable effect in the logft values, which solves the problem of the apparent disagreement between the different first-forbidden transition reported in previous investigations [FGM$^+$04a, DSA$^+$19]. Our new values indicate similar logft values for the three f.f. transitions: $\pi g_{9/2}^{-1} \rightarrow \nu h_{11/2}^{-1}$ with logft=5.5(2), $\pi p_{1/2}^{-1} \rightarrow \nu d_{3/2}^{-1}$ with logft=5.34(13), and $\pi p_{1/2}^{-1} \rightarrow \nu s_{1/2}^{-1}$ with logft=5.40(4).

- The three separate P_n values for three ^{131}In β-decaying states have been derived independently for the first time in this work. The new values are $P_n[^{131g}\text{In}] = 2.4(6)$ %, $P_n[^{131g}\text{In}] = 1.2(6)$ % and $P_n[^{131m2}\text{In}] = 8.9(8)$ %.

- A complete investigation of γ-emitting excited levels placed at very high energies above the neutron separation energies in ^{131}Sn has been performed. There is a large number of these states in ^{131}Sn, showing in some cases transitions between two neutron-unbound levels. Our analysis shows a clear correlation between the appearance of these states and the feeding β-decaying ^{131}In state. This indicates the correlation between the competition of γ-ray and neutron emission with the spin of the available levels in ^{130}Sn, see Figure 6.23.

- The first sub-nanosecond lifetime measurements for this isotope have been performed. The half-life of the neutron single-hole 332-keV ($1/2^+$) state has been derived, $T_{1/2}$=18(4) ps. This short lifetime indicates an enhanced *l-forbidden* M1 character for the 332-keV $\nu 3s_{1/2} \rightarrow \nu 3d_{3/2}$ transition. This value is similar to those measured for the corresponding *l-forbidden* M1 transitions in the ^{208}Pb region.

- Regarding the high-spin levels, the half-life of the 4447+X keV and 4558+X-keV levels have been measured for the first time, and a new value has been obtained for the long-lived 4606+X-keV level. The transition strengths derived from these lifetimes compare very well with those of their corresponding transitions in ^{132}Sn, which reinforces the analogy between the ^{131m2}In and the ^{132}In decays, see Chapter 5. The only striking difference is the 173-keV E1 4447+X→4274+X transition, whose strength is ∼40 times larger than the analogous E1 transition in ^{132}Sn.

The results detailed above provide new information on the β-decay properties of the β-decaying ^{131}In states and on the structure of ^{131}Sn.

7

Lifetime measurements in ^{133}Sn

The ^{133}Sn isotope is built by adding a single neutron in the $N = 82-126$ shell to the doubly magic ^{132}Sn core. Consequently, its low lying excited structure is determined by the neutron located above the $N = 82$ shell gap. Due to the simplicity of this system, along with location far from stability, this tin isotope has attracted the attention of experimental investigations in the last decades.

The level scheme in ^{133}Sn is very similar to that observed in ^{131}Sn, by replacing a neutron particle by a neutron hole, see Figure 1.3 from Chapter 1. Its low-lying levels are identified as single particle states, in this case one neutron in the N=82−128 shell. The excited structure of ^{133}Sn has been investigated using a number of experimental techniques. A previous β-decay study, carried out at ISOLDE by Hoff *et al.* [HBH$^+$96], lead to the first observation of excited states in ^{133}Sn. Three single neutron states were identified, which were populated in the β-n decay of ^{134}In. In a later experiment [ASB$^+$14], ^{133}Sn states were populated in a neutron transfer experiment performed at HRIBF, which expanded the level-scheme in ^{133}Sn, and identified another of the single-particle levels. From all the expected single particle states in ^{133}Sn, the excitation energies for the single particles for $\nu f_{7/2}$ (ground state), $\nu p_{3/2}$ (854 keV), $\nu p_{1/2}$ (1367 keV), $\nu h_{9/2}$ (1561 keV) and $\nu f_{5/2}$ (2005 keV) have been experimentally identified. So far only the excitation energy for the $\nu i_{13/2}$ remains missing. The purity of the single-neutron excited states in ^{133}Sn was proven by the large spectroscopic factors (S≈1) measured for these states, [JAB$^+$10].

At higher energies, above 3 MeV, it becomes possible to excite the ^{132}Sn core, giving rise to a multitude of core-excited levels. Nonetheless, the ^{133}Sn is characterized by a

very low neutron separation energy, S_n=2398.7(27) keV [WAK$^+$17]. Most of the core-excited states appear above this energy and thus they are neutron unbound. In a recent investigation carried out at RIKEN [VJD$^+$17] the population of states above the S_n, de-exciting by γ-ray emission was observed. This feature is similar to what is observed in ^{131}Sn, and described in the previous chapter.

Apart from the energies of the single-neutron states, the information about the lifetime of these levels is interesting from the shell model point of view. Lifetimes provide direct access to matrix elements of pure electromagnetic operators that are expected to connect the single particle levels. To date, the half-life of three of the states in ^{133}Sn have been measured, the $\nu p_{3/2}$ 854-keV state, τ = 30(15) ps [VJD$^+$17], and the $\nu f_{5/2}$ 2002-keV and $\nu p_{1/2}$ 1367-keV states, τ = 480($^{160}_{-100}$) fs and τ = 13($^{10}_{-13}$) fs [ASB$^+$14], respectively. This chapter focuses in the investigation of lifetimes of the excited single-particle levels in ^{133}Sn.

7.1 Feeding of ^{133}Sn states in the β-decay of ^{133}In and ^{134}In

The excited structure of ^{133}Sn has also been studied in our experiment. The excited levels were populated both in the β decay of ^{133}In and ^{134}In. In Figure 7.1 the $\gamma-$ray spectrum measured in the decay of each of the ^{133}In β-decaying states is shown. In the spectrum we can identify γ-rays both in ^{133}Sn and ^{132}Sn, as well as several structures arising from inelastic scattering of the delayed neutrons in the HPGe detectors. As discussed in Section 5.2.3 in Chapter 5, the β-delayed neutron emission is the dominant decay branch for both ^{133}In decaying isomers, with $P_n[^{133g}\text{In}]$=90(3)% and $P_n[^{133m}\text{In}]$=93(3)%. Therefore, the population of excited levels in ^{133}Sn is not much favored in this decay. Nevertheless, several γ-ray transitions belonging to ^{133}Sn can be identified in the spectra.

The investigation of the γ-ray spectra revealed the population of the neutron single-particle states $\nu 2f_{7/2}$, $\nu 3p_{3/2}$, $\nu 3p_{1/2}$ and $\nu 2h_{9/2}$ in the ^{133}In decay. In addition, three states above the neutron-separation energy were also identified in ^{133}Sn, which decay by emission of γ-rays. These levels were suggested to arise from the $\nu f^2_{7/2}h^{-1}_{11/2}$ and $\nu f^2_{7/2}g^{-1}_{7/2}$ configurations. The results derived from our investigation were summarized and published by Piersa *et al.* in [PKF$^+$19]. Figure 7.2 illustrates the decay-scheme of ^{133}In.

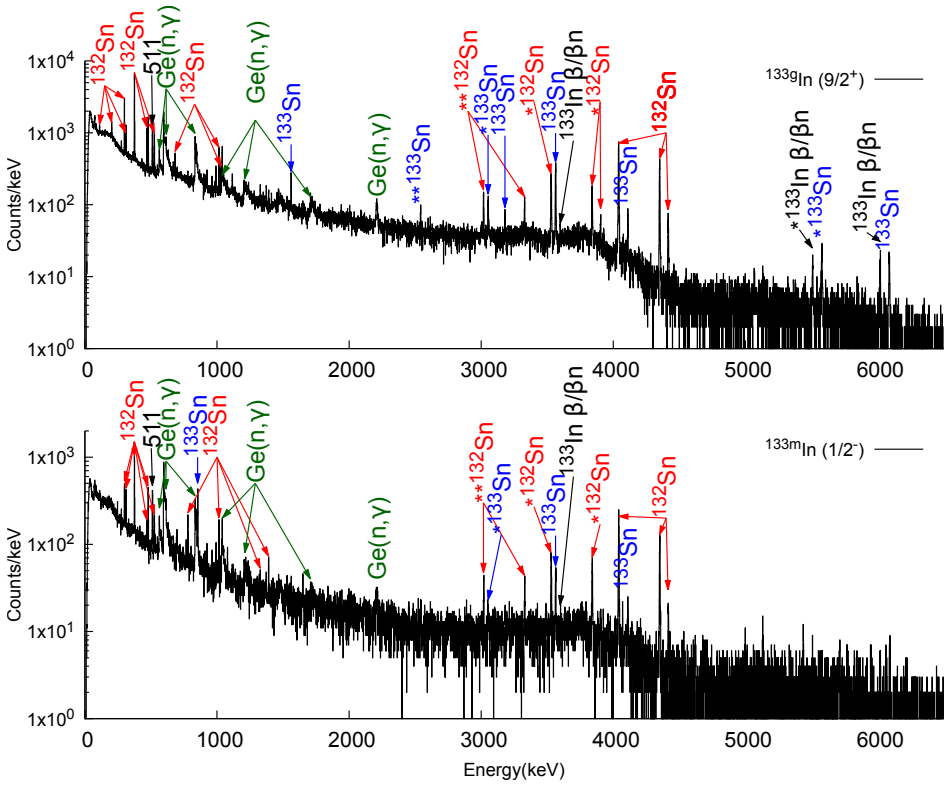

Figure 7.1: HPGe spectra measured in the decay of ^{133}In.

The decay of ^{134}In is also characterized by a large intensity of the β-n decay branch, P_n=65% [HBH$^+$96]. For this reason, the β-decay of ^{134}In is the best method to populate the excited levels in ^{133}Sn. This feature can be clearly observed in Figure 7.3, where the β-gated HPGe spectrum measured in the decay of ^{134}In is displayed. The strongest γ rays correspond to transitions in ^{133}Sn. Several γ rays in ^{134}Sn were identified in this ^{134}In decay for the first time. Additionally, several weak γ lines from ^{132}Sn can also be observed, which indicates that ^{134}In has a β-2n decay branch.

Population to the single-particle states in ^{133}Sn has been observed in the ^{134}In β-n decay. In particular, the $\nu h_{9/2}$ and $\nu f_{7/2}$ states are the ones that receive most of the feeding. Population to the $\nu p_{3/2}$ and the $\nu f_{5/2}$ levels can also be observed, but they are more weakly populated in this decay.

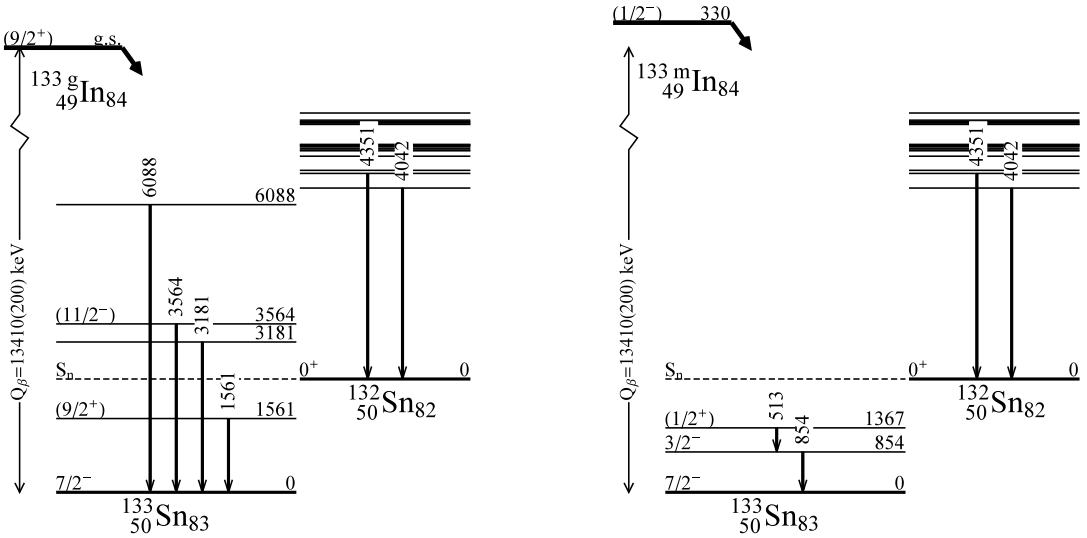

Figure 7.2: Partial β-decay scheme of ^{133}In. Only the levels in ^{133}Sn are labeled. All the states observed below the neutron separation energy are of dominant single-particle nature.

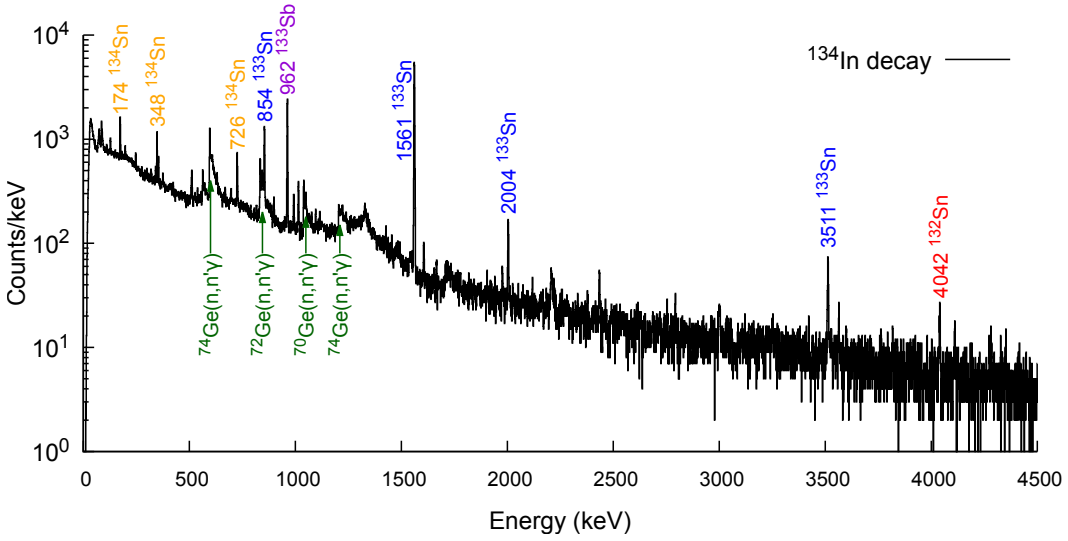

Figure 7.3: β-gated HPGe spectrum for the decay of ^{134}In.

7.2 Half-life of $\nu p_{3/2}$ single neutron state

Among the single-particle states observed in ^{133}Sn, only the lifetime of 854-keV $\nu p_{3/2}$ state that can be measured using the fast-timing technique. The remaining levels are

not reachable either due to their short lifetime, below the ps range, or due to the limited statistics of the de-exciting γ-rays. The population of the 854-keV level has been reported in both the ^{133m}In $(1/2^-)$ β decay and ^{134}In β-n decay [HBH$^+$00]. Nevertheless, only for the data measured the decay of ^{134}In there is enough statistics to derive a reliable lifetime from the fast-timing analysis. For ^{133m}In decay the direct β decay branch is very weak 8(3)%, see subsection 5.2.3 in Chapter 5, thus an extra coincidence with HPGe detectors would be required to cleanly select the 854-keV γ-line in the $LaBr_3$(Ce) detector. However this is not possible given the insufficient statistics recorded in triple coincidence for the higher masses.

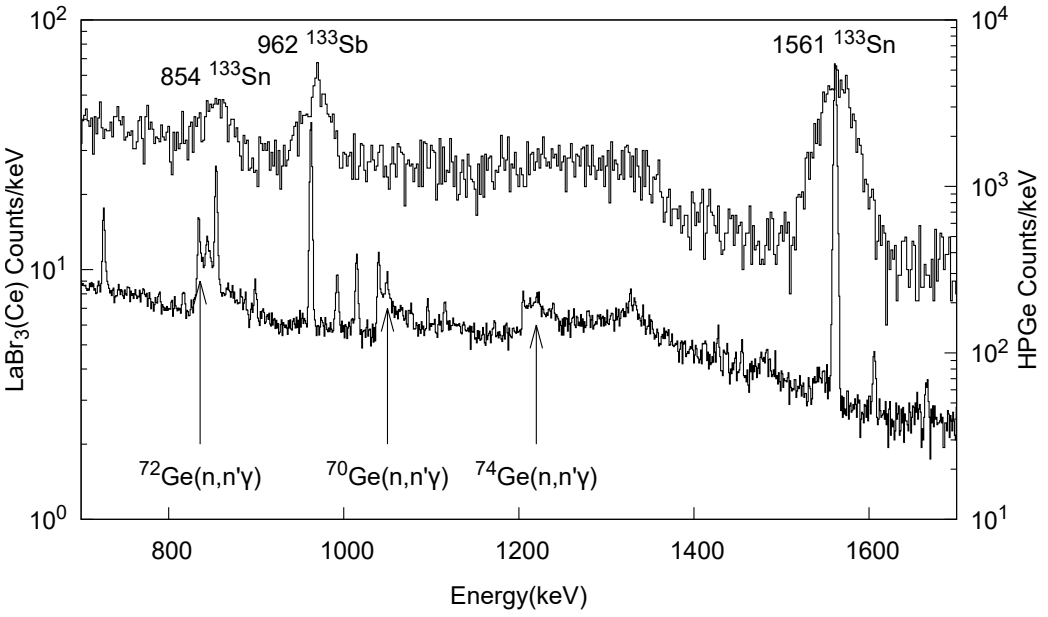

Figure 7.4: β-gated γ-ray spectra measured during ^{134}In decay within the first 600 ms after the proton pulse. The tree dominant γ-lines in the spectra belong to the 1561- and 854-keV transitions in ^{133}Sn, and the 962-keV transition from the daughter ^{133}Sb. Neutron-induced lines are seen in the HPGe detectors, but not in the $LaBr_3$(Ce) crystals.

The half-life of the 854-keV $(3/2^-)$ state has been measured by analyzing the $\beta\gamma$(t) time distribution of the 854-keV γ-rays, selected in the $LaBr_3$(Ce) detectors. Since this level shows a short lifetime, it has to be measured by the centroid shift method, hence the use of a prompt reference is required. The best option to fulfill this role is the 1561-keV γ-ray in ^{133}Sn, which de-excites the 1561-keV $(9/2^-)$ single-particle state, for

which a short lifetime of ∼1ps is expected.

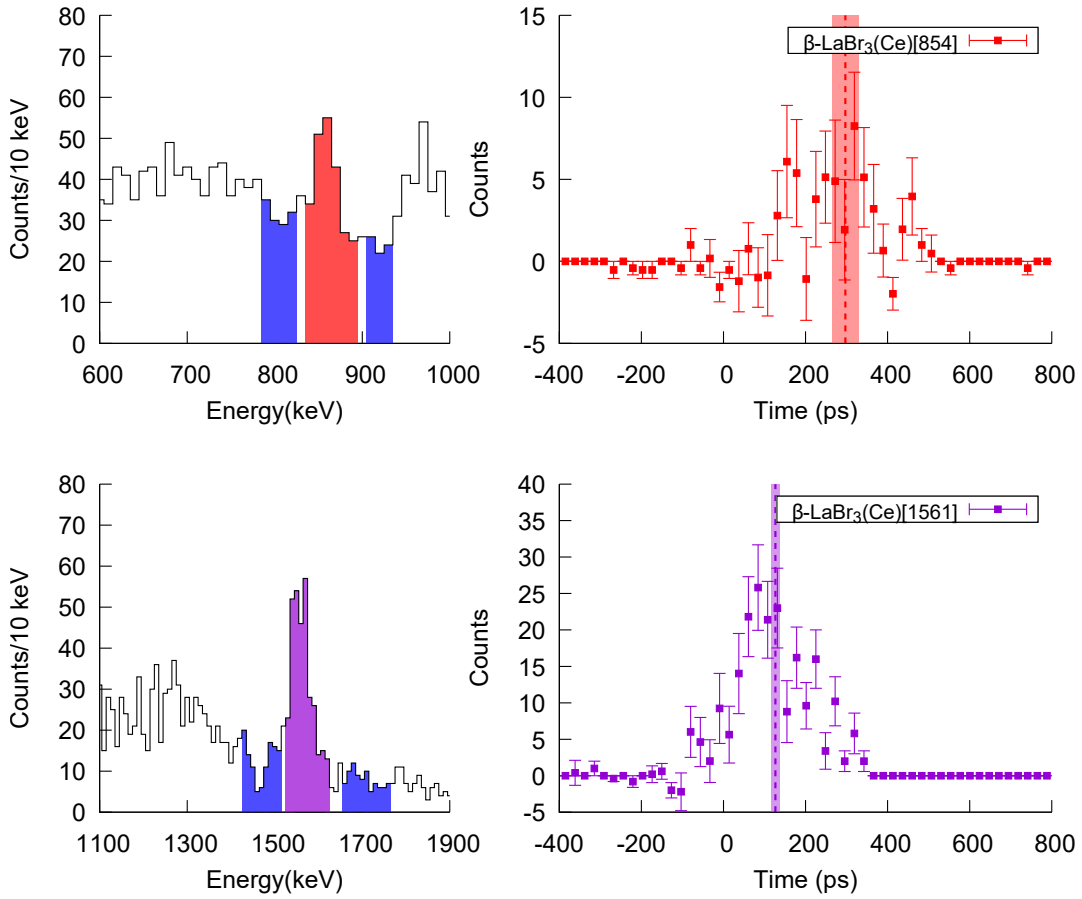

Figure 7.5: $\beta\gamma$(t) Time-delayed analysis for the half-life of 854-keV state (2016 dataset). (Left) β-$LaBr_3$(Ce) energy spectra at the energy regions of the 854- and 1561-keV peaks. The colored areas identify the regions used to estimate the time distributions from the peaks and the background beneath them. (Right) $\beta\gamma$(t) time-delayed distributions for 854- and 1561-keV transitions, after applying all the corrections for the background contributions. Only the events recorded in the first 600 ms after proton impact have been used.

To check that the 854- and 1561-keV peaks can be selected in the $LaBr_3$(Ce) detectors, without admixture of other γ-rays of similar energy, we have studied the β-gated HPGe spectrum obtained under the same conditions. Figure 7.4 shows the comparison between the β-gated γ-ray spectra measured for the HPGe and $LaBr_3$(Ce) detectors restricted to the initial 600 ms after the proton pulse. Regarding the 1561-keV peak,

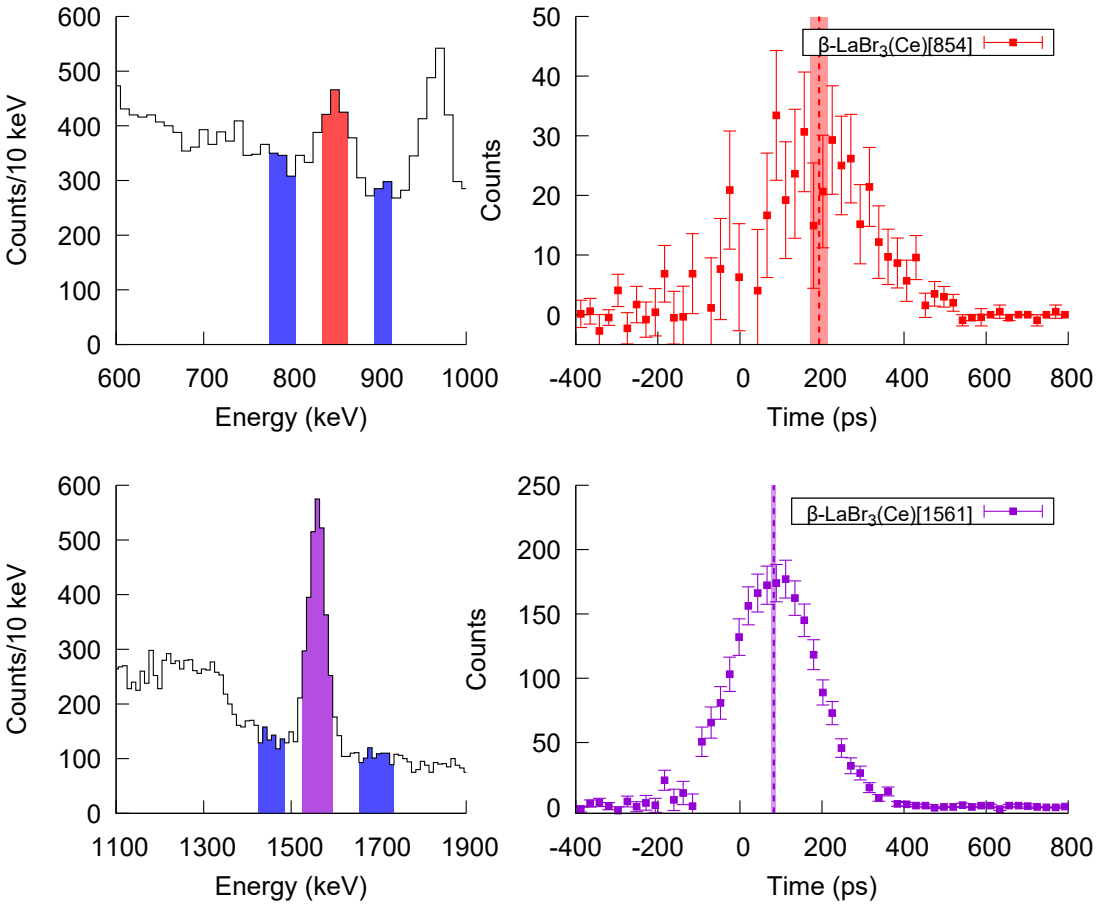

Figure 7.6: $\beta\gamma$(t) Time-delayed analysis for the half-life of 854-keV state (2018 dataset). Same as in Figure 7.5, but for the 2018 dataset.

there is no other γ line with similar intensity close to it, so it can be safely selected in the $LaBr_3$(Ce). On the other hand the 854-keV peak does sit on a structure that has been identified as the interaction of delayed neutrons with the germanium of the HPGe detectors. These broadened lines will not appear in the $LaBr_3$(Ce) detectors and thus the 854-keV γ-line it is also clean in the $LaBr_3$(Ce) spectra.

Figure 7.6 shows the analysis carried out to derive the time-delayed spectra for the 854-keV and 1561-keV γ-rays. The 854-keV γ line sits on a high Compton background. Its contribution has been estimated from the nearby regions of the spectrum and its been removed from the time spectrum. Nevertheless, the low FEP to Compton ratio of $\sim$0.4 notably increases the uncertainty of the 854-keV peak centroid position.

In the measurements carried out in 2016, the limited statistics recorded for the 854-keV peaks was far insufficient for a full fast-timing analysis, see Figure 7.5. Hence it was only possible to obtain an upper limit for this lifetime from this dataset, $\tau < 49$ ps [PKF+19]. A second analysis, performed for the dataset from the 2018 campaign, provided a reliable value thanks to the increase in the statistics accumulated for the ^{134}Sn decay.

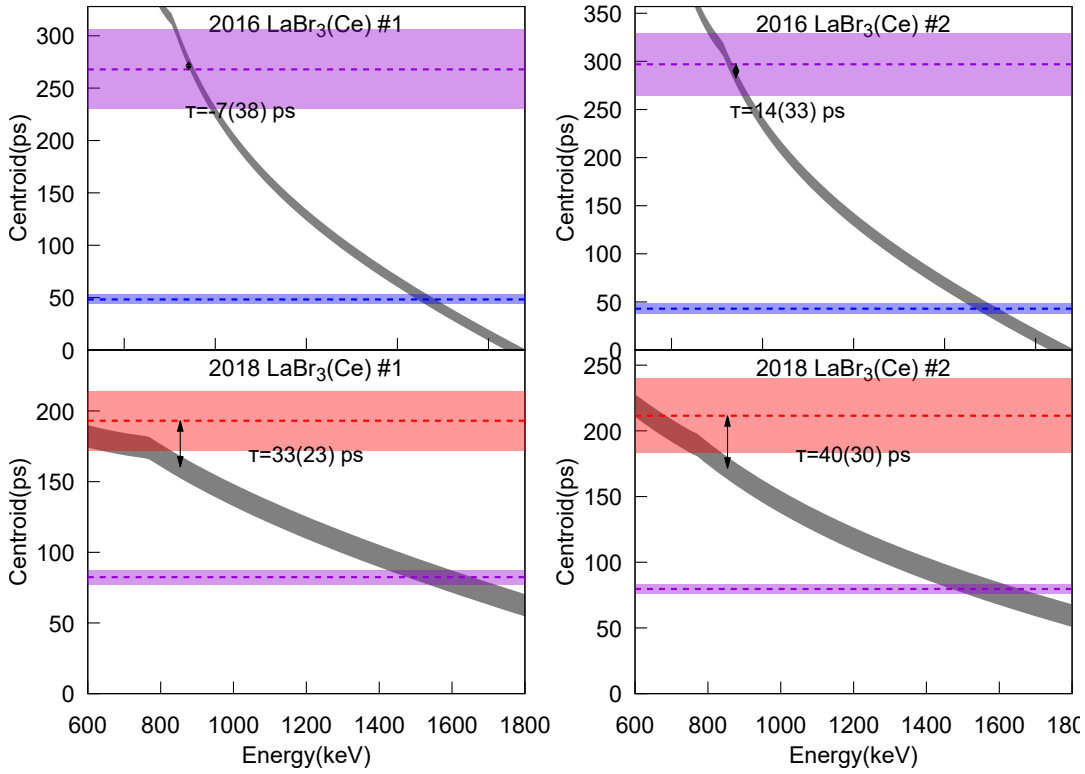

Figure 7.7: Centroid shift analysis for the 854-keV state.

Figure 7.7 shows the shift of the centroid position of the 854-keV time distributions, relative to its position from the FEP calibration curves. Both values have a large uncertainty, consequence of the low peak-to-background ratio. Nevertheless, in both cases the centroid is shifted from the prompt by more than 1σ. In addition, both values are in excellent agreement with each other. The final result was adopted as the weighted average of the two measurements, which gives τ=36(18) ps, equivalent to $T_{1/2}$=25(12) ps. This new measurement obtained for the mean-life of the single particle 854-keV single particle level $\nu p_{3/2}$, is in full agreement with the τ=30(15) ps value obtained by

Vaquero *et al.* [VJD$^+$17] from the Doppler shift analysis of the 854-keV γ-ray at RIBF (RIKEN).

7.3 Comparison with the ^{208}Pb region.

Using the new lifetime a strength of B(E2)=$50(^{+51}_{-34})$ e^{2}fm^4 = $1.2(^{+13}_{-8})$ W.u., was derived for the $\nu p_{3/2} \rightarrow \nu f_{7/2}$ transition. It is worth comparing this value with the B(E2) measured for single particle transitions in the region around ^{208}Pb, which are summarized in Table 7.1. The B(E2) strengths from the doubly-magic lead region have similar values, all the strengths are close to 1 Weisskopf unit, but showing a certain scatter between isotopes. The B(E2)=$1.2(^{13}_{8})$ W.u. measured for ^{133}Sn $\nu p_{3/2} \rightarrow \nu f_{7/2}$ is comparable to the values from lead region.

Table 7.1: B(Xλ) for allowed E2 transitions near ^{208}Pb

Nucleus	$j_i \rightarrow j_f$	B(E2) W.u.
^{207}Pb	$\nu 2f^{-1}_{5/2} \rightarrow \nu 3p^{-1}_{1/2}$	0.972(6)
	$\nu 3p^{-1}_{3/2} \rightarrow \nu 3p^{-1}_{1/2}$	0.92(22)
^{207}Tl	$\pi 3p^{-1}_{3/2} \rightarrow \pi 2f^{-1}_{5/2}$	2.7(7)
^{209}Pb	$\nu 3d_{5/2} \rightarrow \nu 2g_{9/2}$	2.7(7)
	$\nu 4s_{1/2} \rightarrow \nu 3d_{5/2}$	2.13(8)
^{209}Bi	$\pi 2f_{7/2} \rightarrow \pi 1h_{9/2}$	0.44(9)

[a] Values taken from [KL11] and [CK15]

7.4 Conclusions

The excited structure in ^{133}Sn was populated in the β-decay of both ^{133}In and ^{134}In. Thanks to the use of RILIS it was possible to perform an independent investigation of the decay of the ^{133g}In ($9/2^+$) g.s. and the ^{133m}In ($1/2^-$) isomer. Three neutron-unbound states were observed, all of them decaying by γ-rays to the g.s. They can be identified with dominant two-particle one-hole configurations. The competition of electromagnetic and neutron decay is due to the matching of initial and final states. The results concerning the structure of ^{133}Sn populated in the β decay of ^{133}In have already been published, see M. Piersa *et al.* [PKF$^+$19].

The lifetimes of the excited levels in ^{133}Sn states measured using the fast-timing technique were the main focus of this PhD thesis. We have measured a new value for the mean-life of the $p_{3/2}$ single-particle state, τ=36(18) ps. This measurement is in very good agreement with the previous τ=30(15) ps [VJD^{+}17], derived by Doppler shift methods. The corresponding B(E2) strength for the 854-keV γ-ray transition yields B(E2) = 1.2^{+13}_{-8} W.u. for the the $\nu p_{3/2} \rightarrow \nu f_{7/2}$ transition in ^{133}Sn. The strength is comparable to single-particle transitions in the Pb region. The new measurement provides a benchmark for transition rates above ^{132}Sn, although a more precise measurement will be required to draw strong conclusions.

8

Lifetime measurements in ^{134}Sn

Nuclei with few valence particles outside closed shells are sources of information on fundamental nuclear properties. The ^{134}Sn nucleus, having only a couple of neutrons above the doubly-magic ^{132}Sn ($Z = 50$ and $N = 82$), is an excellent example to study the nucleon-nucleon interaction, as well as the single particle nature of their excited levels. The investigation of the excited structure of ^{134}Sn, populated through the β decay of indium, is summarized in this chapter. The work described in this PhD focuses on lifetime measurements of the excited states.

The task of reaching experimentally nuclei far from the valley of stability has been always very challenging. Hence, the empirical information available for tin isotopes beyond $N = 82$ is very scarce. A first insight into the excited structure of ^{134}Sn was provided by prompt-γ spectroscopy measurements, performed with the EUROGAM2 array, from the fragments produced after the spontaneous fission of ^{248}Cm. Results concerning ^{134}Sn were presented by Zhang *et al.* [ZBD$^+$97] and Korgul *et al.* [KURU$^+$00]. Four levels were identified, the first three ones were interpreted as members of the $\nu(\mathrm{f}^2_{7/2})_j$ multiplet, while the other state at 2401 keV was identified to be the $\nu(\mathrm{f}_{7/2}h_{9/2})_{8^+}$ state. These assignments were supported by the comparison to analogous multiplet states in the ^{210}Pb region. In Figure 8.1 the level scheme of ^{134}Sn from Korgul. *et al.* is shown.

The existing experimental information about transition rates in ^{134}Sn is scarce. There is only a direct measurement for the 1248-keV isomeric state lifetime. A value of $T_{1/2}$=80(15) ns is reported [ZBD$^+$97, KURU$^+$00], obtained from the time difference distribution of the 726-keV γ-ray relative to the prompt fission γ-ray burst. A value of B(E2; $6^+ \rightarrow 4^+$)=36(7) e^{2}fm^4, with relatively low precision, is reported [ZBD$^+$97],

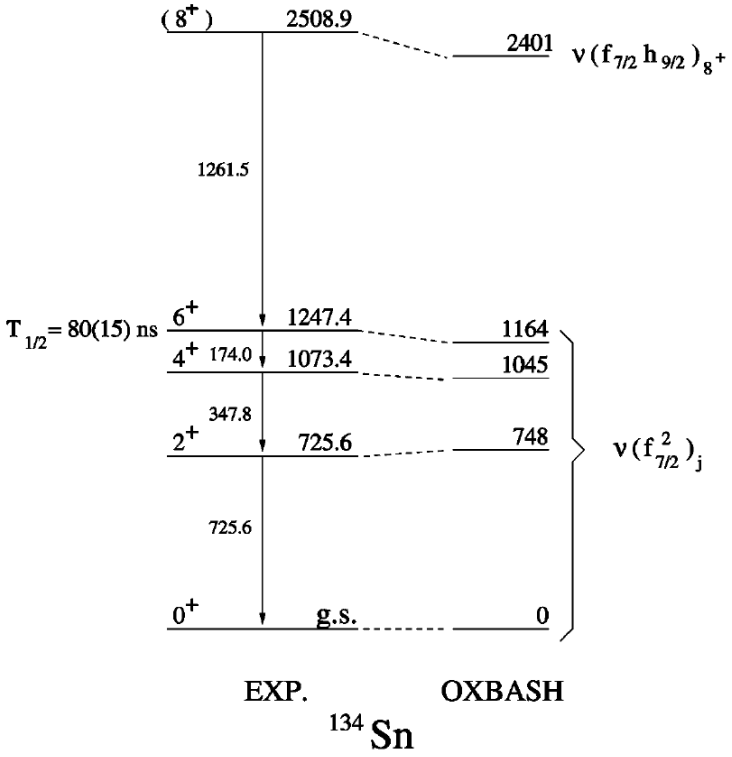

Figure 8.1: Partial level scheme of ^{134}Sn observed in the spontaneous fission of ^{248}Cm. The figure is taken from [KURU^{+}00]. The four levels identified were proposed to correspond to two-neutron configurations.

which is consistent with the assignment of the 6^+ state to the $\nu(f^2_{7/2})$ two single particle multiplet [KURU^{+}00].

Another piece of experimental information was provided by J.R. Beene *et al.* [BVB^{+}04], where the B(E2;$0^+ \rightarrow 2^+$) transition rate in ^{134}Sn was investigated via Coulomb excitation at the Holified Radioactive Ion Beam facility (HRIBF) at ORNL. A preliminary experimental value of B(E2; $2^+ \rightarrow 0^+$)=58(10) e^{2}fm^4 is reported in [BVB^{+}04, VBB^{+}05, RBB^{+}05], which translates in a τ=70(12) ps mean life.

The direct measurement of lifetimes of the states built on the $\nu(f^2_{7/2})$ configuration, will help to support their assignment to the multiplet and identify admixtures in the wave functions.

8.1 Population of excited states in ^{134}Sn

In the IS610 campaign, the excited levels in ^{134}Sn were populated in the β-decay of In, specifically γ-rays in ^{134}Sn level scheme were observed following the β-decay of ^{134}In and, for the first time, the β-delayed neutron decay of ^{135}In was detected. This provides us with an excellent opportunity to study the excited structure in ^{134}Sn populated in a complete different process than those previously used. Furthermore, thanks to the use of the fast-timing setup, it is possible to gain access to the remaining lifetimes from the $\nu(f^2_{7/2})_j$ multiplet. We stress that the IS610 experiment carried out at ISOLDE was the first time that ^{134}Sn was populated in a β-decay experiment. Figure 8.2 shows the γ-ray spectra measured for the decay of ^{134}In (Top) and ^{135}In (Bottom). Gamma rays belonging to transitions between the $\nu(f^2_{7/2})$ multiplet in ^{134}Sn, can be very clearly observed in both spectra.

The indium yield drops enormously as we move to higher masses, hence the amount of statistics recorded for the ^{134,135}In β decays is significantly lower in comparison with the high statistics attained for the lower masses. In the course of the IS610 campaign performed in 2018, we estimate a total of about 10^7 ^{134}In ions, and 10^6 ^{135}In ions implanted at the IDS collection point. For the decay of In with masses above 132, due to the low neutron separation energy, the dominant decay process is the β-decay with the emission of one or two neutrons (see previous chapters). In particular, the probability of ^{134}In decaying directly to ^{134}Sn is lower than 5%, while in ^{135}In the most likely process, more than 90%, is β-n decay to ^{134}Sn. Hence, even though the amount of statistics recorded for A = 135 mass is an order of magnitude lower than for $A = 134$, the statistics attained for ^{134}Sn is similar in both cases. However, the relative γ intensities are different.

8.2 Lifetime measurements

Taking advantage of the fast-timing detectors it is in principle possible to investigate lifetimes in both ^{134}In and ^{135}In decays. But the limited statistics, even though sufficient for a γ-spectroscopy study, is barely enough for a precise timing analysis. Because of this, we have relied on double coincidence events between β and $LaBr_3$(Ce) detectors, and skipped the use of a third coincidence conditions on the HPGe detectors. Therefore a proper understanding of contaminants and background components is required.

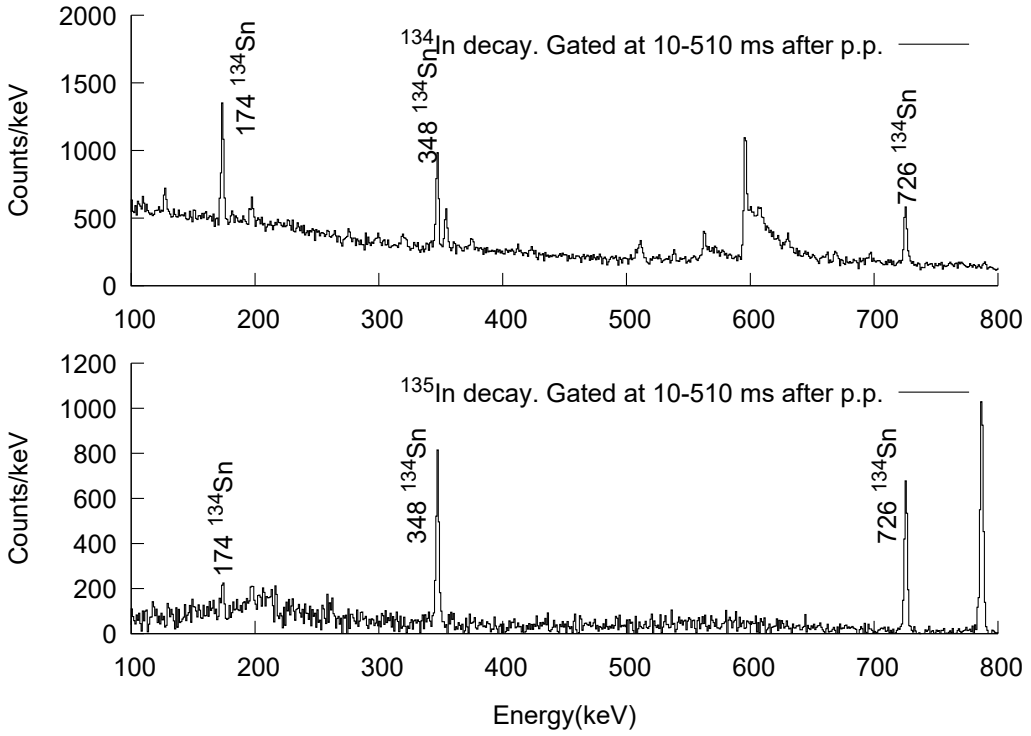

Figure 8.2: ^{134}Sn γ-rays observed in the β-decays of ^{134}In and ^{135}In. (Top) β-gated HPGe spectrum recorded for the β-decay of ^{134}In. (Bottom) Spectrum under the same conditions for the β-decay of ^{135}In. In both spectra, only the events measured within the time window of 10 to 510 ms after proton impact are included. The contribution from long-lived contaminants has been removed by subtracting the spectra measured within the 700−1200 ms time window.

As stated before, ^{134}In decays only to ^{134}Sn with less of the 5%, consequently the spectra is dominated by the γ-rays from ^{133}Sn. Looking at the ^{134}In spectrum shown in Figure 8.2 we can identify an structure around 600-keV, generated by the interaction of β-delayed neutrons with the HPGe detectors. There is also activity arising from the daughter isotopes. However this contribution is highly suppressed by the tape movement. In addition, it can be easily removed by setting the proper conditions in the time difference to the arrival of the proton beam on target. Another, source of background that may arise is ^{134}Cs, which is surface ionized and mass separated for $A = 134$. Fortunately in this case, the only contribution is the 127-keV γ-ray from the internal decay of the isomeric state, which is fully removed by gating on the β-detector,

and is located below our energies of interest.

The same kind of contributions are present for the $A = 135$ measurements. In this case, the main one is due to the ^{134}Sn γ-rays, from the ^{135}In β-delayed neutron decay. Activity from the daughters is reduced by the tape movement, and it can be removed with the proper time conditions.

The most problematic source of background comes from the ^{135m}Cs isomeric state, which completely dominates the spectra. ^{135m}Cs decays by emitting a cascade of two γ-rays of 787 and 846 keV, above the energy of the γ-rays in ^{134}Sn. In principle they should disappear by β-gating, however, they are still present in the spectra due to the contributions of events where one of the two ^{135m}Cs $\gamma-$rays is scattered on the β-detector. Due to the large amount of the ^{135m}Cs contaminant in comparison to the ^{135}In, these marginal events become the dominant contribution in the spectra. A solution for the time analysis is provided below.

8.2.1 Lifetime of $(\nu f_{7/2})^2$ 6^+ state

The lifetime of the 6^+ level in ^{134}Sn, known to be $T_{1/2}$=80(15) ns [ZBD+97], can be obtained from our dataset from the time difference between the feeding β and the de-exciting γ-rays from the 6^+ level. Due to its long lifetime the time difference between the plastic scintillator and the HPGe detectors is used. We can take advantage of the good energy resolution of HPGe detectors to obtain a better selectivity of the γ-transition, and the lifetime can be extracted from the slope in the time distributions. We use the 174-keV γ-ray, which directly de-excites the state. Besides, since the 174-keV transition feeds the 4^+ and 2^+ levels, this lifetime can be also measured from the time distributions of 348- and 726-keV γ-rays, because the 4^+ and 2^+ have much shorter lifetimes.

Analysis of ^{134}In decay data sets

Figure 8.3 (top) shows the HPGe spectrum measured in delayed coincidence with the β detector within the 200-400 ns after the $\beta\gamma$(t) prompt. As can be observed in the spectrum, the contribution from Compton background is negligible with these conditions, contrary to the situation observed the β-gated HPGe spectrum in Figure 8.2. This indicates that the Compton background contributions are much more important in the prompt region, and thus they have a small influence in the slope of the time distributions. The three $\beta\gamma$(t) time-delayed distributions are built by selecting separately

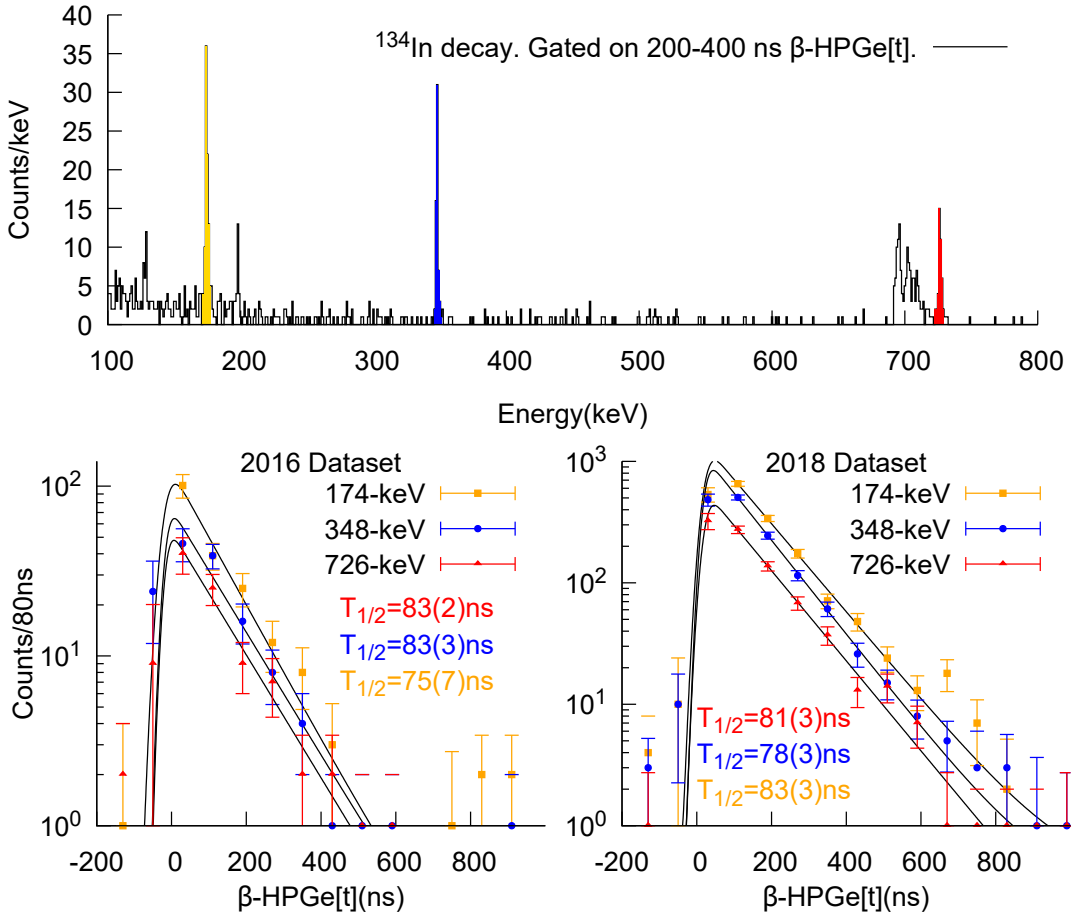

Figure 8.3: Lifetime analysis of the 6^+ state in ^{134}Sn populated in the β decay of ^{134}In. (Top) β-gated HPGe spectrum measured in the ^{134}In β-decay. (Bottom) β-HPGe(t) time distribution of ^{134}Sn γ-rays emitted after the ^{134}In decay.

these three relevant γ-rays. The contribution from Compton events has been estimated from the nearby background and subtracted from the time distributions.

In Figure 8.3 (bottom) the time distributions for the three γ-rays are plotted. The contribution from the Compton background has been estimated and subtracted. Each time distribution has been fit to a exponential decay function convoluted with a Gaussian. A constant background has been included in the fit to account the contribution of random coincidences. The lifetimes of 4^+ and 2^+ states are much shorter and they do not have a big influence on the time distributions of 348-keV and 726-keV γ-rays in this time scale. Thus only one exponential decay component is considered in the fits. Due to the reduced amount of data the statistical fluctuations are high. To reduce them a

bin size of 80 ns has been chosen.

The analysis has been performed separately for the datasets from the 2016 and 2018 campaigns. Hence, 6 separate values have been derived for the lifetime of 6^+ state. The statistics obtained in the 2016 campaign was significantly lower, and consequently the results obtained from this data set are less reliable. The six derived values are compatible among each other, and with the previous value 80(15)ns [ZBD+97].

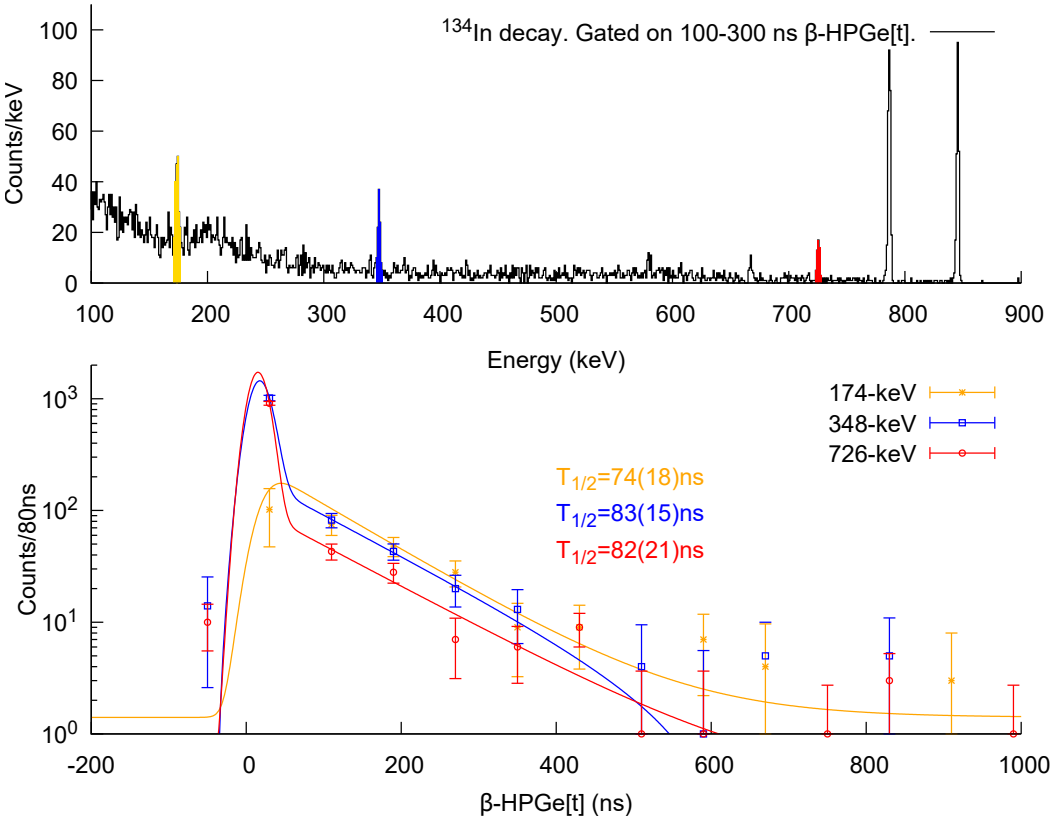

Figure 8.4: β-HPGe(t) Time distribution of ^{134}Sn γ-rays emitted after ^{135}In decay. (Top) β-gated HPGe spectrum. (Bottom) Analysis performed on the time distributions of 174-keV (orange), 348-keV (blue) and 726-keV (red) γ-rays. Both 348-keV and 726-keV transitions show a prompt component due to the direct population of the 4^+ and 2^+ levels.

Analysis of ^{135}In decay data sets

The half-life of the 6^+ states can also be derived from ^{135}In β-decay data. The stronger feeding occurs to the 4^+ level, being the feeding to the 6^+ level relatively

Table 8.1: Summary of $T_{1/2}$ values measured during this investigation.

Dataset	γ-ray (keV)	$T_{1/2}$(ns)
Previous value		80(15)
^{134}In decay 2016	174	75(7)
	348	83(3)
	726	83(2)
^{134}In decay 2018	174	83(3)
	348	78(3)
	726	81(3)
^{135}In decay 2018	174	74(18)
	348	83(15)
	726	82(21)
Final value	Weigthed average	**81.7(12)**

small. Therefore the time distributions of the 348-keV and 726-keV transitions contain two different components, a "prompt" distribution with Gaussian shape corresponding to the direct population of the 4^+ and 2^+ levels, and a "slow" distribution with a slope which corresponds to the population from the 6^+ level. Likewise for the analysis of the ^{134}In decay datasets, time distributions from the 174-, 348- and 726-keV transitions were produced. The lifetime is derived from fit of the slopes. The results from this analysis are displayed in Figure 8.4. They are in perfect agreement with the values measured for ^{134}In β-decay, even though the error bars are significantly larger.

Adopted value and transition rate

Throughout this study 9 independent values were obtained for this specific half-life, which are summarized in Table 8.1. All of them, measured under different conditions, are compatible with each other. A weighted average of $T_{1/2}$=81.7(12) ns is adopted for the 6^+ level in ^{134}Sn. This result is in excellent agreement with the previously reported value [ZBD$^+$97, KURU$^+$00] but with a much improved uncertainty. A reduced transition probability B(E2; $6^+ \rightarrow 4^+$) = 35.4(5) e^2fm^4 = 0.870(13) W.u. is derived.

8.2.2 Lifetime of $\nu f_{7/2}^2$ 4^+ state

There is no previous information about the $\nu f_{7/2}^2$ 4^+ state lifetime. The use of fast-timing detectors along with the good statistics acquired for this isotope make it possible to gain access to this lifetime. A priory, it is expected that the 348-keV transition has a similar B(E2) to that of 174-keV. Since B(E2) $\propto E_\gamma^{-5}\tau^{-1}$, the energy scaling gives a half-life for the 4^+ level of the order of 2 ns, which is ideally suited for the $LaBr_3$(Ce) detectors used in our experiment. As mentioned above, the 4^+ state is strongly populated in both the ^{134}In and the ^{135}In β-decays, therefore it is possible to study this lifetime in both cases.

Analysis of the ^{134}In β-decay data

In the β-decay of ^{134}In, the 4^+ level is indirectly populated by the 174-keV transition from 6^+ level. Consequently, the $\beta\gamma$(t) time distribution of the 348-keV de-exciting transition is influenced by the long lifetime of the 6^+ state. However, the large Compton contribution of γ-rays from the β-n decay branch of ^{134}In, makes it impossible to cleanly select the 348-keV in the $LaBr_3$(Ce) energy spectra. The statistics is not sufficient to apply triple $\beta\gamma\gamma$(t) coincidences either. Hence, the only possibility to measure this lifetime is the analysis of $LaBr_3$(Ce)-$LaBr_3$(Ce) coincidences.

The lifetime of the 4^+ state was derived from the time difference between the feeding 174-keV transition and the 348-keV de-exciting transitions. This method avoids the influence of the long lifetime of the 6^+ level. The events recorded in coincidence between the two $LaBr_3$(Ce) detectors within the time interval of 10 to 600 ms after the proton pulse are plotted in Figure 8.5 (left). The coincidence between the 174- and 348-keV transitions stands out very clearly without major Compton background contributions. Both delayed and anti-delayed time distributions are depicted in Figure 8.5 (right).

In this case, the lifetime of the level is long enough to show an exponential slope, which can be observed in both time distributions. The half life was measured by a χ^2 fit to an exponential decay convoluted with a Gaussian. A constant background was included in the fit to account for the remaining background counts. This analysis yielded two independent measurements, in full agreement with each other, $T_{1/2}$=1.22(8) ns and $T_{1/2}$=1.19(13) ns for the delayed and anti-delayed coincidences, respectively.

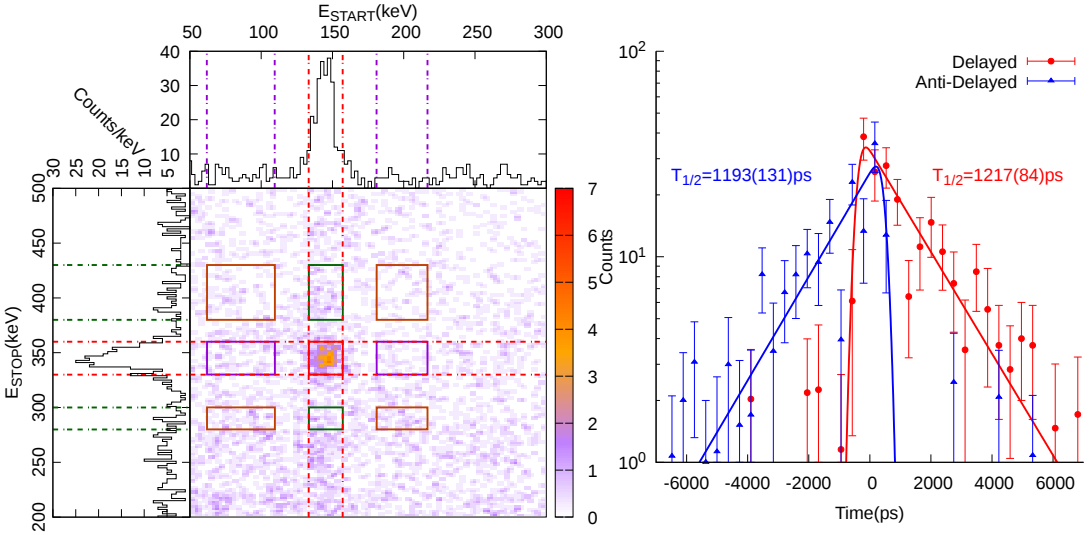

Figure 8.5: $\gamma\gamma$(t) lifetime analysis of the ^{134}Sn 4^+ state. (Left) $\gamma\gamma$ coincidence energy matrix measured for the ^{134}In β-decay dataset. The marked regions indicate the energy gates used to select the 174-348 coincidence peaks, as well as the background contributions. (Right) Time-distributions for the delayed and anti-delayed coincidence events. The half-life values are derived by a χ^2 fit to the time distributions.

Analysis of the ^{135}In β-decay data

The 4^+ level is also populated in the ^{135}In β-decay via the β-n branch. In this case, the main branch is the direct β-n feeding. On the other hand, the 6^+ level is weakly populated in this decay, therefore the lifetime of the 4^+ state cannot be measured from the 174-348 keV $\gamma\gamma$(t) coincidences. Nevertheless, the weak population of 6^+ level opens up the possibility of measuring the lifetime from $\beta\gamma$(t) coincidences.

In Figure 8.6 the β-gated spectra measured in one of the $LaBr_3$(Ce) detectors for the ^{135}In decay is depicted. As discussed for the measurement of the 6^+ level lifetime, the spectrum is dominated by the γ rays from ^{135}Cs, nonetheless the presence of this contaminant is only important around the $\beta\gamma$(t) prompt time position. Its influence is notably reduced after 100 ns from the prompt time position.

The lifetime for the 1073-keV 4^+ level, can be derived by analyzing the $\beta\gamma$(t) time distributions from both 348- and 726-keV γ-rays, which de-excite the 4^+ and 2^+ states, respectively. The contribution from the 2^+ level lifetime can be neglected, since it is expected to be of the order of tens of ps. In order to reduce the contribution of the

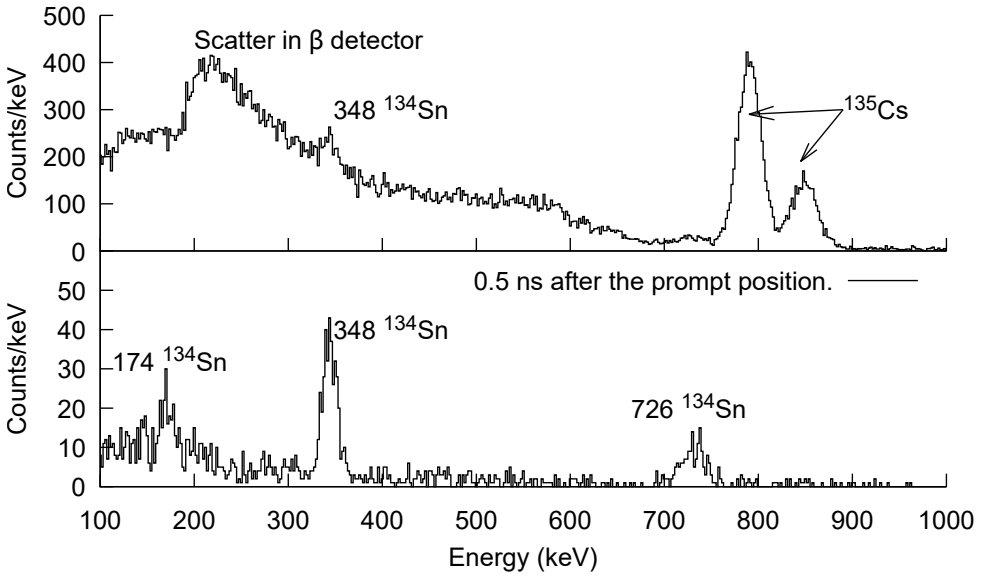

Figure 8.6: β-gated $LaBr_3$(Ce) energy spectra measured for the β decay of ^{135}In
(Top) Full β-gated $LaBr_3$ spectrum, measured for the first 600 ms after proton impact. (Bottom) Spectrum obtained after selecting only the delayed events, measured 100 ns after the prompt $\beta\gamma$ events.

^{135}Cs contaminant, only the events measured for the first 600 ms after the proton pulse were included. The time spectra obtained for both $LaBr_3$(Ce) detectors, after gating on the 348-keV and 726-keV transitions, are depicted in Figure 8.7. The contributions from Compton evens has been estimated and subtracted. The lifetime was measured via a χ^2 fit of the time distribution, convoluted with a Gaussian. In this case, the prompt region was excluded from the fit in order to reduce the caesium background. The contribution from the long 6^+ lifetime was small in both cases, nonetheless its effect was also considered in the fit. The analysis yielded another four independent measurements for this half-life (see Figure 8.7), which are in good agreement between each other and with the other two values obtained from ^{134}In β-decay data.

Final value

To conclude, the lifetime of the $\nu(f^2_{7/2})_{4^+}$ level has been investigated. Six independent values have been measured. They are summarized in Table 8.2. The final value from this work is adopted as the weighted average of the measurements, $T_{1/2}$=1.18(4) ns. From this result, we derive a B(E2)=2.25(7)W.u. rate for the 348-keV transition.

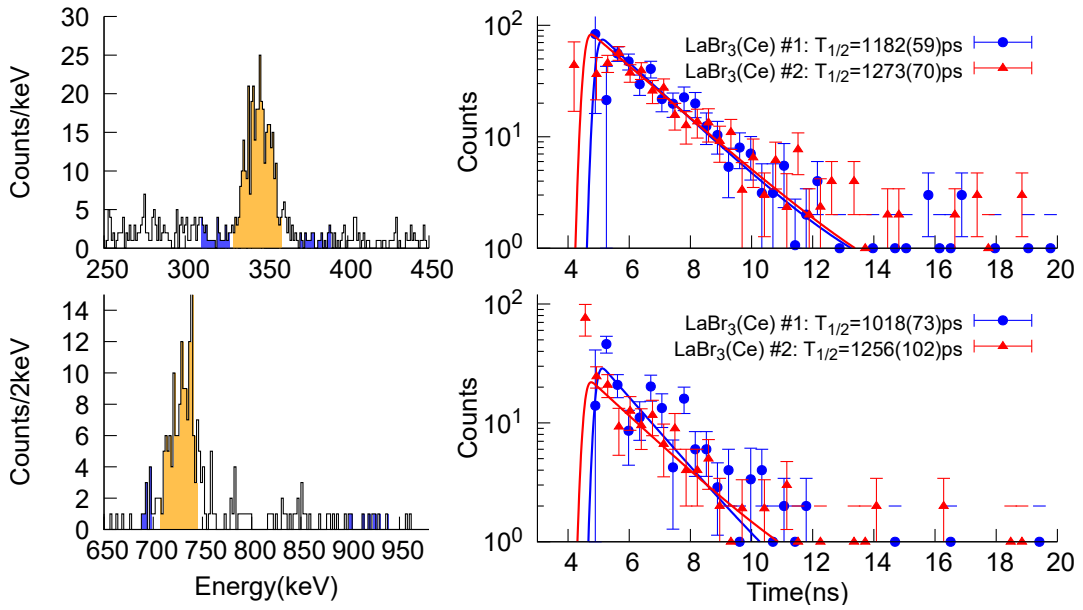

Figure 8.7: β-LaBr$_3$(Ce)(t) analysis for the lifetime of the 4$^+$ state. (Left) β-gated LaBr$_3$(Ce) spectrum measured in the β-decay of ^{135}In. The colored regions show the energy gates used for the 348-keV and 726-keV γ-rays. (Right) Corresponding time distribution for both transitions. The half-lives are derived by fitting the slopes in each time distribution.

Table 8.2: Summary of $T_{1/2}$ values measured in this thesis for the 4$^+$ state

Data set	γ-ray (keV)	$T_{1/2}$(ps)
^{134}In decay	Delayed	1217(84)
	Anti-Delayed	1192(131)
^{135}In decay	348-keV LaBr$_3$ 1	1182(59)
	348-keV LaBr$_3$ 2	1273(70)
	726-keV LaBr$_3$ 1	1018(73)
	726-keV LaBr$_3$ 2	1256(102)
Final value	**1183(40) ps**	

8.2.3 Lifetime of $(\nu f_{7/2})^2$ 2$^+$ state

To complete our investigation on the half-lives of ^{134}Sn levels, the lifetime of its first excited state at 726-keV, corresponding to the 2$^+$ from the $(\nu f_{7/2})^2$ configuration, has been studied. There is no previous direct measurement of this half-life, but a measurement of the B(E2) via Coulomb excitation [BVB$^+$04] exists, yielding 58(4) W.u. Considering

such B(E2) value, a half-life of 48(7) ps is expected for the 2^+ state, very well suited for the centroid shift method. However, the limited statistics hampers the analysis. The 726-keV level is very weakly populated directly, both in the decays of ^{134}In and ^{135}In. This implies that the $\beta\gamma$(t) distribution of 726-keV γ-ray is fully dominated by the long lifetimes of the two high-lying levels. To avoid their influence, the only possibility is to analyze the 348-726 $LaBr_3$-$LaBr_3$(t) coincidences.

The analysis is hindered in the β-n decay of ^{135}In due to the strong presence of ^{135m}Cs, which decays by the emission of two γ-rays of 846-keV and 787-keV in cascade. The higher energy of both transitions, in comparison with the 348-726 keV cascade, generates a very strong background in the $\gamma\gamma$ coincidence matrix, originated by coincidences between Compton events from the 846-keV and 787-keV transitions. In the β-decay of ^{134}In there is not such a contaminant, allowing for the clean selection of the 348-726 coincidence peak. The main limitation is the scarcity of statistics, reduced by the need of detecting two γ-rays, and the lower efficiency at 726-keV. This causes that the only option to study this coincidence is the use of the 2018 dataset.

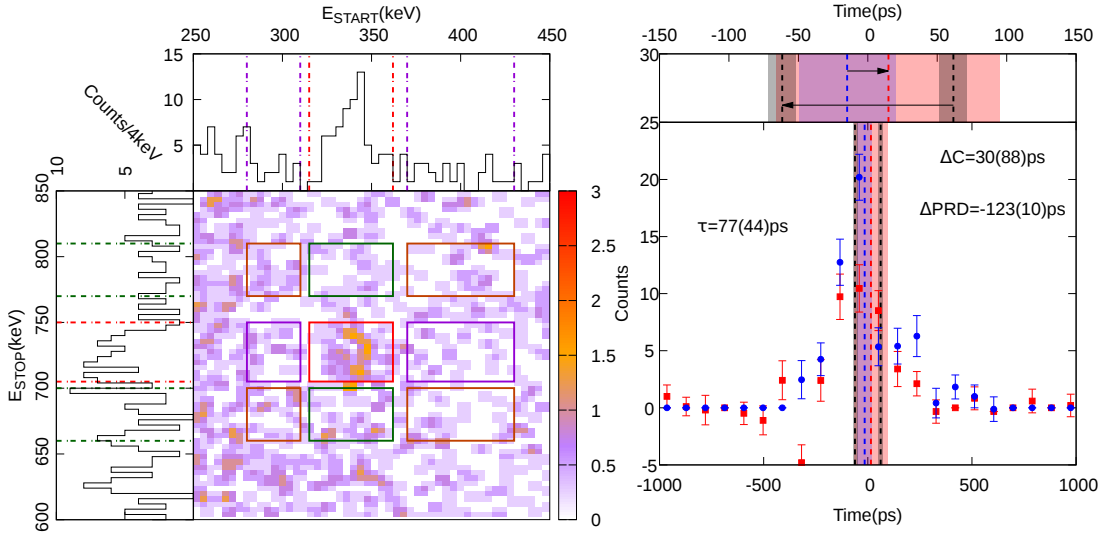

Figure 8.8: $LaBr_3$(Ce)-$LaBr_3$(Ce) γ-γ coincidence matrix. Coincidence γ-γ events recorded with the $LaBr_3$(Ce) detectors during the ^{134}In decay. In the

Figure 8.8 shows the $\gamma\gamma$ coincidence matrix measured for the $LaBr_3$(Ce) detectors, for the ^{134}In β-decay. The gates imposed to obtain the time distributions are marked. It can be noticed how the events from the 348-726-keV coincidence can only be slightly

distinguished from the background. The ratio of FEP-FEP events to background events is estimated to be 1:1. Hence, corrections for the contribution of this background are particularly important in this case. The background contributions have been estimated from the nearby regions and subtracted from the time spectra. At the right-hand side of Figure 8.8 the time distributions for the 346-726 delayed and anti-delayed coincidence peaks are depicted. Due to the low statistics, the uncertainty in the determination of the centroids is very large. Assuming conservative large error bars, our analysis yielded a value of $T_{1/2}$=55(28) ps. In spite of the large uncertainty, the $T_{1/2}$=55(28) ps value is in good agreement with the $T_{1/2}$ 49(7) ps extracted from the previous Coulomb excitation study[BVB$^+$04].

In this chapter, the lifetimes of ^{134}Sn states were measured by investigating the β decay of both ^{134}In and ^{135}In using the fast-timing technique and time differences with the HPGe detectors.

From our investigation a whole set of lifetimes has been measured for the $(\nu f_{7/2})^2$ states in ^{134}Sn. Table 8.3 summarizes the half-lives and the B(E2) γ-ray strengths, assuming pure E2 multipolarity.

Table 8.3: Summary of $T_{1/2}$ values measured on the framework of this PhD.

$J_i^\Pi \rightarrow J_f^\Pi$	$T_{1/2}$	B(E2;$J_i \rightarrow J_f$) (e^2fm^4)	B(E2;$J_i \rightarrow J_f$) (W.u.)
$2^+ \rightarrow 0^+$	55(28) ps	$52(^{+70}_{-20})$	$1.3(^{+17}_{-5})$
$4^+ \rightarrow 2^+$	1.18(4) ns	92(3)	2.25(7)
$6^+ \rightarrow 4^+$	81.7(12) ns	35.4(5)	0.870(13)

8.3 Theoretical Calculations for ^{134}Sn

Sn isotopes with few neutrons above ^{132}Sn have been of great interest from the theoretical point of view. They are excellent test grounds to probe the validity of the shell model description of the nuclear structure in this region. Information on the B(E2) transitions strengths is particularly relevant, since shell model calculations are very sensitive to them. As a consequence, there is a good amount of theoretical calculations for the B(E2) strengths in ^{134}Sn that use different interactions and theoretical models.

Coraggio *et al.* performed shell-model calculations in 2002 for the ^{134,135}Sn isotopes [CCGI02]. A realistic effective interaction derived from the CD-Bonn nucleon-nucleon potential [Mac01, CAC^{+}97] was used. The shell model space included the $1f_{7/2}$, $2p_{3/2}$, $0h_{9/2}$, $2p_{1/2}$, $1f_{5/2}$ and $0i_{13/2}$ orbitals. The single particle energies were extracted from the experimental spectrum of ^{133}Sn [HBH^{+}96], as known at that time. The energy of the $0i_{13/2}$ remains without experimental confirmation. However, this energy has been proposed at 2.7(2) MeV from the position of the $(\pi g_{7/2},\nu i_{13/2})_{10^+}$ state in ^{134}Sb [WWA^{+}99]. For the B(E2) calculation, an effective neutron charge of $e_n^{eff} = 0.7e$ was assumed. Note that this value was chosen in order to reproduce the known B(E2; $6^+ \rightarrow 4^+$) transition rate [ZBD^{+}97, KURU^{+}00]. The predicted B(E2) values for ^{134}Sn states from Ref, [CCGI02] are summarized in Table 8.4.

Kartamyshev *et al.* also carried out shell-model calculations for tin isotopes with $A = 134-142$ [KEHJO07]. The same model space and single particle energies as Coraggio *et al.* were used. A perturbative many-body scheme was employed to derive the effective interaction starting with a realistic model for the free nucleon-nucleon interaction [MSS96]. For the calculations of the B(E2) transition rates, an effective neutron charge $e_n^{eff} = 0.64e$ was employed. This e_n^{eff} value was chosen in order to obtain the best agreement to both the experimental B(E2; $6^+ \rightarrow 4^+$) [ZBD^{+}97] and B(E2; $2^+ \rightarrow 0^+$) [BVB^{+}04] values in ^{134}Sn available at that time. The calculated B(E2) values for ^{134}Sn states from Ref. [KEHJO07] are summarized in Table 8.4.

With the tuning of the effective charge an overall good agreement between the theoretical calculations and the experimental measurements for the available B(E2) rates is achieved. However, the experimental information was limited to the B(E2) rates for the decay transitions from the 6^+ [ZBD^{+}97] and the 2^+ [BVB^{+}04] levels in ^{134}Sn. Consequently, the ability of the calculations to predict transitions rates from other levels or in other Sn isotopes has not yet been verified. The limitation of the existing calculations was pointed out in the publication in 2014 of the new measurements for the ^{136,138}Sn isotopes by Simpson *et al* [SGJ^{+}14]. In that experiment, the B(E2) values of the decay transitions of the 6^+ isomers in both isotopes were measured. A striking result was the quite large B(E2) value for ^{136}Sn in comparison to the calculated values from shell model calculations and the seniority scheme.

The appearance of new experimental data, along with the seemingly anomalous behavior of ^{136}Sn, motivated new shell-model calculations. Jain and Maheshwari per-

Table 8.4: Theoretical B(E2) transition rates in ^{134}Sn.

	B(E2;$J_i^\pi \rightarrow J_f^\pi$) [$e^2fm^4$]						
	[CCGI02]	[KEHJO07]	[JM17]				
$J_i^\pi \rightarrow J_f^\pi$	CD-BONN	CD-BONN	RCDBN	RCDBN1	RCDBN2	RCDBN3	Exp.
$2^+ \rightarrow 0^+$	70.6	61.1	64.5	64.9	65.51	65.9	$52(^{+70}_{-20})$
$4^+ \rightarrow 2^+$	69.7	62.3	66.7	68.6	67.7	67.7	92(3)
$6^+ \rightarrow 4^+$	35.8	33.8	35.9	35.9	36.6	36.5	35.4(5)

formed calculations for $^{134-139}$Sn isotopes [JM17]. The doubly magic ^{132}Sn was taken as an inert core and a re-normalized charge-dependent (RCDBN) effective interaction was used. The most recent values for the s.p. energies were employed and an effective neutron charge of 0.65 was chosen. The calculations were able to reproduce the experimental results for the B(E2) values in ^{134}Sn, however they were not able to reproduce the aforementioned ^{136}Sn anomaly. In order to resolve this issue, the RCDBN was modified in order to achieve the best agreement with the experimental data. In the RCDBN1 modified interaction, the position for the s.p. energy of the $i_{13/2}$ orbital was shifted up by 1.2 MeV. In a second modified interaction, RCDBN2, the energy of the $i_{13/2}$ orbital was left unchanged, while the two-body matrix elements (TBME) were reduced to 25 keV. For the third interaction (RCDBN3) both changes were applied at the same time, achieving the best fit to the measured values, including the ^{136}Sn anomaly. The results reported in [JM17] are also summarized in Table 8.4.

8.4 Discussion of the lifetime values

The experimental reduced transition probabilities calculated from the lifetime values. They are compared to the theoretical calculations, described above, in Table Table 8.4.

Regarding the 2^+ state, a B(E2;$2^+ \rightarrow 0^+$)=$52(^{+70}_{-20})$ e^2fm^4 value was derived from our measurement. This new value helps to support the previous B(E2;$2^+ \rightarrow 0^+$)=58(8) e^2fm^4 measured in Coulomb excitation [BVB+04]. Due to the limitation in statistics it was not possible to improve the precision. In Figure 8.9 the theoretical values available in the literature for the B(E2;$2^+ \rightarrow 0^+$) transition rate, along with the new value derived from this work, and the previous experimental value, are plotted. Both experimental measurements are drawn with their respective error bars. Since the error bar from our measurement is so large, it is difficult to draw conclusions. The theoretical values are

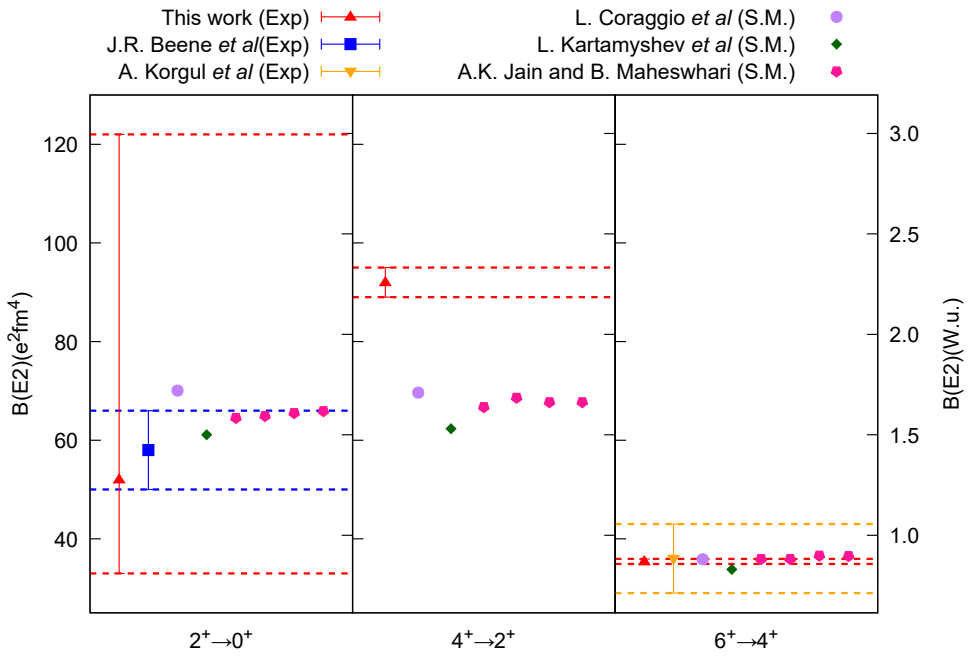

Figure 8.9: Comparison with theoretical B(E2) strengths in ^{134}Sn. The red triangles correspond to the experimental measurements derived from this work. The blue and orange points are the previous experimental measurements for the $2^+ \rightarrow 0^+$ and $6^+ \rightarrow 4^+$ transitions respectively. The values predicted by the different shell model calculations from Table 8.4 are drawn, together with their reference.

in overall good agreement with the measurement reported by Beene *et al*, except for the B(E2)=70.6 e^2fm^4 calculated by Coraggio *et al.* [CCGI02]. However, it should be noted that these calculations are the only ones that were published before the measurement by Beene *et al.*, when the only experimental information available was the B(E2;$6^+ \rightarrow 4^+$) for ^{134}Sn. The remaining two shell model calculations where performed after the publication of the Coulomb excitation measurement by tuning them to both experimental B(E2) values in ^{134}Sn.

We have performed the first experimental measurement of the 4^+ level lifetime, from which a B(E2;$4^+ \rightarrow 2^+$) = 92(3) e^2fm^4 is obtained. The result is very striking because all the different shell model calculations are in agreement to each other, but underestimate by ∼40% the value measured in this work.

Regarding the transition rate for the $6^+ \rightarrow 4^+$ transition, our new measurement is in full agreement with the previous information, but with higher precision. The

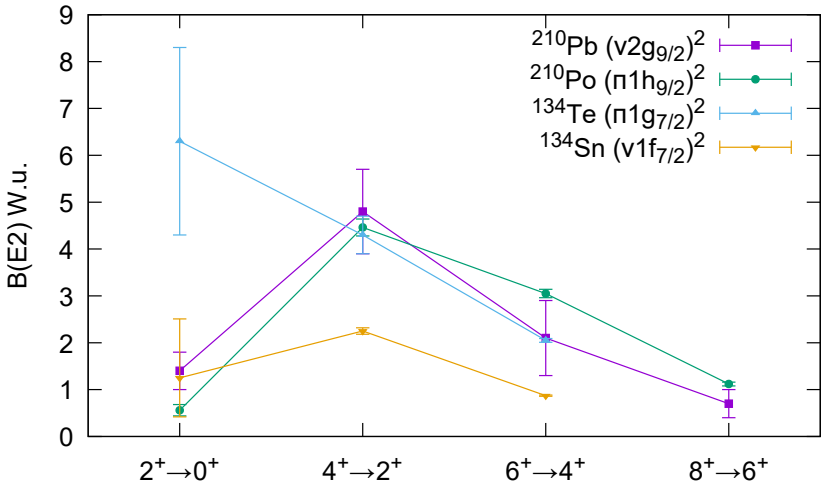

Figure 8.10: Systematic of B(E2) values in equivalent two nucleons systems. The B(E2) values of ^{134}Te, ^{210}Po and ^{210}Pb transitions have been taken from their nuclear data-sheets[Son04, Bas14]

values predicted by the different shell model calculations are also in agreement with our measurements, some of them lying slightly off the error bars.

It is interesting to compare the B(E2) in ^{134}Sn with those in similar two-nucleon systems. In the region around ^{132}Sn, the low lying states in ^{134}Te, are identified with a system of two protons in the $\pi 1g_{7/2}$ orbital. In the region around doubly magic ^{208}Pb we can find similar nuclei, whose transition rates are also measured. The ^{210}Pb isotope, which has two neutrons in the $\nu 2g_{9/2}$ orbital, and the ^{210}Po nucleus with two protons in the $\pi 1h_{9/2}$ orbital.

The systematics of the B(E2) rate values for similar two nucleons systems is represented in Figure 8.10. The transition rates have been taken from Ref. [Son04, Bas14]. For ^{134}Sn, we use the values measured in this work. It can be observed in the figure that the the trend of B(E2) rates in ^{134}Te, ^{210}Pb and ^{210}Po are similar. However, the values are systematically lower for ^{134}Sn. The enhancement of the B(E2;$4^+ \rightarrow 2^+$) strength compared to the B(E2;$6^+ \rightarrow 4^+$) one is common to all isotopes, and in the case of ^{134}Sn is almost equal to that in ^{210}Pb, the analog two-neutron system in the ^{208}Pb region.

8.5 Summary of the chapter

In this chapter the analysis of the excited structure of ^{134}Sn, populated in the β-decay of ^{134}In and ^{135}In, is described. Our study focuses on the measurement of the lifetimes of the excited levels in ^{134}Sn. The half-life of the three states from the $\nu f_{7/2}^2$ multiplet have been measured. For the 2^+ state, the result confirms the B(E2) rate measured by Coulomb excitation [BVB$^+$04, VBB$^+$05, RBB$^+$05], but with lower precision. For the 4^+ state, we have performed the first experimental measurement, yielding a half-life of 1.18(4) ns. A half-life of 81.7(12) ns was derived for the 6^+ level, whose precision is notably improved with regard to previous measurements.

These new measured half-life values, where used to obtain the B(E2) transition strengths. By comparing our experimental values to theoretical calculations, we found that the theoretical predictions notably underestimate the B(E2; $4^+ \rightarrow 2^+$) transition rate. A systematic study also showed that the B(E2) transition rates in ^{134}Sn are systematically lower than those measured for similar two nucleons systems in the ^{132}Sn and ^{208}Pb regions, but they are consistent with the analogous two-neutron ^{210}Pb isotope.

Conclusions and outlook

The evolution of the nuclear shell structure for nuclei with large neutron to proton ratios is an open problem in nuclear physics. The experimental study of the regions around exotic doubly-magic nuclei play an important role in the understanding of how the shell structure evolves, and provides useful input to shell-model calculations, which can be used over larger areas of the nuclear chart. The region around ^{132}Sn is of utmost importance, since it is the heaviest doubly-magic nuclei located outside of the valley of stability that can be produced at several radioactive beam facilities at present.

The goal of this PhD Thesis is the investigation of the excited level structure of tin isotopes around ^{132}Sn (Z=50 and N=82) region. With this aim, we have investigated the isotopes ^{131}Sn, ^{132}Sn, ^{133}Sn and ^{134}Sn, populated in the β decay of $^{131-135}$In. Our study was performed at the ISOLDE facility in the framework of the IS610 experiment, where low-energy radioactive beams were produced by neutron induced fission on a UC_X target. One of the key aspect of the experiment was the use of the ISOLDE resonant ionization laser ion source (RILIS), with the capability of selective isomer ionization for certain isotopes. The measurements were performed at the ISOLDE decay station, and included high-resolution γ-ray spectroscopy and fast-timing measurements using $LaBr_3$(Ce) scintillators as γ-ray detectors.

The main achievements of this PhD thesis are outlined below.

Data analysis

A set of programs has been written to perform the data analysis in order to measure the lifetimes of the levels under study. The analysis of the β-walk showed the existence of two components in the β spectrum, a fast one related to the transmission peak, and a slow component coming from a wider energy spectrum, with a relative weight depending

on the available β energy. This behaviour has been taken into account in the analysis. In addition, a new methodology has been implemented to account and correct for the contributions of Compton background in the fast-timing measurements.

Results on doubly magic ^{132}Sn

The excited structure of ^{132}Sn has been studied in detail from the β decay of ^{132}In. By taking advantage of the isomer selectivity capabilities of the ISOLDE RILIS source, independent investigations of the β-decay of the ^{133g}In ($9/2^+$) g.s. and the ^{133m}In ($1/2^-$) isomer has been performed. The results derived from this investigation have been published by J. Benito *et al* in *Physical Review* C [BFK$^+$20].

- A total of 17 new levels and 68 new γ transitions have been added. A complete fast-timing investigation of the excited levels in ^{132}Sn has been performed as well, confirming and extending previous results.

- An interpretation of the level structure is provided in terms of particle-hole configurations arising from core breaking states across the gap, both from the N = 82 and Z = 50 shells. The interpretation is based on empirical calculations [MFH$^+$95, FHJ$^+$95, Blo98]. The identification of all remaining missing levels from the $\nu f_{7/2}h^{-1}_{11/2}$ and $\nu f_{7/2}d^{-1}_{3/2}$ neutron-hole configurations has been completed. A tentative interpretation has been provided for the remaining of observed states, where we have been able to observe most of the expected particle-hole levels with angular momenta close to 7.

- A new, more precise, value for the half-life of the ^{132}In g.s, $T_{1/2}$=202.2(2), ms have been measured. The measurement was obtained by analyzing the time distribution of the ten strongest γ-rays emitted in ^{132}In β-decay.

- Based on gamma intensities, the β-delayed neutron emission probabilities have been measured for the decay of ^{132}In, P_n=12(2)%, and separately for the decay of ^{133g}In, P_n=90(3)%, and ^{133m}In, P_n=93(3)%.

- The lifetimes of 7 excited levels have been remeasured in this analysis. These new measurements show an excellent agreement with previous values [FHJ$^+$95]. Additionally, upper half-life limits were obtained for another 8 levels.

The structure of the single-hole nucleus ^{131}Sn

The excited structure of the single-hole nucleus ^{131}Sn was populated in the β-decay of the three ^{131}In β-decaying states, ^{131g}In $(9/2^+)$, ^{131m1}In $(1/2^-)$ and ^{131m2}In $(21/2^+)$. Thanks to the use of RILIS it was possible to separate very well the ionization of the ^{131m1}In and ^{131g}In states. The results derived from this study are summarized below.

- The half-lives of the three β-decaying states in ^{131}In have been measured with better precision than previously achieved. The three new values, $T_{1/2}[^{131g}\text{In}]$=261.8(4) ms, $T_{1/2}[^{131m1}\text{In}]$=335.7(6) ms and $T_{1/2}[^{131m2}\text{In}]$=343(2) ms, are in good agreement with previous values.

- The level-scheme of ^{131}Sn has been notably expanded in the work of this thesis, with the addition of 28 new γ lines and 22 new excited levels.

- The population of a μs isomeric state in ^{131}Sn at 4680+X-keV has been tentatively suggested in our work, based on the analysis of the γ-γ delayed coincidences with the 158-keV transition. This level would correspond to the $27/2^-$ member of the $\nu d_{3/2}h^{-2}_{11/2}$ multiplet. Nonetheless, a more detailed measurement is required to confirm this assignment.

- An exhaustive analysis has been carried out to confirm the energy position of the $\nu h^{-1}_{11/2}$ single-hole state in ^{131}Sn via $\gamma - \gamma$ coincidences. Evidence that supports the 65.1-keV assignment proposed in [FGM$^+$04a] was found in our analysis. Nevertheless, there is no definitive confirmation yet. According to our analysis a more detailed investigation of the high-lying excited levels populated in the ^{131g}In decay will likely shed light on the position of the $(11/2^-)$ state, via the identification of levels that de-excite both to the 2434-keV $(7/2^+)$ level and the unconfirmed $(11/2^-)$ state.

- The direct feeding to the β-decaying levels in ^{131}Sn has been derived in this work from the daughter decay intensities. The isomer selectivity allowed us to separate the contributions from the β-decay of the ^{131g}In, ^{131m1}In and ^{131m2}In. As a result, the β-intensity values have been strongly revised compared to the existing ones. This revision has a sizable effect on the $\log ft$ values, which solves the problem of the disagreement between the different f.f. transitions reported on

previous works [FGM$^+$04a, DSA$^+$19]. Our values indicate similar logft values for the three f.f. transitions: $\pi g_{9/2}^{-1} \rightarrow \nu h_{11/2}^{-1}$ with logft=5.5(2), $\pi p_{1/2}^{-1} \rightarrow \nu d_{3/2}^{-1}$ with logft=5.34(13), and $\pi p_{1/2}^{-1} \rightarrow \nu s_{1/2}^{-1}$ with logft=5.40(4).

- The P_n values for the three ^{131}In β-decaying states have been derived independently for the first time. The new values are $P_n[^{131g}\text{In}]$=2.4(6) %, $P_n[^{131g}\text{In}]$=1.2(6) % and $P_n[^{131m2}\text{In}]$=8.9(8) %. Neutron spectroscopy measurements are required to confirm them.

- A large number of γ-decaying states located above the neutron separation energy have been identified in ^{131}Sn. Our analysis shows a clear correlation between the appearance of these states and the β-decaying state in ^{131}In that populates them, pointing to a low l-value decay to the levels in ^{130}Sn.

- The half-life of the neutron single-hole 332-keV $(1/2^+)$ state has been measured, yielding $T_{1/2}$=18(4) ps. This short lifetime indicates an enhanced *l-forbidden* M1 character for the 332-keV $\nu 3s_{1/2} \rightarrow \nu 3d_{3/2}$ transition. This value is similar to those measured for similar *l-forbidden* M1 transitions in the ^{208}Pb region.

- Regarding the high-spin levels populated in ^{131m2}In decay, the half-life of the 4447+X keV and 4558+X-keV levels have been measured for the first time, and a new value has been obtained for the long-lived 4606+X-keV level. The transition strengths derived from these lifetimes reinforce the analogy between the ^{131m2}In and ^{132}In decays. Most of the transition strengths are comparable to those of their analogous transitions in ^{132}Sn. The most striking difference is shown by the 173-keV E1 4447+X$\rightarrow$4274+X transition, whose B(E1) is $\sim$40 times larger than its corresponding E1 transition in ^{132}Sn.

Results for ^{133}Sn

The excited structure in ^{133}Sn was populated in the β-decay of both ^{133}In and ^{134}In isotopes. Thanks to the use of RILIS it was possible to separate the decay of the ^{133g}In $(9/2^+)$ g.s. and the ^{133m}In $(1/2^-)$ isomer. The lifetimes of the excited levels in ^{133}Sn states measured using the fast-timing technique were the main focus of this PhD thesis. We have measured a new value for the mean-life of the $p_{3/2}$ single-particle state,

τ=36(19) ps, in very good agreement with the previous value of τ=30(15) ps [VJD$^+$17] obtained by Doppler shift methods. The corresponding B(E2) strength for the 854-keV γ-ray transition between the $\nu p_{3/2}$ and $\nu f_{7/2}$ states is B(E2) = 1.2($^{+13}_{-8}$) W.u., which is consistent with the strength of neutron single-particle transitions in the Pb region.

Lifetime measurements in ^{134}Sn

The excited states in ^{134}Sn were populated in the β decay of ^{134}In and the β-n decay of ^{135}In. In this PhD thesis we have performed a complete study of the lifetimes of the low-lying states in ^{134}Sn. In particular, the half-lives of the three states that arise from the $\nu f^2_{7/2}$ configuration have been measured.

- A new measurement of the half-life of the 6^+ state has been performed, yielding $T_{1/2}$=81.7(12) ns. This value is in agreement with the previously available $T_{1/2}$=80(15) ns [ZBD$^+$97, KURU$^+$00], but has a much higher precision.

- The lifetime of the 4^+ state has been measured for the first time, yielding a result of $T_{1/2}$=1.18(4) ns.

- Regarding the 2^+ state, we have obtained an experimental value of $T_{1/2}$=55(28) ps. This value confirms the B(E2) rate measured in Coulomb excitation [BVB$^+$04, VBB$^+$05, RBB$^+$05].

- The B(E2) transition strengths were derived from our half-life measurements. By comparing them to those calculated by theory it is apparent that the theoretical calculations underestimate the B(E2; $4^+ \rightarrow 2^+$) transition rate. This underestimation seems to be motivated by the lack of information about the half-lives for the Sn isotopes beyond ^{132}Sn.

- The B(E2) transition rates in ^{134}Sn were compared to those measured for similar nuclei with two valence particle outside a doubly-magic core providing an overall picture of two-neutron systems above doubly-magic core nuclei.

In conclusion, the results obtained in this PhD thesis provide new information on the structure of Sn isotopes around the double Z=50, N=82 shell closure. The structure of ^{131}Sn, ^{132}Sn, ^{133}Sn and ^{134}Sn has been investigated. Lifetime measurements have been

performed for all four tin isotopes. The level schemes of ^{131}Sn and ^{132}Sn, populated in the β and β-n decay of In isotopes, have been greatly expanded.

In spite of the recent experimental progress, spectroscopic information is still lacking in the ^{132}Sn region. Similar measurements as those described in this PhD thesis, including γ spectroscopy and lifetime measurements can be extended to other nuclei, for example n-rich In (Z=50) isotopes populated in the β-decay of cadmium. Complementary studies can profit from low-energy transfer reactions and high-energy knock-out experiments.

List of Figures

List of Tables

References

[ACC+97] F. Andreozzi, L. Coraggio, A. Covello, A. Gargano, T. T. S. Kuo, and A. Porrino. Structure of neutron-rich nuclei around ^{132}Sn. *Phys. Rev. C*, 56:R16–R19, Jul 1997. 7

[AHS57] Akito Arima, Hisashi Horie, and Mitsuo Sano. The l-Forbidden Magnetic Dipole Transitions. *Progress of Theoretical Physics*, 17(4):567–580, 04 1957. 201

[ARM+13] T. Alharbi, P. H. Regan, P. J. R. Mason, N. Mărginean, Zs. Podolyák, A. M. Bruce, E. C. Simpson, A. Algora, N. Alazemi, R. Britton, M. R. Bunce, D. Bucurescu, N. Cooper, D. Deleanu, D. Filipescu, W. Gelletly, D. Ghiţă, T. Glodariu, G. Ilie, S. Kisyov, J. Lintott, S. Lalkovski, S. Liddick, C. Mihai, K. Mulholland, R. Mărginean, A. Negret, M. Nakhostin, C. R. Nita, O. J. Roberts, S. Rice, J. F. Smith, L. Stroe, T. Sava, C. Townsley, E. Wilson, V. Werner, M. Zhekova, and N. V. Zamfir. Electromagnetic transition rates in the $N = 80$ nucleus $^{138}_{58}$Ce. *Phys. Rev. C*, 87:014323, 2013. 42

[ASB+14] J. M. Allmond, A. E. Stuchbery, J. R. Beene, A. Galindo-Uribarri, J. F. Liang, E. Padilla-Rodal, D. C. Radford, R. L. Varner, A. Ayres, J. C. Batchelder, A. Bey, C. R. Bingham, M. E. Howard, K. L. Jones, B. Manning, P. E. Mueller, C. D. Nesaraja, S. D. Pain, W. A. Peters, A. Ratkiewicz, K. T. Schmitt, D. Shapira, M. S. Smith, N. J. Stone, D. W. Stracener, and C.-H. Yu. Double-magic nature of ^{132}Sn and ^{208}Pb through lifetime and cross-section measurements. *Phys. Rev. Lett.*, 112:172701, Apr 2014. 8, 9, 217, 218

[Bas14] M. [Shamsuzzoha Basunia]. Nuclear data sheets for a = 210. *Nuclear Data Sheets*, 121:561 – 694, 2014. 244

[Baz] D. Bazzacco. Gaspware. https://github.com/sztaylor89/GASPware-1. 49

[BBB+86] T. Björnstad, M. J. G. Borge, J. Blomqvist, R. D. Von Dincklage, G. T. Ewan, P. Hoff, B. Jonson, K. Kawade, A. Kerek, O. Klepper, G. Lövhöiden, S. Mattsson, G. Nyman, H. L. Ravn, G. Rudstam, K. Sistemich, and O. Tengblad. The doubly closed shell nucleus 13250sn82. *Nuclear Physics A*, 453(3):463–485, 1986. 99, 148

REFERENCES

[BDZ+01] P. Bhattacharyya, P. J. Daly, C. T. Zhang, Z. W. Grabowski, S. K. Saha, R. Broda, B. Fornal, I. Ahmad, D. Seweryniak, I. Wiedenhöver, M. P. Carpenter, R. V. F. Janssens, T. L. Khoo, T. Lauritsen, C. J. Lister, P. Reiter, and J. Blomqvist. Magic nucleus ^{132}sn and its one-neutron-hole neighbor ^{131}sn. *Phys. Rev. Lett.*, 87:062502, Jul 2001. 9, 99, 107, 149, 156, 157, 189, 209, 211

[BFK+20] J. Benito, L. M. Fraile, A. Korgul, M. Piersa, E. Adamska, A. N. Andreyev, R. Álvarez-Rodríguez, A. E. Barzakh, G. Benzoni, T. Berry, M. J. G. Borge, M. Carmona, K. Chrysalidis, C. Costache, J. G. Cubiss, T. Day Goodacre, H. De Witte, D. V. Fedorov, V. N. Fedosseev, G. Fernández-Martínez, A. Fijałkowska, M. Fila, H. Fynbo, D. Galaviz, P. Galve, M. García-Díez, P. T. Greenlees, R. Grzywacz, L. J. Harkness-Brennan, C. Henrich, M. Huyse, P. Ibáñez, A. Illana, Z. Janas, J. Jolie, D. S. Judson, V. Karayonchev, M. Kici ńska Habior, J. Konki, J. Kurcewicz, I. Lazarus, R. Lică, A. López-Montes, M. Lund, H. Mach, M. Madurga, I. Marroquín, B. Marsh, M. C. Martínez, C. Mazzocchi, N. Mărginean, R. Mărginean, K. Miernik, C. Mihai, R. E. Mihai, E. Nácher, A. Negret, B. Olaizola, R. D. Page, S. V. Paulauskas, S. Pascu, A. Perea, V. Pucknell, P. Rahkila, C. Raison, E. Rapisarda, J.-M. Régis, K. Rezynkina, F. Rotaru, S. Rothe, D. Sánchez-Parcerisa, V. Sánchez-Tembleque, K. Schomacker, G. S. Simpson, Ch. Sotty, L. Stan, M. Stănoiu, M. Stryjczyk, O. Tengblad, A. Turturica, J. M. Udías, P. Van Duppen, V. Vedia, A. Villa-Abaunza, S. Viñals, W. B. Walters, R. Wadsworth, and N. Warr. Detailed spectroscopy of doubly magic ^{132}Sn. *Phys. Rev. C*, 102:014328, Jul 2020. 121, 248

[BGE+80] T. Björnstad, L.-E. De Geer, G.T. Ewan, P.G. Hansen, B. Jonson, K. Kawade, A. Kerek, W.-D. Lauppe, H. Lawin, S. Mattsson, and K. Sistemich. Structure of the levels in the doubly magic nucleus 50132sn82. *Physics Letters B*, 91(1):35 – 37, 1980. 99

[BHK55] Z. Bay, V. P. Henri, and H. Kanner. Statistical theory of delayed-coincidence experiments. *Phys. Rev.*, 100:1197–1208, Nov 1955. 69

[BHR73] S. Borg, G. B. Holm, and B. Rydberg. Proton particle states in the region around 13250sn82. *Nuclear Physics A*, 212(1):197–206, 1973. 7

[BKF83] J. Blomqvist, Andras Kerek, and B. Fogelberg. The single proton nucleus ^{133}sb. *European Physical Journal A - EUR PHYS J A*, 314:199–204, 06 1983. 122

[BKWMP16] J. Barnes, D. Kasen, M.-.R. Wu, and G. Martinez-Pinedo. Radioactivity and thermalization in the ejecta of compact object mergers and their impact on kilonova light curves. *The Astrophysical Journal*, 821, 2016. 14

[Blo98] Jan Blomqvist. Private Communication, 1998. 147, 148, 153, 248

[BT77] C. J. Bischof and W. L. Talbert. Gamma-ray decay schemes for ^{93}Kr, ^{93}Rb, and ^{93}Sr. *Phys. Rev. C*, 15:1047–1067, Mar 1977. 30

[BVB+04] J. Beene, R. Varner, C. Baktash, Alfredo Galindo-Uribarri, C. Gross, J. Campo, M. Halbert, P. Hausladen, Yves Larochelle, J. Liang, J. Mas, and Paul Mueller. Coulomb excitation studies of sn-132,sn-134. *Nuclear Physics A - NUCL PHYS A*, 746:471–474, 12 2004. 228, 238, 240, 241, 242, 245, 251

[CAB+17] R Catherall, W Andreazza, M Breitenfeldt, A Dorsival, G J Focker, T P Gharsa, Giles T J, J-L Grenard, F Locci, P Martins, S Marzari, J Schipper, A Shornikov, and T Stora. The ISOLDE facility. *Journal of Physics G: Nuclear and Particle Physics*, 44(9):094002, aug 2017. 37

[CAC+97] A. Covello, F. Andreozzi, L. Coraggio, A. Gargano, T.T.S. Kuo, and A. Porrino. Nuclear structure calculations with realistic effective interactions. *Progress in Particle and Nuclear Physics*, 38:165 – 172, 1997. 4 pi High Resolution Gamma Ray Spectroscopy and Nuclear Structure. 241

[CBV+17] P. S. Cowperthwaite, E. Berger, V. A. Villar, B. D. Metzger, M. Nicholl, R. Chornock, P. K. Blanchard, W. Fong, R. Margutti, M. Soares-Santos, K. D. Alexander, S. Allam, J. Annis, D. Brout, D. A. Brown, R. E. Butler, H. . Y. Chen, H. T. Diehl, Z. Doctor, M. R. Drout, T. Eftekhari, B. Farr, D. A. Finley, R. J. Foley, J. A. Frieman, C. L. Fryer, J. García-Bellido, M. S. S. Gill, J. Guillochon, K. Herner, D. E. Holz, D. Kasen, R. Kessler, J. Marriner, T. Matheson, E. H. Neilsen, E. Quataert, A. Palmese, A. Rest, M. Sako, D. M. Scolnic, N. Smith, D. L. Tucker, P. K. G. Williams, E. Balbinot, J. L. Carlin, E. R. Cook, F. Durret, T. S. Li, P. A. A. Lopes, A. C. C. Lourenço, J. L. Marshall, G. E. Medina, J. Muir, R. R. Muñoz, M. Sauseda, D. J. Schlegel, L. F. Secco, A. K. Vivas, W. Wester, A. Zenteno, Y. Zhang, T. M. C. Abbott, M. Banerji, K. Bechtol, A. Benoit-Lévy, E. Bertin, E. Buckley-Geer, D. L. Burke, D. Capozzi, A. Carnero Rosell, M. Carrasco Kind, F. J. Castander, M. Crocce, C. E. Cunha, C. B. D'Andrea, L. N. d. a. Costa, C. Davis, D. L. DePoy, S. Desai, J. P. Dietrich, A. Drlica-Wagner, T. F. Eifler, A. E. Evrard, E. Fernandez, B. Flaugher, P. Fosalba, E. Gaztanaga, D. W. Gerdes, T. Giannantonio, D. A. Goldstein, D. Gruen, R. A. Gruendl, G. Gutierrez, K. Honscheid, B. Jain, D. J. James, T. Jeltema, M. W. G. Johnson, M. D. Johnson, S. Kent, E. Krause, R. Kron, K. Kuehn, N. Nuropatkin, O. Lahav, M. Lima, H. Lin, M. A. G. Maia, M. March, P. Martini, R. G. McMahon, F. Menanteau, C. J. Miller, R. Miquel, J. J. Mohr, E. Neilsen, R. C. Nichol, R. L. C. Ogando, A. A. Plazas, N. Roe, A. K. Romer, A. Roodman, E. S. Rykoff, E. Sanchez, V. Scarpine, R. Schindler, M. Schubnell, I. Sevilla-Noarbe, M. Smith, R. C. Smith, F. Sobreira, E. Suchyta, M. E. C. Swanson, G. Tarle, D. Thomas, R. C. Thomas, M. A. Troxel, V. Vikram, A. R. Walker, R. H. Wechsler, J. Weller, B. Yanny, and J. Zuntz. The electromagnetic counterpart of the binary neutron

star merger ligo/virgo gw170817. ii. uv, optical, and near-infrared light curves and comparison to kilonova models. *The Astrophysical Journal*, 848, 2017. 14

[CCG+09] L. Coraggio, A. Covello, A. Gargano, N. Itaco, and T. T. S. Kuo. Shell-model study of the $n = 82$ isotonic chain with a realistic effective hamiltonian. *Phys. Rev. C*, 80:044320, Oct 2009. 10

[CCGI02] L. Coraggio, A. Covello, A. Gargano, and N. Itaco. Structure of sn isotopes beyond $n = 82$. *Phys. Rev. C*, 65:051306, Apr 2002. 241, 242, 243

[CCGI13a] L. Coraggio, A. Covello, A. Gargano, and N. Itaco. Evolution of single-particle states beyond ^{132}sn. *Phys. Rev. C*, 87:034309, Mar 2013. 10

[CCGI13b] L. Coraggio, A. Covello, A. Gargano, and N. Itaco. Shell-model study of single-neutron strength fragmentation in ^{137}xe. *Phys. Rev. C*, 87:021301, Feb 2013. 10

[CK15] J. Chen and F.G. Kondev. Nuclear data sheets for a = 209. *Nuclear Data Sheets*, 126:373 – 546, 2015. 206, 225

[CTT91] John J. Cowan, Friedrich-Karl Thielemann, and James W. Truran. The r-process and nucleochronology. *Physics Reports*, 208(4):267 – 394, 1991. 12

[DBT+99] G. Duchêne, F.A. Beck, P.J. Twin, G. [de France], D. Curien, L. Han, C.W. Beausang, M.A. Bentley, P.J. Nolan, and J. Simpson. The clover: a new generation of composite ge detectors. *Nuclear Instruments and Methods in Physics Research Section A: Accelerators, Spectrometers, Detectors and Associated Equipment*, 432(1):90 – 110, 1999. 40, 41

[DdHvE95] P. Dorenbos, J.T.M. de Haas, and C.W.E. van Eijk. Non-proportionality in the scintillation response and the energy resolution obtainable with scintillation crystals. *IEEE Transactions on Nuclear Science*, 42(6):2190–2202, 1995. 56

[DGH80] L. E. De Geer and G. B. Holm. Energy levels of ^{127,129,131}Sn populated in the β^- decay of ^{127,129,131}In. *Phys. Rev. C*, 22:2163–2177, Nov 1980. 9, 155

[DLSS78] J.S. Dehesa, W.D. Lauppe, K. Sistemich, and J. Speth. Structure calculations for the doubly magic nucleus 50132sn82. *Physics Letters B*, 74(4):309 – 312, 1978. 99

[DSA+19] R. Dunlop, C. E. Svensson, C. Andreoiu, G. C. Ball, N. Bernier, H. Bidaman, V. Bildstein, M. Bowry, D. S. Cross, I. Dillmann, M. R. Dunlop, F. H. Garcia, A. B. Garnsworthy, P. E. Garrett, G. Hackman, J. Henderson, J. Measures, D. Mücher, B. Olaizola, K. Ortner, J. Park, C. M. Petrache, J. L. Pore, J. K. Smith, D. Southall, M. Ticu, J. Turko, K. Whitmore, and T. Zidar. β decay and

β-delayed neutron decay of the $n = 82$ nucleus $^{131}_{49}\mathrm{In}_{82}$. *Phys. Rev. C*, 99:045805, Apr 2019. 9, 30, 53, 157, 158, 161, 163, 165, 166, 172, 175, 176, 180, 183, 198, 200, 207, 211, 212, 214, 250

[Elj] Eljen Technologies. EJ-232. https://eljentechnology.com/products/plastic-scintillators/ej-232-ej-232q. 42

[Els33] W.M. Elsasser. Sur le principe de pauli dans les noyaux. *J. Phys. Radium*, 4:549–556, 10 1933. 1

[Els34a] W.M. Elsasser. Sur le principe de pauli dans les noyaux ii. *J. Phys. Radium*, 5:389–397, 8 1934. 1

[Els34b] W.M. Elsasser. Sur le principe de pauli dans les noyaux iii. *J. Phys. Radium*, 5:635–639, 12 1934. 1

[FB84] B. Fogelberg and J. Blomqvist. Single-hole and three-quasiparticle levels in ^{131}Sn observed in the decay of ^{131g,m1,m2In}In. *Nuclear Physics A*, 429(2):205 – 217, 1984. 9, 156, 158, 189

[FBD+01] B. Fornal, R. Broda, P. J. Daly, P. Bhattacharyya, C. T. Zhang, Z. W. Grabowski, I. Ahmad, D. Seweryniak, I. Wiedenhöver, M. P. Carpenter, R. V. F. Janssens, T. L. Khoo, T. Lauritsen, C. J. Lister, P. Reiter, and J. Blomqvist. Few particle excitations of $n = 83$ isotones ^{134}Sb and ^{135}Te from ^{248}Cm fission. *Phys. Rev. C*, 63:024322, Jan 2001. 10

[FCG+17] Valentin Fedosseev, Katerina Chrysalidis, Thomas Day Goodacre, Bruce Marsh, Sebastian Rothe, Christoph Seiffert, and Klaus Wendt. Ion beam production and study of radioactive isotopes with the laser ion source at ISOLDE. *Journal of Physics G: Nuclear and Particle Physics*, 44(8):084006, jul 2017. 34, 35

[Fer19] María Victoria Vedia Fernández. Fast-timing investigation with labr$_3$(ce) arrays: detector optimization and measurements in ^{136}te. Tesis de la Universidad Complutense de Madrid, Facultad de Ciencias Físicas, Departamento de Estructura de la Materia, Física Térmica y Electrónica, leída el 10-12-2018, April 2019. 42

[FGM+04a] B. Fogelberg, H. Gausemel, K. A. Mezilev, P. Hoff, H. Mach, M. Sanchez-Vega, A. Lindroth, E. Ramström, J. Genevey, J. A. Pinston, and M. Rejmund. Decays of ^{131}In, ^{131}Sn, and the position of the $h_{11/2}$ neutron hole state. *Phys. Rev. C*, 70:034312, Sep 2004. 9, 15, 30, 155, 156, 158, 161, 172, 175, 183, 184, 185, 186, 189, 214, 249, 250

[FGM+04b] B. Fogelberg, H. Gausemel, K. A. Mezilev, P. Hoff, H. Mach, M. Sanchez-Vega, A. Lindroth, E. Ramström, J. Genevey, J. A. Pinston, and M. Rejmund. Decays of ^{131}In, ^{131}Sn, and the position of the $h_{11/2}$ neutron hole state. *Phys. Rev. C*, 70:034312, Sep 2004. 166, 171

[FHJ+94] B. Fogelberg, M. Hellström, D. Jerrestam, H. Mach, J. Blomqvist, A. Kerek, L. O. Norlin, and J. P. Omtvedt. Detailed spectroscopy of the doubly closed shell nucleus ^{132}Sn : first observation of octupole collectivity. *Phys. Rev. Lett.*, 73:2413–2416, Oct 1994. 99, 106, 130, 136, 142, 143, 144, 145, 146, 147, 148, 150, 151

[FHJ+95] B Fogelberg, M Hellström, D Jerrestam, H Mach, J Blomqvist, A Kerek, L O Norlin, and J P Omtvedt. The doubly closed shell nucleus ^{132}sn: Collectivity and p-h states. *Physica Scripta*, T56:79–83, 1995. 99, 130, 139, 147, 150, 151, 153, 248

[FHS81] B. Fogelberg, K. Heyde, and J. Sau. Energy levels and transition probabilities in 130sn. *Nuclear Physics A*, 352(2):157 – 180, 1981. 52

[FKT17] Hans Fynbo, Oliver S Kirseboom, and Olof Tengblad. ISOLDE decay station for decay studies of interest in astrophysics and exotic nuclei. *Journal of Physics G: Nuclear and Particle Physics*, 44(4):044005, mar 2017. 39

[FM57] Jun-ichi Fujita and Hironari Miyazawa. Pion Theory of Three-Body Forces. *Progress of Theoretical Physics*, 17(3):360–365, 03 1957. 4

[Fra17] L M Fraile. Fast-timing spectroscopy at ISOLDE. *Journal of Physics G: Nuclear and Particle Physics*, 44(9):094004, aug 2017. 39

[FZS88] B. Fogelberg, Ye Zongyuan, and L. Spanier. A determination of proton hole energies in 131in. *Physics Letters B*, 209(2):173–176, 1988. 8

[GCG+09] M. Górska, L. Cáceres, H. Grawe, M. Pfützner, A. Jungclaus, S. Pietri, E. Werner-Malento, Z. Podolyák, P.H. Regan, D. Rudolph, P. Detistov, S. Lalkovski, V. Modamio, J. Walker, T. Beck, P. Bednarczyk, P. Doornenbal, H. Geissel, J. Gerl, J. Grębosz, R. Hoischen, I. Kojouharov, N. Kurz, W. Prokopowicz, H. Schaffner, H. Weick, H.-J. Wollersheim, K. Andgren, J. Benlliure, G. Benzoni, A.M. Bruce, E. Casarejos, B. Cederwall, F.C. L. Crespi, B. Hadinia, M. Hellström, G. Ilie, A. Khaplanov, M. Kmiecik, R. Kumar, A. Maj, S. Mandal, F. Montes, S. Myalski, G.S. Simpson, S.J. Steer, S. Tashenov, O. Wieland, Zs. Dombrádi, P. Reiter, and D. Sohler. Evolution of the n=82 shell gap below 132sn inferred from core excited states in 131in. *Physics Letters B*, 672(4):313–316, 2009. 10

[GLMP07] H Grawe, K Langanke, and G Martínez-Pinedo. Nuclear structure and astrophysics. *Reports on Progress in Physics*, 70(9):1525–1582, 2007. 7, 8, 12, 13

[GML+14] A. Gottberg, T.M. Mendonca, R. Luis, J.P. Ramos, C. Seiffert, S. Cimmino, S. Marzari, B. Crepieux, V. Manea, R.N. Wolf, F. Wienholtz, S. Kreim, V.N.

Fedosseev, B.A. Marsh, S. Rothe, P. Vaz, J.G. Marques, and T. Stora. Experimental tests of an advanced proton-to-neutron converter at isolde-cern. *Nuclear Instruments and Methods in Physics Research Section B: Beam Interactions with Materials and Atoms*, 336:143 – 148, 2014. 34

[Gob] Saint Gobain. Brillance 380 Brochure, https://www.crystals.saint-gobain.com/products/standard-and-enhanced-lanthanum-bromide. 41

[GTA+19] V. Guadilla, J. L. Tain, A. Algora, J. Agramunt, D. Jordan, M. Monserrate, A. Montaner-Pizá, E. Nácher, S. E. A. Orrigo, B. Rubio, E. Valencia, M. Estienne, M. Fallot, L. Le Meur, J. A. Briz, A. Cucoanes, A. Porta, T. Shiba, A.-A. Zakari-Issoufou, A. A. Sonzogni, J. Äystö, T. Eronen, D. Gorelov, J. Hakala, A. Jokinen, A. Kankainen, V. S. Kolhinen, J. Koponen, I. D. Moore, H. Penttilä, I. Pohjalainen, J. Reinikainen, M. Reponen, S. Rinta-Antila, K. Rytkönen, V. Sonnenschein, A. Voss, L. M. Fraile, V. Vedia, E. Ganioğlu, W. Gelletly, M. Lebois, J. N. Wilson, and T. Martinez. Total absorption γ-ray spectroscopy of the β-delayed neutron emitters ^{137}I and ^{95}Rb. *Phys. Rev. C*, 100:044305, Oct 2019. 30

[Gug34a] K. Guggenheimer. Remarques sur la constitution des noyaux atomiques - i. *J. Phys. Radium*, 5:253–256, 6 1934. 1

[Gug34b] K. Guggenheimer. Remarques sur la constitution des noyaux atomiques - ii. *J. Phys. Radium*, 5:475–485, 9 1934. 1

[Ham] Hamamatsu Photonics. Photomultiplier Tube H6610 Specifications. 42

[Ham75] W D Hamilton. Electromagnetic interaction in nuclear spectroscopy. 1 1975. 24, 28

[Ham09a] Hamamatsu Photonics. Photomultiplier Tube R9779 Specifications, 2009. 42

[Ham09b] Hamamatsu Photonics. Photomultiplier Tube R9779 Specifications, 2009. 56

[HBH+96] P. Hoff, P. Baumann, A. Huck, A. Knipper, G. Walter, G. Marguier, B. Fogelberg, A. Lindroth, H. Mach, M. Sanchez-Vega, R. B. E. Taylor, P. Van Duppen, A. Jokinen, M. Lindroos, M. Ramdhane, W. Kurcewicz, B. Jonson, G. Nyman, Y. Jading, K.-L. Kratz, A. Wöhr, G. Løvhøiden, T. F. Thorsteinsen, and J. Blomqvist. Single-neutron states in ^{133}sn. *Phys. Rev. Lett.*, 77:1020–1023, Aug 1996. 8, 123, 217, 219, 241

[HBH+00] P. Hoff, P. Baumann, A. Huck, A. Knipper, G. Walter, G. Marguier, B. Fogelberg, A. Lindroth, H. Mach, M. Sanchez-Vega, R.B.E. Taylor, P. van Duppen, A. Jokinen, M. Lindroos, M. Ramdhane, W. Kurcewicz, B. Jonson, G. Nyman, Y. Jading, K.-L. Kratz, A. Wöhr, G. Løvhøiden, T.F. Thorsteinsen, and J. Blomqvist.

Nuclear spectroscopy at ^{133}sn. *Hyperfine Interactions*, 129(1):141–148, Dec 2000. 8, 221

[HJS49] Otto Haxel, J. Hans D. Jensen, and Hans E. Suess. On the "magic numbers" in nuclear structure. *Phys. Rev.*, 75:1766–1766, Jun 1949. 1

[HPRS81] H. Huck, M. L. Pérez, J. J. Rossi, and H. M. Sofía. ^{131}Sn decay. *Phys. Rev. C*, 24:2227–2234, Nov 1981. 112, 173

[IDS] The IDS collaboration. http://isolde-ids.web.cern.ch/isolde-ids/. 38

[JAB+10] K. L. Jones, A. S. Adekola, D. W. Bardayan, J. C. Blackmon, K. Y. Chae, K. A. Chipps, J. A. Cizewski, L. Erikson, C. Harlin, R. Hatarik, R. Kapler, R. L. Kozub, J. F. Liang, R. Livesay, Z. Ma, B. H. Moazen, C. D. Nesaraja, F. M. Nunes, S. D. Pain, N. P. Patterson, D. Shapira, J. F. Shriner, M. S. Smith, T. P. Swan, and J. S. Thomas. The magic nature of 132sn explored through the single-particle states of 133sn. *Nature*, 465(7297):454–457, 2010. 8, 217

[JGG+16] A. Jungclaus, A. Gargano, H. Grawe, J. Taprogge, S. Nishimura, P. Doornenbal, G. Lorusso, Y. Shimizu, G. S. Simpson, P.-A. Söderström, T. Sumikama, Z. Y. Xu, H. Baba, F. Browne, N. Fukuda, R. Gernhäuser, G. Gey, N. Inabe, T. Isobe, H. S. Jung, D. Kameda, G. D. Kim, Y.-K. Kim, I. Kojouharov, T. Kubo, N. Kurz, Y. K. Kwon, Z. Li, H. Sakurai, H. Schaffner, K. Steiger, H. Suzuki, H. Takeda, Zs. Vajta, H. Watanabe, J. Wu, A. Yagi, K. Yoshinaga, S. Bönig, L. Coraggio, J.-M. Daugas, F. Drouet, A. Gadea, S. Ilieva, N. Itaco, T. Kröll, A. Montaner-Pizá, K. Moschner, D. Mücher, H. Nishibata, A. Odahara, R. Orlandi, and A. Wendt. First observation of γ rays emitted from excited states south-east of ^{132}Sn: The $\pi g_{9/2}^{-1} \bigotimes \nu f_{7/2}$ multiplet of $^{132}\mathrm{In}_{83}$. *Phys. Rev. C*, 93:041301, Apr 2016. 100, 114

[JHT+11] Hua Jin, Munetake Hasegawa, Shigeru Tazaki, Kazunari Kaneko, and Yang Sun. Large-scale shell-model calculation with core excitations for neutron-rich nuclei beyond ^{132}sn. *Phys. Rev. C*, 84:044324, Oct 2011. 11

[JM17] Ashok Kumar Jain and Bhoomika Maheshwari. Generalized seniority states and isomers in tin isotopes. *Physica Scripta*, 92(7):074004, jun 2017. 242

[JNA+11] K. L. Jones, F. M. Nunes, A. S. Adekola, D. W. Bardayan, J. C. Blackmon, K. Y. Chae, K. A. Chipps, J. A. Cizewski, L. Erikson, C. Harlin, R. Hatarik, R. Kapler, R. L. Kozub, J. F. Liang, R. Livesay, Z. Ma, B. Moazen, C. D Nesaraja, S. D. Pain, N. P. Patterson, D. Shapira, J. F. Shriner, M. S. Smith, T. P. Swan, and J. S. Thomas. Direct reaction measurements with a ^{132}sn radioactive ion beam. *Phys. Rev. C*, 84:034601, Sep 2011. 8

[KAA+12] R. L. Kozub, G. Arbanas, A. S. Adekola, D. W. Bardayan, J. C. Blackmon, K. Y. Chae, K. A. Chipps, J. A. Cizewski, L. Erikson, R. Hatarik, W. R. Hix, K. L.

Jones, W. Krolas, J. F. Liang, Z. Ma, C. Matei, B. H. Moazen, C. D. Nesaraja, S. D. Pain, D. Shapira, J. F. Shriner, M. S. Smith, and T. P. Swan. Neutron single particle structure in ^{131}Sn and direct neutron capture cross sections. *Phys. Rev. Lett.*, 109:172501, Oct 2012. 9

[KBT+08] T. Kibédi, T.W. Burrows, M.B. Trzhaskovskaya, P.M. Davidson, and C.W. Nestor. Evaluation of theoretical conversion coefficients using bricc. *Nuclear Instruments and Methods in Physics Research Section A: Accelerators, Spectrometers, Detectors and Associated Equipment*, 589(2):202 – 229, 2008. 109, 144, 191, 213

[KBU+15] A. Korgul, P. Bączyk, W. Urban, T. Rzaça-Urban, A. G. Smith, and I. Ahmad. Investigation of the $i_{13/2}$ neutron orbital in the ^{132}Sn region: New excited levels in ^{135}Sb. *Phys. Rev. C*, 91:027303, Feb 2015. 9

[KEHJO07] M. P. Kartamyshev, T. Engeland, M. Hjorth-Jensen, and E. Osnes. Effective interactions and shell model studies of heavy tin isotopes. *Phys. Rev. C*, 76(2):024313, 2007. 241, 242

[KHDGB73] A. Kerek, G. B. Holm, L. E. De Geer, and S. Borg. The first excited state in the doubly-closed-shell nucleus 132sn populated in the 0.12 s β-decay of 132in. *Physics Letters B*, 44(3):252–254, 1973. 99

[KL11] F.G. Kondev and S. Lalkovski. Nuclear data sheets for a = 207. *Nuclear Data Sheets*, 112(3):707 – 853, 2011. 206, 225

[KMR06] Yu. Khazov, I. Mitropolsky, and A. Rodionov. Nuclear data sheets for a = 131. *Nuclear Data Sheets*, 107(11):2715 – 2930, 2006. 161, 162, 164, 165, 168, 175, 182, 191

[Kra88] Kenneth S Krane. *Introductory nuclear physics*. Wiley, New York, NY, 1988. 4, 21, 22, 24

[KRSS05] Yu. Khazov, A.A. Rodionov, S. Sakharov, and Balraj Singh. Nuclear data sheets for a = 132. *Nuclear Data Sheets*, 104(3):497 – 790, 2005. 53, 100, 103, 106, 132, 145

[KSB+82] K. Kawade, K. Sistemich, G. Battistuzzi, H. Lawin, K. Shizuma, and J. Blomqvist. Evidence for the doubly magic structure of123sn. *Zeitschrift für Physik A Atoms and Nuclei*, 308(1):33–38, Mar 1982. 99

[KURU+00] A. Korgul, W. Urban, T. Rząca-Urban, M. Rejmund, J.L. Durell, M.J. Leddy, M.A. Jones, W.R. Phillips, A.G. Smith, B.J. Varley, N. Schulz, M. Bentaleb, E. Lubkiewicz, I. Ahmad, and L.R. Morss. Properties of n=84, even-even nuclei populated in the spontaneous fission of 248cm. *The European Physical Journal A - Hadrons and Nuclei*, 7(2):167–176, Feb 2000. 227, 228, 234, 241, 251

REFERENCES

[LAB+01] I. Lazarus, E. E. Appelbe, P. A. Butler, P. j. Coleman-Smith, J. R. Cresswell, S. J. Freeman, R. D. Herzberg, I. Hibbert, D. T. Joss, S. C. Letts, R. D. Page, V. F. E. Pucknell, P. H. Regan, J. Sampson, J. Simpson, J. Thornhill, and R. Wadsworth. The great triggerless total data readout method. *IEEE Transactions on Nuclear Science*, 48(3):567–569, 2001. 46

[LHA+80] E. Lund, P. Hoff, K. Aleklett, O. Glomset, and G. Rudstam. Delayed neutron emission probabilities of gallium, bromine, rubidium, indium, antimony, iodine, and cesium precursors. *Zeitschrift für Physik A Atoms and Nuclei*, 294(3):233–240, Sep 1980. 114

[Lica] Lică. Nutaq4IDS. https://github.com/rlica/nutaq4ids. 47

[Licb] R. Lică. Private communication, 2018. 59, 60

[LMF+16] R. Lică, H. Mach, L. M. Fraile, A. Gargano, M. J. G. Borge, N. Mărginean, C. O. Sotty, V. Vedia, A. N. Andreyev, G. Benzoni, P. Bomans, R. Borcea, L. Coraggio, C. Costache, H. De Witte, F. Flavigny, H. Fynbo, L. P. Gaffney, P. T. Greenlees, L. J. Harkness-Brennan, M. Huyse, P. Ibáñez, D. S. Judson, J. Konki, A. Korgul, T. Kröll, J. Kurcewicz, S. Lalkovski, I. Lazarus, M. V. Lund, M. Madurga, R. Mărginean, I. Marroquín, C. Mihai, R. E. Mihai, A. I. Morales, E. Nácher, A. Negret, R. D. Page, J. Pakarinen, S. Pascu, V. Paziy, A. Perea, M. Pérez-Liva, E. Picado, V. Pucknell, E. Rapisarda, P. Rahkila, F. Rotaru, J. A. Swartz, O. Tengblad, P. Van Duppen, M. Vidal, R. Wadsworth, W. B. Walters, and N. Warr. Fast-timing study of the l-forbidden $1/2^+ \rightarrow 3/2^+ m1$ transition in ^{129}Sn. *Phys. Rev. C*, 93:044303, Apr 2016. 39, 204, 205

[LNX+15] G. Lorusso, S. Nishimura, Z. Y. Xu, A. Jungclaus, Y. Shimizu, G. S. Simpson, P.-A. Söderström, H. Watanabe, F. Browne, P. Doornenbal, G. Gey, H. S. Jung, B. Meyer, T. Sumikama, J. Taprogge, Zs. Vajta, J. Wu, H. Baba, G. Benzoni, K. Y. Chae, F. C. L. Crespi, N. Fukuda, R. Gernhäuser, N. Inabe, T. Isobe, T. Kajino, D. Kameda, G. D. Kim, Y.-K. Kim, I. Kojouharov, F. G. Kondev, T. Kubo, N. Kurz, Y. K. Kwon, G. J. Lane, Z. Li, A. Montaner-Pizá, K. Moschner, F. Naqvi, M. Niikura, H. Nishibata, A. Odahara, R. Orlandi, Z. Patel, Zs. Podolyák, H. Sakurai, H. Schaffner, P. Schury, S. Shibagaki, K. Steiger, H. Suzuki, H. Takeda, A. Wendt, A. Yagi, and K. Yoshinaga. β-decay half-lives of 110 neutron-rich nuclei across the $n = 82$ shell gap: Implications for the mechanism and universality of the astrophysical r process. *Phys. Rev. Lett.*, 114:192501, May 2015. 161

[LRB+19] R. Lică, F. Rotaru, M. J. G. Borge, S. Grévy, F. Negoiţă, A. Poves, O. Sorlin, A. N. Andreyev, R. Borcea, C. Costache, H. De Witte, L. M. Fraile, P. T. Greenlees, M. Huyse, A. Ionescu, S. Kisyov, J. Konki, I. Lazarus, M. Madurga, N. Mărginean, R. Mărginean, C. Mihai, R. E. Mihai, A. Negret, F. Nowacki,

R. D. Page, J. Pakarinen, V. Pucknell, P. Rahkila, E. Rapisarda, A. Şerban, C. O. Sotty, L. Stan, M. Stănoiu, O. Tengblad, A. Turturică, P. Van Duppen, N. Warr, Ph. Dessagne, T. Stora, C. Borcea, S. Călinescu, J. M. Daugas, D. Filipescu, I. Kuti, S. Franchoo, I. Gheorghe, P. Morfouace, P. Morel, J. Mrazek, D. Pietreanu, D. Sohler, I. Stefan, R. Şuvăilă, S. Toma, and C. A. Ur. Normal and intruder configurations in ^{34}Si populated in the β^- decay of ^{34}Mg and ^{34}Al. *Phys. Rev. C*, 100:034306, Sep 2019. 39

[Mac01] R. Machleidt. High-precision, charge-dependent bonn nucleon-nucleon potential. *Phys. Rev. C*, 63:024001, Jan 2001. 241

[Mac14] Henryk Mach. Private Communication, 2014. 147

[May48] Maria G. Mayer. On closed shells in nuclei. *Phys. Rev.*, 74:235–239, Aug 1948. 3

[May49] M. Goeppert Mayer. On closed shells in nuclei. ii. *Physical Review*, 75(12):1969, 1949. 1

[MBB+10] N. Mărginean, D.L. Balabanski, D. Bucurescu, S. Lalkovski, L. Atanasova, G. Căta-Danil, I. Căta-Danil, J.M. Daugas, D. Deleanu, P. Detistov, G. Deyanova, D. Filipescu, G. Georgiev, D. Ghiţă, K.A. Gladnishki, R. Lozeva, T. Glodariu, M. Ivaşcu, S. Kisyov, C. Mihai, R. Mărginean, A. Negret, S. Pascu, D. Radulov, T. Sava, L. Stroe, G. Suliman, and N.V. Zamfir. In-beam measurements of sub-nanosecond nuclear lifetimes with a mixed array of HPGe and $LaBr_3$(Ce) detectors. *The European Physical Journal A*, 46(3):329–336, 2010. 42

[MF95] H Mach and B Fogelberg. Fast timing studies of the neutron-rich singly-magicN= 82 nuclei. *Physica Scripta*, T56:270–271, jan 1995. 85, 97, 99

[MFH+95] H. Mach, B. Fogelberg, M. Hellström, D. Jerrestam, J. Blomqvist, A. Kerek, L.O. Norlin, J.P. Omtvedt, K.I. Erokhina, and V.I. Isakov. Detailed spectroscopy of doubly-magic ^{132}Sn and its neighbours; perspective for further studies at piafe. *Nuclear Physics A*, 588(1):c179 – c184, 1995. Proceedings of the Fifth International Symposium on Physics of Unstable Nuclei. 147, 148, 153, 248

[MGM89] H. Mach, R. L. Gill, and M. Moszyński. A method for picosecond lifetime measurements for neutron-rich nuclei (1) Outline of the method. *Nuclear Instruments and Methods in Physics Research A*, 280:49–72, 1989. 39, 66, 76, 84

[Mie14] K. Miernik. β-delayed multiple-neutron emission in the effective density model. *Phys. Rev. C*, 90:054306, Nov 2014. 29

[MKM16] M. R. Mumpower, T. Kawano, and P. Möller. Neutron-γ competition for β-delayed neutron emission. *Phys. Rev. C*, 94:064317, Dec 2016. 29

REFERENCES

[MM89] M. Moszyński and H. Mach. A method for picosecond lifetime measurements for neutron-rich nuclei (2) Timing study with scintillation counters. *Nuclear Instruments and Methods in Physics Research A*, 277:407–417, 1989. 39, 41, 66, 84

[MMPD+10] B. D. Metzger, G. Martínez-Pinedo, S. Darbha, E. Quataert, A. Arcones, D. Kasen, R. Thomas, P. Nugent, I. V. Panov, and N. T. Zinner. Electromagnetic counterparts of compact object mergers powered by the radioactive decay of r-process nuclei. *Monthly Notices of the Royal Astronomical Society*, 406(4):2650–2662, 11/24/2019 2010. 14

[MNP+95] K A Mezilev, Yu N Novikov, A V Popov, B Fogelberg, and L Spanier. Experimental masses at doubly magic nuclide 132sn. T56:272–275, 1995. 7

[MPMZ+07] G. Martínez-Pinedo, D. Mocelj, N. T. Zinner, A. Kelić, K. Langanke, I. Panov, B. Pfeiffer, T. Rauscher, K. H. Schmidt, and F. K. Thielemann. The role of fission in the r-process. *Progress in Particle and Nuclear Physics*, 59(1):199–205, 2007. 14

[MSS96] R. Machleidt, F. Sammarruca, and Y. Song. Nonlocal nature of the nuclear force and its impact on nuclear structure. *Phys. Rev. C*, 53:R1483–R1487, Apr 1996. 241

[MW85] G J Mathews and R A Ward. Neutron capture process in astrophysics. *Reports on Progress in Physics*, 48(10):1371–1418, oct 1985. 14

[NSP+75] F.M. Nuh, D.R. Slaughter, S.G. Prussin, K.-L. Kratz, H. Franz, and G. Herrmann. Gamma-ray competition with neutron emission in the decay of 137i. *Physics Letters B*, 53(5):435 – 438, 1975. 30

[nut] Nutaq data acquisition systems. `https://www.nutaq.com/`. 43, 45

[OFM+13] B. Olaizola, L M. Fraile, H. Mach, A. Aprahamian, J.A. Briz, J. Cal-González, D. Ghiţă, U. Köster, W. Kurcewicz, S.R. Lesher, D. Pauwels, E. Picado, A. Poves, D. Radulov, G.S. Simpson, and J. M. Udías. β^-decay of ^{65}Mn to ^{65}Fe. *Phys. Rev. C*, 88:044306, 2013. 42

[OPA+18] R. Orlandi, S.D. Pain, S. Ahn, A. Jungclaus, K.T. Schmitt, D.W. Bardayan, W.N. Catford, R. Chapman, K.A. Chipps, J.A. Cizewski, C.G. Gross, M.E. Howard, K.L. Jones, R.L. Kozub, B. Manning, M. Matos, K. Nishio, P.D. O' Malley, W.A. Peters, S.T. Pittman, A. Ratkiewicz, C. Shand, J.F. Smith, M.S. Smith, T. Fukui, J.A. Tostevin, and Y. Utsuno. Neutron-hole states in 131sn and spin-orbit splitting in neutron-rich nuclei. *Physics Letters B*, 785:615 – 620, 2018. 9

[OSF+05] T. Otsuka, T. Suzuki, R. Fujimoto, H. Grawe, and Y. Akaishi. Evolution of nuclear shells due to the tensor force. *Phys. Rev. Lett.*, 95(23):232502, 2005. 5

[PIM+16] W.A. Peters, S. Ilyushkin, M. Madurga, C. Matei, S.V. Paulauskas, R.K. Grzywacz, D.W. Bardayan, C.R. Brune, J. Allen, J.M. Allen, Z. Bergstrom, J. Blackmon, N.T. Brewer, J.A. Cizewski, P. Copp, M.E. Howard, R. Ikeyama, R.L. Kozub, B. Manning, T.N. Massey, M. Matos, E. Merino, P.D. O'Malley, F. Raiola, C.S. Reingold, F. Sarazin, I. Spassova, S. Taylor, and D. Walter. Performance of the versatile array of neutron detectors at low energy (vandle). *Nuclear Instruments and Methods in Physics Research Section A: Accelerators, Spectrometers, Detectors and Associated Equipment*, 836:122 – 133, 2016. 39

[PKF+19] M. Piersa, A. Korgul, L. M. Fraile, J. Benito, E. Adamska, A. N. Andreyev, R. Álvarez-Rodríguez, A. E. Barzakh, G. Benzoni, T. Berry, M. J. G. Borge, M. Carmona, K. Chrysalidis, J. G. Correia, C. Costache, J. G. Cubiss, T. Day Goodacre, H. De Witte, D. V. Fedorov, V. N. Fedosseev, G. Fernández-Martínez, A. Fijałkowska, M. Fila, H. Fynbo, D. Galaviz, P. T. Greenlees, R. Grzywacz, L. J. Harkness-Brennan, C. Henrich, M. Huyse, A. Illana, Z. Janas, K. Johnston, D. S. Judson, V. Karanyonchev, M. Kici ńska Habior, J. Konki, J. Kurcewicz, I. Lazarus, R. Lică, H. Mach, M. Madurga, I. Marroquín, B. Marsh, M. C. Martínez, C. Mazzocchi, N. Mărginean, R. Mărginean, K. Miernik, C. Mihai, E. Nácher, A. Negret, B. Olaizola, R. D. Page, S. Paulaskalas, S. Pascu, A. Perea, V. Pucknell, P. Rahkila, E. Rapisarda, J.-M. Régis, F. Rotaru, S. Rothe, V. Sánchez-Tembleque, G. Simpson, Ch. Sotty, L. Stan, M. Stănoiu, M. Stryjczyk, O. Tengblad, A. Turturica, J. M. Udías, P. Van Duppen, V. Vedia, A. Villa, S. Viñals, R. Wadsworth, W. B. Walters, and N. Warr. β decay of ^{133}In: γ emission from neutron-unbound states in ^{133}Sn. *Phys. Rev. C*, 99:024304, Feb 2019. 8, 17, 30, 53, 106, 121, 123, 153, 166, 218, 224, 225

[PKT97] B. Pfeiffer, K. L. Kratz, and F. K. Thielemann. Analysis of the solar-system r-process abundance pattern with the new etfsi-q mass formula. *Zeitschrift für Physik A Hadrons and Nuclei*, 357(3):235–238, Sep 1997. 14

[RAS93] G. Rudstam, K. Aleklett, and L. Sihver. Delayed-neutron branching ratios of precursors in the fission product region. *Atomic Data and Nuclear Data Tables*, 53(1):1 – 22, 1993. 114

[RBB+05] D.C. Radford, C. Baktash, C.J. Barton, J. Batchelder, J.R. Beene, C.R. Bingham, M.A. Caprio, M. Danchev, B. Fuentes, A. Galindo-Uribarri, J. Gomez del Campo, C.J. Gross, M.L. Halbert, D.J. Hartley, P. Hausladen, J.K. Hwang, W. Krolas, Y. Larochelle, J.F. Liang, P.E. Mueller, E. Padilla, J. Pavan, A. Piechaczek, D. Shapira, D.W. Stracener, R.L. Varner, A. Woehr, C.-H. Yu, and N.V. Zamfir. Coulomb excitation and transfer reactions with rare neutron-rich isotopes.

Nuclear Physics A, 752:264 – 272, 2005. Proceedings of the 22nd International Nuclear Physics Conference (Part 2). 228, 245, 251

[RMS+13] J.-M. Régis, H. Mach, G.S. Simpson, J. Jolie, G. Pascovici, N. Saed-Samii, N. Warr, A. Bruce, J. Degenkolb, L.M. Fraile, C. Fransen, D.G. Ghita, S. Kisyov, U. Köster, A. Korgul, S. Lalkovski, N. Mărginean, P. Mutti, B. Olaizola, Zs. Podolyak, P.H. Regan, O.J. Roberts, M. Rudigier, L. Stroe, W. Urban, and D. Wilmsen. The generalized centroid difference method for picosecond sensitive determination of lifetimes of nuclear excited states using large fast-timing arrays. *Nuclear Instruments and Methods in Physics Research Section A: Accelerators, Spectrometers, Detectors and Associated Equipment*, 726:191 – 202, 2013. 66, 84

[RPJR10] J.-M. Régis, G Pascovici, J Jolie, and M Rudigier. The mirror symmetric centroid difference method for picosecond lifetime measurements via γ-γ coincidences using very fast $LaBr_3$(Ce) scintillator detectors. *Nuclear Instruments and Methods in Physics Research A*, 622:83–92, 2010. 66, 72

[RRF+17] B. C. Rasco, K. P. Rykaczewski, A. Fijałkowska, M. Karny, M. Woli ńska Cichocka, R. K. Grzywacz, C. J. Gross, D. W. Stracener, E. F. Zganjar, J. C. Blackmon, N. T. Brewer, K. C. Goetz, J. W. Johnson, C. U. Jost, J. H. Hamilton, K. Miernik, M. Madurga, D. Miller, S. Padgett, S. V. Paulauskas, A. V. Ramayya, and E. H. Spejewski. Complete β-decay pattern for the high-priority decay-heat isotopes ^{137}I and ^{137}**Xe** determined using total absorption spectroscopy. *Phys. Rev. C*, 95:054328, May 2017. 30

[RSB+14] J.-M. Régis, G.S. Simpson, A. Blanc, G. de France, M. Jentschel, U. Köster, P. Mutti, V. Paziy, N. Saed-Samii, T. Soldner, C.A. Ur, W. Urban, A. M. Bruce, F. Drouet, L. M. Fraile, S. Ilieva, J. Jolie, W. Korten, T. Kr
oll, S. Lalkovski, H. Mach, N. Marginean, G. Pascovici, Zs. Podolyak, P.H. Regan, O.J. Roberts, J. F. Smith, C. Townsley, A. Vancraeyenest, and N. Warr. Germanium-gated $\gamma - \gamma$ fast timing of excited states in fission fragments using the exill-fatima spectrometer. *Nuclear Instruments and Methods in Physics Research Section A: Accelerators, Spectrometers, Detectors and Associated Equipment*, 763(0):210 – 220, 2014. 42

[RSR+18] D. Rosiak, M. Seidlitz, P. Reiter, H. Naïdja, Y. Tsunoda, T. Togashi, F. Nowacki, T. Otsuka, G. Colò, K. Arnswald, T. Berry, A. Blazhev, M. J. G. Borge, J. Cederkäll, D. M. Cox, H. De Witte, L. P. Gaffney, C. Henrich, R. Hirsch, M. Huyse, A. Illana, K. Johnston, L. Kaya, Th. Kröll, M. L. Lozano Benito, J. Ojala, J. Pakarinen, M. Queiser, G. Rainovski, J. A. Rodriguez, B. Siebeck, E. Siesling, J. Snäll, P. Van Duppen, A. Vogt, M. von Schmid, N. Warr, F. Wenander, K. O. Zell, MINIBALL, and HIE-ISOLDE Collaborations. Enhanced

quadrupole and octupole strength in doubly magic ^{132}Sn. *Physical Review Letters*, 121(25):252501–, 12 2018. 147

[Rut11] E. Rutherford. The scattering of α and β particles by matter and the structure of the atom. *Philosophical Magazine*, 21:669–688, 1911. 1

[SFW89] Craig A. Stone, Scott H. Faller, and William B. Walters. Structure of odd-odd ^{132}Sb. *Phys. Rev. C*, 39:1963–1971, May 1989. 112, 114

[SGJ+14] G. S. Simpson, G. Gey, A. Jungclaus, J. Taprogge, S. Nishimura, K. Sieja, P. Doornenbal, G. Lorusso, P.-A. Söderström, T. Sumikama, et al. Yrast 6^+ Seniority Isomers of ^{136,138}Sn. *Phys. Rev. Lett.*, 113(13):132502, 2014. 241

[Sin01] Balraj Singh. Nuclear data sheets for a = 130. *Nuclear Data Sheets*, 93(1):33 – 242, 2001. 114

[SLK+78] K. Sistemich, W. D. Lauppe, T. A. Khan, H. Lawin, H. A. Selič, J. P. Bocquet, E. Monnand, and F. Schussler. The level scheme of133sb. *Zeitschrift für Physik A Atoms and Nuclei*, 285(3):305–313, 1978. 7

[SLN+16] A. Spyrou, S. N. Liddick, F. Naqvi, B. P. Crider, A. C. Dombos, D. L. Bleuel, B. A. Brown, A. Couture, L. Crespo Campo, M. Guttormsen, A. C. Larsen, R. Lewis, P. Möller, S. Mosby, M. R. Mumpower, G. Perdikakis, C. J. Prokop, T. Renstrøm, S. Siem, S. J. Quinn, and S. Valenta. Strong neutron-γ competition above the neutron threshold in the decay of ^{70}Co. *Phys. Rev. Lett.*, 117:142701, Sep 2016. 30

[SMA] Rebecca Surman, Matthew Mumpower, and Ani Aprahamian. *The Sensitivity of γ-Process Nucleosynthesis to Individual β-Delayed Neutron Emission Probabilities*. 14

[SNSEP72] D.R. Slaughter, F.M. Nuh, A.A. Shihab-Eldin, and S.G. Prussin. Gamma-ray emission in competition with neutron emission in the beta decay of 87br. *Physics Letters B*, 38(1):22 – 24, 1972. 30

[Son03] A.A. Sonzogni. Nuclear data sheets for a = 138. *Nuclear Data Sheets*, 98(3):515 – 664, 2003. 76

[Son04] A.A. Sonzogni. Nuclear data sheets for a = 134. *Nuclear Data Sheets*, 103(1):1 – 182, 2004. 244

[Sto87] C. A. Stone. *Experimental and theoretical characterization of effective interactions near ^{132}Sn*. PhD thesis, 1987. Bibliographic information available from INIS: http://inis.iaea.org/search/search.aspx?orig_q=RN:21092381; University Microfilms, PO Box 1764, Ann Arbor, MI 48106, Order No.87-25,580. 174, 180

REFERENCES

[SVFM+98] M. Sanchez-Vega, B. Fogelberg, H. Mach, R. B. E. Taylor, A. Lindroth, and J. Blomqvist. First identification of the $d_{3/2}$ state and measurements of single proton transition rates in ^{133}Sb. *Phys. Rev. Lett.*, 80:5504–5507, Jun 1998. 7

[SVFM+99] M. Sanchez-Vega, B. Fogelberg, H. Mach, R. B. E. Taylor, A. Lindroth, J. Blomqvist, A. Covello, and A. Gargano. Single-proton and core-coupled states in ^{133}Sb. *Phys. Rev. C*, 60:024303, Jun 1999. 152

[TJG+14] J. Taprogge, A. Jungclaus, H. Grawe, S. Nishimura, P. Doornenbal, G. Lorusso, G. S. Simpson, P.-A. Söderström, T. Sumikama, Z. Y. Xu, H. Baba, F. Browne, N. Fukuda, R. Gernhäuser, G. Gey, N. Inabe, T. Isobe, H. S. Jung, D. Kameda, G. D. Kim, Y.-K. Kim, I. Kojouharov, T. Kubo, N. Kurz, Y. K. Kwon, Z. Li, H. Sakurai, H. Schaffner, K. Steiger, H. Suzuki, H. Takeda, Zs. Vajta, H. Watanabe, J. Wu, A. Yagi, K. Yoshinaga, G. Benzoni, S. Bönig, K. Y. Chae, L. Coraggio, A. Covello, J.-M. Daugas, F. Drouet, A. Gadea, A. Gargano, S. Ilieva, F. G. Kondev, T. Kröll, G. J. Lane, A. Montaner-Pizá, K. Moschner, D. Mücher, F. Naqvi, M. Niikura, H. Nishibata, A. Odahara, R. Orlandi, Z. Patel, Zs. Podolyák, and A. Wendt. $1p_{3/2}$ proton-hole state in ^{132}Sn and the shell structure along $n = 82$. *Phys. Rev. Lett.*, 112:132501, Apr 2014. 8

[TJG+16] J. Taprogge, A. Jungclaus, H. Grawe, I. N. Borzov, S. Nishimura, P. Doornenbal, G. Lorusso, G. S. Simpson, P. A. Söderström, T. Sumikama, Z. Y. Xu, H. Baba, F. Browne, N. Fukuda, R. Gernhäuser, G. Gey, N. Inabe, T. Isobe, H. S. Jung, D. Kameda, G. D. Kim, Y. K. Kim, I. Kojouharov, T. Kubo, N. Kurz, Y. K. Kwon, Z. Li, H. Sakurai, H. Schaffner, Y. Shimizu, K. Steiger, H. Suzuki, H. Takeda, Zs. Vajta, H. Watanabe, J. Wu, A. Yagi, K. Yoshinaga, G. Benzoni, S. Bönig, K. Y. Chae, L. Coraggio, J. M. Daugas, F. Drouet, A. Gadea, A. Gargano, S. Ilieva, N. Itaco, F. G. Kondev, T. Kröll, G. J. Lane, A. Montaner-Pizá, K. Moschner, D. Mücher, F. Naqvi, M. Niikura, H. Nishibata, A. Odahara, R. Orlandi, Z. Patel, Zs. Podolyák, and A. Wendt. Proton-hole and core-excited states in the semi-magic nucleus^{131}In. *The European Physical Journal A*, 52(11):347, 2016. 8, 11

[TVA+15] J. L. Tain, E. Valencia, A. Algora, J. Agramunt, B. Rubio, S. Rice, W. Gelletly, P. Regan, A.-A. Zakari-Issoufou, M. Fallot, A. Porta, J. Rissanen, T. Eronen, J. Äystö, L. Batist, M. Bowry, V. M. Bui, R. Caballero-Folch, D. Cano-Ott, V.-V. Elomaa, E. Estevez, G. F. Farrelly, A. R. Garcia, B. Gomez-Hornillos, V. Gorlychev, J. Hakala, M. D. Jordan, A. Jokinen, V. S. Kolhinen, F. G. Kondev, T. Martínez, E. Mendoza, I. Moore, H. Penttilä, Zs. Podolyák, M. Reponen, V. Sonnenschein, and A. A. Sonzogni. Enhanced γ-ray emission from neutron unbound states populated in β decay. *Phys. Rev. Lett.*, 115:062502, Aug 2015. 30

[UKK+00] W. Urban, W. Kurcewicz, A. Korgul, P. J. Daly, P. Bhattacharyya, C. T. Zhang, J. L. Durell, M. J. Leddy, M. A. Jones, W. R. Phillips, A. G. Smith, B. J. Varley, M. Bentaleb, E. Lubkiewicz, N. Schulz, I. Ahmad, L. R. Morss, and J. Blomqvist. Medium-spin structure of single valence-proton nucleus ^{133}Sb. *Phys. Rev. C*, 62:027301, Jul 2000. 10

[VBB+05] R. L. Varner, J. R. Beene, C. Baktash, A. Galindo-Uribarri, C. J. Gross, J. Gomez del Campo, M. L. Halbert, P. A. Hausladen, Y. Larochelle, J. F. Liang, J. Mas, P. E. Mueller, E. Padilla-Rodal, D. C. Radford, D. Shapira, D. W. Stracener, J.-P. Urrego-Blanco, and C.-H. Yu. Coulomb excitation measurements of transition strengths in the isotopes ^{132,134}Sn. *The European Physical Journal A - Hadrons and Nuclei*, 25(1):391–394, Sep 2005. 228, 245, 251

[VCGF+17] V Vedia, M Carmona-Gallardo, LM Fraile, H Mach, and JM Udías. Performance evaluation of novel $LaBr_3$(Ce) scintillator geometries for fast-timing applications. *Nuclear Instruments and Methods in Physics Research Section A: Accelerators, Spectrometers, Detectors and Associated Equipment*, 857:98–105, 2017. 42

[VJA+20] V. Vaquero, A. Jungclaus, T. Aumann, J. Tscheuschner, E. V. Litvinova, J. A. Tostevin, H. Baba, D. S. Ahn, R. Avigo, K. Boretzky, A. Bracco, C. Caesar, F. Camera, S. Chen, V. Derya, P. Doornenbal, J. Endres, N. Fukuda, U. Garg, A. Giaz, M. N. Harakeh, M. Heil, A. Horvat, K. Ieki, N. Imai, N. Inabe, N. Kalantar-Nayestanaki, N. Kobayashi, Y. Kondo, S. Koyama, T. Kubo, I. Martel, M. Matsushita, B. Million, T. Motobayashi, T. Nakamura, N. Nakatsuka, M. Nishimura, S. Nishimura, S. Ota, H. Otsu, T. Ozaki, M. Petri, R. Reifarth, J. L. Rodríguez-Sánchez, D. Rossi, A. T. Saito, H. Sakurai, D. Savran, H. Scheit, F. Schindler, P. Schrock, D. Semmler, Y. Shiga, M. Shikata, Y. Shimizu, H. Simon, D. Steppenbeck, H. Suzuki, T. Sumikama, D. Symochko, I. Syndikus, H. Takeda, S. Takeuchi, R. Taniuchi, Y. Togano, J. Tsubota, H. Wang, O. Wieland, K. Yoneda, J. Zenihiro, and A. Zilges. Fragmentation of single-particle strength around the doubly magic nucleus ^{132}Sn and the position of the $0f_{5/2}$ proton-hole state in ^{131}In. *Phys. Rev. Lett.*, 124:022501, Jan 2020. 8

[VJD+17] V. Vaquero, A. Jungclaus, P. Doornenbal, K. Wimmer, A. Gargano, J. A. Tostevin, S. Chen, E. Nácher, E. Sahin, Y. Shiga, D. Steppenbeck, R. Taniuchi, Z. Y. Xu, T. Ando, H. Baba, F. L. Bello Garrote, S. Franchoo, K. Hadynska-Klek, A. Kusoglu, J. Liu, T. Lokotko, S. Momiyama, T. Motobayashi, S. Nagamine, N. Nakatsuka, M. Niikura, R. Orlandi, T. Saito, H. Sakurai, P. A. Söderström, G. M. Tveten, Zs. Vajta, and M. Yalcinkaya. Gamma decay of unbound neutron-hole states in ^{133}Sn. *Phys. Rev. Lett.*, 118:202502, May 2017. 8, 30, 166, 218, 225, 226, 251

[VMF+15] V. Vedia, H. Mach, L M. Fraile, J.M. Udías, and S. Lalkovski. Enhanced time

response of 1-inch $LaBr_3(Ce)$ crystals by leading edge and constant fraction techniques. *Nuclear Instruments and Methods in Physics Research Section A: Accelerators, Spectrometers, Detectors and Associated Equipment*, 795:144 – 150, 2015. 41, 42, 56

[VTA+17] E. Valencia, J. L. Tain, A. Algora, J. Agramunt, E. Estevez, M. D. Jordan, B. Rubio, S. Rice, P. Regan, W. Gelletly, Z. Podolyák, M. Bowry, P. Mason, G. F. Farrelly, A. Zakari-Issoufou, M. Fallot, A. Porta, V. M. Bui, J. Rissanen, T. Eronen, I. Moore, H. Penttilä, J. Äystö, V.-V. Elomaa, J. Hakala, A. Jokinen, V. S. Kolhinen, M. Reponen, V. Sonnenschein, D. Cano-Ott, A. R. Garcia, T. Martínez, E. Mendoza, R. Caballero-Folch, B. Gomez-Hornillos, V. Gorlichev, F. G. Kondev, A. A. Sonzogni, and L. Batist. Total absorption γ-ray spectroscopy of the β-delayed neutron emitters ^{87}Br, ^{88}Br, and ^{94}Rb. *Phys. Rev. C*, 95:024320, Feb 2017. 30

[WAK+17] Meng Wang, G. Audi, F. G. Kondev, W.J. Huang, S. Naimi, and Xing Xu. The AME2016 atomic mass evaluation (II). tables, graphs and references. *Chinese Physics C*, 41(3):030003, mar 2017. 7, 8, 21, 62, 99, 100, 114, 166, 172, 202, 218

[Wei51] V. F. Weisskopf. Radiative transition probabilities in nuclei. *Phys. Rev.*, 83:1073–1073, Sep 1951. 28

[WGK+17] Han-Kui Wang, S. K. Ghorui, Kazunari Kaneko, Yang Sun, and Z. H. Li. Large-scale shell-model study for excitations across the neutron $n = 82$ shell gap in $^{131--133}$Sb. *Phys. Rev. C*, 96:054313, Nov 2017. 168

[WSJ+13] Han-Kui Wang, Yang Sun, Hua Jin, Kazunari Kaneko, and Shigeru Tazaki. Structure analysis for hole-nuclei close to ^{132}sn by a large-scale shell-model calculation. *Phys. Rev. C*, 88:054310, Nov 2013. 11

[WWA+99] W. Urban, W. Kurcewicz, A. Nowak, T. Rzaca-Urban, J.L. Durell, M.J. Leddy, M.A. Jones, W.R. Phillips, A.G. Smith, B.J. Varley, M. Bentaleb, E. Lubkiewicz, N. Schulz, J. Blomqvist, P.J. Daly, P. Bhattacharyya, C.T. Zhang, I. Ahmad, and L.R. Morss. Neutron single-particle energies in the ^{132}sn region. *Eur. Phys. J. A*, 5(3):239–241, 1999. 241

[ZBD+96] C. T. Zhang, P. Bhattacharyya, P. J. Daly, R. Broda, Z. W. Grabowski, D. Nisius, I. Ahmad, T. Ishii, M. P. Carpenter, L. R. Morss, W. R. Phillips, J. L. Durell, M. J. Leddy, A. G. Smith, W. Urban, B. J. Varley, N. Schulz, E. Lubkiewicz, M. Bentaleb, and J. Blomqvist. Yrast excitations around doubly magic ^{132}Sn from fission product γ-ray studies. *Phys. Rev. Lett.*, 77:3743–3746, Oct 1996. 10

[ZBD+97] C. T. Zhang, P. Bhattacharyya, P. J. Daly, R. Broda, Z. W. Grabowski, D. Nisius, I. Ahmad, M. P. Carpenter, T. Lauritsen, L. R. Morss, W. Urban, J. L. Durell,

W. R. Phillips, M. J. Leddy, A. G. Smith, B. J. Varley, N. Schulz, E. Lubkiewicz, M. Bentaleb, and J. Blomqvist. $(\nu f_{7/2})^2$ multiplet and e2 effective charge in $^{134}_{50}\mathrm{sn}_{84}$. *Zeitschrift für Physik A Hadrons and Nuclei*, 358(1):9–10, 1997. 227, 231, 233, 234, 241, 251

Scientific publications and conferences contributions

During this PhD Thesis the following investigations were published in international journals relevant in the field, or presented at international conferences.

Scientific publications in indexed international journals

1. **J. Benito**, L. M. Fraile, A. Korgul, M. Piersa, E. Adamska, A. N. Andreyev, R. Álvarez-Rodríguez, A. E. Barzakh, G. Benzoni, T. Berry, M. J. G. Borge, M. Carmona, K. Chrysalidis, C. Costache, J. G. Cubiss, T. Day Goodacre, H. De Witte, D. V. Fedorov, V. N. Fedosseev, G. Fern¸ez-Martínez, A. Fijałkowska, M. Fila, H. Fynbo, D. Galaviz, P. Galve, M. García-Díez, P. T. Greenlees, R. Grzywacz, L. J. Harkness-Brennan, C. Henrich, M. Huyse, P. Ibáñez, A. Illana, Z. Janas, J. Jolie, D. S. Judson, V. Karayonchev, M. Kicińska-Habior, J. Konki, J. Kurcewicz, I. Lazarus, R. Lică, A. López-Montes, M. Lund, H. Mach, M. Madurga, I. Marroquín, B. Marsh, M. C. Martínez, Mazzocchi, C. N. Mărginean, R. Mărginean, K. Miernik, C. Mihai, R. E. Mihai, E. Nácher, A. Negret, B. Olaizola, R. D. Page, S. V. Paulauskas, S. Pascu, A. Perea, V. Pucknell, P. Rahkila, C. Raison, E. Rapisarda, J.-M. Régis, K. Rezynkina, F. Rotaru, S. Rothe, D. Sánchez-Parcerisa, V. Sánchez-Tembleque, K. Schomacker, G. S. Simpson, Ch. Sotty, L. Stan, M. Stănoiu, M. Stryjczyk, O. Tengblad, A. Turturica, J. M. Udías, P. Van Duppen, V. Vedia, A. Villa-Abaunza, S. Viñals, W. B. Walters, R. Wadsworth, N. Warr. Detailed spectroscopy of doubly magic ^{132}Sn. *Phys. Rev. C, 102:014328, 2020.*
2. M. Piersa, A. Korgul, L. M. Fraile, **J. Benito**, E. Adamska, A. N. Andreyev, R. Álvarez-Rodríguez, A. E. Barzakh, G. Benzoni, T. Berry, M. J. G. Borge, M. Carmona, K. Chrysalidis, J. G. Correia, C. Costache, J. G. Cubiss, T. Day Goodacre, H. De Witte, D. V. Fedorov, V. N. Fedosseev, G. Fernéz-Martínez, A. Fijałkowska, M. Fila, H. Fynbo, D. Galaviz, P. T. Greenlees, R. Grzywacz, L. J. Harkness-Brennan, C. Henrich, M. Huyse, A. Illana, Z. Janas, K. Johnston, D. S. Judson, V. Karanyonchev, M. Kicińska-Habior, J. Konki, J. Kurcewicz, I. Lazarus, R. Lică, H. Mach, M. Madurga, I. Marroquín, B. Marsh, M. C. Martínez, C. Mazzocchi, N. Mărginean, R. Mărginean, K. Miernik, C.

Mihai, E. Nácher, A. Negret, B. Olaizola, R. D. Page, S. Paulaskalas, S. Pascu, A. Perea, V. Pucknell, P. Rahkila, E. Rapisarda, J.-M. Régis, F. Rotaru, S. Rothe, V. Sánchez-Tembleque, G. Simpson, Ch. Sotty, L. Stan, M. Stănoiu, M. Stryjczyk, O. Tengblad, A. Turturica, J. M. Udías, P. Van Duppen, V. Vedia, A. Villa, S. Viñals, R. Wadsworth, W. B. Walters, N. Warr. β decay of ^{133}In: γ emission from neutron-unbound states in ^{133}Sn. *Phys. Rev. C, 99:024304, 2019.*

3. B. Olaizola, H. Mach, L. M. Fraile, **J. Benito**, M. J. G. Borge, R. Boutami, P. A. Butler, Z. Dlouhy, H. O. U. Fynbo, P. Hoff, S. Hyldegaard, H. B. Jeppesen, A. Jokinen, C. Jollet, A. Korgul, U. Köster, Th. Kröll, W. Kurcewicz, F. Marechal, J. Mrazek, T. Nilsson, W. A. Płóciennik, E. Ruchowska, R. Schuber, W. Schwerdtfeger, M. Sewtz, G. S. Simpson, M. Stanoiu, O. Tengblad, P. G. Thirolf, D. T. Yordanov. High-sensitivity study of levels in ^{30}**Al** following β decay of ^{30}**Mg**. *Phys. Rev. C, 94:054318, 2016.*

4. R. Lică, G. Benzoni, A. I. Morales, M. J. G. Borge, L. M. Fraile, H. Mach, M. Madurga, C. Sotty, V. Vedia, H. De Witte, **J. Benito**, T. Berry, N. Blasi, A. Bracco, F. Camera, S. Ceruti, V. Charviakova, N. Cieplicka-Oryńczak, C. Costache, F. C. L. Crespi, J. Creswell, G. Fernández-Martínez, H. Fynbo, P. Greenlees, I. Homm, M. Huyse, J. Jolie, V. Karayonchev, U. Köster, J. Konki, T. Kröll, J. Kurcewicz, T. Kurtukian-Nieto, I. Lazarus, S. Leoni, M. Lund, N. Marginean, R. Marginean, C. Mihai, R. Mihai, A. Negret, A. Orduz, Z. Patyk, S. Pascu, V. Pucknell, P. Rahkila, J. M. Regis, F. Rotaru, N. Saed-Sami, V. Sánchez-Tembleque, M. Stanoiu, O. Tengblad, M. Thuerauf, A. Turturica, P. Van Duppen, N. Warr. β decay studies of n-rich Cs isotopes with the ISOLDE Decay Station. *Journal of Physics G: Nuclear and Particle Physics, 44:054002, 2017.*

5. R. Lică, G. Benzoni, T. R. Rodríguez, M. J. G. Borge, L. M. Fraile, H. Mach, A. I. Morales, M. Madurga, C. O. Sotty, V. Vedia, H. De Witte, **J. Benito**, R. N. Bernard, T. Berry, A. Bracco, F. Camera, S. Ceruti, V. Charviakova, N. Cieplicka-Oryńczak, C. Costache, F. C. L. Crespi, J. Creswell, G. Fernez-Martínez, H. Fynbo, P. T. Greenlees, I. Homm, M. Huyse, J. Jolie, V. Karayonchev, U. Köster, J. Konki, T. Kröll, J. Kurcewicz, T. Kurtukian-Nieto, I. Lazarus, M. V. Lund, N. Mărginean, R. Mărginean, C. Mihai, R. E. Mihai, A. Negret, A. Orduz, Z. Patyk, S. Pascu, V. Pucknell, P. Rahkila, E. Rapisarda, J. M. Regis, L. M. Robledo, F. Rotaru, N. Saed-Samii, V. Sánchez-Tembleque, M. Stanoiu, O. Tengblad, M. Thuerauf, A. Turturica, P. Van Duppen, N. Warr. Evolution of deformation in neutron-rich Ba isotopes up to $A = 150$. *Phys. Rev. C, 97:024305, 2018.*

6. L.M. Fraile, V. Sánchez-Tembleque, **J. Benito**, M. García-Díez, J.M. Udías, V. Vedia. Advanced scintillators for fast-timing applications.*Nuclear Instruments and Methods in Physics Research Section B: Beam Interactions with Materials and Atoms, 463:394-397, 2020.*

7. R. L. Canavan, M. Rudigier, P. H. Regan, M. Lebois, J. N. Wilson, N. Jovancevic, P.-A. Söderström, S. M. Collins, D. Thisse, **J. Benito**, S. Bottoni, M. Brunet, N. Cieplicka-Oryńczak, S. Courtin, D. T. Doherty, L. M. Fraile, K. Hadyńska-Klęk, G. Häfner, M.

Heine, W. Iskra, Ł. V. Karayonchev, A. Kennington, P. Koseoglou, G. Lotay, G. Lorusso, M. Nakhostin, C. R. Niţă, S. Oberstedt, Zs. Podolyák, L. Qi, J.-M. Régis, V. Sánchez-Tembleque, R. Shearman, V. Vedia, W. Witt. Half-life measurements in ^{164,166}Dy using $\gamma-\gamma$ fast-timing spectroscopy with the ν-Ball spectrometer. *Phys. Rev. C, 101:024313, 2020.*

8. M. Rudigier, P.M. Walker, R.L. Canavan, Zs.Podolyák, P.H. Regan, P.-A. Söderström, M. Lebois, J.N. Wilson, N. Jovancevic, A. Blazhev, **J. Benito**, S. Bottoni, M. Brunet, N. Cieplicka-Oryńczak, S. Courtin, D.T. Doherty, L.M. Fraile, K. Hadynska-Klek, M. Heine, Ł.W. Iskra, J. Jolie, V. Karayonchev, A. Kennington, P. Koseoglou, G. Lotay, G. Lorusso, M. Nakhostin, C.R. Nita, S. Oberstedt, L. Qi, J.-M. Régis, V. Sánchez-Tembleque, R. Shearman, W. Witt, V. Vedia, K.O. Zell. Multi-quasiparticle sub-nanosecond isomers in ^{178}W. *Physics Letters B, 801:135140, 2020.*

Peer-reviewed publications stemming from presentations at international conferences

1. M. Piersa, A. Korgul, L.M. Fraile, **J. Benito**, E. Adamska, R. Álvarez-Rodríguez, A.E. Barzakh, G. Benzoni, T. Berry, M.J.G. Borge, M. Carmona, K. Chrysalidis, G. Correia, C. Costache, T. Day Goodacre, D.V. Fedorov, V.N. Fedosseev, G. Fern¸ez-Martínez, M. Fila, D. Galaviz, R. Grzywacz, C. Henrich, A. Illana, Z. Janas, K. Johnston, V. Karanyonchev, M. Kicińska-Habior, R. Lică, M. Madurga, I. Marroquín, B. Marsh, C. Martínez, C. Mazzocchi, K. Miernik, R. Mihai, B. Olaizola, S. Paulaskalas, J.-M. Rģis, S. Rothe, V. Sánchez-Tembleque, G. Simpson, Ch. Sotty, L. Stan, M. Stănoiu, M. Stryjczyk, A. Turturica, J.M. Udías, V. Vedia, A. Villa, W.B. Walters. Investigation of Low-lying States in ^{133}Sn Populated in the β Decay of ^{133}In Using Isomer-selective Laser Ionization. *Acta Phys. Pol. B, 49:523, 2018.*

2. S. Viñals, E. Nácher, O. Tengblad, **J. Benito**, M.J.G. Borge, P. Figuera, L.M. Fraile, H.O.U. Fynbo, A. Gad, J. Jensen, B. Jonson, R. Lică, I. Marroquín, M. Munch, T. Nilsson, J.D. Ovejas, A. Perea, K. Riisager, S. Smain, C. Sotty. The Most Accurate Determination of the ^{8}B Half-life. *Acta Phys. Pol. B, 51:717 2020.*

3. E. Adamska, A. Korgul, A. Fijałkowska, K. Miernik, M. Piersa, R. Canavan, D. Etasse, N. Jovančević, M. Lebois, M. Rudigier, D. Thisse, J.N. Wilson, P. Adsley, A. Algora, M. Babo, K. Belvedere, **J. Benito**, A. Blazhev, G. Benzoni, A. Boso, S. Bottoni, M. Bunce, R. Chakma, N. Cieplicka-Oryńczak, M. Ciemała, S. Collins, L. Cortés, P. Davies, C. Delafosse, M. Fallot, B. Fornal, L.M. Fraile, R.-B. Gerst, D. Gjestvang, A. Gottardo, V. Guadilla, G. Hafner, K. Hauschild, M. Heine, C. Henrich, I. Homm, F. Ibrahim, Ł.W. Iskra, P. Koseoglou, T. Kröll, T. Kurtukian-Nieto, L. Le-meur, S. Leoni, J. Ljungvall, A. Lopez-Martens, R. Lozeva, I. Matea, J. Nemer, S. Oberstedt, W. Paulsen, Y. Popovitch, L. Qi, D. Ralet, P.H. Regan, D. Reygadas Tello, K. Rezynkina, V. Sánchez-Tembleque,

C. Schmitt, P.-A. Söderström, C. Surder, G. Tocabens, V. Vedia, D. Verney, N. Warr, B. Wasilewska, J. Wiederhold, M. Yavahchova, F. Zeiser. γ-ray Spectroscopy of ^{85}Se Produced in ^{232}Th Fission. *Acta Phys. Pol. B, 51:843, 2020.*

Conference presentations

1. VIII CPAN Days, Zaragoza, Spain. November, 28-30, 2016.

   Talk: *Gamma and Fast-timing spectroscopy of ^{29,30}Mg nuclei.*

   Authors: **J. Benito**, L.M. Fraile, and the IS414 collaboration

2. 3rd conference Advances in Radiactive Isotope Science (ARIS2017). Keyston Colorado, U.S.A. May 28- June 2, 2017.

   Talk: *Gamma and fast-timing spectroscopy around ^{132}Sn from the β-decay of In isotopes.*

   Authors: **J. Benito**, L.M. Fraile, A. Korgul, M. Piersa, and the IS610 collaboration.

3. XXXVI Reunión Bienal de la Real Sociedad Española de Física. Santiago, Spain. July 17-21, 2017.

   Talk: *Gamma and fast-timing spectroscopy around ^{132}Sn from the β-decay of In isotopes.*

   Authors: **J. Benito**, L.M. Fraile, A. Korgul, M. Piersa, and the IS610 collaboration.

4. Nuclear Structure and Dynamics 2019 (NSD2019). Venice, Italy. May 12-17, 2019.

   Talk: *Gamma and fast-timing spectroscopy around ^{132}Sn from the β-decay of In isotopes.*

   Authors: **J. Benito**, L.M. Fraile, A. Korgul, M. Piersa, and the IS610 collaboration.

5. International Nuclear Physics Conference 2019 (INPC2019). Glasgow, U.K. July 29-August 2, 2019.

   Talk: *Observation of the β-decay of ^{135}In.*

   Authors: **J. Benito**, M. Piersa, L.M. Fraile, A. Korgul, and the IS610 collaboration

6. XI CPAN Days. Oviedo, Spain. October 21-23, 2019.

   Talk: *Fast-timing studies of ^{133}Sn and ^{134}Sn excited states.*

   Authors: **J. Benito**, M. Piersa, L.M. Fraile, A. Korgul, and the IS610 collaboration